Development of the C* Fracture Test for Asphalt Concrete Mixtures

by

Jeffrey Stempihar

A Dissertation Presented in Partial Fulfillment
of the Requirements for the Degree
Doctor of Philosophy

Approved April 2013 by the
Graduate Supervisory Committee:

Kamil Kaloush, Chair
Matthew Witczak
Michael Mamlouk

ARIZONA STATE UNIVERSITY

May 2013

ABSTRACT

Laboratory assessment of crack resistance and propagation in asphalt concrete is a difficult task that challenges researchers and engineers. Several fracture mechanics based laboratory tests currently exist; however, these tests and subsequent analysis methods rely on elastic behavior assumptions and do not consider the time-dependent nature of asphalt concrete. The C* Line Integral test has shown promise to capture crack resistance and propagation within asphalt concrete. In addition, the fracture mechanics based C* parameter considers the time-dependent creep behavior of the materials. However, previous research was limited and lacked standardized test procedure and detailed data analysis methods were not fully presented.

This dissertation describes the development and refinement of the C* Fracture Test (CFT) based on concepts of the C* line integral test. The CFT is a promising test to assess crack propagation and fracture resistance especially in modified mixtures. A detailed CFT test protocol was developed based on a laboratory study of different specimen sizes and test conditions. CFT numerical simulations agreed with laboratory results and indicated that the maximum horizontal tensile stress (Mode I) occurs at the crack tip but diminishes at longer crack lengths when shear stress (Mode II) becomes present.

Using CFT test results and the principles of time-temperature superposition, a crack growth rate master curve was successfully developed to describe crack growth over a range of test temperatures. This master curve can be applied to pavement design and analysis to describe crack propagation as a function of traffic conditions and pavement temperatures.

Several plant mixtures were subjected to the CFT and results showed differences in resistance to crack propagation, especially when comparing an asphalt rubber mixture to a conventional one. Results indicated that crack propagation is ideally captured within a given range of dynamic modulus values.

Crack growth rates and C* prediction models were successfully developed for all unmodified mixtures in the CFT database. These models can be used to predict creep crack propagation and the C* parameter when laboratory testing is not feasible. Finally, a conceptual approach to incorporate crack growth rate and the C* parameter into pavement design and analysis was presented.

ACKNOWLEDGEMENTS

I begin by expressing my most sincere gratitude, love and respect to my wife and best friend Jaime Stempihar. She has been alongside me through this journey and provided companionship and support along the way. Her encouragement during exciting and challenging times helped me to remain focused on the outcome.

Dr. Kamil Kaloush, my advisor and mentor during my graduate work at Arizona State University, deserves my utmost appreciation and thanks. He was integral in recruiting me to ASU and has since helped me grow academically, professionally, and personally. He secured financial funding for my research work and supported my ideas and efforts. His passion for teaching and efforts to encourage student education and success will serve as a model for my future academic endeavors.

I want to thank Dr. Matthew Witczak for serving on my committee and for constantly challenging and pushing me in courses and research efforts. I need to especially thank him for allowing me to co-instruct the Airport Pavement Design course at ASU. This allowed me to begin pursuing one of my career goals of educating future engineers and scientists.

Thank you to Dr. Michael Mamlouk for serving on my committee and for providing valuable feedback on my research work and for supporting my professional development at ASU. I want to thank Dr. Claudia Zapata and Dr. Shane Underwood for their support, valuable discussions, ideas and feedback on my research work. My appreciation goes to Dr. Soyoung Ahn for use of her video recording equipment during this project. Also, I owe much gratitude and thanks to Dr. Krishna Biligiri, Dr. Waleed Zeiada, Dr. Mena Souliman and Dr. M. Carolina Rodezno. Their efforts helped my

transition to Arizona State University and I want to thank them for their assistance, guidance, friendship and inspiring conversations.

Special thanks to Kenneth Witczak for providing training with laboratory equipment and practices. His friendship and overall assistance were significant contributions to me personally and professionally. Thanks to Peter Goguen for laboratory support assistance and efforts to maintain research equipment.

Dr. Hansoo Kim provided essential support and training with finite element modeling software and methods and his guidance was very important. His efforts are much appreciated and I owe him thanks and gratitude.

Thanks and appreciation is due to Tina Pourshams, David Ramsey, Padmini Gudipudi and Ryan Stevens. Their assistance in the laboratory and with data analysis helped immensely with my research projects.

I express my gratitude to Mr. Bob McGennis of Holly Frontier, Mr. Doug Carlson of Liberty Tire Recycling, Mr. Mark Belshe of the Rubber Pavements Association, Mark Edsall of Tri State Materials and Mr. George Way of Consulpav for their efforts in identifying and providing materials which were tested in this study.

Finally, thank you to my ASU friends who have helped me to grow personally and professionally: Jordan Reed, Daniel Rosenbalm, Ramadan Salim, Abdulaziz Alosta, Ashraf Alrajhi, Matild Dosa, Carmen Parks, Rubben Lolly, Ali Fakih and Sam Enmon.

TABLE OF CONTENTS

Page

CHAPTER Page

CHAPTER Page

CHAPTER Page

LIST OF FIGURES

FIGURE Page

FIGURE Page

FIGURE Page

FIGURE Page

FIGURE Page

FIGURE Page

FIGURE Page

FIGURE Page

LIST OF TABLES

TABLE Page

TABLE Page

Chapter 1

1 INTRODUCTION

Historically, asphalt concrete has been the most widely used paving material in the United States; accounting for nearly 94% of paved roadways (FHWA, 2001). Since its first application to a road surface in the U.S. in 1876, asphalt concrete has been continuously improved and modified to provide a safe and passable road surface (Huang, 2004). However, this material has a finite lifespan and premature deterioration and failure of a pavement structure can cost transportation agencies millions of dollars in repair and replacements. Pavement failure can result from a number of distress mechanisms but traditionally, the major distresses are permanent deformation (rutting) and cracking. Thus, pavement design strives to achieve long lasting asphalt concrete pavements by minimizing or prolonging common distresses that lead to deterioration and failure. Of the major pavement distresses, this research focuses on evaluation of cracking in asphalt concrete pavements.

1.1 Background of Cracking in Asphalt Pavements

Cracking in asphalt concrete pavements can be divided into two categories: load associated fatigue cracking and thermal cracking. Typically, fatigue cracking is the result of repetitive traffic loading in combination with degradation in material properties over time. These cracks typically occur longitudinally in the wheel path. In comparison, transverse thermal cracking is the result of a tensile stress development in pavements due to diurnal or seasonal temperature changes.

In cold months/climates, cracks allow water and deicing chemicals to enter the pavement structure and subsequent freeze-thaw cycles can advance crack deterioration

and produce uneven pavement surfaces. Also, in warm or hot months/climates, water in the base layer can cause pumping or loss of fines. This typically results in settlement in the vicinity of the crack. All of these issues affect ride quality, safety and directly impact the service life of a pavement (Vinson et al, 1989). In addition, excessive cracking presents a challenge for future pavement rehabilitation strategies and can result in reflective cracking in asphalt concrete overlays.

1.1.1 Load Associated Fatigue Cracking

Classical load-related fatigue cracking has been described as bottom-up cracking and typically occurs in thin asphalt concrete layers (<8"). In this cracking mechanism, tensile stresses develop at the bottom of the asphalt concrete pavement and progress upward with repeated loading cycles.

Another load-related fatigue cracking mechanism is top-down cracking which typically occurs in thick asphalt concrete layers (>8") when large tensile stresses and strains develop at a shallow depth below the surface; about one top one third of the total thickness. Traffic loading causes a crack to initiate at this critical depth and it propagates from the top of the pavement layer downward.

In either case, crack propagation rate and extent of cracking is dependent on the material stiffness, load/tire pressure, stresses and fracture properties of asphalt concrete.

1.1.2 Thermal Cracking

Thermal cracking in asphalt pavements can occur by two different mechanisms; low temperature cracking and thermal fatigue cracking. Low temperature cracking is the result of large thermally induced stress development as the pavement shrinks. When induced stresses exceed the tensile strength of the asphalt concrete, a transverse crack

develops and eventually propagates through the pavement layer. Thermal fatigue cracking occurs in regions where cyclic or diurnal temperature differentials exist. These temperature differentials produce a thermal gradient in a pavement layer which results in development of thermal stresses. Although these stresses may be less than the tensile strength of the material, repetitive diurnal cycles eventually induce a fatigue related thermal crack in the pavement (Vinson et al, 1989b).

1.2 Incorporation of Fracture Mechanics into Pavement Design

Even with modern advances in pavement engineering, attempts to quantify and model cracking in asphalt pavement have proved extremely challenging due to the visco-elastic behavior of asphalt concrete and the complex stress states which exist in pavement layers due to loading or thermally induces stresses. Since its introduction to asphalt concrete by Majidzadeh (1976), fracture mechanics has been used to a limited extent to characterize cracking in flexible pavement design.

The American Association of State Highway Transportation Officials (AASHTO) Mechanistic-Empirical Pavement Design Guide (MEPDG, or now Pavement ME) is the most advanced pavement design procedure available and predicts thermal cracking through use of the fracture mechanics based TCMODEL. TCMODEL utilizes the stress intensity factor (K) to describe crack tip stresses and the Paris law to describe crack propagation. While considered a significant advancement, TCMODEL has shortcomings and does not accurately characterize the crack resistance of certain modified asphalt mixtures when compared to field data (Zborowski, 2007). To predict thermal cracking, TCMODEL uses material properties obtained from the indirect tensile creep and strength tests. These properties include the tensile strength (S_t) at -10°C and the slope of creep

compliance (m). Work performed by Zborowski (2007) at Arizona State University recommended the addition of the following parameters to TCMODEL: total fracture energy (G_f) and intercept of the creep compliance master curve. TCMODEL uses these inputs to predict the stress intensity factor (K) and the "A" and "m" parameters of the Paris law which gives a relationship to describe crack propagation.

In addition to prediction of thermal cracking during design, laboratory evaluation of crack resistance of asphalt concrete has also proven to be a difficult task. Several laboratory tests have either been developed or extended from other materials to asphalt concrete in order to measure fracture mechanics parameters in the laboratory. The more common laboratory fracture tests include the semi-circular bend test (SCB), direct compact tension test (DCT), single edge notched beam (SEB) and indirect tension test (IDT). Common linear elastic fracture mechanics (LEFM) parameters obtained from these tests include: stress intensity factor (K) and fracture energy (G) which require the assumption of linear elastic material behavior. The *J* parameter can also be obtained from certain tests and assumes elastic-plastic behavior. Although the aforementioned tests deserve great merit and consideration, a standard test or a single parameter has not been fully developed which can provide reliable fracture properties of asphalt concrete (Wagoner et al, 2005a). In addition, Ioannides (1997) discusses the limitations of the K and G parameters in that they are highly specimen-size dependent and states that they do not truly represent intrinsic material properties.

The C* Line Integral Test has been used to a limited extent in asphalt concrete cracking evaluation despite being identified as a promising test method (Vinson et al, 1989). Data recorded include load and crack length as a function of time. This test uses

a notched disk specimen and standard indirect tension test (IDT) equipment and the simple test geometry allow for specimens to be obtained easily from the Superpave gyratory compactor and from cores taken from field pavements.

Since its application to asphalt pavement by Abdulshafi (1983), the test has been used to successfully rank crack resistance of asphalt pavements (Abdulshafi, 1983; Abdulshafi and Kaloush, 1988; Kaloush et al, 2010). The C* parameter obtained from this test considers the time-dependent behavior of asphalt and can be converted to the stress intensity factor (K) when elastic behavior of asphalt concrete prevails at low temperatures. This alone makes the C* a very universal parameter to describe crack resistance behavior of asphalt concrete. Research efforts are needed to develop a standard test procedure, improved measurement of crack propagation and to evaluate stress and strain distributions within the notched disk specimen geometry.

Finally, the C* parameter and crack propagation rate information from the C* Fracture Test may potentially be used to develop a model for top-down cracking or to improve the thermal cracking module (TCMODEL) in the Pavement ME by describing the crack propagation phase. However, refinement of the test procedure and a more thorough understanding of the C* parameter itself must first be developed.

1.3 Problem Statement

The ability to distinguish crack resistance behavior and rank mixture performance in the laboratory can be a crucial asset to pavement engineers and also can serve in forensic analysis of pavement failures. In recent years, use of modified asphalt pavement such as asphalt-rubber and fiber reinforcement has increased due to desirable crack resistance properties, among others. Thus, it is essential to standardize a laboratory test

within the pavement community which can be used to evaluate crack resistance of asphalt concrete mixtures.

In addition, the TCMODEL in the Mechanistic Empirical Pavement Design Guide (MEPDG), used to predict thermal cracking during design, is limited in that it only considers a single asphalt layer system and has difficulty in predicting cracking for modified asphalt mixtures. Many pavement designs now utilize multiple layers consisting of asphalt concrete with different properties and it is difficult to select properties from only one layer to represent the pavement system. Use of C* and crack propagation rate may help to model cracking through multi-layered systems.

Although several laboratory tests have been considered and have received significant research effort, existing fracture tests for asphalt concrete produce variable results. These tests often use specimen geometries which can be time-consuming to produce and the stress is applied to the crack tip through indirect means (eg, 3-point bending). Also, initial test startup can be costly and may not be performed on common laboratory equipment. In addition, the stress intensity factor (K) parameter which is commonly used to describe the stress field surrounding a crack tip, assumes asphalt concrete exhibits linear elastic behavior. Although this is considered valid at low temperatures, the viscous response should be considered when evaluating pavement performance at intermediate temperatures.

The overall goal of this study is to develop a standard test procedure for the C* Fracture Test and to evaluate it as a suitable crack resistance and propagation test. In addition, the C* parameter will be used to rank crack resistance of field produced, virgin

and modified asphalt mixtures. Finally, a conceptual method to incorporate the C* parameter into pavement analysis and design is presented.

1.4 Research Objectives

The overall objectives of the research study include the following tasks:

1. Conduct an extensive literature search regarding asphalt concrete fracture test methodologies including the C* Fracture Test. This search will also encompass crack propagation models.
2. Evaluate and refine the current C* Fracture Test method by performing laboratory tests and finite element analysis of different test geometries and conditions. From these analyses, recommend a standard C* Fracture Test (CFT) procedure.
3. Evaluate the potential of the CFT and C* parameter to distinguish between asphalt concrete mixtures in terms of crack resistance and propagation using laboratory and plant produced mixtures Data will be compiled into an ASU CFT database.
4. Develop initial C* and crack growth rate prediction models which can potentially be used as input for mechanistic-empirical pavement design software. In addition, outline a conceptual method to incorporate the C* parameter into pavement design and analysis.

1.5 Scope of Research

In order to accomplish the research objectives identified as part of the project, the scope of work is divided into five main tasks which are described in the following paragraphs.

Task 1 includes an extensive literature review pertaining to asphalt concrete fracture test methodologies, fracture mechanics concepts, and existing thermal cracking models. Specifically, this effort focuses on the C* Line Integral Test, C* parameter, crack propagation models and other fracture mechanics based laboratory tests.

Task 2 involves development of a standard C* Fracture Test (CFT) procedure. To accomplish this task, finite element analysis of potential specimen geometries will be conducted to better understand the stress distributions within the sample. A CFT laboratory study will simultaneously consider test temperature, sample size, loading rate and data acquisition methods.

Task 3 evaluates the ability of the CFT and C* parameter to distinguish between asphalt concrete mixtures in terms of crack resistance and propagation. Modified and unmodified plant produced mixtures from several sources will be compacted in the ASU laboratory and tested using the proposed CFT procedure. All data will be complied into a C* database which can be used in future studies to correlate laboratory CFT results to actual field performance.

Task 4 will develop initial C* and crack growth rate prediction models using CFT data collected in Task 2 and Task 3. These models can potentially serve to describe crack growth rates in pavement layers at the intermediate temperature range. A conceptual method to incorporate the C* parameter and crack growth into pavement analysis and design is presented.

1.6 Report Outline

This document has been divided in to the following Chapters:

1. Introduction
2. Background – Fracture Mechanics
3. Literature Review
4. C* Specimen Geometry and Test Condition Study
5. Finite Element Modeling of C* Fracture Test Specimens
6. Development of a Crack Growth Rate Master Curve
7. Development of ASU C* Database
8. Development of C* and a* Prediction Models
9. Summary, Conclusions and Recommendation

References

Appendices

Chapter 2

2 BACKGROUND – FRACTURE MECHANICS

Modern work on the fracture of materials dates back to the early 1900's when the increased use of engineered materials led catastrophic failures over time. Typically, high strength materials have low fracture toughness and the presence of cracks may cause these types of materials to fail at stresses well below design strength. This fracture of high strength material under low stresses led to the development of fracture mechanics (Broek, 1986).

Research and development of fracture mechanics concepts accelerated after the end of World War II. By 1960, researchers had established linear elastic fracture mechanics and began to consider crack tip plasticity. Around 1980, the background was sound for elastic-plastic fracture mechanics. Since that time, research has accelerated and time-dependent fracture mechanics based on non-linear viscoelastic or viscoplastic material behavior has been developed (Anderson, 2005).

Majidzadeh et al (1976) first applied fracture mechanics to asphalt concrete in attempt to improve the design of bituminous concrete. Since then, the extension of fracture mechanics concepts and principles to asphalt concrete materials has mainly been modeled after work done on metals, rocks and other solid materials and efforts remained focused on linear elastic fracture mechanics.

More recently, fracture mechanics concepts have been incorporated into the current American Association of State Highway Transportation Officials (AASHTO) Mechanistic-Empirical Pavement Design Guide (MEPDG) for pavements through use of the TCMODEL module for thermal cracking prediction. TCMODEL uses material

property inputs to predict the stress intensity factor (K) and the "A" and "m" parameters of the Paris law which gives a relationship to describe crack propagation (Zborowski, 2007). These concepts will be discussed further in the following chapter.

It is important to note that concepts presented in this section are not material specific but rather a summary of fracture mechanics principles that are applicable to asphalt concrete as well as other solid materials. Specific application to asphalt concrete will be discussed in subsequent chapters. The main areas of fracture mechanics covered herein include linear elastic, elastic-plastic and time-dependent fracture mechanics.

2.1 Fracture Mechanics Concepts

The field of fracture mechanics has experienced extensive developments over time through use of modern technology and well established historical work. Specifically, the effects of material properties on fracture have led to the development of several fracture mechanic approaches which can be applied to materials with applicable behavior. Figure 1 presents an abbreviated schematic of the development of these principles over time with respect to material behavior.

Initial developments in fracture mechanics could only be applied to linear-elastic material under quasi-static conditions. However, advances in technology and research led to elastic-plastic fracture mechanics which considered plastic deformation under quasi-static conditions. Recent advances in fracture mechanics led to viscoelastic, viscoelastic and dynamic theories which consider time as an additional variable. Elastic-plastic, viscoelastic and viscoplastic are typically referred to as non-linear fracture mechanics (Anderson, 2005).

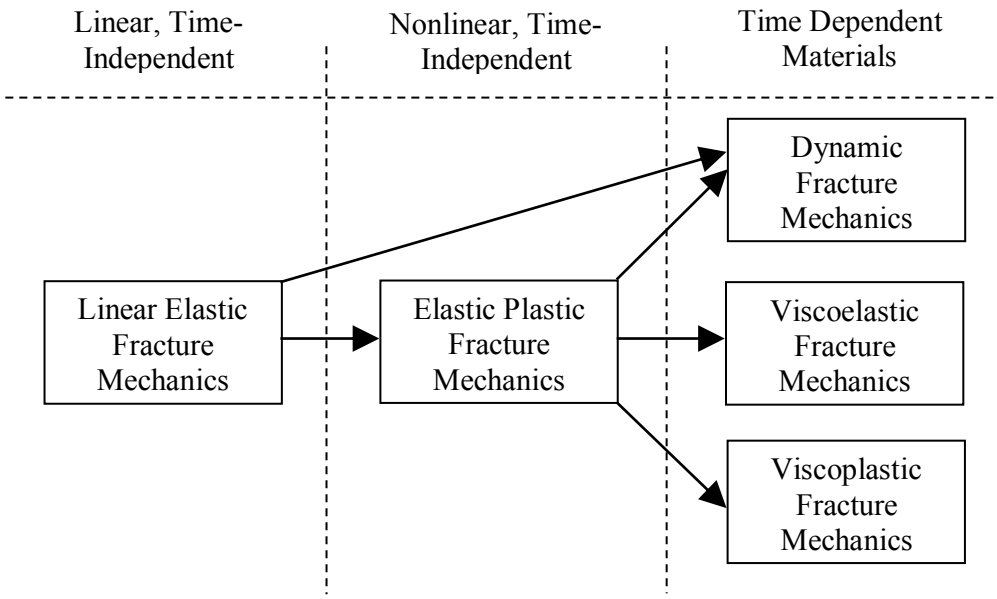

Figure 1 Schematic development of fracture mechanic approaches over time (Anderson, 2005).

2.1.1 Loading Modes

In fracture mechanics, three main modes of stress can be applied to a crack in a solid material. Mode I (opening mode) exists when a stresses are applied perpendicular to the crack plane resulting in a tensile stress at the crack tip. Sliding mode (Mode II) can be described when shear stresses along the crack plane are the result of opposite loads applied in the direction of the crack plane. Finally, Mode III results from shear stresses acting perpendicular to the crack plane (Broek, 1986). Figure 2 depicts three common crack stress modes. It is important to note that stresses can be applied in single or combination of these three modes. All three modes can exist in asphalt pavement individually or in combination.

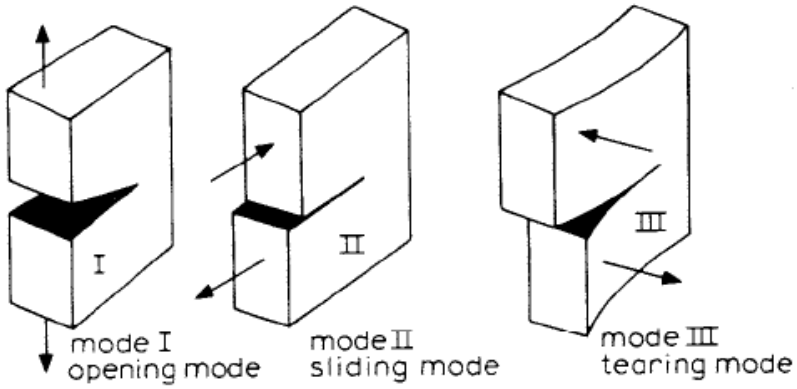

Figure 2 Modes of crack stresses (Broek, 1986).

As part of SHRP A-005A, Lytton, Uzan et al. (1993) report that mode II loading is the most predominant mode for crack propagation in asphalt pavements. This is based on finite element analysis of pavement structures. In this analysis, mode I stress intensity factors became negative after short crack length values and it was concluded that mode I loading may be more critical to describe crack initiation. In comparison, Mode II stress intensity factors continually increased with increasing crack depth. Thus, it was concluded that mode II loading will result in crack propagation to the surface.

Uzan (1997) reported that crack propagation is a combination of Mode I (opening) and Mode II (shearing). However, under opening mode, cracks propagate to about approximately two thirds of the pavement thickness. In comparison, shearing contributes to crack propagation throughout the entire pavement layer. Thus, it can be concluded mixed mode cracking should be considered to describe crack propagation in pavement layers.

2.1.2 Plane Stress versus Plane Strain

Plane stress is a stress state in which the normal stress (σ_z) and shear stresses (τ_{yz}, τ_{zx}) acting perpendicular to the x-y plane are assumed to be zero (Janssen et al, 2002). A

typical geometry satisfying these conditions is that with one dimension (ie, thickness) which is much smaller compared to the others such as a thin asphalt core loaded diametrically. Loading is typically uniform over the thickness of the specimen. Large plastic deformation zones typically promote plane stress conditions (Broek, 1986).

In comparison, plane strain conditions exist when the strain (ε_z) perpendicular to the x-y plane and shear strains (ε_{yz}, ε_{zx}) are assumed to be zero (Janssen et al, 2002). Specimens adhering to this condition typically have one dimension (z-direction) much larger with respect to the other two such as a thick asphalt core loaded diametrically. Broek (1986) reports that small plastic zones typically promote plane strain. Due to material constraint in the thickness direction, yielding is minimal.

2.2 Linear Elastic Fracture Mechanics

Linear elastic fracture mechanics (LEFM) is the oldest and most straightforward concept to employ when considering fracture of materials. These methods, developed in the early 1900's, can only be applied to materials which obey Hooke's law and do not account for plastic deformation near the crack tip. The main two methods used in LEFM include the stress intensity and the energy release rate approaches (Anderson, 2005).

2.2.1 Elastic Stress Field Approach

In LEFM, the stress intensity approach is characterized by a stress intensity factor (K_I) which is used to describe the stress field surrounding a crack tip in a solid body. If the assumption is made that the stress field surrounding the crack tip is linear elastic, K_I can be used to describe all the stresses surrounding the crack tip (Broek, 1986; Anderson, 2005).

To present a better understanding of the relationship of the stress intensity factor to the stress field surrounding a crack tip, consider a crack in any solid body along with stresses acting on any element *dxdy* within that body (Figure 3). For this theoretical concept, it is important to assume that the crack is extended throughout the entire thickness of the specimen and that the material is elastic.

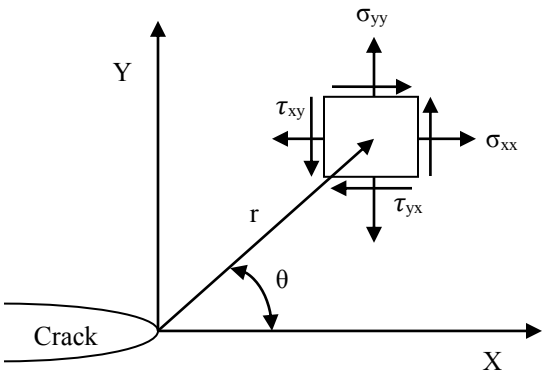

Figure 3 Stresses near a crack tip acting on any element dxdy (Anderson, 2005*).*

For Mode I loading, the stresses acting on any element *dxdy* within the body at any distance "r" from the crack tip and angle "θ" with respect to the crack plane can be related to the stress intensity factor (K_I) according to Equations 2.1, 2.2 and 2.3 (Anderson, 2005*)*:

$$\sigma_{xx} = \frac{K_I}{\sqrt{2\pi r}} * cos\left(\frac{\theta}{2}\right)\left[1 - sin\left(\frac{\theta}{2}\right)sin\left(\frac{3\theta}{2}\right)\right] \quad \textbf{2.1}$$

$$\sigma_{yy} = \frac{K_I}{\sqrt{2\pi r}} * cos\left(\frac{\theta}{2}\right)\left[1 + sin\left(\frac{\theta}{2}\right)sin\left(\frac{3\theta}{2}\right)\right] \quad \textbf{2.2}$$

$$\tau_{xy} = \frac{K_I}{\sqrt{2\pi r}} * cos\left(\frac{\theta}{2}\right)sin\left(\frac{\theta}{2}\right)cos\left(\frac{3\theta}{2}\right) \quad \textbf{2.3}$$

Where:

$\sigma_{xx}, \sigma_{yy}, \tau_{xy}, \tau_{yx}$ = stresses acting on any element *dxdy*,

K_I = stress intensity factor for Mode I loading,

θ = angle with respect to the crack plane, and

r = distance from crack tip to element *dxdy*.

For pure Mode I loading and (θ=0), the stresses in the x and y directions are equivalent according to Equation 2.4 in which all variables have been previously defined (Anderson, 2005). This assumes the principle plane follows the crack plane and thus no shear stresses along the crack plane are zero.

$$\sigma_{xx} = \sigma_{yy} = \frac{K_I}{\sqrt{2\pi r}} \qquad \textbf{2.4}$$

As the radius (r) approaches zero near the crack tip, the stresses become asymptotic to infinity or radius equals zero and thus is considered a stress singularity condition. The above equation is only valid in the zone surrounding the crack tip defined by the $1/\sqrt{r}$ stress singularity (Anderson, 2005). Figure 4 shows a conceptual plot of the stress normal to the crack plane versus distance from the crack tip.

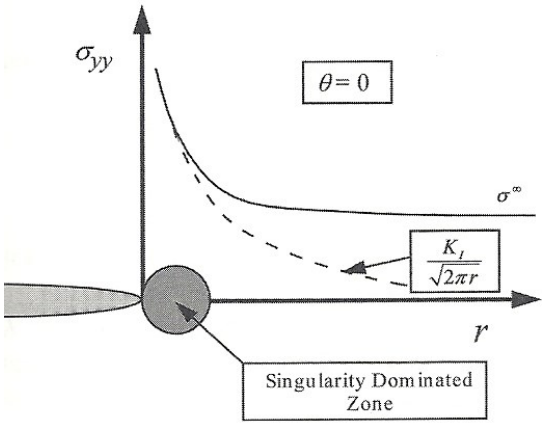

Figure 4 Normal stress versus distance from crack tip (Anderson, 2005).

The K_I parameter can be computed numerically through use of Equation 2.5 (Anderson, 2005). Accepted equations for the f (a/W) parameter have been derived for various geometries and can be found in fracture mechanics textbooks.

$$K_I = \frac{P}{B\sqrt{W}} f\left(\frac{a}{W}\right) \qquad \textbf{2.5}$$

Where:

P = applied force,

B = specimen thickness, and

$f\left(\frac{a}{W}\right)$ = dimensionless function based on specimen geometry.

Consider the assumption that local failure occurs at a given critical combination of stresses and strains. Thus, fracture occurs at this critical stress and strain state which is considered the critical stress intensity factor (K_{IC}). This K_{IC} parameter can be used to characterize the fracture toughness or to describe the ability of a material to resist cracking (Anderson, 2005; Li and Marasteanu, 2009). However, it is important to note that K_{IC} has a strong dependence on specimen size (Ioannides, 1997; Janssen et al, 2002).

2.2.2 Energy Balance Approach

The energy release rate (G) was first proposed by Irwin in the mid 1950's as an equivalent and more practical method to the Griffith energy balance which considered crack formation or growth under a net decrease in energy (1st law of thermodynamics). Griffith noted that crack formation or crack propagation can occur if the respective action causes total energy decreases or remains constant. According to this theory, crack growth can occur when the available potential energy within a body exceeds the surface tension.

Comparatively, the energy release rate (G) can be defined as a negative rate of potential energy change per change in crack area. Equation 2.6 can be used to represent the energy release rate for a wide plate in plane stress conditions and having a crack length of 2a (Anderson, 2005):

$$G = \frac{\pi \sigma^2 a}{E} \qquad \textbf{2.6}$$

Where:

G = energy release rate,

σ = applied stress,

a = crack length, and

E = modulus of elasticity

In this approach, G_c represents the critical value at which crack extension begins and thus can be considered the fracture toughness of the material of interest. The energy release rate can also be called the crack driving or crack extension force (Anderson, 2005).

The previously discussed stress intensity factor, K and G are related for linear elastic materials according to the following equation (Anderson, 2005).

$$G = \frac{K_I^2}{E'} \qquad \textbf{2.7}$$

Where:

E' = Young's modulus, E (plane stress)

$E' = E/(1 - \nu^2)$ (plane strain)

ν = Poisson's ratio

2.2.3 Crack Tip Plasticity

In linear elastic fracture mechanics (LEFM), the stresses at the crack tip are considered infinite. However, in reality the stresses at the crack tip must be finite because a crack tip radius exists. Relaxation of crack tip stresses can occur due to plasticity and thus linear elastic fracture mechanics becomes a less accurate approach. In cases with moderate plastic deformation, correction factors can be applied to LEFM. However, as the inelastic region surrounding the crack tip grows and large-scale yielding occurs, parameters describing non-linear material behavior must be applied to any analysis (Anderson, 2005).

Two methods are available to estimate the size of the crack tip plastic zone based on LEFM corrections: the Irwin approach and the strip-yield model. Of the two methods, the most common is the Irwin approach which is described below. The Irwin approach assumes that yielding occurs when the normal stress in the y-direction exceeds the yield strength of the material. At this point where plastic deformation begins, stresses must redistribute in order to remain in equilibrium and the size of plastic zone increases (Anderson, 2005). Figure 5 is a conceptual figure showing Irwin's first order (r_y) and second order (r_p) estimates of the plastic zone size. The hatched area represents stresses that need to be redistributed to surrounding material. The first order estimate is based on an elastic crack tip solution whereas the second order estimate considers the redistribution of stresses in an elastic-plastic material.

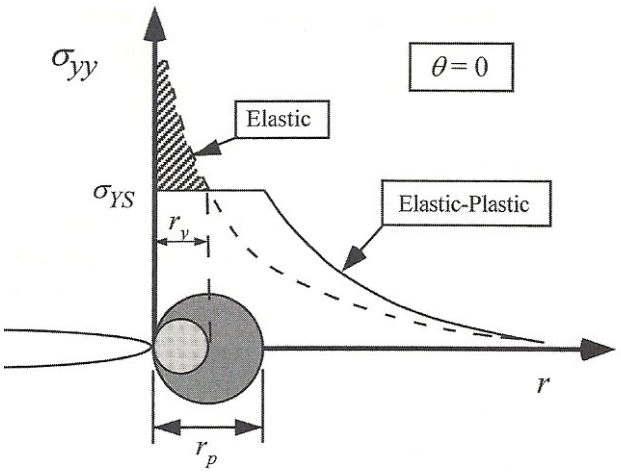

Figure 5 Schematic of Irwin's first and second order plastic zone size (Anderson, 2005).

The general shape of the plastic zone surrounding the crack tip in mode I failure is provided in Figure 6 for plan strain and plane stress conditions according to the Von Mises and Tresca criterion which are described in detail in Broek (1986) and Anderson (2005).

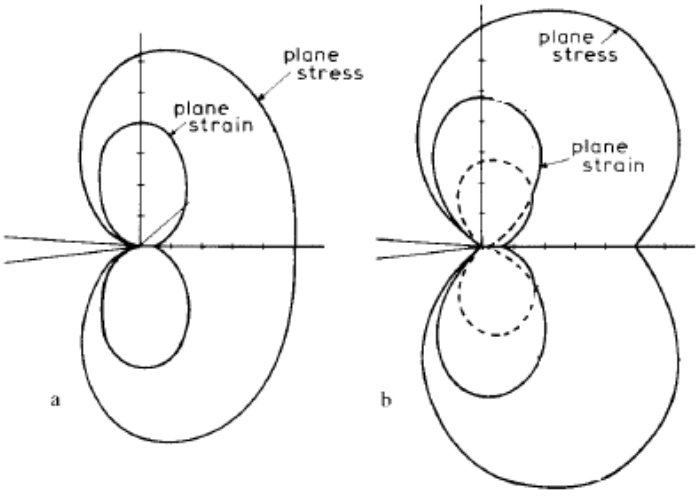

Figure 6 Schematic of crack-tip plastic zone shapes for plane stress and plane strain conditions according to a) Von Mises criterion and b) Tresca criterion (Broek, 1986).

Based on the limitation of LEFM and evolution of fracture mechanics, elastic plastic behavior should be considered in materials which exhibit this behavior. Subsequent sections of this chapter describe this approach of fracture mechanics.

2.3 Elastic-Plastic Fracture Mechanics

In reality, the application of LEFM to certain materials is not an accurate method to describe the conditions surrounding the crack tip in certain materials which have time-dependent, non-linear behavior. The crack tip region in materials which experience plastic deformation can better be described using elastic-plastic fracture mechanics.

The main elastic-plastic fracture mechanics parameters include the *J*-integral and crack tip opening displacement (CTOD). These parameters are size independent and can be used to measure fracture toughness and are not as limited as LEFM parameters (Anderson, 2005).

2.3.1 J-Integral

The *J*-integral can be described as a path independent line integral representing the non-linear energy release rate (*J*) in a cracked material (Rice, 1968). Thus, the *J*-integral provides a method of describing the energy release rate when plasticity in a material must be considered. Additional work has shown that *J* can be used to characterize the stress and strain surrounding the crack tip in non-linear material (Rice and Rosengren, 1968; Hutchinson, 1968).

This parameter is defined along an arbitrary contour surrounding the crack tip as the change in potential energy for an incremental crack extension which follows the form of Equation 2.8 (Broek, 1986; Anderson, 2005). Figure 7 provides an example of an arbitrary contour (Γ) surrounding a crack tip.

$$J = -\frac{dU}{da} \qquad \textbf{2.8}$$

Where:

dU = potential energy

da = crack length

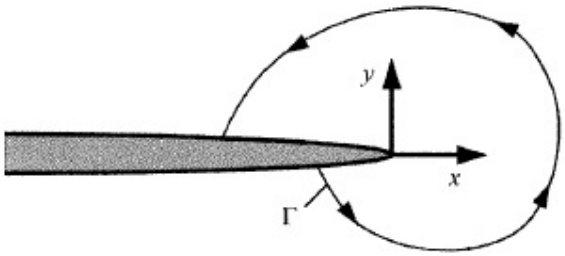

Figure 7 Example contour surrounding a crack tip (Anderson, 2005).

In a linear elastic material, *J* is related to G according to the following equation for plane stress conditions and mode I loading (Broek, 1986; Anderson, 2005):

$$J = G = \frac{K^2}{E} \qquad \textbf{2.9}$$

Where:

G = elastic energy release rate or crack driving force (force/unit crack extension)

K = stress intensity factor

E = Young's modulus

Thus, the *J*-integral can be applied to linear elastic material as well as materials that which exhibit plastic behavior. However, when considering use of this parameter, it is important to note that the *J*-integral has a limitation that unloading follows the same loading curve that is non-linear but displays elastic recovery (Broek, 1986). Also, since strain energy absorbed by an elastic-plastic material during crack growth is not

recoverable, *J* represents the energy difference absorbed by specimens with incrementally different crack lengths (Anderson, 2005).

The *J*-integral can be determined by obtaining the load – displacement curves of specimens with different crack lengths or from the same specimen with incremental increases in crack length. From these plots, the area between load – displacement curves for different specimens or for different crack lengths represents the J-integral. The *J*-integral is plotted against crack displacement (v) or crack length (a) (Broek, 1986). Figure 8 shows an example plot of *J* versus displacement as a function of increasing crack length.

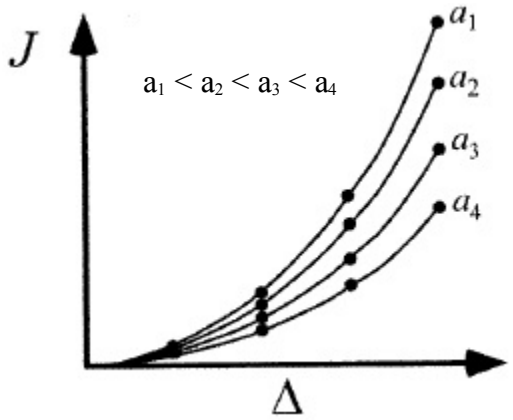

Figure 8 Example of *J*-integral versus displacement (Anderson, 2005).

2.4 Time-Dependent Fracture

When considering fracture in asphalt concrete, time must also be considered as a variable because this material can experience creep or rate-dependent deformation at certain temperatures. Due to creep behavior, linear elastic and elastic-plastic fracture mechanics are not the most accurate methods to describe crack behavior and at times can produce misleading results. The limiting factor in these methods is the assumption of quasi-static and rate independent deformation (Anderson, 2005). Figure 9 presents

typical creep behavior of a material under constant stress loading which depicts three stages of creep behavior. The initial strain (ε_o) occurs when the load is applied and the material still exhibits elastic behavior. The primary creep stage begins shortly after application of the initial load and represents the region where the creep rate begins to slow. The creep rate reaches a constant rate during the secondary sage and the material is relatively stable. In the tertiary stage, the creep rate accelerates and the material approaches failure (Anderson, 2005).

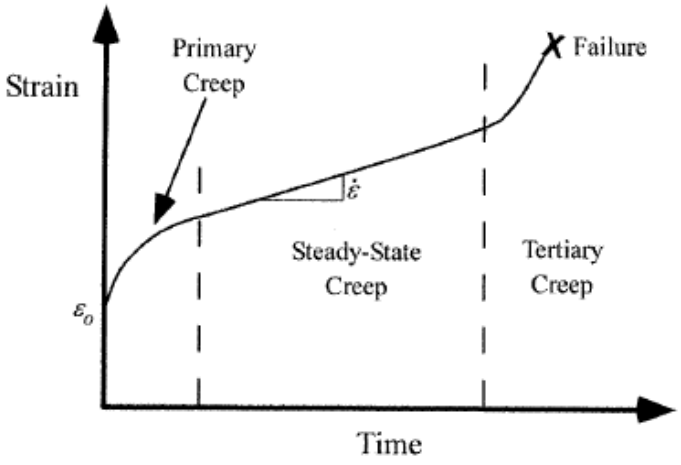

Figure 9 Typical creep behavior of a material under constant stress loading (Anderson, 2005).

Figure 10 shows a schematic of the three creep regions surrounding an arbitrary crack tip. Since the material is failing ahead of the crack tip, it makes sense that this material is in the tertiary creep stage. Thus, the materials surrounding the crack tip can be in various stages of creep behavior (Anderson, 2005). However, given the case when steady-state creep leads to global deformation, the elastic and tertiary creep can be ignored.

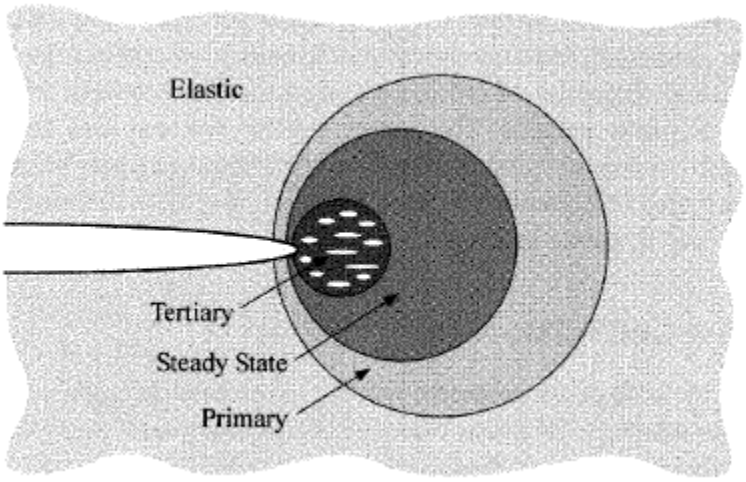

Figure 10 Creep regions near crack tip (Anderson, 2005).

Two main mechanisms are important in time-dependent fracture: creep deformation characterized by crack tip blunting and formation of micro cracks due to the accumulation of creep damage which leads to macro cracking. Crack growth occurs when the energy exceeds a critical value for either of the two methods. When equilibrium is achieved between both mechanisms, steady-state crack growth occurs in the material (O. Abdulshafi, 1992). Historically, the C* parameter has been used to characterize cracking in materials which exhibit time-dependent behavior.

2.4.1 C* Parameter

The C* parameter was first applied to fracture mechanics by Landes and Begley (1976) to describe the stresses and strains surrounding the crack tip region in metals at high temperatures. C* can be described as an energy rate line integral that describes the stress and strain rate field surrounding the crack tip in a viscous material as shown in Figure 11. This parameter was developed based on the *J*-integral which describes the crack tip conditions in elastic or elastic-plastic materials (Landes and Begley, 1976; Wu

et al., 1984; Anderson, 2005). However, the C* parameter can provide a more general case for materials which exhibit brittle and creep fracture (Abdulshafi, 1992). For stationary steady-state creep conditions, C* is a parameter which relates the creep power dissipation rate to crack propagation (Wu et al., 1984).

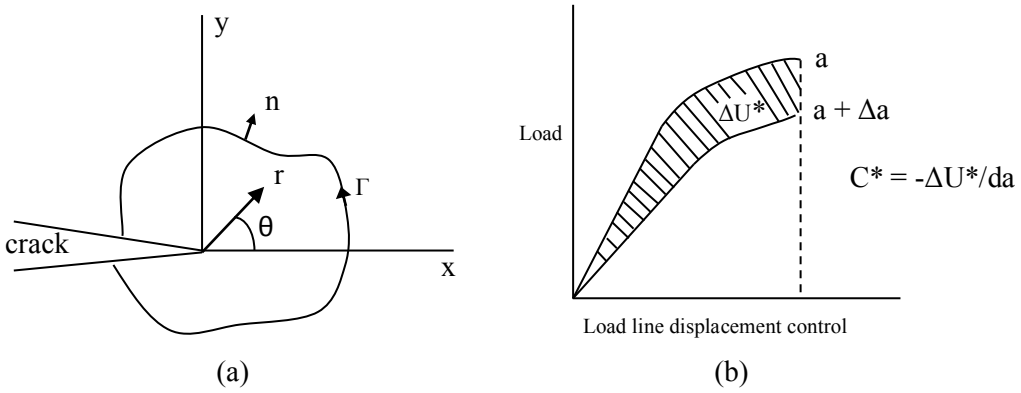

Figure 11 a) Example line integral contour and crack tip coordinate system, b) schematic of energy rate interpretation of C* (Saxena, 1980).

It is important to note that this parameter assumes that a nonlinear, steady-state creep law applies to the material which means that C* is only applicable to long-term behavior. Also, authors note that C* is not applicable to characterize creep crack growth in all ranges of cracking behavior. C* can be defined according to Equation 2.10 (Landes and Begley, 1976):

$$C^* = \int_\Gamma W^* \, dy - T_i \left(\frac{\partial \mathrm{u}}{\partial \mathrm{x}}\right) dS \qquad \textbf{2.10}$$

Where:

W*= strain energy density corresponding to σ_{ij} and $\dot{\varepsilon}_{ij}$ according to:

$$W^* = \int_0^{\dot{\varepsilon}_{mn}} \sigma_{ij} \, d \, \dot{\varepsilon}_{ij}$$

Γ = line contour from the lower crack surface, counterclockwise to the upper crack surface,

σ_{ij} = point stress,

$\dot{\varepsilon}_{ij}$ = strain rate,

T_i = traction vector defined by outward normal vector (n_j),

u_i = displacement vector, and

S = arc length along Γ.

Experimental measurement of C* is can be accomplished due to the relationship between the *J*-integral and C* parameter. *J* is defined as the energy difference between two specimens that have incrementally differing crack lengths for the same applied load. In comparison, C* can be calculated as power or energy rate difference between two specimens, loaded the same, with incrementally differing crack lengths (Landes and Begley, 1976). It is important to note that C* is typically not equal to d*J*/dt however, comparison of the values is possible (Wu et al., 1984). Given two identical specimens with different crack lengths, C* is a measure of the change in power necessary to propagate each crack a distance of "*dl"* within the material. Mathematically, C* can be expressed by Equation 2.11. Since potential energy is a function of crack length, load and displacement, the partial derivative must be taken for a fixed load (P) and displacement (û). Recall that potential energy can be found as the area under the load-displacement rate curve for any given specimen (Landes and Begley, 1976).

$$C^* = -\frac{\partial U^*}{\partial l} \qquad \textbf{2.11}$$

Where:

U* = power or energy rate for a given load, P and displacement û, given by:

$$U^* = \int_0^{\hat{u}} P d\hat{u}$$

It is important to note the equations presented by Landes and Begley (1976) are applicable for a specimen of unit thickness. Therefore, analysis of C* must consider the thickness of the specimen in calculations and can be represented by Equation 2.12 where "b" represents the specimen thickness and all other variables are previously defined (Abdulshafi, 1983).

$$C^* = \left(-\frac{1}{b} * \frac{dU^*}{dl}\right)_{P,\hat{u}} \qquad \textbf{2.12}$$

Goldman and Hutchinson (1975) developed the following proportional relationships between the C* parameter and stress and strain rate fields surrounding the crack tip. In these relationships, "r" represents the radial distance from the crack tip to the point of interest and "n" represents the creep parameter.

$$\sigma_{ij} \ \alpha \ \left(\frac{C^*}{r}\right)^{1/(n+1)} \qquad \textbf{2.13}$$

$$\dot{\epsilon}_{ij} \ \alpha \ \left(\frac{C^*}{r}\right)^{n/(n+1)} \qquad \textbf{2.14}$$

2.4.2 Experimental Evaluation of C*

Wu et al (1984) reported that since the application of the C* parameter to fracture mechanics by Landes and Beagley (1976), two methods for C* evaluation in metals have been proposed. Landes and Beagley (1976) introduced a graphical method and Harper and Ellison (1977) developed general expressions for C* based on limit analysis.

The method proposed by Landes and Beagley (1976) is summarized according to the following steps which are shown graphically in Figure 12.

1. For static loading, plot load (P) and crack length (a) as a function of time.
2. Use Step 1 data to plot load (P) versus displacement rate (Δ^*) for each incremental crack length (a). The area under each P- Δ^* curve per incremental crack length represents the power or energy rate (U*).
3. Plot U* versus crack length for each displacement rate. C* is taken as the slope of these plots.
4. Plot C* versus displacement rate, and
5. Plot the crack growth rate (a*) as a function of C*.

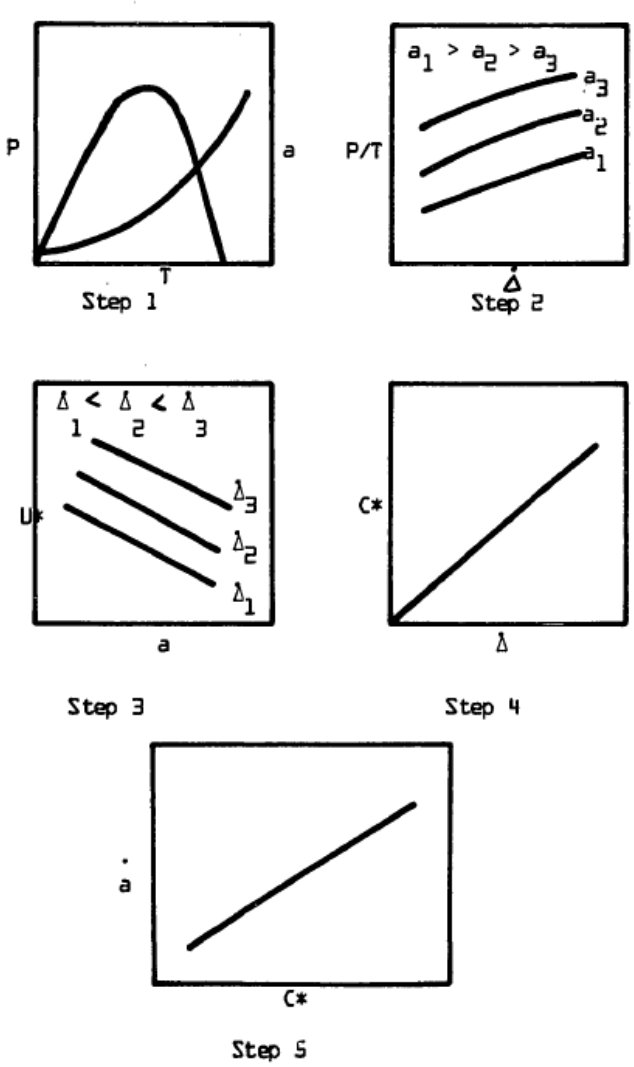

Figure 12 Schematic representation of steps used to determine C* parameter (Landes and Begley, 1976)

Harper and Ellison (1977) noted that the several steps required in this C* analysis technique can be cumbersome and also data are required from several tests to complete this analysis. In addition, this graphical technique is essentially a smoothing process of the C* data which presents the average C* over different crack lengths.

Recognizing the limitations of the previously described methods to evaluate C* from test data, Harper and Ellison (1977) used limit analysis to derive Equation 2.15

which can be used to easily calculate C* values at any point during a creep crack propagation test where load, displacement and crack growth data are collected. This approach was developed to be applicable to general cases which consider deformation ahead of the crack tip.

$$C^* = -\frac{n}{n+1} * \frac{P\dot{\Delta}}{BW}\left[\frac{1}{m} * \frac{dm}{d(\frac{a}{W})}\right] \qquad \textbf{2.15}$$

Where:

P = applied load,

$\dot{\Delta}$ = displacement rate,

B = specimen width,

W = specimen length,

a = crack length,

n = creep exponent, and

m = yield point load ratio of the tensile load limit of an un-cracked specimen to that of a cracked specimen.

Figure 13 shows a relationship between *m, dm/d(a/W)* and *(1/m)*[dm/d(a/W)]* for compact tension specimens. Harper and Ellison (1977) report that similar relationships have been formulated and are presented by Haigh and Richards (1974) for common geometries used in fracture testing. It should be noted that these developments and analysis were based on fracture in metals.

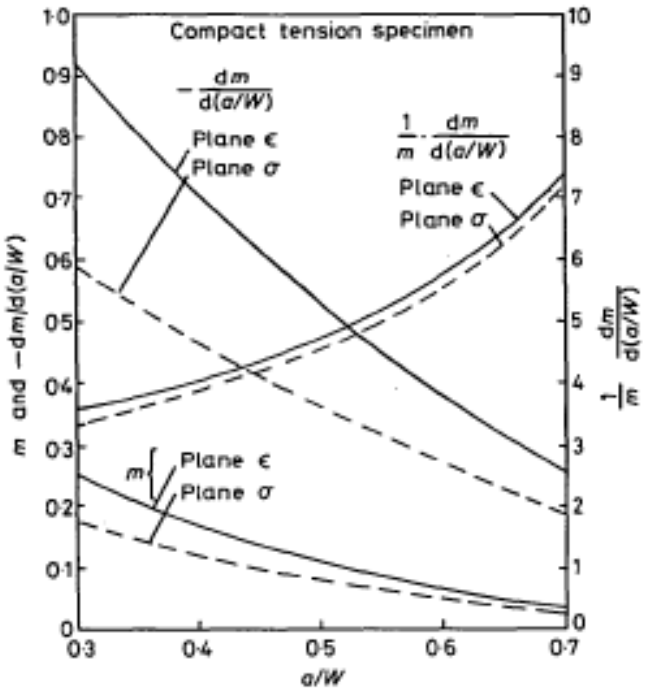

Figure 13 Relationship between *m, dm/d(a/W)* and *(1/m)*[dm/d(a/W)]* for compact tension specimens (Harper and Ellison, 1977).

2.4.3 Limitations of the C* Parameter

Application of the C* parameter relies on the assumption of steady-state creep and the ability of C* to characterize the stress and strain rate fields may be limited when large stress redistribution occurs during crack propagation (Harper and Ellison, 1977).

Harper and Ellison (1977) report that one of the conceptual issues with the C* parameter lies in the fact that there is no physical meaning of the U* function in creep theory. Specifically, the creep energy dissipation rate which equals the power applied to the specimen does not have physical meaning. U* is proportional to the power applied and thus, C* can be considered the rate of change of creep energy dissipation rate as a function of crack length. However, the C* parameter may not be able to describe total

energy dissipation with crack extension because energy associated with stress redistribution is assumed negligible.

2.5 Crack Propagation Models

The Paris Law has been applied as a mechanistic method of fatigue induced cracking in asphalt pavements. This law was introduced by Paris and Erdogan (1963) after it was observed that experimental data that crack propagation rate (dc/dN) was proportional to the fourth power of the change in stress intensity factor (K) according to Equation 2.16.

$$\frac{dc}{dN} = AK^m \qquad \textbf{2.16}$$

Where:

$\frac{dc}{dN}$ = crack propagation rate,

K = stress intensity factor, and

A, m = regression coefficients

This fourth power relationship appeared valid for several materials tested in the original study. However, additional experimental data on several different metals indicate that the value of "m" in the equation varies based on test conditions and material properties. This also holds true for asphalt concrete materials (Majidzadeh et al, 1976). For asphalt concrete pavements, the Paris Law has been used by numerous researchers (Kuai et al, 2009; Anderson, 2005; Mull et al, 2005; Von Quintus, 1994; Lytton, Uzan et al, 1993) as a relationship to relate fatigue life or crack growth as a function of applied load cycles or thermal cycles. The stress intensity factor (K) in Equation 2.16 can also be replaced with ΔK, J or ΔJ depending on the fracture parameter of interest. One drawback

of the Paris law lies in the fact that it cannot describe crack propagation behavior throughout pavement service life, however; the regression constants can be used to rank resistance to crack propagation (Mull et all, 2005).

For asphalt concrete materials, the "A" and "n" values in Equation 2.16 depend on material properties and several relationships have been developed. Equations 2.17, 2.18 and 2.19 represent relationships proposed by Schapery (1984, 1986) to relate the m-parameter or slope of the log creep compliance master curve to the n-parameter in the Paris Law (Lytton, Uzan et al, 1993).

$$n = \frac{2}{m} \quad \textbf{2.17}$$

$$n = 2\left(\frac{1}{m} + 1\right) \quad \textbf{2.18}$$

$$n = 0.8\left(\frac{1}{m} + 1\right) \quad \textbf{2.19}$$

Lytton, Uzan et al. (1983) report that the A-parameter can be represented according to Equation 2.20 (Majidzadeh et al, 1970) and Equations 2.21 and 2.22 (Molenaar, 1983).

$$A\ x\ 10^9 = 0.23213 + 2613\frac{\sigma_t}{E^*} - 3{,}2334 * 10^{-4} * K_{IC} \quad \textbf{2.20}$$

Where:

A = Paris Law parameter,

σ_t = indirect tensile strength (US customary units),

E* = complex modulus (US customary units), and

K_{IC} = fracture toughness.

$$|\log A| = 0.977 + 1.628 * n \quad \textbf{2.21}$$

$$\log A = 4.389 - 2.52 * \log(E) * \sigma_t * n \quad \textbf{2.22}$$

Where:

A, n = Paris Law parameters,

E = stiffness modulus at specified conditions, and

σ_t = indirect tensile strength (SI units).

The Paris Law has been incorporated into the latest version of the AASHTO Mechanistic-Empirical Pavement Design Guide as part of the thermal cracking model used to predict thermal cracking in asphalt concrete (Zborowski, 2007).

Uzan (1997) utilized the crack propagation model (Paris-Erdogan Law) shown in Equation 2.23 which determines the number of load cycles necessary to propagate a crack to the pavement surface (bottom-up cracking).

$$N_p = \frac{1}{A} * \int_{c_0}^{h} \frac{dc}{K^n} = \frac{1}{A} * I_k \quad \textbf{2.23}$$

Where:

N_p = number of cycles required to propagate a crack to the surface from an initial length of c_o,

c_o = initial crack length,

h = layer thickness,

K = stress intensity factor (Mode I or Mode II),

A, k = material property parameters, and

$I_k = N_p * A$

Abdulshafi (1983) reports work done by Riedel in the early 1980's pertaining to creep crack growth. It was found that the crack growth rate as a function of time (*da/dt*)

is proportional to C* raised to the (n/n+1) power. When considering cyclic loading with constant frequency, crack growth per cycle can be defined according to Equation 2.24. This equation assumes small elastic strains in comparison to creep strains, steady-state creep behavior, cyclic tensile fracture and time-dependent crack growth.

$$\ln\frac{da}{dN} = \ln(R) + q\ln(C_m) \qquad \textbf{2.24}$$

Where:

$R = m\int_0^{2\pi}[f(\omega t)]^{\left(\frac{n}{n+1}\right)}dt$

$q = \frac{n}{n+1}$

m = material constant

Since C* represents crack-tip conditions in a viscous material, crack growth rate depends on C* according to Equation 2.25 (Anderson, 2005)

$$\dot{a} = \gamma(C^*)^m \qquad \textbf{2.25}$$

Where:

$\dot{a}$ = crack growth rate, and

γ, m = material constants

Perhaps a worthy model for consideration is presented in Equation 2.26 (Saxena, 2002). In this model, crack growth combines fatigue behavior and crack growth associated with creep for a given hold time of loading.

$$\frac{\mathrm{da}}{\mathrm{dN}} = \mathrm{A}(\Delta\mathrm{K})^{\mathrm{n}} + \mathrm{bC}_{\mathrm{t}}^{\mathrm{q}} * \mathrm{t}_{\mathrm{h}} \qquad \textbf{2.26}$$

Where:

da/dN = crack growth as a function of load cycle,

ΔK = change in stress intensity factor,

C_t = energy release rate parameter for small scale creep,

t_h = hold time of load, and

A, n, b, q = regression parameters.

2.6 Relationship between Static and Dynamic Loading

Nikbin and Webster (1988) conducted a study on metals at high temperatures to investigate the prediction of crack growth under creep-fatigue loading conditions. Authors found that cracking is governed by fatigue process at high frequencies and creep process at low frequencies and little creep-fatigue interaction existed for the conditions examined. Tests were conducted under static conditions, constant load amplitude and constant displacement conditions. It was found that for low frequencies (<0.1 Hz), cyclic crack growth rates could be predicted using static crack growth rates (da/dt) and that the cyclic creep crack propagation rate (da/dN) could be correlated to the C* parameter. Authors concluded the stress intensity factor (ΔK) could be used to predict crack growth per cycle at high frequencies whereas the C* parameter can characterize crack growth rate at lower frequencies.

Kleemans et al (1997) conducted a study which investigated fatigue and creep crack growth in fine sand asphalt mixtures. Four-point bending and center-cracked tensile (CCT) specimens were subjected to constant amplitude load tests (1, 10 and 29.3 Hz), constant ΔK tests, and constant load tests (3 and 5 kN). In the constant amplitude test results, authors noted a large frequency effect when comparing plots of da/dn versus ΔK. However, these plots at different frequencies could be reduced to a single scatter plot of da/dt versus ΔK using the conversion presented in Equation 2.27.

$$\frac{da}{dt} = f * \frac{da}{dN} \qquad \textbf{2.27}$$

Where:

da/dt = crack speed,

f = load frequency (1/s), and

da/dN = crack growth per load cycle.

Based on these findings, authors concluded that a creep crack growth mechanism is the dominant factor in crack growth, rather than a purely fatigue mechanism. Thus, crack growth is present only during the time at which an applied stress is present. Authors successfully predicted fatigue crack growth from creep crack growth test results.

Chapter 3

3 LITERATURE REVIEW

3.1 Application of Fracture Mechanics to Asphalt Concrete

Asphalt concrete is unique material which exhibits visco-elastic behavior. At low temperatures and increased loading frequencies, bituminous materials can typically be described using linear elastic fracture mechanics (LEFM). Thus, common linear-elastic analysis parameters and formulas can be used to describe crack behavior and the fatigue damage. These parameters include the stress intensity factor (K) and fracture energy (G) and their critical values, K_c and G_c (O. Abdulshafi, 1992).

However, the viscous response of asphalt material cannot always be ignored, especially with increased temperatures or reduced loading frequencies. Plastic strain can accumulate under loading and have significant effects on crack propagation within asphalt material (Krans et al, 1996). Similar to LEFM, non-linear fracture mechanics can be applied to asphalt materials. In cases where materials behave in a ductile manner, the *J*-integral parameter and critical value (J_c) is most effective in describing crack behavior.

Finally, asphalt materials exhibit time-dependent behavior which can support creep fracture. In this case, the C* is the most promising parameter to describe crack behavior and fatigue damage (O. Abdulshafi, 1992). Since the C* parameter can be reduced to K_c or G_c, it has the potential to be the most effective parameter to describe fracture and fatigue in asphalt materials with time-dependent or brittle fracture behavior.

O. Abdulshafi (1992) presented Figure 14 which correlates fracture mechanics parameters to various zones surrounding a crack tip.

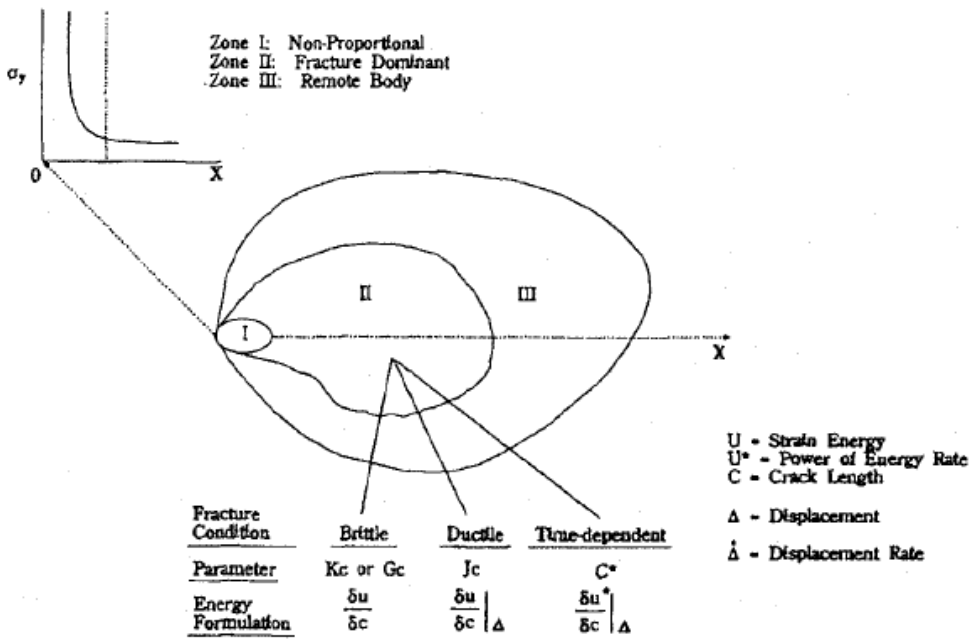

Figure 14 Crack regions and characterization parameters (O. Abdulshafi, 1992).

This goal of this chapter is to present an overview of the more common laboratory tests that have been used to evaluate or estimate the aforementioned fracture mechanics parameters of asphalt concrete materials. Test background, methods, selected case studies and advantages and disadvantages are presented.

Since the application of fracture mechanics to asphalt concrete is a developing and evolving topic, several laboratory tests are under development or have recently become standard procedures. However, a standalone test or fracture parameter has not been advanced to the point where consistent measurements of asphalt fracture properties can be obtained (Wagoner et al, 2005a). Part of the difficulty in accepting a standard cracking test lies in the fact that research efforts are lacking which relate fracture mechanics parameters obtained in the laboratory to field performance of in-service pavements.

Finally, crack propagation monitoring methods are discussed and incorporation of fracture mechanics concepts into the AASHTO MEPDG is presented.

3.2 Semi-Circular Bend Test

One method of evaluating cracking in asphalt pavements that has gained much popularity in recent years is the semi-circular bend test (SCB). This test is typically used to measure the stress intensity factor (K), fracture toughness (K_{IC}) or energy dissipation rate (*J*) of asphalt concrete under static loading conditions. In addition, the fracture energy (G_f) can be determined from the SCB test (Li and Marasteanu, 2004).

While these parameters can be used to describe crack behavior or compare different asphalt mixtures, they cannot be used to estimate the number of cycles or time until failure. Under dynamic loading conditions, analysis of SCB test data can yield the Paris Law coefficients which can in turn, provide an estimation of crack growth as a function of load cycles (Krans et al., 1996).

Mainly due to the fact that test samples can easily be prepared using a gyratory compactor or taken from field cores of thick or thin pavements, many researchers around the world have adopted this test method to evaluate fracture resistance of asphalt concrete (Molenaar, A. et al, 2002; Li and Marasteanu, 2004; Mull et al, 2005; Li and Marasteanu, 2009).

3.2.1 SCB Test Method

The current test method for the SCB is outlined in the European standard, EN 12697-44 (2010), *"Bituminous mixtures – Test methods for hot mix asphalt – Part 44: Crack propagation by semi-circular bending test."* In this test procedure, a 50 mm thick specimen with a 150mm diameter is cut in half and positioned in a load frame shown in

Figure 15. To simulate an initial crack, a 0.35 mm wide by 10 mm deep notch is cut into the center of the specimen.

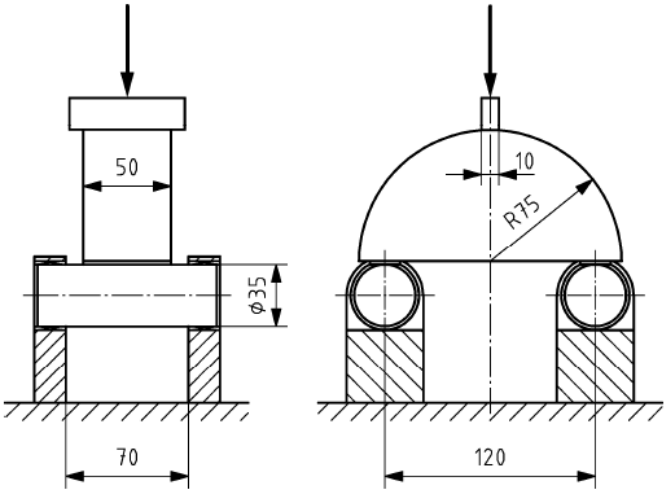

Figure 15 Standard test frame and specimen dimensions (mm) for the SCB-test (EN 12697-44, 2010).

Typically, the SCB test is carried out at 0°C to simulate a temperature where failure of asphalt concrete is typically controlled by cracking. According to the European standard, sufficient load must be applied to exert the specimen to a constant deformation rate of 5.0 mm/min. During the test, the force and vertical displacement are recorded to be used in calculation of the fracture toughness (K_{IC}) of the material according to Equation 3.1 (EN 12697-44, 2010).

$$K_{IC} = \sigma_{max} * \sqrt{\pi * a} * f\left(\frac{a}{W}\right) \qquad \textbf{3.1}$$

Where:

K_{IC} = Fracture toughness ($N/mm^{3/2}$) ,

σ_{max} = maximum applied stress (N/mm^2) ,

a = notch depth of specimen (mm),

W = height of specimen (mm), and

f(a/W) = specimen geometric factor as defined in EN 12697-44.

Although not yet standardized, the SCB test has also been carried using cyclic loading conditions to evaluate fatigue life or crack growth as a function of applied load cycles. In this analysis approach, a crack driving force in the form of LEFM parameters is measured, calculated and correlated with crack propagation as a function of load cycles according to the Paris Equation (Mull et al., 2005).

3.2.2 Selected Case Studies

The SCB test has become increasingly popular due to the simplicity of the test and the fact that diametrically halved cores yield twice the number of specimens from a gyratory compacted sample when compared to the indirect tensile test (IDT). In addition, SCB test can be carried out using IDT test equipment with only minor modifications to the test set-up (Krans et al., 1996). Since the SCB requires loads 2-3 times smaller than the IDT test, the undesirable effects of plastic deformation near the loading points are reduced which can produce more desirable results (Krans et al., 1996).

The SCB test was originally applied to asphalt concrete mixtures by Krans et al. (1996) in the Netherlands. The test itself was previously developed and utilized in stone and ice mechanics but adopted to asphalt in attempt to develop a simple, reliable and inexpensive test that could be used during quality control. In this study, cyclic and static loading was applied at 0, 20 and 30 °C to determine the max force and number of cycle until failure. Samples were tested with and without starter cracks. This initial study concluded that the SCB can be an effective test to determine crack behavior in asphalt material.

The SCB test was used by Mull et al. (2005) to perform fatigue characterization of asphalt concrete. Authors consider linear elastic fracture mechanics to be insufficient to characterize asphalt fracture performance. Given the visco-elastic behavior of asphalt concrete, the J-integral is considered a more applicable parameter. The rate of crack propagation was modeled using a power law based on the Paris Equation. It is noted that the Paris Equation cannot model crack propagation over service life but can be an indicator to rank mixtures based on fatigue crack propagation. Testing was conducted at 0.5 Hz under with load control between 66.72N to 667.2 N. All tests were conducted at 24°C on 150mm diameter specimens. When examining crack speed versus energy release rate (J), authors were successful in ranking the three mixtures in terms of crack resistance.

A study by Huang et al. (2005) compared the SCB to the IDT test in an effort to characterize the tensile strength of asphalt concrete. SCB specimens measured 6 inches (150 mm) in diameter by 1 in (25 mm) thick whereas the IDT specimens measured 4 inches (100 mm) in diameter and 2.56 inches (65 mm) in thickness. All testing was conducted at 77 °C (25°C) at a loading rate of 2 in/min (51mm/min). Tensile strengths from the IDT tests were approximately 3.8 times those obtained from the SCB test which can be attributed to different stress states within the sample during loading. Authors concluded that the SCB and IDT tensile strength test results were fully comparable and convertible and the SCB characterized tensile strength with good repeatability.

Li and Marasteanu (2009) used the SCB test to evaluate the fracture properties of six different asphalt mixtures. Test data were evaluated by calculating the fracture energy (G_f) in accordance to the RILEM TC 50-FMC specification. The experimental

plan included different air voids, binder type, binder modification and aggregate type. The test was conducted at -6 °C, -18°C and -30°C using loading rates of 0.00015, 0.0005 and 0.005 mm/s and initial crack lengths of 5, 15 and 30 mm. From this study, authors concluded that the SCB represents a repeatable low temperature fracture test for asphalt materials. Different test temperatures and loading rates produced significant effects on fracture energy. Specifically, fracture energy increases with decreasing temperature and decreases with increased loading rate at all test temperatures. Finally, notch length had a less pronounced effect at the two lower temperatures but exhibited a significant effect at the highest temperature.

3.2.3 Advantages and Disadvantages

Since its application to asphalt concrete by Krans et al. (1996), the SCB test has been investigated as a test to evaluate fracture resistance of asphalt concrete. During these studies, several advantages and disadvantages have surfaced. Since the test requires diametrically halved cores, it is possible to reduce the number of cores needed to obtain test specimens. Also, circular geometry allows specimens to be easily obtained from the field and from thin pavement sections (Li and Marasteanu, 2009). In addition, failure of SCB specimens only require approximately one-half to one-third of the load applied in the more widely used IDT strength test which reduces the undesirable effects of plastic deformation under loading (Krans et al., 1996; Arabani, 2009). Huang et al (2005) also noted that the ultimate bearing capacity ratio of SCB to IDT tests was in the range of 0.6-0.7 which confirms the finding that less permanent deformation will occur at the loading platens of the SCB test.

In contrast, the size of the specimen may constrain the crack ligament because of its location with respect to the top of the specimen where compressive stresses develop due to loading. Next, a short initial ligament length coupled with a small fracture surface may create boundary effects on the fracture process zone (Wagoner, 2005a). This statement is supported by research performed by Li and Marasteanu (2006) that determined the size of the fracture process zone to be 20-30 mm (0.8-1.2 in) length and 3-6 mm (0.12-0.24 in) wide in SCB specimens. This information discredits the assumption of linear elastic fracture mechanics for analysis of SCB specimens (Li and Marasteanu, 2009).

3.3 Disk Shaped Compact Tension Test

The disk shaped, compact tension test, DC(T), for asphalt concrete was applied to asphalt concrete as a method of evaluating fracture properties of laboratory and field cored specimens. Typically, this test can be used to determine the fracture energy by measuring the applied load and crack mouth opening displacement (CMOD). This test has been proven to be effective in evaluating the fracture resistance of asphalt concrete (Wagoner et al, 2005a).

3.3.1 Background

DC(T) was originally developed and commonly used in studying the toughness of metallic materials according to ASTM E399, "Standard Test Method for Plane-Strain Fracture Toughness of Metallic Metals." In an effort to develop an efficient fracture test for asphalt concrete using easily obtained disk specimens, the DC(T) was first applied to asphalt concrete by Wagoner et al (2005a).

The DC(T) is considered advantageous to other fracture resistance tests due to the fact that field specimens or specimens prepared in the Superpave gyratory compactor can be directly tested. Also, the larger specimen size provides a large fracture area and thus, the potential exists to reduce the variability of the fracture energy test results.

3.3.2 Test Method

Research on this test procedure has led to the standardization of the test method according to: ASTM D7313 - 07a Standard Test Method for Determining Fracture Energy of Asphalt-Aggregate Mixtures Using the Disk-Shaped Compact Tension Geometry (ASTM D7313, 2010).

According to this ASTM standard, the DC(T) test is used to determine the total fracture energy (G_f) which can be used to compare asphalt mixtures on the basis of fracture resistance. Figure 16 shows a schematic of a DC(T) test specimen which requires fabrication of two holes to accommodate the loading apparatus and a starter notch is introduced to facilitate crack initiation.

Laboratory test specimens shall be 50 mm (2 in) in thickness and field specimens shall be the thickness of the lift or 50 mm (2 in) if the lift thickness exceeds 50 mm (2 in). The diameter of the test specimens for field and laboratory samples shall be 150 mm (6 in) with a starter notch of depth of 35 mm (1.38 in) and be 1.5 mm (0.06 in) wide. The test temperature is recommended to be 10°C (18°F) or lower but is suggested as 10°C (18°F) above the low performance grade of the asphalt binder.

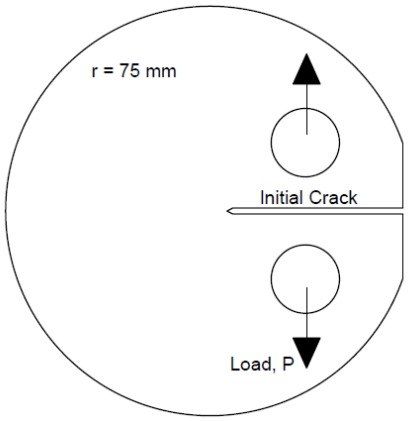

Figure 16 DC(T) specimen configuration.

The DC(T) should be performed at a constant crack mouth opening displacement (CMOD) of 0.017 mm/s (0.00067 in/s) be terminated when post-peak load level is less than 0.1 kN (22 lbf). It is important to note that test results may not produce valid results in certain temperature ranges for a given binder which is further described in the ASTM D7313 - 07a specification. From the test results, the fracture energy can be computed according to Equation 3.2.

$$G_f = \frac{AREA}{B * (W - a)} \qquad \textbf{3.2}$$

Where:

G_f = fracture energy (J/M2 (in-lbf/in2),

AREA = area under load – CMOD curve,

B = specimen thickness (m (in), and

W-a = initial ligament length (m (in)).

3.3.3 Selected Case Studies

Wagoner et al (2005a) developed and applied a disk-shaped compact tension test as a method for determining fracture energy of asphalt concrete. As part of this study,

ideal specimen geometry was proposed that maximized ligament length yet reduced potential for specimen rupture adjacent to the loading holes. Based on the aggregate sized (9.5mm nominal maximum and smaller) included in this study, the recommended specimen diameter was 150 mm (6 in) and thickness was 50 mm (2 in). The initial crack introduced into the specimen should be a maximum of 27.5 mm (1.08 in) beyond the center of the loading holes. Tests were carried out at -20°C, -10°C and 0°C, at loading rates of 10, 5, 1 and 0.1 mm/min (0.4, 0.2, 0.04 and 0.004 in/min). Equation 3.2 was used to calculate fracture energy using measured load and crack mouth opening displacement (CMOD) data.

Authors found that the coefficient of variation (COV) from the DC(T) test results were comparable to the range for the single-edge notched beam and the semi-circular bend test. During testing, authors noted that cracking tended to travel around the aggregate at higher temperatures whereas, as low temperatures, the fracture surface passed through aggregates due to the brittle nature of the material. In certain cases, the crack deviated from the vertical centerline of the specimen. Temperatures and loading rates were found to effect DC(T) test results and crack deviation from the centerline of loading does not have a distinct effect on fracture energy. It is important to note that this study did not consider the effect of thickness on fracture energy. As a result of this study, the DC(T) test can be considered a favorable test to determine fracture energy.

In a parallel study, Wagoner et al (2005b) concluded that fracture energy increased with thicker specimens but test variability did not increase. Authors confirmed the 150 mm (6 in) diameter by 50 mm (2 in) thick specimen for further testing but

acknowledged that additional research is needed to investigate the thickness effect on fracture properties.

3.3.4 Advantages and Disadvantages

Wagoner et al (2005b) report the advantages and disadvantages of the DC(T). Two main advantages include ease of obtaining field specimens along standard fracture test configuration and larger area for potential fracture.

However, the major disadvantages of the DC(T) include crack deviation from center and unknown applicability to asphalt concrete. Since the test for asphalt concrete is relatively new, authors recommend further analysis to interpret DC(T) results.

3.4 Indirect Tensile Test

The indirect tensile test (IDT) is probably the most common test that has historically been applied to asphalt concrete to evaluate tensile strength. It is also the test that is adopted by most state highway agencies (Huang et al, 2005). The test typically consists of loading a disk shaped specimen diametrically at a constant loading rate. Tensile stresses develop perpendicular to the loading axis and eventually cause the specimen to split or crack in the direction of loading. Vertical force and deformation are monitored with respect to time and the maximum tensile strength and fracture energy can be determined from test data.

3.4.1 Background and Test Method

The IDT test is typically conducted on 4 inch (100 mm) diameter by 2inch (50.8 mm) specimens at a loading rate of 2.0 in/min (50 mm/min). The standard test protocol is ASTM D6931-07, “Standard Test Method for Indirect Tensile (IDT) Strength of

Bituminous Mixtures" which recommends a test temperature of 25°C (77°F). Figure 17 shows the schematic of the IDT test setup.

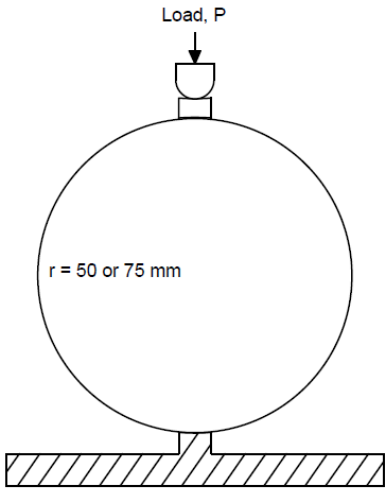

Figure 17 Schematic of IDT Test.

Results obtained from the IDT test can include indirect tensile strength (S_t) calculated using Equation 3.3 and fracture energy (G_f) using Equation 3.4 (ASTM D6931-07).

$$S_t = \frac{2P}{\pi dt} \quad \textbf{3.3}$$

Where:

S_t = indirect tensile strength, kPa (psi),

P = maximum load applied, N (lbf),

d = specimen diameter, mm (in), and

t = specimen thickness before loading, mm (in).

$$G_f = \frac{AREA}{td} \quad \textbf{3.4}$$

Where:

G_f = fracture energy, J/m^2 (in-lbf/in^2),

AREA = area under the load-displacement curve, N-m (in-lbf),

d = specimen diameter, m (in), and

t = specimen thickness before loading, m (in).

The Superpave IDT test builds on the existing IDT principles and is used to determine creep compliance and indirect tensile strength at low to mid-range pavement temperatures. This modified IDT test uses a 5.91-6.06 inch (150 – 154 mm) diameter by 1.57-2.36 inch (40-60 mm) thick specimen that can easily be obtained from a gyratory compacted sample (Christensen and Bonaquist, 2004). The typical loading rate for this test is 0.5 in/min (12.5 mm /min) for thermal cracking evaluation. In addition, two LVDT's are placed at right angles on each side of the specimen to measure horizontal and vertical deflections during the test as shown in Figure 18 (AASHTO T322, 2007).

. These data are necessary in the calculation of creep compliance parameters. Testing is typically carried out at -20, -10 and 0 °C (-4, 14, 32 °F) to describe performance at low and mid-range pavement temperatures. Results obtained from this test can be used in performance prediction models, such as the TCMODEL in the AASHTO Mechanistic-Empirical Pavement Design Guide (MEPDG), to predict thermal and fatigue cracking at low and intermediate temperatures, respectively.

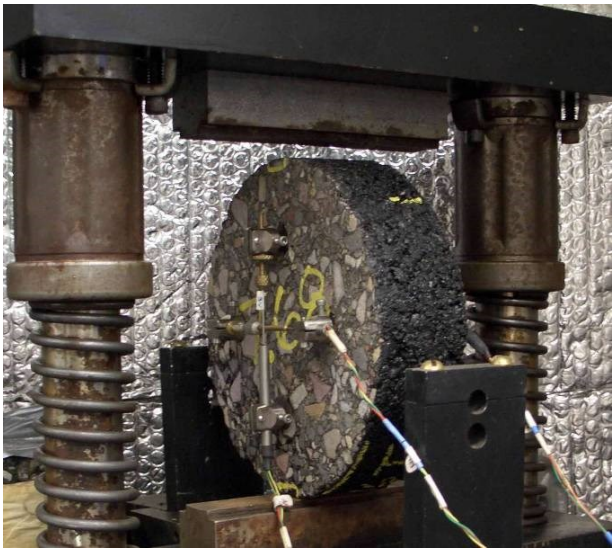

Figure 18 Superpave IDT Test with LVDT Sensors (Zborowski, 2007).

3.4.2 Selected Case Studies

The IDT strength test has been used by numerous researchers to evaluate cracking in asphalt concrete and studies are commonplace within literature. Kim and Wen (2002) used the IDT test, field data and cores from WesTrack to evaluate the effectiveness of fracture energy (G_f) as an indicator of fatigue performance. Using WesTrack data and field cores, authors concluded that fracture energy obtained from the IDT test at 20°C (100mm diameter specimens) can be used as an indicator of fatigue cracking performance.

In comparison, Witczak et al (2002) report that the IDT strength parameters (tensile strength, tensile strain at failure, fracture energy and energy at failure) have poor correlation to cracking for WesTrack (fatigue cracking), MnRoad (thermal cracking) and ALF (fatigue cracking) test sections included in the study.

Roque et al (1999) used a modified Superpave IDT specimen to investigate fracture properties of asphalt concrete. In this study, an 8-mm hole was drilled into the

middle of the specimen and tests were carried out at 10°C to represent intermediate pavement temperatures. Stress intensity factor (K_I) obtained for different loading cycles were used in the Paris Law to describe crack propagation. However, Marasteanu et al (2007) summarizes work by Zhang et al (2001) which shows that permanent deformation near the crack tip is significant for this IDT geometry and the Paris Law and LEFM are not applicable.

3.4.3 Advantages and Disadvantages

Huang et al (2005) and Kim and Wen (2002) provide a good summary of the advantages and disadvantages of the IDT test. One of the main advantages of the IDT is the simplicity of conducting the test which means it can be conducted worldwide without highly specialized test equipment. For example, existing equipment such as the Marshall test system can be utilized. Samples can easily be obtained from field cores or gyratory samples. Research has shown that, the stress state near the center of the specimen is similar to the bottom of a pavement layer and that failure may not be significantly affected by surface conditions. Also, failure begins in the region which exhibits relatively uniform tensile stresses.

However, permanent deformation occurs at the loading strips and can influence test results and high stresses induced at these supports can cause local failure. The test can only be carried out under controlled stress. Also, the stress state within the sample is not realistic of the stress state of the entire pavement structure. Specifically, the maximum vertical stress at the center is three times the maximum horizontal stress. Finally, compressive failure may control if the compressive strength is less than three times the tensile strength of the specimen.

3.5 Single Edge Notched Beam

According to Wagoner et al (2005c) and Marasteanu et al (2007), the single edge notched beam SE(B) test has been used by many researchers to analyze fracture properties of asphalt concrete material. This test can yield several material parameters such as the stress intensity factor (K), crack growth rate according to Paris's Law, crack length, J-contour and other fracture properties. However, various test procedures and beam dimensions have been utilized in studies and no standard test procedure or data analysis method exists (Wagoner, et al, 2005c).

3.5.1 Background and Test Procedure

Although no standard test procedure exists for the single edge notched beam test, the general concept of test procedures applied to asphalt concrete follows ASTM E399, "Standard Test Method for Linear-Elastic Plane-Strain Fracture Toughness KIC of Metallic Materials" (Marasteanu et al., 2007). An asphalt beam is fabricated using various compaction techniques and a water cooled saw is used to trim the compacted beam to remove edge effects from density variations and aggregate segregation. To simulate a crack, a notch is introduced at the center of the beam. The beam is loaded in three-point bending and loading is typically controlled by either constant crack mouth opening displacement (CMOD) or load line displacement. A typical SE(B) test setup is presented in Figure 19. From test data, common fracture mechanics parameters are calculated.

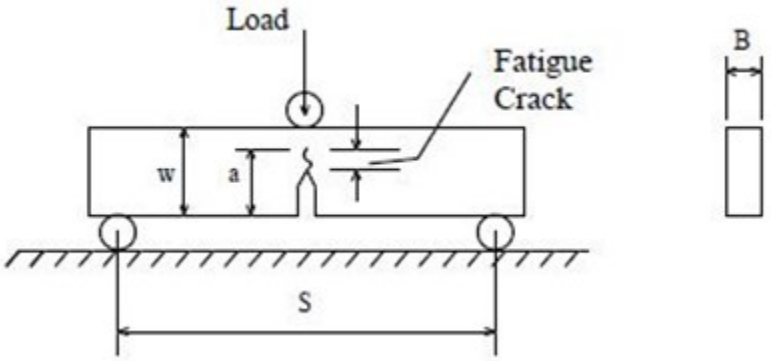

Figure 19 Typical single edge notch beam test configuration (Marasteanu et al., 2007).

3.5.2 Selected Case Studies

The single edge notched beam was originally applied to asphalt binders by Lee and Hesp (1994) and Lee et al (1995). Beam specimens were prepared that were 12.5 mm (0.5 in) thick by 175 mm (6.9 in) long and had a span of 100 mm (4 in). Testing was conducted at -20°C at a constant displacement rate of 0.01 mm/s. Total strain energy was computed and the J-integral was determined as the rate of change of total strain energy with respect to change in crack length, normalized by specimen thickness. Authors found that specimens prepared with modified asphalt binder yielded higher fracture when compared to virgin binder specimens (Marasteanu et al., 2007).

Mobasher et al (1997) carried out a study to gain insight into crack propagation properties of asphalt concrete. In this study, the SE(B) was used to obtain and evaluate low-temperature fracture properties of asphalt-rubber (AR) and conventional asphalt mixtures. Authors used the R-Curve approach and compliance approach which are both based on non-linear fracture mechanics. Asphalt beams were prepared with the following dimensions 406 x 89 x 89 mm (16 x 3.5 x 3.5 in) and a 20mm (0.8 in) deep by 5 mm (0.2 in) wide initial notch was introduced to simulate an initial crack. Samples were tested at

-7°C (20°F) and -1°C (30°F) under three point bending conditions. Loading was constant at a rate of 127 x 10-6 mm/s (5 x 10-6 in/s) (CMOD) until 0.2mm (.008 in) and unloading was controlled at 90 N/s (20 lb/s). Load-unloading cycles were repeated until CMOD of 2.5 mm (0.1 in). Using these approaches, authors found that as temperature increased, fracture toughness decreased for both mixtures. However, the AR mixture exhibited higher toughness. Authors concluded that the R-curve approach yielded a suitable method to characterize fracture properties of asphalt concrete and methodology used in this study can be utilized to develop fatigue failure criterion.

Wagoner et al (2005c) provides excellent documentation of previous applications of the SE(B) test and also performed a study to further develop the SE(B) test for asphalt concrete. In this study, tests were conducted to develop the test procedure, understand crack tip characteristics, evaluate mixed mode fracture and quantify the effect of temperature on fracture energy. Asphalt beams were produced to dimensions of 375 x 100 x 75 mm (14.8 x 4 x 3 in) and a notch was cut into the center of the specimen to a depth of 19 mm (0.75 in). Loading was controlled at 0.7 mm/min CMOD and specimens were tested at 0°C (32°F), -10°C (14°F) and -20°C (-4°F). Fracture energy was computed as the area under the load-CMOD curve. In addition, authors investigated mix mode fracture by offsetting the crack by 65 mm (2.6 in) from the center of the beam. Conclusions from this study indicate that the crack path is influenced by the aggregate, variability of data collected from this study is reasonable for asphalt concrete and the SE(B) test provides reasonable results for fracture energy for the given range of test temperatures. Authors note that the SE(B) test is the most promising test for evaluation of fracture in asphalt concrete.

3.5.3 Advantages and Disadvantages

The SE(B) can be a reliable test to access fracture resistance because of the simple load configuration, stable propagation of mode I fracture and reduced edge effects due to large specimen size. In addition, the SE(B) can be used in mixed-mode fracture testing by shifting the location of the initial notch from the center of the beam (Wagoner et al, 2005a). In comparison, the SE(B) test requires the use of asphalt beams which are difficult and not always practical to obtain from field pavements (Wagoner et al, 2005a; Marasteanu et al., 2007). Also, the lack of a formal test procedure for asphalt concrete restricts the use of this test.

3.6 C* Line Integral Test

Since its development, the C* Line Integral test has been used to a limited extent when evaluating fracture resistance of asphalt concrete mixtures which. This fracture test and subsequent analysis using an energy approach was first applied to asphalt concrete by Abdualshafi (1983) to predict fatigue life using crack initiation and crack propagation. Abdulshafi and Kaloush (1988) used this test procedure to evaluate the fracture resistance of modified asphalt concrete used for airfield pavements. Most recently, Kaloush et al (2010), used the C* line integral to evaluate the crack propagation of fiber-reinforced asphalt concrete mixtures.

3.6.1 C* Test Method

C* can be determined for asphalt concrete by applying different constant displacement rates to multiple specimens. Abdulshafi (1983) used notched disk specimens with an initial crack to evaluate the crack propagation in the typical test setup presented in Figure 20. Diametrical specimens were used in this test were 4 inches in

diameter and 2.5 inches thick which authors believed provided suitable thickness to satisfy plane strain conditions (Abdulshafi and Kaloush, 1988). A right angle wedge was carefully cut into the specimen to a depth of 0.75 inches to accommodate the loading apparatus. To monitor crack propagation, a light colored paint and scaled reference system was applied to one face of the specimen. Constant displacement loading rates were applied to a sequence of test specimens at 70°F. Load and crack length as a function of time was recorded during the test to be used in subsequent data analysis. It should be noted that crack length was measured using visual observation.

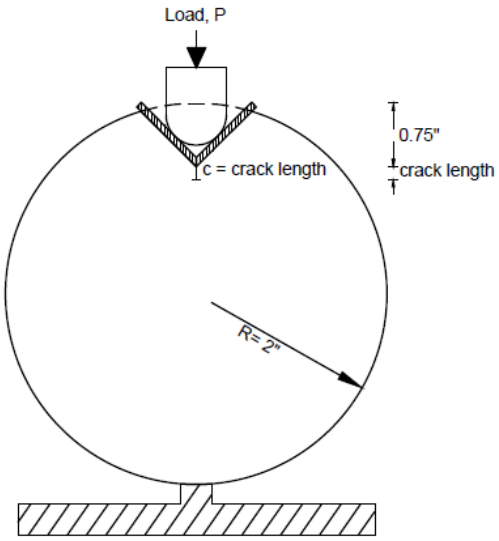

Figure 20 Schematic of C* test set-up (Abdulshafi and Kaloush, 1988).

3.6.2 Selected Case Studies

Abdulshafi (1983) initially presented a simplified method of evaluating C* of asphalt concrete in the laboratory. This laboratory test method utilized the test apparatus presented in Figure 20 which was developed to evaluate crack propagation in asphalt concrete. In this study, monotonic loading was applied at constant displacement rates to notched disk Marshall specimens. Displacement rates included 0.0035, 0.007, 0.009,

0.014, 0.018, 0.021, 0.028, 0.036 and 0.054 inches per minute. A small notch was introduced to the specimen to simulate crack initiation and all testing was performed at 70°F. Figure 21 presents the relationship between C* and crack growth rates for three mixtures evaluated. As a result of this study, the author concluded that C* appears to be an appropriate material parameter that can describe cracking in asphalt concrete. This C* line integral could be a future test to compare or evaluate fracture potential of asphalt pavements.

In this same study, Abdualshafi (1983) applied cyclic loading at different stress levels to notched disk Marshall specimens (Figure 20) in order to predict normalized crack length as a function of normalized load and C*. Cyclic loading consisted of a 0.4 second load followed by a 0.6 second rest period. Figure 22 provides an example of data collected during this study and the relationship between crack length and number of loading cycles.

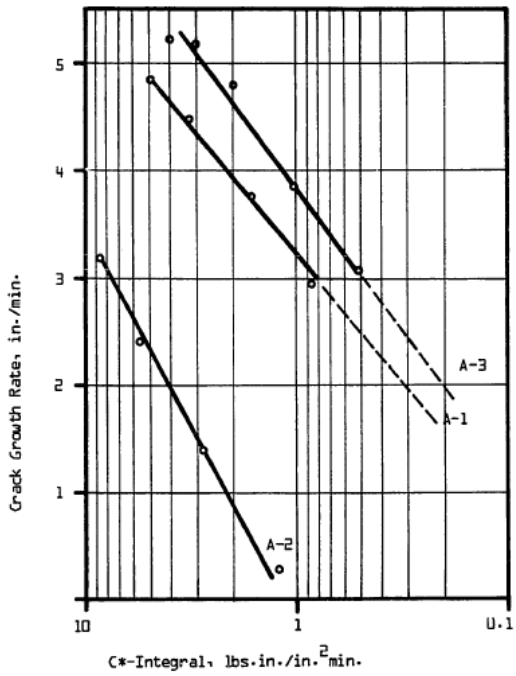

Figure 21 Relationship between C* and crack growth rate (Abdulshafi, 1983).

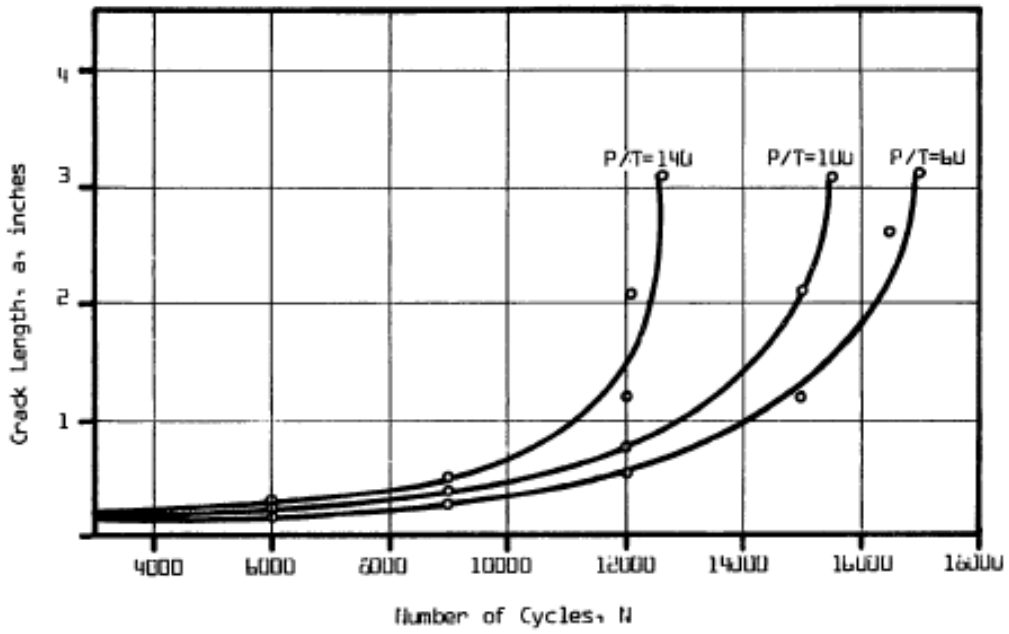

Figure 22 Example relationship between crack length and number of loading cycles (Abdulshafi, 1983).

These data were used to develop regression equations similar to Equation 3.5 for all mixtures and normalized load (P/T) included in the study. These relationships were

differentiated with respect to load cycles (N) to obtain change in crack length as a function of load cycle. These differentiated equations were used to relate normalized crack length (a/w) to C* based on different P/T values.

$$a = ba_0 * \exp(cN) \quad \textbf{3.5}$$

Where:

a = crack propagation rate,

a_o = initial crack length (0.2 inches),

N = number of load cycles, and

b, c = regression coefficients.

Abdulshafi and Kaloush (1988) performed a study to develop selection criteria to compare performance of modified asphalt concrete mixtures for airfield applications. As part of this work, the C* line integral test was used to evaluate crack propagation in asphalt concrete as shown in Figure 23. Marshall specimens, measuring 4 inches (100 mm) in diameter by 2.5 inches (63.5 mm) thick, were used in the C* test. A right angle wedge of 0.75 inch depth was cut through the entire specimen thickness and monotonic loading was applied at 0.01, 0.013 and 0.019 inches per minute at a temperature of 70°F. Authors concluded that C* is a potential test which can be useful to evaluate crack propagation of asphalt mixtures with or without modifiers.

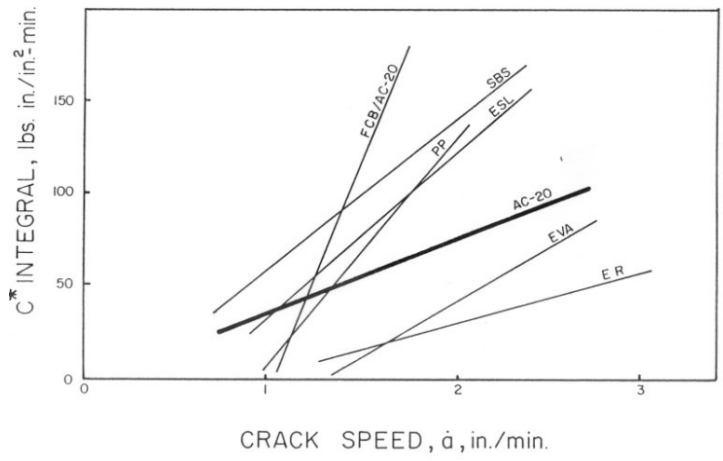

Figure 23 C* versus crack growth rate for mixtures with various modifiers (Abdulshafi and Kaloush, 1988).

Kaloush et al (2010) performed a study performance of control and fiber reinforced asphalt concrete mixtures. Fiber reinforcement included a blend of polypropylene and aramid at a dosage rate of 1-lb fibers/ton asphalt mixture. Resistance to crack propagation was evaluated using the C* line integral test. One modification to the original C* test procedure included using 6 inch (150 mm) gyratory compacted specimens that were prepared in accordance with AASHTO TP9-02, "Standard Test Method for Determining the Creep Compliance and Strength of Hot Mix Asphalt (HMA) Using the Indirect Tensile Test Device." All testing was conducted at 70° F and loading was applied using constant displacement rates of 0.005, 0.01, 0.015, 0.02 and 0.025 inches per minute.

Figure 24 presets the C* test results from this study. In terms of resistance to crack propagation, authors concluded the fiber-reinforced asphalt mixture outperformed the control mixture as indicated by the higher slope value of the linear fit. For a given

crack propagation rate, fiber reinforced asphalt mixture requires more power or a higher energy rate and thus provides better crack resistance to crack propagation.

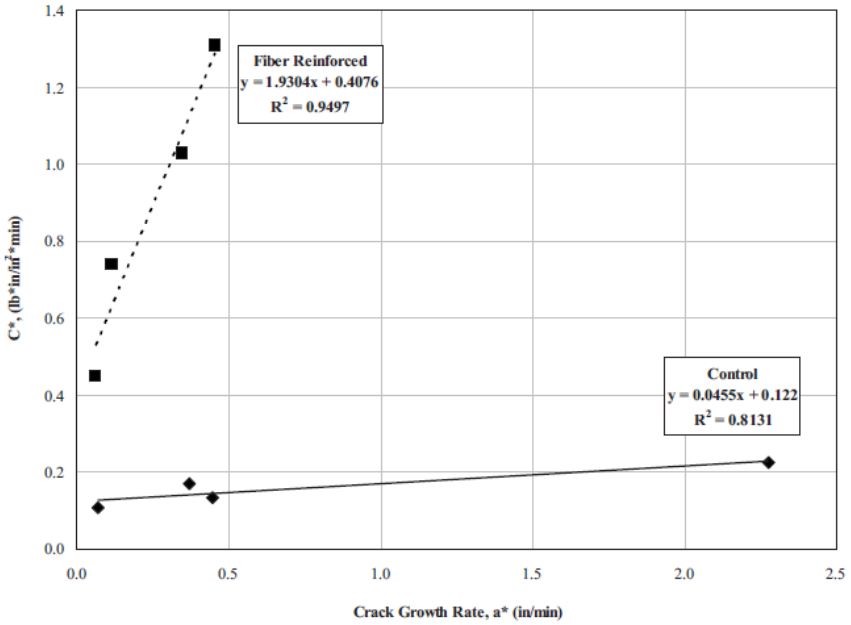

Figure 24 C* versus crack growth rate (Kaloush, 2010).

Authors supported these test results by observing that the fiber reinforced specimens did not split at the completion of the test which was common among control specimens. A pavement condition survey, conducted approximately two years after construction, found that the control section had approximately three times the amount of low severity cracking as the fiber reinforced sections (Kaloush et al, 2010).

3.6.3 Advantages and Disadvantages

One main benefit of the C* Fracture Test is the ability to measure the crack propagation rate within asphalt concrete. Most tests only measure energy to drive a crack whereas the crack speed can be obtained from this test. In addition, analysis of C* data assumes time-dependent fracture mechanics which can be more representative of the behavior of asphalt concrete (Abdulshafi, 1992).

A main disadvantage of the C* line integral is the difficulty of specimen preparation. Additional effort is required to produce a uniformly notched specimen as well as monitor the crack propagation rate throughout the duration of the test. Also, due to specimen size effects (based on 100 mm diameter), this test may not be applicable to mixtures with large aggregate sizes (Vinson, et al., 1989). Finally, few studies regarding the application of C* to asphalt concrete are available literature.

3.7 Fénix Test

The Fénix test was developed by the Road Research Laboratory of the Technical University of Catalonia, Barcelona, Spain in an effort to assess asphalt cracking by calculating dissipated energy during cracking (Pérez-Jiménez et al, 2010). The test uses half cylindrical specimens (101.6 mm in diameter by 63.5 mm thick) prepared by Marshall or gyratory compaction methods. Steel plates are glued to the specimen faces as shown in Figure 25 and a 6 mm initial crack is introduced between the plates. The specimen is subjected to a constant displacement rate of 1 mm/min at a given temperature. Parameters obtained from the Fénix test include dissipated energy during cracking (GD and the tensile stiffness index (IRT).

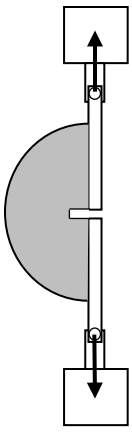

Figure 25 Fénix Test Setup (Pérez-Jiménez et al, 2010).

Researchers were able to use the Fénix test to characterize crack behavior when comparing binder contents and test temperatures. In addition, specimens can be tested at a wide range of temperatures to evaluate post peak softening behavior of asphalt concrete. Test results indicated good repeatability with COV values similar to those obtained from the SE(B), DC(T) and SCB tests. Finally, it was observed that Fénix test parameters correlated well with three-point bending beam fatigue parameters (a, b).

3.8 Wedge Splitting Test

The wedge splitting test (Tschegg et al, 2011) used a sample geometry and test setup as shown in Figure 26. The specimen is 130 mm wide, 120 mm tall and approximately 60 mm thick. A series of lines are marked on the front of the specimen and crack propagation as a function of time is recorded with a video camera. Tests were carried out at -10°C, 0°C and 10°C and stress intensity factors were computed from data obtained from this test.

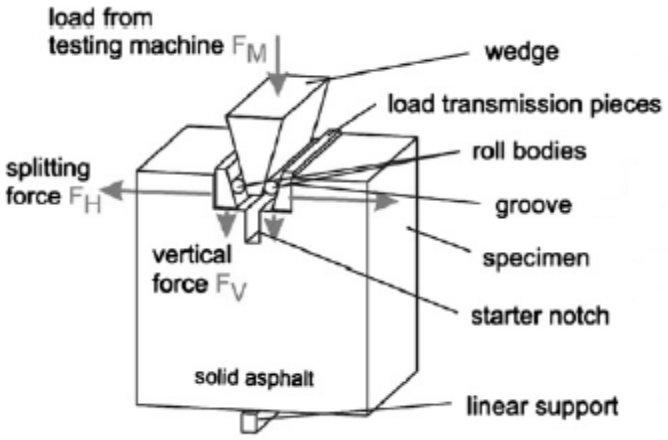

Figure 26 Wedge splitting test (Tschegg et al., 2011).

Authors concluded the practical wedge splitting test was suitable to characterize fatigue crack growth of asphalt concrete and repeatable results were produced during testing.

3.9 Comparison Study of Common Fracture Tests

Walubita et al (2011) conducted a study to compare four cracking test methods in order to investigate methods to screen and select crack resistant HMA mixes which can potentially mitigate fatigue cracking. The four laboratory tests included the overlay tester (OT), direct tension (DT), indirect tension (IDT), and semicircular bending (SCB. Authors used an evaluation criteria based on: test rationality and comparison to field performance; repeatability, variability and practicality; ease of specimen fabrication; and effort required for data analysis.

Authors determined that the DT, IDT and SCB tests produced more repeatable results, however; they could not properly distinguish crack resistance based on tensile strength and strain parameters. The OT test produced less repeatable results.

Authors concluded that none of the tests considered would be recommended as a simple laboratory test to access fatigue. The study recommended further evaluation of the IDT and SCB test using repeated loading and comparison to field performance. Of the two, the IDT was recommended as the primary choice for further analysis.

3.10 Specimen Geometry and Test Conditions

As discussed in previous sections, the different fracture tests applied to asphalt concrete utilize a wide range of specimen geometries, dimensions, initial crack length, test temperatures, loading rates and loading control. Because of these differences, selection of test conditions has been based on limited research and further investigation and validation is required. Table 1 presents a summary of the wide range of test conditions and sample sized applied to various cylindrical fracture mechanics based tests. This figure is not exhaustive but rather is intended to emphasize the different parameters used in the more common fracture tests.

One major concern with current fracture tests applied to asphalt concrete revolves around the application of plane stress or plane strain assumptions. In the case of plane strain, the specimen must be large in the z-direction for the diametrically loaded disk specimens. This condition can be difficult to achieve and assumption of plane stress must be adapted. Regardless, the selection of thickness appears to be controlled by practical field lift thicknesses and subsequent stress or stain assumptions are adopted based on these values.

Wagoner et al (2005a) report that the specimen thickness should be between 25 and 100 mm in order to represent practical pavement layer thickness. Authors also note that specimen dimensions should be four times larger than the maximum aggregate size

in order to reduce variability. Thus, for a 9.5mm maximum aggregate size, a 50 mm thick specimen was sufficient.

The Superpave IDT test for creep and fracture evaluation requires specimen thickness to be between 40-60 mm for a 150 mm diameter specimen. However, according to NCHRP Report 530, a 50 mm thick specimen has not been evaluated to determine if it meets the representative volume element (RVE) conditions required to assume a homogeneous sample (Christensen et al., 2004).

In terms of initial crack length, ASTM recommends and "a/W" ratio (crack length/ specimen width) between 0.45 and 0.55 to make sure the test specimen is in accordance with small-scale yielding criterion. However, deep-notched specimens necessary to meet these ratio limits may produce undesirable effects in asphalt concrete. Therefore, an "a/W" ratio of 0.25 was used in DC(T) tests conducted by Wagoner et al (2005a) to allow for a larger fracture area and to reduce variability caused by the lack of homogeneity in asphalt samples.

Overall, considerable effort is needed to evaluate test conditions and specimen geometry for asphalt concrete fracture tests needs significant research effort. These efforts should focus on stress states within each sample in effort to identify the most practical test setup to evaluate fracture resistance of asphalt concrete.

Table 1 Test conditions for fracture tests on cylindrical specimens from selected studies.

Test	Thickness (mm)	Diameter (mm)	Initial Crack Length (mm)	Loading Control*	Temperature (°C)	Load Rate (mm/min)	Load Rate (mm/min)	Reference
DC(T)	50	150	27.5	CMOD	-20, -10, 0	0.1-10	G_f	Wagoner et al (2005a)
C*	63.5	100	12.5	LLD	21	0.9-0.17	C*	Abdulshafi (1983)
C*	63.5	100	12.5	LLD	21	0.25-0.48	C*	Abdulshafi and Kaloush (1988)
C*	40	150	<2	LLD	21	0.13-0.64	C*	Kaloush et al (2010)
SCB	25, 50	150	15	CMOD	-40, -30	0.3	K_{IC},G_f	Li and Molenaar (2004)
SCB	25	150	5, 15, 30	CMOD	-30, -18, -30	0.009-0.3	K_{IC}	Li and Molenaar (2009)
SCB	25	150	10	CMOD	0, 25	5.1	G_f	Arbani (2009)

** LDD – Load Line Displacement, CMOD – Crack Mouth Opening Displacement*

3.11 Crack Propagation Monitoring Systems

Crack length as a function of time or load cycles can be a tedious parameter to obtain in the laboratory. Previously, several methods have been used to monitor crack extension under static or cyclic loading in asphalt concrete or metal specimens. These monitoring methods include visual, crack opening displacement (COD), optical methods, thin conductor wires, conductor paths, strain foil gauges and mortar displacement (Hofman et al, 2003; Tschegg et al, 2010).

Hofman et al (2003) reports challenges of the visual method include test operator experience and associated with continual monitoring of the crack extension. Examination of foil gauges has shown that measured crack extension does not match optical measurements. Finally, COD and mortar displacement methods were unable to capture crack irregularities and crack branches which were observed optically. More advanced methods include piezoelectric sensors or other electrical monitoring equipment.

Tschegg et al (2011) and Jacobs (1995) monitored crack propagation using a series of thin electrical wires mounted on the face of the specimen. Crack length was recorded when the electrical wires were severed. However, one problem with this method was that the series of wires could not be used in subsequent testing because they were destroyed during the test.

Tschegg et al (2011) used a conductive paint to spray nine thin conductor paths across the specimen face as shown in Figure 27. The passing crack severed the conductor path and opened the electrical circuit which can be detected by and correlated to crack tip location. Authors found that at 10°C, the method produced reasonable results. However,

at -10°C and 0°C the crack opening was not sufficient to break the conductor paths and the crack location was not detected by the electrical method.

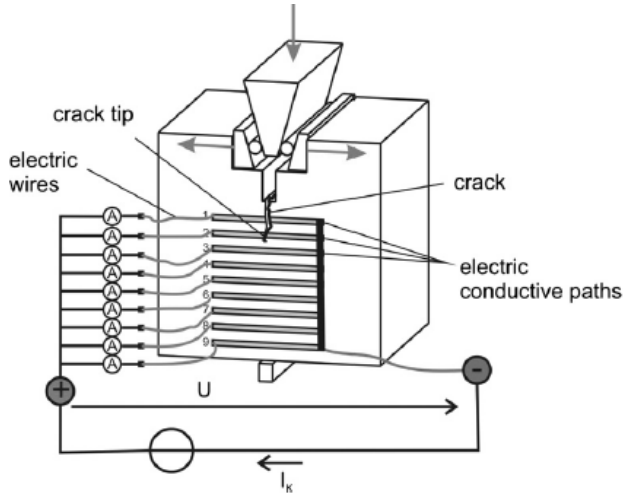

Figure 27 Electrical detection method for determining crack growth (Tschegg et al, 2011).

Due to the inconsistencies in the electrical conductor path method, a camera was also used to monitor crack growth. Computer control was utilized to automatically take photos at one minute intervals; which were later analyzed. Authors concluded that the optical method was sufficient to monitor crack growth and it also corresponded well with measurements taken visually.

Wagoner (2006) used crack detection gages to evaluate macro cracking in single edge notched beam and direct compact tension geometries. These gages consisted of a single wire glued to the surface. A passing macro crack caused the gage to break at approximately 3% strain and the voltage loss was recorded to determine the time at a specified crack location. Gages were placed on both sides of the specimen and it was found that they did not break at the same time, indicating a non-uniform crack front.

Private correspondence with the authors indicated that crack detection by the gages lagged behind the damage front and was more characteristic of a discrete crack.

Based on the literature, the optical method of monitoring the crack propagation with a camera currently appears to be the best method to evaluate crack propagation in an asphalt concrete test specimen (Hofman et al, 2003; Tschegg et al, 2010).

3.12 Fracture Process Zone

The fracture process zone (FPZ) can be described as the non-linear zone ahead of the crack tip which experiences increased softening. Micro-cracking and plastic deformation is characteristic of FPZ and traction across the crack decreases as crack separation increases. A schematic drawing of the FPZ concept in asphalt concrete is presented in Figure 28. The FPZ requires a significant portion loading energy and thus it is important for the fracture response after peak loading (Kim et al, 2009).

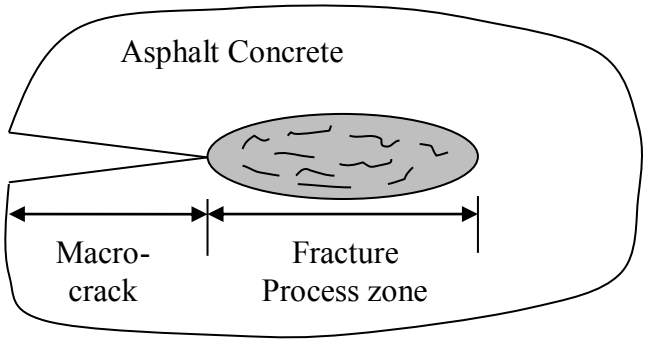

Figure 28 Schematic concept of FPZ in asphalt concrete.

Kim et al (2009) explored the FPZ concept using discrete element modeling (DEM) simulations of a DC(T) specimen. Figure 29 shows the compressive, tension, softening and fracture zones as a result of DEM simulations of the DC(T) specimen (150 mm diameter, -10°C). It evident that the softening zone begins before peak load is reached and ultimately the fracture zone overtakes the softening zones. The softening zone is also

dependent on its location in comparison to specimen boundaries. Authors concluded that the PFZ in asphalt concrete was approximately 40 mm.

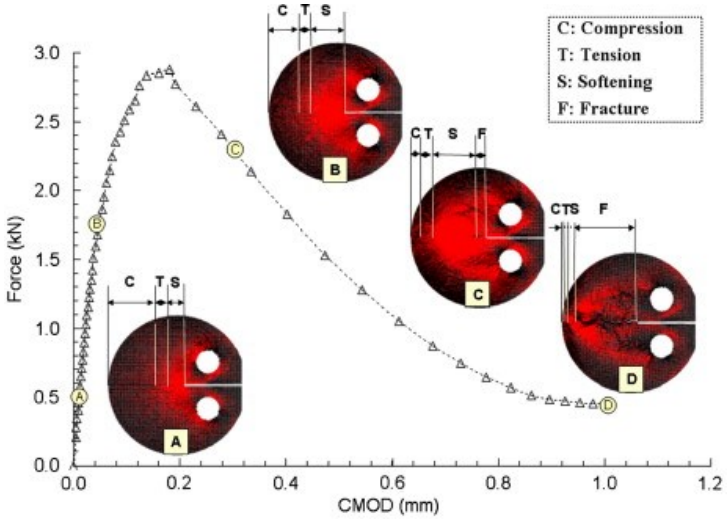

Figure 29 Progressive fracture process simulation (Kim et al, 2009).

Li and Marasteanu (2010) used acoustic emission to explore the FPZ of SCB specimens. In addition, numerical simulations were conducted and compared to test data. For the test conditions of the study, authors concluded that higher air voids and shorter initial notch lengths produced a longer FPZ. No FPZ size difference was noticed for different asphalt contents or the loading rates used in the study. As for aggregate type, the PFZ was wider for a softer limestone aggregate compared to granite aggregate, indicating less fracture resistance. Authors concluded that the size of the fracture process zone was approximately 30 mm at -30°C. For most fracture tests, this FPZ is of sufficient size in discredit the application of linear-elastic fracture mechanics.

3.13 Fracture Mechanics Incorporation into MEPDG

Fracture mechanics has been integrated into the thermal cracking module (TCMODEL) in the AASHTO Mechanistic-Empirical Pavement Design Guide (MEPDG). Through use of the Paris law for cracking propagation, the stress intensity factor (K), is used to relate the change in crack depth over one cooling cycle (Von Quintus, 1994). Equation 3.6 shows the crack depth fracture model incorporated into TCMODEL.

$$\Delta C = A(\Delta K)^n \quad \textbf{3.6}$$

Where:

ΔC = change in crack depth due to a cooling cycle (one day),

ΔK = change in stress intensity factor over one cooling cycle, and

A, n = fracture parameters.

Obtaining fracture properties of materials as part of Superpave mixture design is not practical and thus determination of the *A* and *n* parameters must be based on material properties obtained during standard tests (Lytton, Uzan et al, 1993; Marasteanu et al, 2007; Zborowski, 2007). Relationships have been developed by Molenaar (1983) (Equation 3.7) and Schapery (1984, 1986) (Equation 3.8) to relate the *A* and *n* parameters, respectively to the *m*-value and failure limit of asphalt concrete (Vinson et al, 1989b; Zborowski, 2007).

$$\log A = 4.389 - 2.52 * \log(E * \sigma_m * n) \quad \textbf{3.7}$$

Where:

E = mixture stiffness, and

σ_m = tensile strength.

$$n = 0.8 * \left(1 + \frac{1}{m}\right) \quad \textbf{3.8}$$

Where:

m = slope of creep compliance at -10°C.

An improved equation for calculating the Paris law "A" parameter was developed by Zborowski and Kaloush (2011) based on the original Schapery's general "A" parameter equation for viscoelastic materials. Tensile strength (S_t) and total fracture energy (G_f), used in calculating the "A" parameter, were interpolated from the three laboratory measured values for temperature, at which the maximum stress occurred. Thus, "A" is no longer a constant material property, but is temperature-dependent and changes with every cycle. This new feature of the crack depth fracture model is considered a big improvement over the old model, especially for rubber-modified mixtures. The new "A" parameter is calculated according to Equation 3.9.

$$A = \frac{\pi}{6\sigma_m^2 I_1^2}\left[\frac{(1 - 0.12^2)D_1}{2\Gamma}\right]^{\frac{1}{m}} \quad \textbf{3.9}$$

Where:

σ_m = tensile strength at maximum stress temperature (GPa),

m = slope of the creep compliance curve,

Γ = total fracture energy at maximum stress temperature (MN-m), and

I_1 = value of the integral of the dimensionless stress-strain curve of the material. Its value ranges between 1 and 2.

The stress intensity factor (K) in Equation 3.6 is computed using the regression model presented in Equation 3.10. This model is based on computations of a finite

element program CRACKTIP for a single crack, which was developed at the Texas Transportation Institute (Lytton, Uzan et al, 1993; Zborowski, 2007).

$$K = \sigma(0.45 + 1.99 * C_o^{0.56}) \quad \textbf{3.10}$$

Where:

K = stress intensity factor,

σ = far-field stress at crack tip (from pavement response model), and

C_o = current crack length.

TCMODEL has a restriction that the crack can only propagate through one of four assigned sub-layers of an asphalt concrete layer even if the magnitude of stress justifies a full-depth crack. Thus, four extremely cold days are required to fully propagate the crack through the entire layer (Marasteanu et al, 2007).

3.14 Crack Growth Rate Master Curve

Seo et al (2004) introduced the reduced crack growth rate concept in order to determine if crack growth rates can be predicted between temperatures. Considering the time-temperature superposition principle, Equation 3.11 describes the relationship between time and reduced time using the linear visco-elastic shift factor for temperature (T) from the complex modulus test.

$$\xi = \frac{t}{a_T} \quad \textbf{3.11}$$

Where:

ξ = reduced time,

t = time, and

a_T = linear visco-elastic shift factor for temperature (T) from the complex modulus test.

Authors converted crack growth data to a reduced crack growth rate at a reference temperature of 25°C according to Equation 3.12.

$$\dot{a}_{\xi} = \frac{da}{dt} * a_T \qquad \textbf{3.12}$$

Where:

a_{ξ} = reduced crack growth rate,

da/dt = crack growth rate, and

a_T = linear visco-elastic shift factor for temperature (T) from the complex modulus test.

Using this concept, reduced crack growth rate master curves were developed as a function of ΔK_I for cyclic loading. Authors concluded that that time temperature superposition principle can be successfully applied to develop crack growth rate predictions for different temperatures.

Schwartz et al. (2002) performed a study to determine whether time-temperature superposition principles are applicable to large strain rates. Constant displacement rate, uniaxial compression tests were applied to asphalt concrete specimens. Authors concluded that temperature superposition is valid at large strain rates and the temperature shift function may not be largely influenced by strain level. Practically, differences between the small-strain and large-strain temperature shift functions may not be of importance.

Chapter 4

4 C* SPECIMEN GEOMETRY AND TEST CONDITION STUDY

4.1 Background

Initial work on the C* Line Integral Test used Marshall sized specimens with 100 mm diameter, 63.5 mm thickness and specimens were tested at 21°C (Abdulshafi, 1983; Abdulshafi and Kaloush, 1988). Subsequent tests carried out by Kaloush (2010), utilized 150 mm diameter by approximately 45 mm thick specimens obtained from gyratory specimens and also carried out the test at 21°C. In both instances, various constant displacement loading rates were applied to multiple specimens needed for the test. However, it was evident that specimen size effects and test conditions should be evaluated in order to recommend a final test procedure.

This chapter describes two parallel studies; a specimen geometric study and a test temperature study that were carried out in order to develop a standardized test procedure. These studies considered three notched disk specimen geometries and five test temperatures that will be described in subsequent sections. In addition, the graphical C* data analysis method was examined and modifications were proposed for application to asphalt concrete.

4.2 Asphalt Mixture Properties and Gradation

Asphalt concrete samples used for testing in this part of the study were prepared in the laboratory using local Arizona materials and asphalt binder. The asphalt mixture consisted of a typical dense-graded, Arizona Department of Transportation (ADOT) mixture using a nominal maximum aggregate size of 19 mm. PG70-10 binder was used

at a rate of 4.6% by total weight. G_{mm} of the mixture was determined in the laboratory as 2.482 and the target laboratory air voids was 6.0 ± 0.75%.

The gradation, presented in Table 2, was created using Salt River aggregates obtained from the CEMEX Inc. asphalt plant located in Phoenix, Arizona. Aggregates were obtained, dried and blended from five stockpiles: 19 mm (18%), 12.5 mm (12%), 9.5 mm (12%), washed sand (15%) and crusher fines (43%). Blended batches of aggregates were sieved into individual sizes in order to control the gradation of the laboratory samples and materials were stored in covered 5-gallon plastic buckets.

Table 2 Aggregate gradation for ADOT mixture.

Sieve Size (mm)	% Passing
25	100
19	91
12.5	83
9.375	76
4.75	60
2.36	46
1.18	32
0.6	22
0.3	13
0.15	8
0.075	4.9

4.3 Sample Preparation

The following steps summarize the specimen mixing process used in the laboratory to prepare test specimens.

1. 6800g aggregate batches were created from the sieved buckets according to the standard mix design gradation.

2. Asphalt binder and aggregate were heated to the mixing temperature of 300°F (149°C) and binder was added to the hot aggregate in a mixing bucket by weight.
3. Mixing was conducted in a bucket mixer using a paddle for approximately two minutes and mixture was immediately transferred to a 2' x 2' x 3" deep pan and covered.
4. Short term again was conducted according to AASHTO PP2 Superpave aging protocol.
5. Mixture was introduced to an IPC Superpave gyratory compactor mold in three equal lifts to ensure good compaction and to eliminate large voids created when filling the mold.
6. A filled mold was reheated for approximately 30 minutes to ensure a proper compaction temperature of 300 °F (149°C) and was then compacted to a pre-specified height of 170 mm. The mass to mold, required to achieve target air voids, was determined according to several mass to mold trials conducted beforehand.
7. After cooling, specimens were cored and/or saw cut using water cooled diamond blades to desired diameter and thickness.
8. After air drying, bulk specific gravity and air voids were calculated according to ASTM D2726-11.
9. A right-angle notch was carefully cut into the specimen using a water-cooled diamond blade and a jig to hold the specimen. The specimen was rotated 45° in each direction from the vertical centerline to facilitate cutting the notch edges vertically.

10. Finally, a diamond coated scroll saw blade (100 mm length by 1.6 mm wide) manufactured by Kent Blades was used to introduce a 3 mm deep by 1.6 mm wide initial crack into the specimen.
11. The final step in specimen preparation included painting the face of the specimen and placing an incremental marking system on the specimen face to monitor crack progression during the test. The paint type is described in Section 4.3.1.

In order to reduce variability in test data, care was taken during specimen preparation to meet the target air void level of 6% (±0.75%) and the target thickness of 50mm (± 4mm) or 25mm (± 3mm). Table 3 provides air voids and thicknesses of the test specimens, along with descriptive statistics. The air voids and thickness values are very close to the target values and the low coefficient of variation values indicate consistent test samples.

Table 3 Sample air void and thickness summary

Test Conditions		Air Void Summary			Thickness Summary		
Size (mm)	Temp °C	Average (%)	St. Dev.	C.V.	Average (mm)	St. Dev.	C.V.
150 x 50	21	6.10	0.29	4.7%	50.53	1.19	2.4%
100 x 50	21	5.97	0.41	6.9%	50.45	1.30	2.6%
150 x 25	21	5.95	0.23	3.8%	26.13	0.79	3.0%
150 x 50	4.4	5.87	0.46	7.8%	50.07	0.92	1.8%
150 x 50	10	5.79	0.27	4.7%	50.60	0.67	1.3%
150 x 50	37.8	6.06	0.38	6.3%	49.95	1.29	2.6%

4.3.1 Paint Selection

Acrylic craft paint purchased from JoAnn Fabric Products was used to paint the face of the specimen to provide a highly visible contrast of the crack location. This paint was selected because it did not have crack resistance properties found in certain

latex paints. Crack resistant paints should be avoided as they introduce crack location error and at times the crack is not observed on the surface under the paint.

Originally, high visibility orange and flat white paints were selected to determine the best option to visualize the crack location. However, during trial tests the orange paint displayed elastic behavior and crack location was sometimes masked by the paint or it was difficult to determine the crack location. The white paint was selected for future testing as it provided the best contrast to determine crack location. Figure 30 presents an example of using white paint to enhance crack visibility on a tested specimen. From this figure, the crack at each 10 mm reference mark can easily be observed and documented.

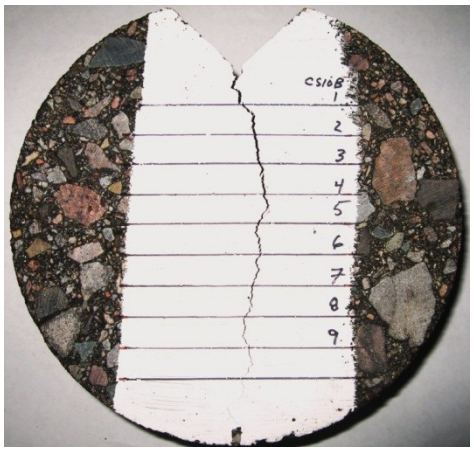

Figure 30 Crack visibility using white paint.

4.3.2 Specimen Marking Template

In order to simplify specimen marking and to facilitate marking the right-angle notch and initial crack, a marking template was created using Mylar type material. From the tip of the initial crack, 10 mm increments were marked on each specimen to be used as a reference system to monitor crack length over time. The number of reference lines depended on the diameter of the test specimen. Figure 31 shows an example template

used to mark a 150 mm diameter test specimen. It is important to note that this template was also used to mark the right angle notch and also the length of the initial crack.

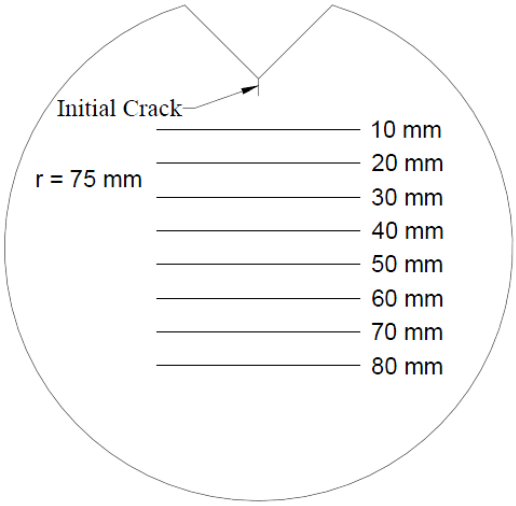

Figure 31 Specimen marking template for 150 mm diameter specimen.

Figure 32 presents an example of the final CFT specimen ready for testing. Note that the crack length markings are very visible with the white paint used as the background.

Figure 32 Example of final CFT specimen.

4.4 C* Fracture Test Apparatus

The CFT apparatus was based on the setup developed by Abdulshafi (1983) and modified by Kaloush et al. (2010). Two stainless steel loading plates (3 mm thick) with right-angled edges were used to form the loading plates placed in the notched cut. A Lottman Breaking Head was modified at the ASU machine shop to produce a loading head with appropriate radius such that a point load is applied at a distance halfway along each notch face. The bottom loading platen was curved to match the 100 mm or 150 mm radius and came standard on each respective Lottman Breaking Head. Figure 33 presents a schematic of the CFT apparatus and photo of an actual specimen loaded into the apparatus.

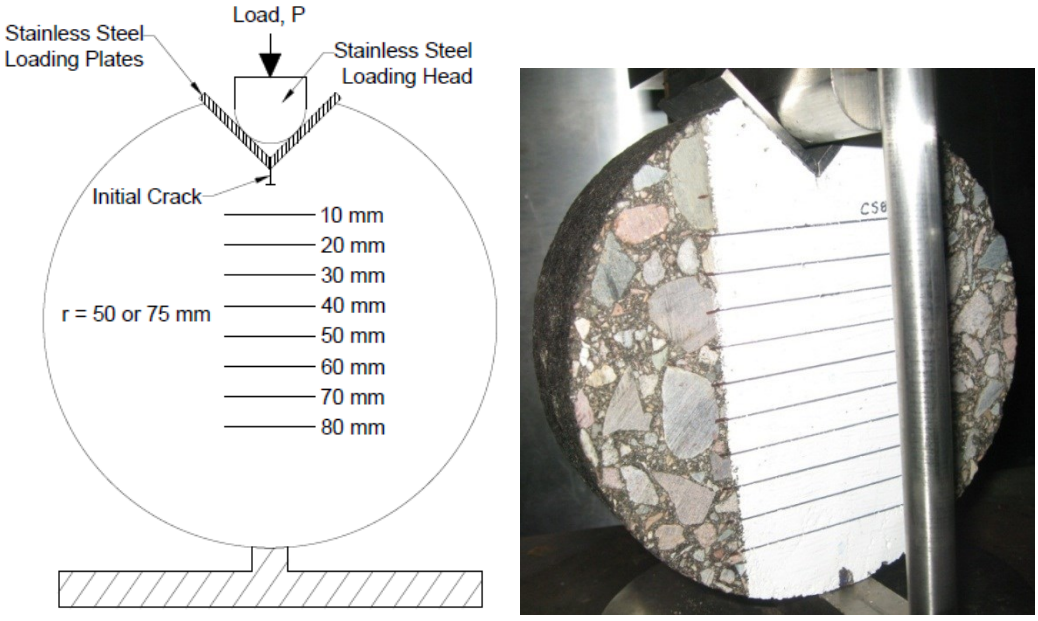

Figure 33 C*Fracture Test apparatus.

The dimensions of the modified loading head which mounted to the top plate of the Lottman Breaking Head are presented in Figure 34. Again, these dimensions were

formulated such that a point load was transferred to the stainless steel loading plates at the midpoint of the notch in the asphalt concrete specimen.

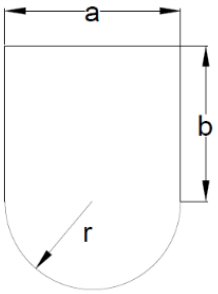

Specimen Diameter (mm)	Loading Head Dimension (mm)		
	a	b	r
150	25.3	19.8	12.65
100	17	15	8.5

Figure 34 Dimensions of loading head.

4.5 Experimental Plan for Geometric and Test Temperature Study

The experimental plan to investigate specimen geometry and test temperature was developed considering test temperatures and specimen sizes commonly used in laboratory testing of bituminous concrete. The factors considered included: specimen diameter, test temperature and specimen thickness. This experiment plan was divided into two smaller studies: 1) Geometric Study and 2) Test Temperature Study. The intent was to establish a standardized test procedure including sample size prior to considering additional test temperatures.

Table 4 presents the experimental plan for these two studies, which considered 100 and 150 mm diameter specimens and five test temperatures; 0, 4.4, 10, 21 and 37.8°C. Specimens with these diameters can easily be obtained from field cores or from gyratory prepared specimens. Once a test procedure was established in the geometric study, the test temperature study was carried out at four additional temperatures in order to determine the effect of temperature on the C* parameter and crack growth rates and to define any practical limits of the CFT.

Displacement rates presented in Table 4 for 21°C were initially selected based on the ranges found in literature (Abdulshafi, 1983; Abdulshafi and Kaloush, 1988; Kaloush et al, 2010). These displacement rates were reduced for lower temperatures of 4.4°C and 10°C because crack speed was too rapid to record using the video camera if specimens were subjected to 21°C displacement rates. Displacement rates were increased for 37.8°C since lower rates typically resulted in branch cracking.

In total, 35 specimens were required for the geometric study while an additional 40 specimens were necessary to complete the test temperature portion of the experimental plan. Initially, only two replicates were considered at all temperatures. However, a third replicate was added to the 150 x 50 mm specimen size tested at 21°C to examine the effects of test replicates on the C* parameter and crack growth rates.

4.6 Data Analysis

The following section describes the data analysis procedures utilized to analyze C* and crack growth rate information from the C* fracture test method.

4.6.1 Extraction of Crack Length and Load Data from the CFT

Crack length and applied load as a function of time are the two necessary data sets collected from the C* Fracture Test. Typically, test data from the IPC UTM 100 equipment is exported in CSV format which contains important test data. A Microsoft Excel file was created to analyze the output CSV file and automatically match the time at which the crack was at each specified length with an associated actuator load.

Table 4 Experimental plan.

	Test Temperature	Diameter (Thickness)	Displacement Rate (mm/min)	Number of Replicates
Geometric Study	21°C	150 mm (25 mm)	0.15	2
			0.228	2
			0.3	2
			0.378	2
			0.45	2
	21°C	150 mm (50 mm)	0.15	3
			0.228	3
			0.3	3
			0.378	3
			0.45	3
	21°C	100 mm (50 mm)	0.15	2
			0.228	2
			0.3	2
			0.378	2
			0.45	2
Test Temperature Study	0°C	150 mm (50 mm)	0.042	2
			0.078	2
			0.114	2
			0.15	2
			1.186	2
	4.4°C	150 mm (50 mm)	0.03	2
			0.06	2
			0.102	2
			0.15	2
			0.3	2
	10°C	150 mm (50 mm)	0.072	2
			0.15	2
			0.228	2
			0.30	2
			0.378	2
	37.8°C	150 mm (50 mm)	0.378	2
			0.60	2
			0.90	2
			1.20	2
			1.50	2

In order to determine crack length as a function of time, a high definition JVC Everio G-series digital video camera was used and was manually started at the beginning of each test. Videos were later analyzed on a large computer monitor and the times at which the crack passed the specified markings were recorded. Time at each incremental crack length was recorded as the average of two separate viewings of each video segment as this typically provided a more reliable crack speed measurement. Using extracted data, load-time (P-T) and crack growth (a-T) plots were generated for each test sample similar to those shown in Figure 35, which represents constant displacement rates of 0.15 and 0.378 mm/min. Typically, fracture initiated shortly after peak load and applied load was reduced as crack length increased.

It is important to note the non-linear crack growth as a function of time in Figure 35 and the associated non-linear load trend. In the upper graph, crack growth appears to be relatively constant throughout the depth of the specimen. However, the lower figure indicates a potential response of crack growth observed in the notched disk specimens at 21°C when samples were subjected to higher constant displacement loading rates. At a certain point, crack growth slows that may be the result of entering a zone of compressive stresses generated at the bottom of the specimen or a reduction of crack tip stress based on the specimen geometry. For the 150 mm diameter specimens, this reduction of crack propagation rate generally occurred after crack lengths of 70 mm (a/W = 0.57). This trend was not as pronounced in the 100 mm diameter specimens; however, non-linearity typically occurred after crack length of 50 mm (a/W = 0.62).

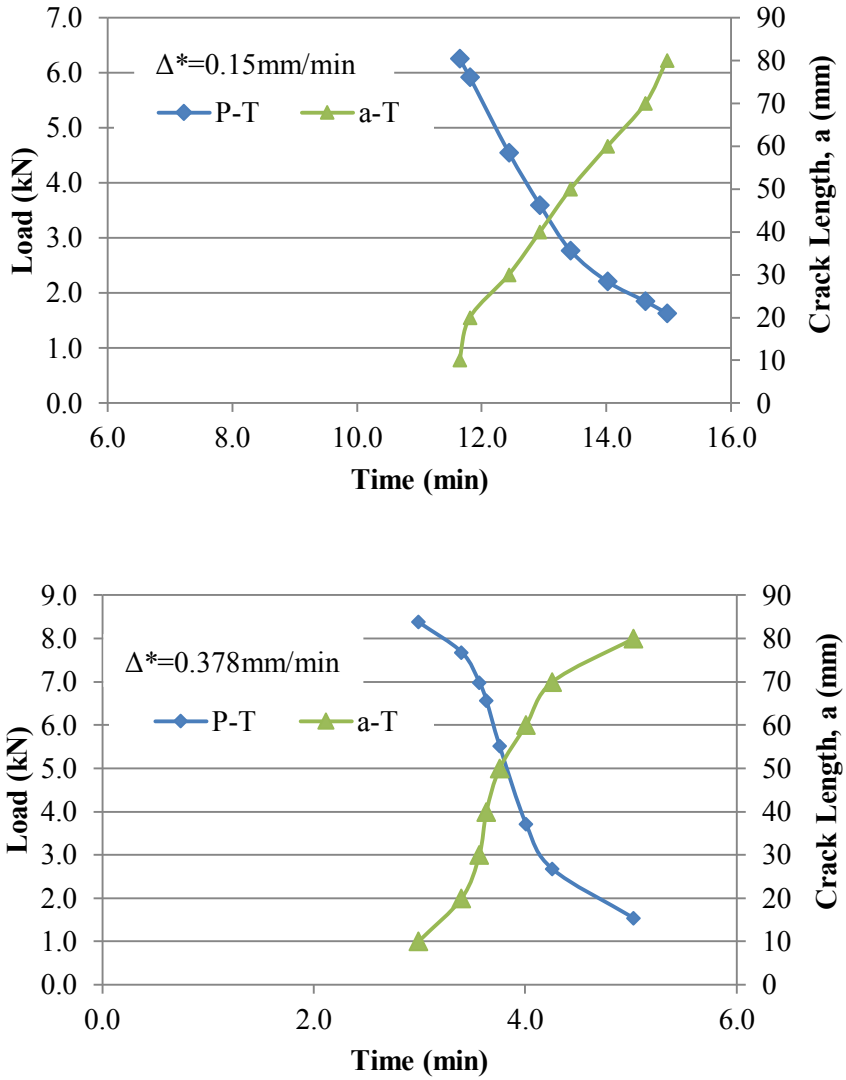

Figure 35 Example P-T and a-T relationships for 150 x 50 mm specimens at 21° C.

Once load and crack length data were obtained as a function of time, the next step was to normalize the load at each crack length interval by dividing by the specimen thickness; a step that is required for calculation of the C* parameter. Table 5 shows example data from a 150 mm diameter sample tested at 21°C. The crack growth rate (a*) in this example was calculated using a linear fit of the crack length versus time data (10-80 mm interval) found in the first two columns of the table.

Table 5 Example data extracted from CFT (150 x 50 mm), 21°C).

Sample ID:		Average Thickness, b (mm):	Displacement Rate, Δ* (mm/min)	
CS17T		51.99	0.150	
Crack Length, a (mm)	Time, T (Min)	Force (kN)	Force per Unit Thickness, P/t (N/mm)	Crack Growth Rate, a* (m/hr)
10	11.64	6.26	120.32	1.17
20	11.81	5.92	113.84	
30	12.43	4.55	87.53	
40	12.93	3.60	69.23	
50	13.43	2.77	53.23	
60	14.02	2.21	42.44	
70	14.63	1.85	35.56	
80	14.97	1.63	31.37	
			R^2 =	0.99

4.6.2 Calculation of U* Data

U* is the energy rate and can be calculated as the area under the normalized load-displacement rate (P-Δ*) plots (between 0 and Δ*) for each crack length increment (Refer to Equation 2.11). Thus for a given test temperature, normalized load data from all displacement rates were extracted and sorted according to incremental crack lengths (e.g. 10mm, 20 mm, etc.). Figure 36 presents an example of a typical normalized load versus displacement rate plot for 150 x 50 mm specimens at 21°C (a=10 mm). The range of displacement rates for selected test conditions were between 0.15 and 0.45 mm/min.

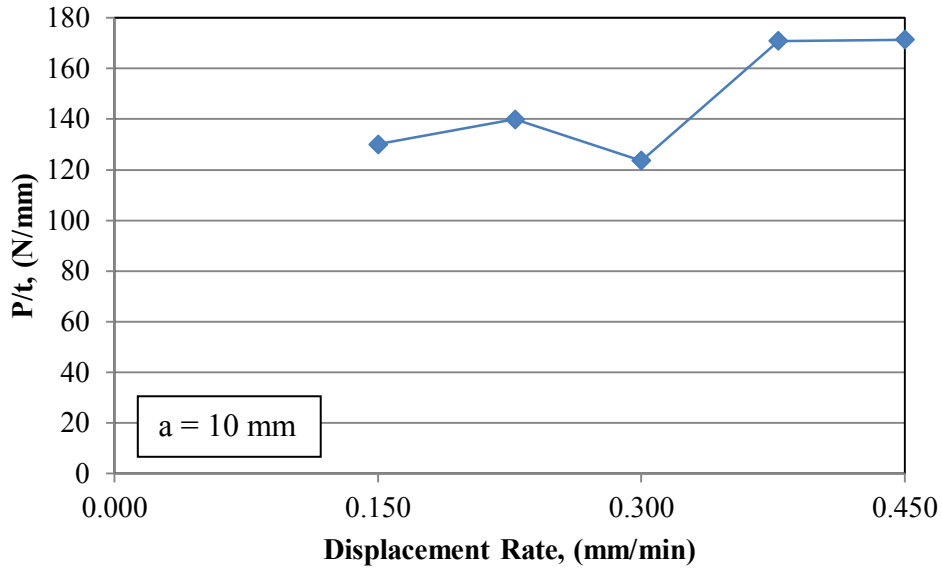

Figure 36 Example P-Δ* data at 21°C (150 x 50mm specimens).

Common methods to calculate area under a curve include integration of a function fitted to experimental data or use of the average end area method. Both methods were considered and compared in order to determine an appropriate method for calculation of U* data.

4.6.3 Integrated Power Model versus Average End Area Method

Analysis of experimental data indicated that a power model could be used to represent P-Δ* data which is consistent with C* data reduction methods utilized by Abdulshafi (1982) for C* analysis of asphalt concrete. Thus, in this example, U* can be calculated as the integral of the power model of data between 0 and 0.45 mm/min. The average end area method was used as an alternative or more simplified method to determine the energy rate (U*). Figure 37 provides an example of a P-Δ* plot for a crack length of 10 mm (21°C, 150 x 50mm specimens) and shows power model and average end area representations of the data.

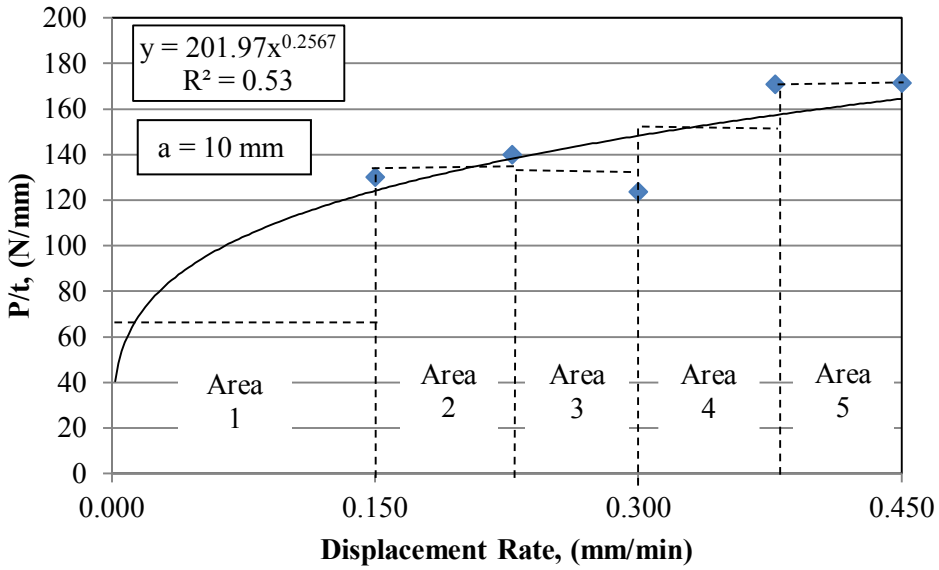

Figure 37 Example power fit and average end area method (21°C, 150 x 50mm specimens).

Table 6 and Table 7 present U* data calculated using the integrated power model and average end area methods, respectively. The integrated power model method simply calculated the area under the curve (U*) as the integral of the power function between 0 and Δ*. In comparison, the average end area method calculated area under the curve according to Equation 4.1 where A_i represents the average end area of the i^{th} interval.

$$U^* = \sum_{0}^{\Delta_i^*} A_i \qquad \textbf{4.1}$$

Typically, integration of the power model produces higher U* values due to the fact that the average end area method has the potential to considerably underestimate the first area interval (Area 1), 0-0.15 mm/min as shown in Figure 37.

Table 6 U* data calculation based on integrated power model method (21°C, 150mm x 50mm specimens).

Crack Length (mm)	Average Energy Rate, U* (N-mm/mm-min)				
	Displacement Rate, (mm/min)				
	0.15	0.228	0.30	0.378	0.45
10	14.8	25.1	35.4	47.3	58.9
20	13.9	23.6	33.4	44.6	55.6
30	11.8	20.4	29.3	39.7	50.0
40	10.9	18.6	26.6	35.8	44.9
50	9.8	16.6	23.4	31.4	39.1
60	6.6	11.7	17.0	23.3	29.7
70	5.1	8.7	12.3	16.5	20.6
80	3.1	4.6	6.1	7.6	9.0

Table 7 U* data calculation based on average end area method (21°C, 150mm x 50mm specimens).

Crack Length (mm)	Average Energy Rate, U* (N-mm/mm-min)				
	Displacement Rate, (mm/min)				
	0.15	0.228	0.30	0.378	0.45
10	9.75	20.28	29.76	41.25	53.57
20	9.23	19.43	28.28	38.70	50.57
30	8.11	17.46	25.48	34.84	46.07
40	7.27	15.64	22.96	31.22	40.97
50	6.41	13.82	20.17	26.98	35.35
60	4.29	9.92	15.32	20.94	27.41
70	3.69	7.46	10.51	14.23	18.80
80	3.13	6.23	8.44	10.71	13.39

Figure 38 provides a graphical comparison of integrated power model versus average end area U* data, along with the line of equality. Graphically, it is evident that the integrated power model method calculates higher U* values than the average end area method.

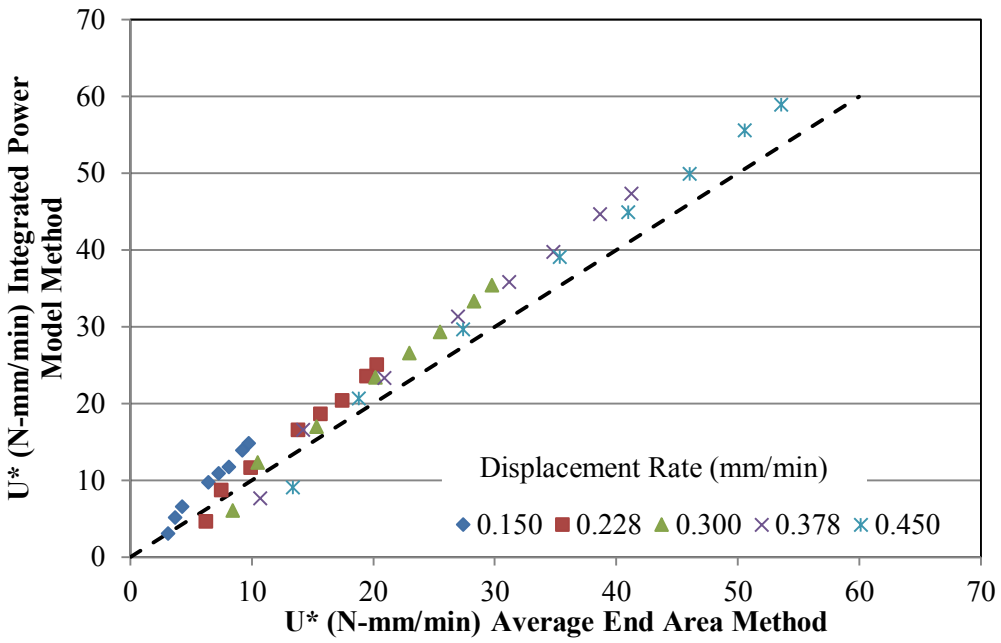

Figure 38 Comparison of U* data using the power model and average end area methods (21°C, 150mm x 50mm specimens).

One potential disadvantage of using the power model to represent P-Δ* data is depicted in Figure 39 that represents data at 21°C (150 x 50mm specimen) for a crack length of 80 mm. This trend can potentially be observed at long crack lengths (70+ mm) toward the bottom of a CFT specimen. In this example, the normalized load data decreases with increasing displacement rate. The power model displays a negative exponent, which is not reasonable, and a R^2-value less than 0.1 indicates a no fit of the experimental data. Also, for any crack length, if the data point for the first loading rate is higher than at other loading rates, the power model can potentially exhibit a negative exponent and produces a model similar to Figure 39.

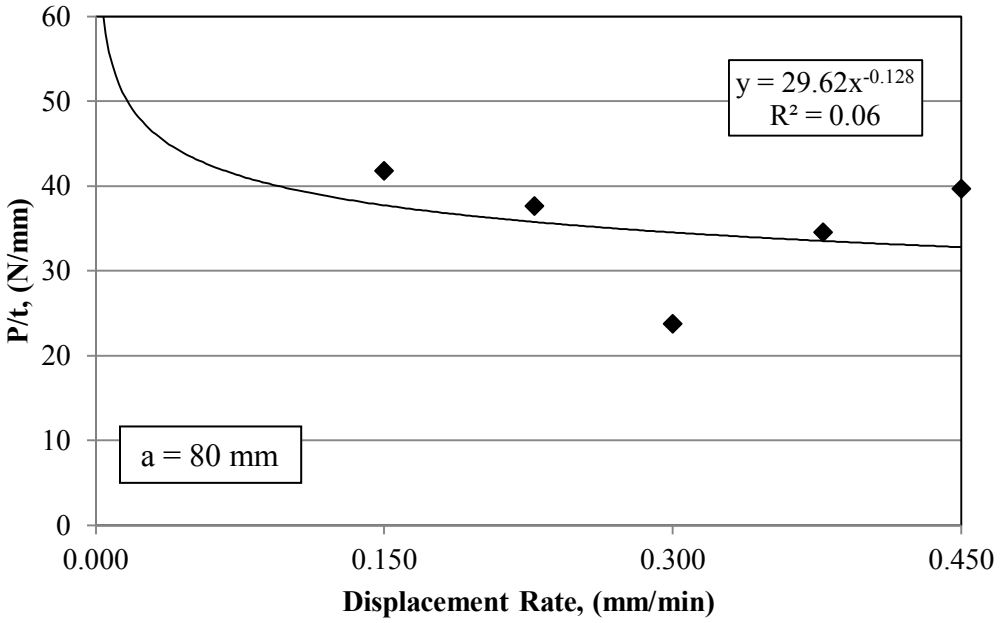

Figure 39 Example of poor power model fit of load-displacement rate data at 21°C (150 x 50mm specimens).

Since the average end method calculation of U* is a summation, it relies heavily on the computation of the area of the 1st interval (Area 1) shown in Figure 37. In the case of these example data at 21°C, the lowest applied displacement rate in the test was 0.15 mm/min. However, as the minimum (or initial) displacement rate is increased, which is the case as test temperature increases, computation of the first interval of U* data could potentially depart further from U* data obtained by an integrated power model representation of the data. Thus, an area correction factor was needed to account for the U* difference between calculation methods in order to improve the accuracy of the U* data obtained using the average end area method.

Most of the error associated with computation of U* values using the average end area method is due to the fact that the data begins at the origin and forms a triangle with the first data point. Area of a triangle can be used which equals 0.5 times the y-value

multiplied by the x-value. Figure 40 presents a schematic that shows increasing error between the average end area method and integrated power function as the initial displacement rate increases. If X_1 is greater than X_o, the error associated with area under the power function curve is greater in the latter case.

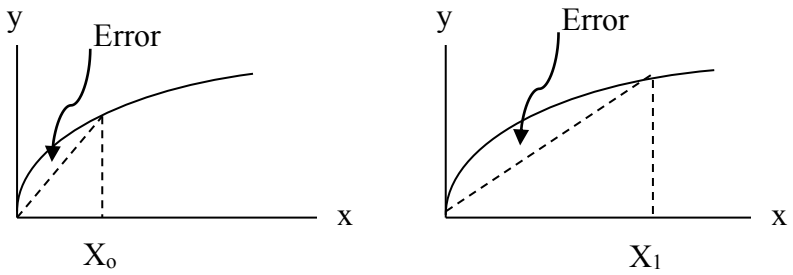

Figure 40 Schematic showing area calculation errors using average end area method.

The correction factor was derived through use of a generic power function provided in Equation 4.2. When fitting normalized load versus applied displacement rate laboratory data with power functions, as described in Section 4.6.3, the exponent (b-parameter) of the power fit of these data typically ranged between 0.05 and 0.5 for the ADOT mixture (all crack lengths). Thus, this power exponent range was considered during development of the correction factor using Equation 4.2.

$$y = (\Delta^*)^b \qquad \textbf{4.2}$$

Where:

y = value of the power function,

Δ^* = displacement rate of CFT test (mm/min), and

b = power exponent.

Three ranges of displacement rates were considered: 0.06-0.3 mm/min, 0.15-0.45 mm/min and 0.378-1.5 mm/min. These ranges were based on laboratory observations of

CFT tests conducted at different temperatures of 4.4°C, 21°C and 37.8°C, respectively. Noticeably, lower displacement rates are best suited to capture crack propagation at lower temperatures. U* values were computed using the average end area method and by integrating Equation 4.2 and percent error between the two methods was computed. The initial b-value of the power function was set at 0.05 and the correction factor was iterated from a starting value of 0.5 until the percent error was approximately 5% or less. Once the percent error between the two methods met this criterion, the b-value was increased and % error was again checked. After several iterations, a correction factor of 0.8 yielded approximately 5% error or less across all b-values and displacement rate ranges as shown in Table 8.

Table 8 Percent error comparison between average end area and integrated power function methods.

% Error in Area			
b-value	Δ_o* (mm/min)		
	0.06	0.15	0.378
0.05	-1.57	-5.07	-3.79
0.1	-1.22	-3.63	-2.69
0.2	-0.71	-1.15	-0.86
0.25	-0.53	-0.09	-0.12
0.3	-0.39	0.85	0.53
0.4	-0.18	2.45	1.59
0.5	-0.03	3.72	2.37

Therefore, the area of the first interval between zero and the first displacement rate should be calculated according to Equation 4.3.

$$Area_1 = 0.8 * (P/t)_o * \Delta_o^* \qquad \textbf{4.3}$$

Where:

$(P/t)_o$ = normalized load value at the initial displacement rate, and

Δ_o* = initial displacement rate of CFT test (mm/min).

Figure 41 presents a comparison of U* calculation methods after applying the correction factor of 0.8. These data follow the line of equality except for a few data points at low U* values. Recall that a power fit of the actual data can potentially have low R^2-values, especially at long crack lengths. These data points which fall below the line represent these differences between actual data and the modeled function.

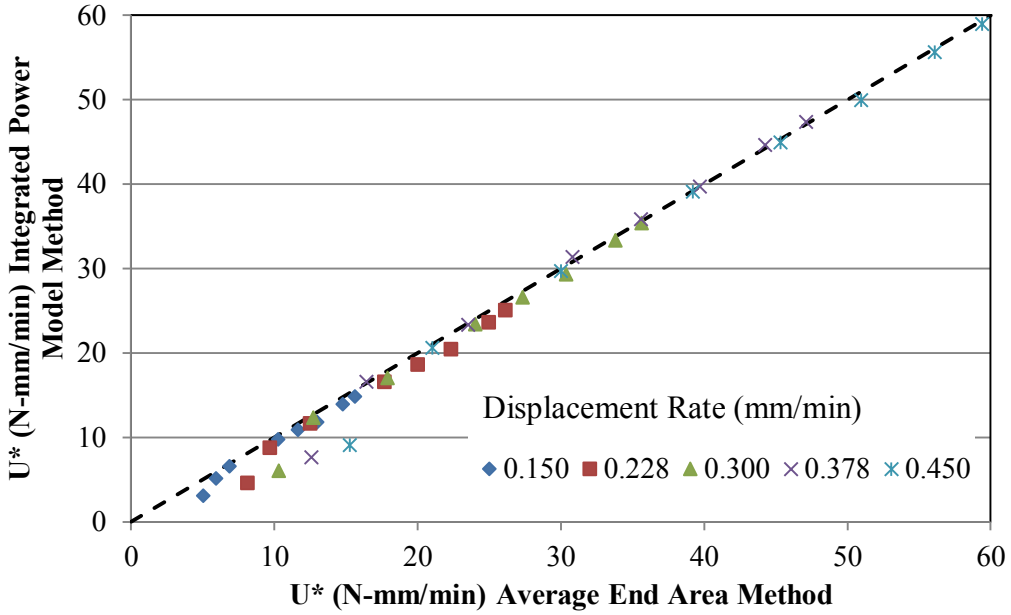

Figure 41 Comparison of U* data with correction factor (21°C, 150mm x 50mm specimens).

Based on analysis presented in this section, it is recommended that calculation of U* data (area under the normalized load versus displacement rate curves) be accomplished using the average end area method with the modification of using Equation 4.3 to calculate the area of the first interval between zero on the initial displacement rate.

4.6.4 Calculation of C* Data

The C* parameters corresponding to each displacement rate for 150 x 50 mm specimens tested at 21°C are taken as the slope of the U*- crack length(a) data provided in Table 6, Table 7 and shown graphically in Figure 42. Linear fit of these average U* data are excellent with R^2-values greater than 0.98. Recall that each data point represents the average of two replicates meaning each U*-a relationship was generated using two CFT specimens. A summary of average U*-a slope values and C* parameters and standard deviation values are presented in Table 9. To obtain the proper units of MJ/m^2-hr, slope values are multiplied by a factor of -0.06. Overall, the C* parameters in this example show very low variability across all displacement rates.

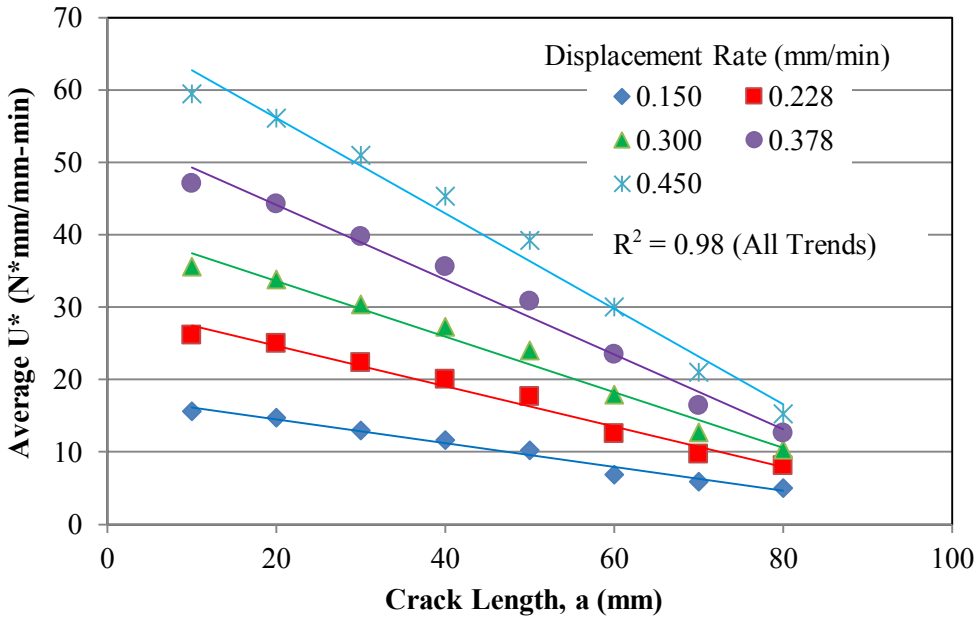

Figure 42 Average U*-a plot for 21°C using average end area method (150 x 50mm specimens).

Table 9 Average C*-values based on two replicates for 21°C (150 x 50 mm).

Parameter	Displacement Rate, (mm/min)				
	0.150	0.228	0.300	0.378	0.450
Slope	-0.164	-0.279	-0.385	-0.516	-0.659
R^2	0.98	0.98	0.98	0.98	0.98
C* (MJ/m^2-hr)	0.010	0.017	0.023	0.031	0.040
St. Dev.(C)*	*0.00017*	*0.00020*	*0.00013*	*0.00016*	*0.00031*

4.7 Determination of Data Analysis Range

The original crack analysis range considered in evaluation of CFT data was 10-80 mm for 150 mm diameter specimens and 10-50 mm for 100 mm diameter specimens. This range was selected to cover crack growth and the C* parameter in the linear and non-linear portions of crack growth as shown previously in Figure 35. However, justification of these original intervals is a necessary component in development of the CFT in order to provide recommendations of a data analysis range. Different data collection ranges were analyzed and compared in an effort to determine the optimal data collection rage for the CFT.

To investigate the effects of excluding these non-linear regions on crack growth rates, the following intervals were considered to determine the C* parameter and crack growth rate. For the 150 mm diameter specimens, additional data analysis ranges of 10-60 mm and 20-80 mm were considered while 10-40 mm and 20-50 mm data analysis ranges were included for analysis of the 100 mm diameter specimens. Figure 43 presents a schematic of the analysis ranges for a 150 mm diameter specimen: Range A (10-60 mm), Range B (10-80 mm) and Range C (20-80 mm).

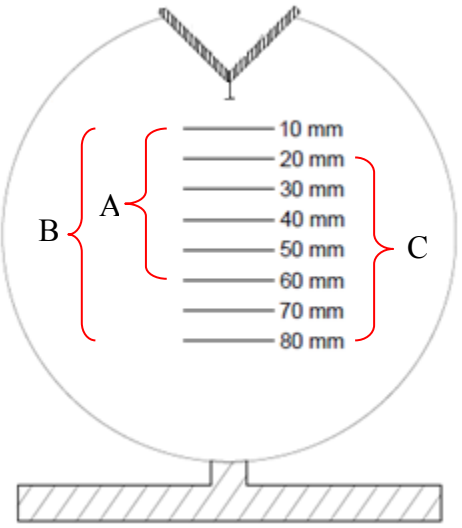

Figure 43 Data analysis ranges for 150 mm diameter specimens.

4.7.1 Data Analysis Range Comparison using Geometric Study Data

For each of the three specimen sizes included in the geometric study, two replicates were tested at each loading rate and power function regression parameters were fitted to CFT test data extracted from data analysis Ranges A, B and C. The coefficient of determination (R^2) was used to determine how well the fitted power trends described the replicate data. Recall that CFT's were conducted at 21°C. Table 10 presents the regression parameters and R^2-values for the replicate data.

For the 150 mm diameter specimens, the 10-60 mm interval showed the least fit of the data as indicated by R^2-values of 0.59 and 0.61 for the 50 mm and 25 mm thick specimens, respectively. In comparison, the 20-80 mm interval shows the highest R^2-values of 0.87 and 0.73 for the 50 mm and 25 mm thick specimens, respectively. For the 100 mm diameter specimens, the highest R^2-value of 0.73 was determined from a fit of data extracted from the 10-50 mm range. It is important to note that of the three specimen sizes, data from the 150 x 50 mm specimens produced the highest R^2-values.

Thus, a* and C* data in the 20-80 mm crack length range from the CFT on 150 x 50 mm specimens has the least amount of variability.

Table 10 Regression parameter comparison using replicate a* and C* data.

Temperature (°C)	Specimen Size (mm)	Interval (mm)	Regression		
			a	b	R^2
21	150 x 50	10-60	46.574	0.7721	0.59
		10-80	58.781	0.8651	0.82
		20-80	81.548	0.9565	0.87
	150 x 25	10-60	202.29	1.0837	0.61
		10-80	235.47	1.1492	0.73
		20-80	272.69	1.2036	0.73
	100 x 50	10-40	210.52	1.2088	0.71
		10-50	71.824	0.9488	0.73
		20-50	55.414	0.9145	0.64

Based on these data, the final data analysis range for 150 mm and 100 mm diameter specimens should be 20-80 mm and 10-50 mm, respectively. Selection of these ranges also helped to eliminate the nonlinear effects of crack growth at shallow crack lengths (<10 mm) and long crack lengths (>80 mm for 150 mm diameter or >50 mm for 100 mm diameter).

For further comparison, the average a* and C* data were fitted using power models. Table 11 presents the regression fitting parameters and R^2-values for these average a* and C* data from test replicates in the geometric study. For the 150 x 50 mm specimens, the highest R^2-value was determined using the 20-80 mm data analysis range. In comparison, the highest R^2-value for the 150 x 25 mm specimens was observed in the 10-80 mm range (0.93) and for the 100 x 50 mm specimens; the 10-40 mm data analysis range produced the highest R^2-value of 0.92. In all cases, the average data for the recommended intervals produced trends with excellent R^2-values.

Table 11 Regression parameter comparison using average a* and C* data.

Temperature (°C)	Specimen Size (mm)	Interval (mm)	Regression		
			a	b	R^2
21	150 x 50	10-60	112.97	0.9997	0.87
		10-80	64.521	0.8858	0.94
		20-80	84.468	0.9618	0.98
	150 x 25	10-60	1372.0	1.5647	0.92
		10-80	456.13	1.3178	0.93
		20-80	454.44	1.3366	0.90
	100 x 50	10-40	371.48	1.3555	0.92
		10-50	92.429	1.0158	0.88
		20-50	72.303	0.9874	0.77

Figure 44 presents a graphical comparison of a*-C* trends for the 150 mm diameter specimens tested at 21°C. It is evident that the 10-80 and 20-80 mm analysis ranges produce similar trends while the trend fitted to 10-60 mm data appears shifted to the left with more scatter in the data.

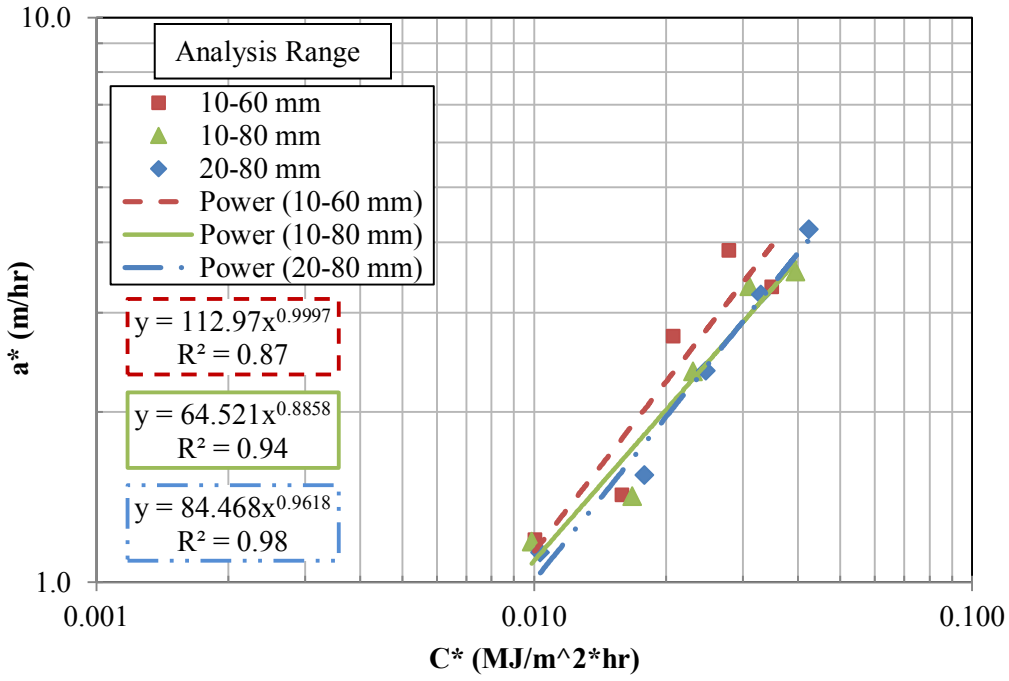

Figure 44 Data analysis range comparison (150 x 50 mm specimens).

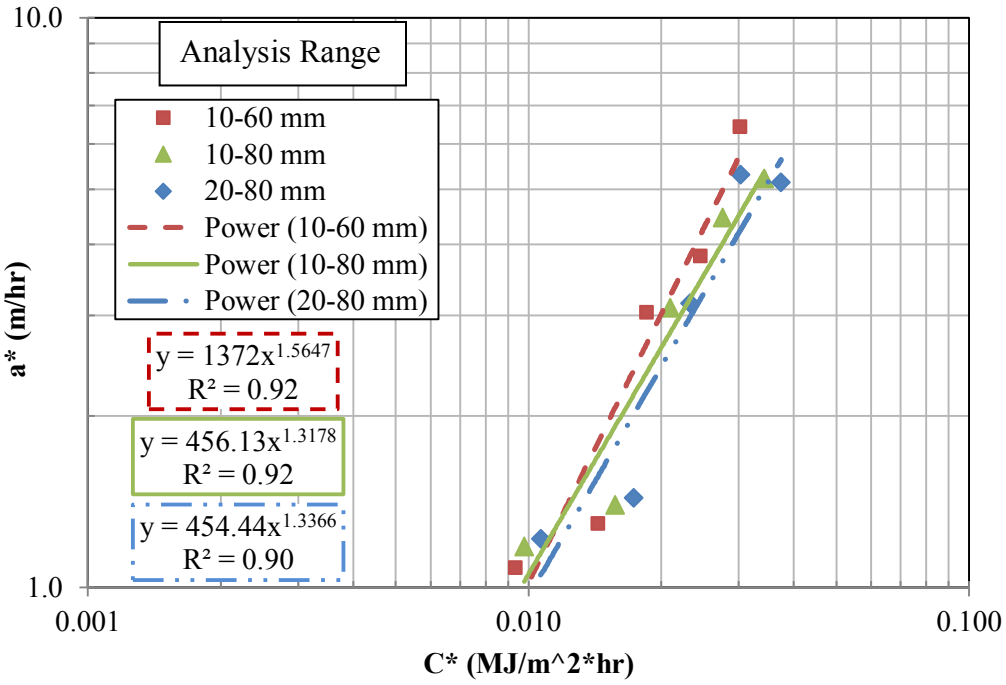

Figure 45 Data analysis range comparison (150 x 25 mm specimens).

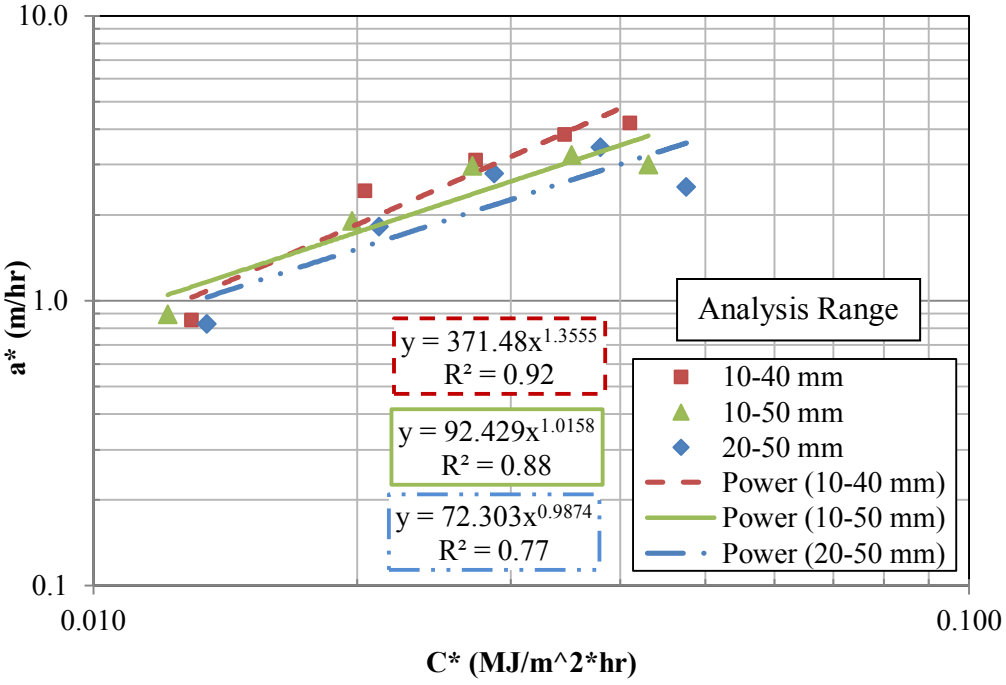

Figure 46 Data analysis range comparison (100 x 50 mm specimens).

4.7.2 Data Analysis Range Justification – Test Temperature Study Data

To further assess the data analysis range consideration, CFT data conduced on the ADOT mixture as part of the test temperature study was also included in this analysis. Tests were conducted at four additional temperatures; 4.4, 10 and 37.8°C. Table 12 presents regression parameter comparison these test conditions for the ADOT mixture. For 4.4 and 10 °C, the 20-80 mm interval produces the highest R^2-values. However, for 37.8 °C the 10-60 mm interval indicated the best fit of the replicate data. For comparison, trends of the average a* and C* data are shown in Table 13. For 10°C, data obtained in the 10-60 mm range has the most variability and this interval should not be used in CFT data analysis. At all other temperatures, fit of the average CFT data provides excellent R^2 values at any analysis range.

Table 12 Regression parameter comparison for ADOT mixture based on replicate data.

Temperature (°C)	Specimen Size (mm)	Interval (mm)	Regression		
			a	b	R^2
4.4	150 x 50	10-60	6453.10	1.2984	0.849
		10-80	14132.00	1.5462	0.864
		20-80	14043.00	1.5031	0.928
10	150 x 50	10-60	245.29	0.8481	0.399
		10-80	415.85	1.0759	0.794
		20-80	469.26	1.1142	0.861
37.8	150 x 50	10-60	172.87	1.2108	0.984
		10-80	135.30	1.1317	0.980
		20-80	152.60	1.1796	0.944

Table 13 Regression parameter comparison for ADOT mixture based on average data.

Temperature (°C)	Specimen Size (mm)	Interval (mm)	Regression		
			a	b	R^2
4.4	150 x 50	10-60	6025.70	1.272	0.984
		10-80	13802.00	1.529	0.988
		20-80	13885.00	1.496	0.998
10	150 x 50	10-60	714.20	1.090	0.678
		10-80	558.25	1.143	0.954
		20-80	620.55	1.175	0.988
37.8	150 x 50	10-60	174.75	1.213	0.998
		10-80	137.91	1.137	0.995
		20-80	157.77	1.189	0.973

Figure 47, Figure 48 and Figure 49 exhibit graphical comparison of a*-C* trends for CFT data obtained at 4.4°C, 10°C and 37.8°C, respectively. Except for 37.8°C, the 10-60 mm trends appears shifted and/or rotated in comparison to data collected in the 10-80 mm and 20-80 mm analysis ranges.

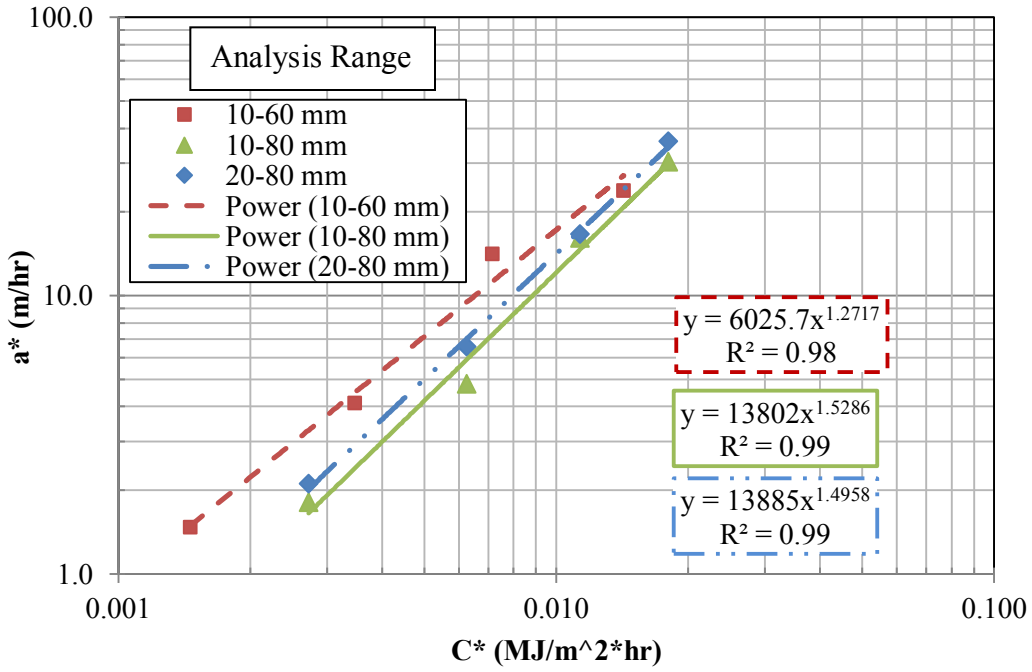

Figure 47 Data analysis range comparison for ADOT mixture at 4.4°C.

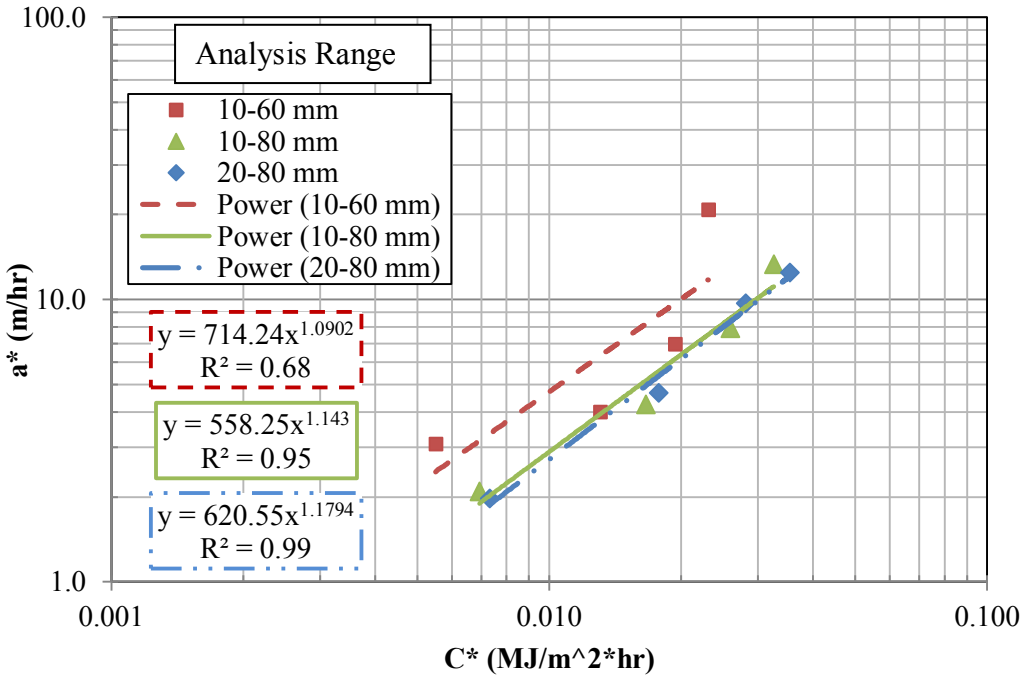

Figure 48 Data analysis range comparison for ADOT mixture at 10°C.

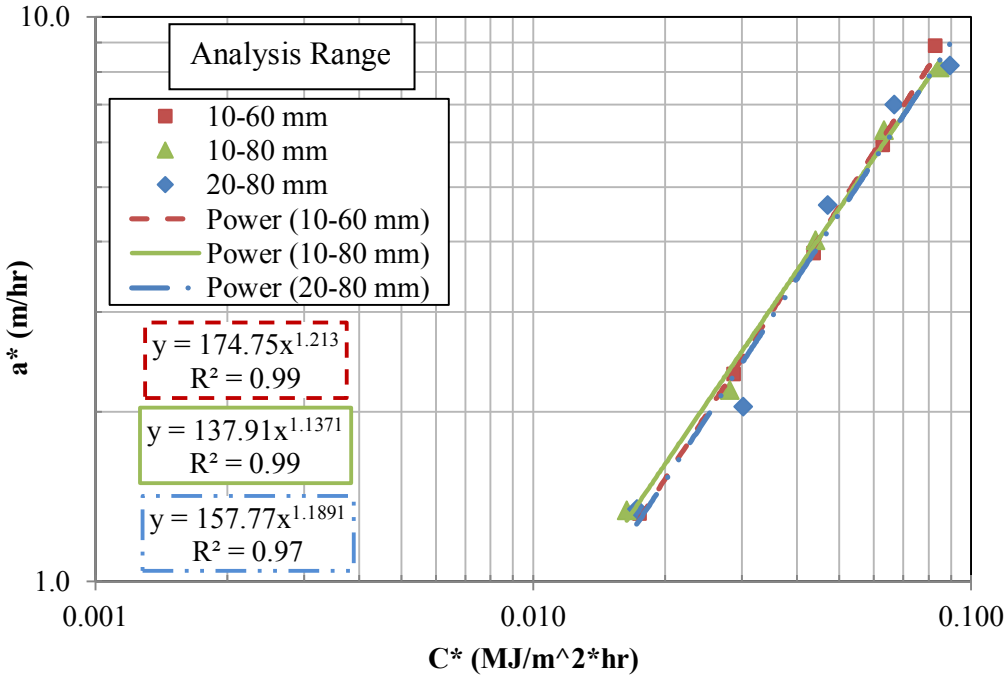

Figure 49 Data analysis range comparison for ADOT mixture at 37.8°C.

4.7.3 Data Analysis Range Justification Using Existing ASU Data

To further explore the CFT data analysis range, mixtures previously subjected to the C* Line Integral Test at ASU were re-analyzed using the aforementioned data analysis ranges. Consideration of this data adds an additional six mixtures to the overall analysis; and includes specialty mixtures modified with rubber, polymer and fibers. The existing ASU CFT database contains two source mixtures named: Swedish Stockholm and Evergreen which will be described in detail in a subsequent chapter. The three Swedish, gap-graded mixtures consisted of unmodified (control), polymer modified and rubber-modified binders. Table 14 provides the regression parameters for the three Swedish mixtures. It is important to note that testing was conducted using one replicate at five displacement rates. For the control and rubber-modified mixtures, trends of data from the 10-60 mm interval provided the best fit. For the polymer-modified mixture, fitted models with the highest R^2-values were obtained from data in the 10-80 mm or 20-80 intervals. Figure 50, Figure 51 and Figure 52 exhibit these comparisons graphically.

Table 14 Regression parameter comparison of Swedish Mixtures at 4 °C.

Temperature (°C)	Mixture Modification	Range (mm)	Regression		
			a	b	R^2
4	Control	10-60	43.038	1.0198	0.83
		10-80	40.835	1.0212	0.74
		20-80	31.788	0.9316	0.60
	Polymer	10-60	30.606	0.7262	0.50
		10-80	47.374	0.9395	0.76
		20-80	49.591	0.9758	0.75
	Rubber	10-60	15.017	0.7917	0.72
		10-80	12.825	0.7657	0.68
		20-80	12.106	0.7536	0.63

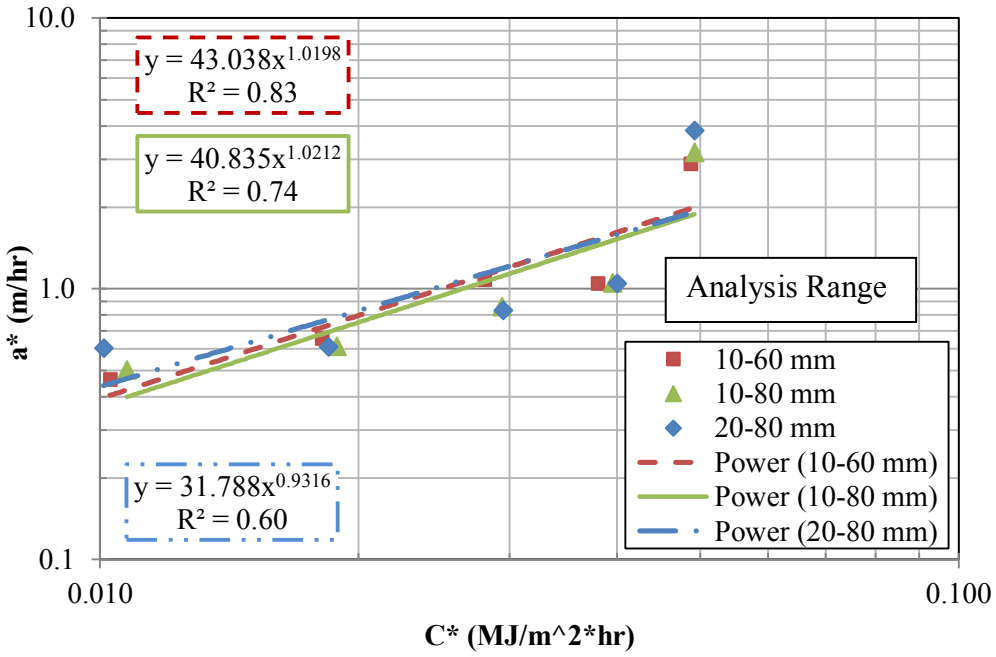

Figure 50 Data analysis range comparison for Swedish control mixture.

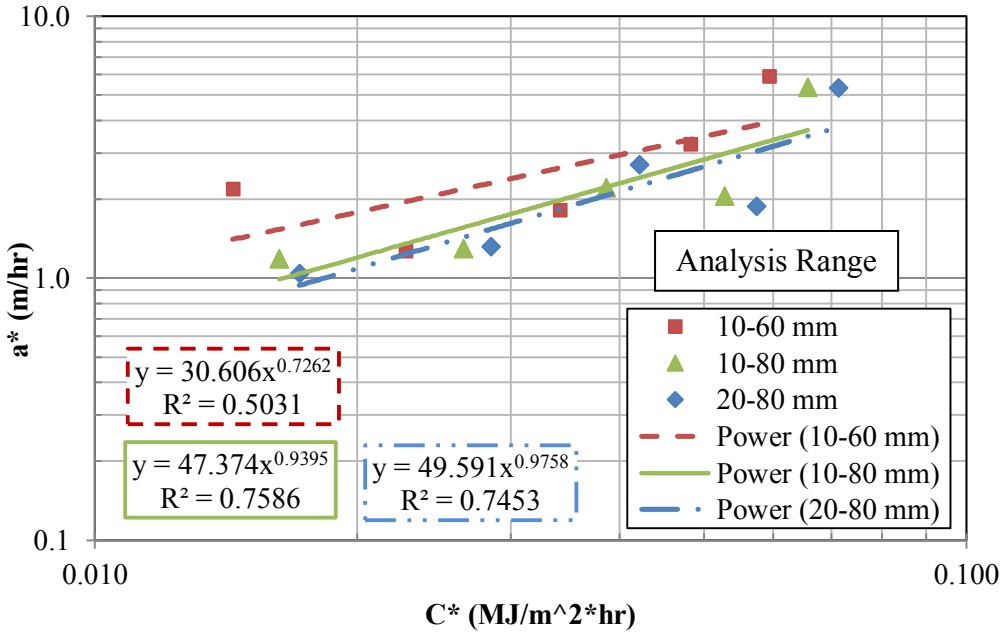

Figure 51 Data analysis range comparison for Swedish polymer mixture.

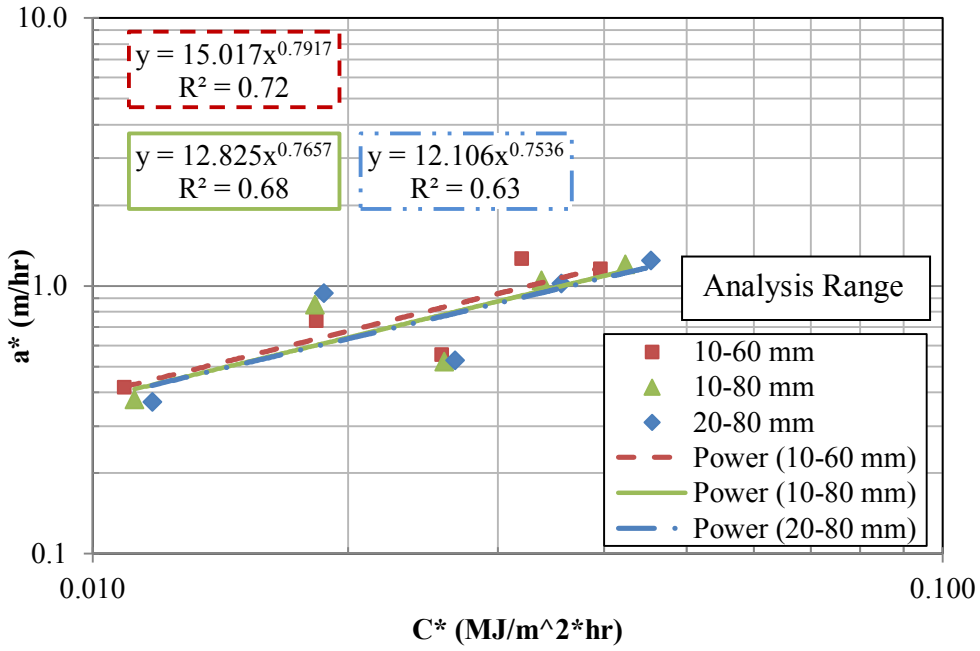

Figure 52 Data analysis range comparison for Swedish rubber mixture.

The three Evergreen, dense graded mixtures consisted of an unmodified (control) mixture along with mixtures modified with two dosage rates of a blend of polypropylene and aramid fibers (1 pound & 2 pound fibers/ton asphalt). Table 15 provides the regression summary for the Evergreen mixtures tested at 21°C.

Table 15 Regression parameter comparison of Evergreen Mixtures at 21 °C

Temperature (°C)	Mixture Modification	Range (mm)	Regression		
			a	b	R^2
21	Control	10-60	70.086	0.4778	0.23
		10-80	181.92	0.6603	0.59
		20-80	1100.7	0.9502	0.84
	Fiber-1 (1 lb/ton)	10-60	20343	1.7991	0.83
		10-80	5661.6	1.5901	0.94
		20-80	1549.6	1.3152	0.96
	Fiber-2 (2 lb/ton)	10-60	54.679	0.6518	0.21
		10-80	421.03	1.1086	0.39
		20-80	23711	1.9649	0.73

According to these data, regressions on the 20-80 mm data provide the highest R^2-values for the three mixtures. Figure 53, Figure 54 and Figure 55 present fitted regressions of the CFT data for the Evergreen control, Fiber 1 (1 lb/ton) and Fiber 2 (2 lb/ton) mixtures, respectively.

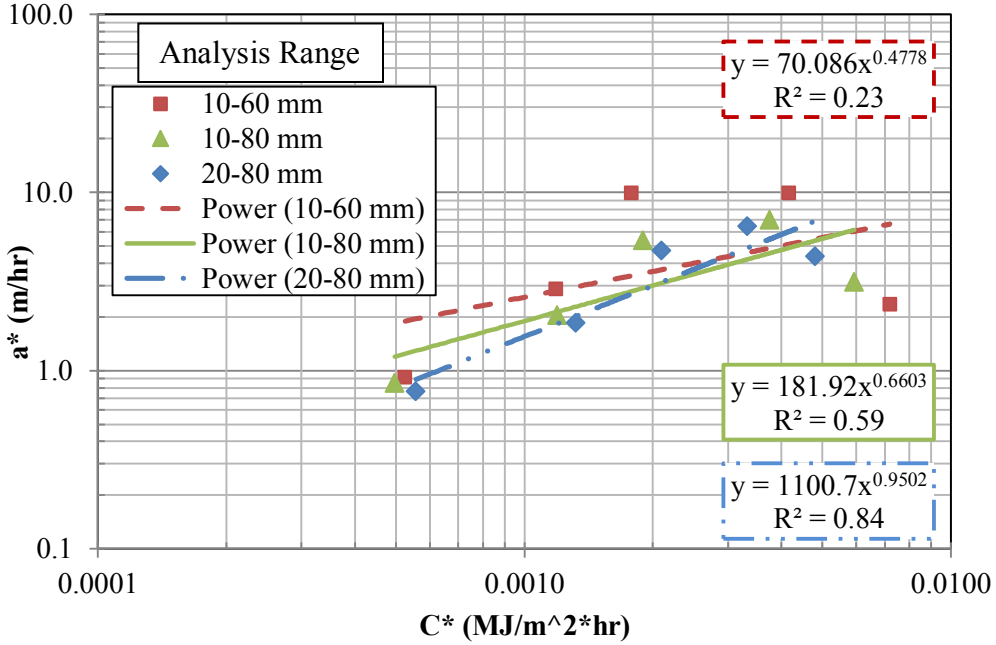

Figure 53 Data analysis range comparison of Evergreen control mixture.

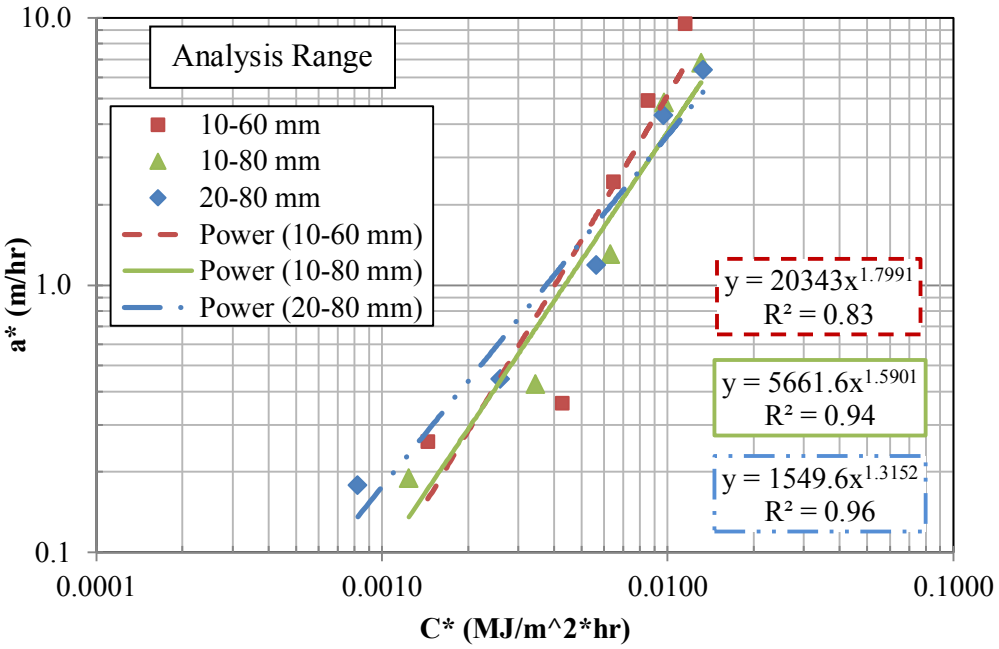

Figure 54 Data analysis range comparison of Evergreen Fiber-1 mixture.

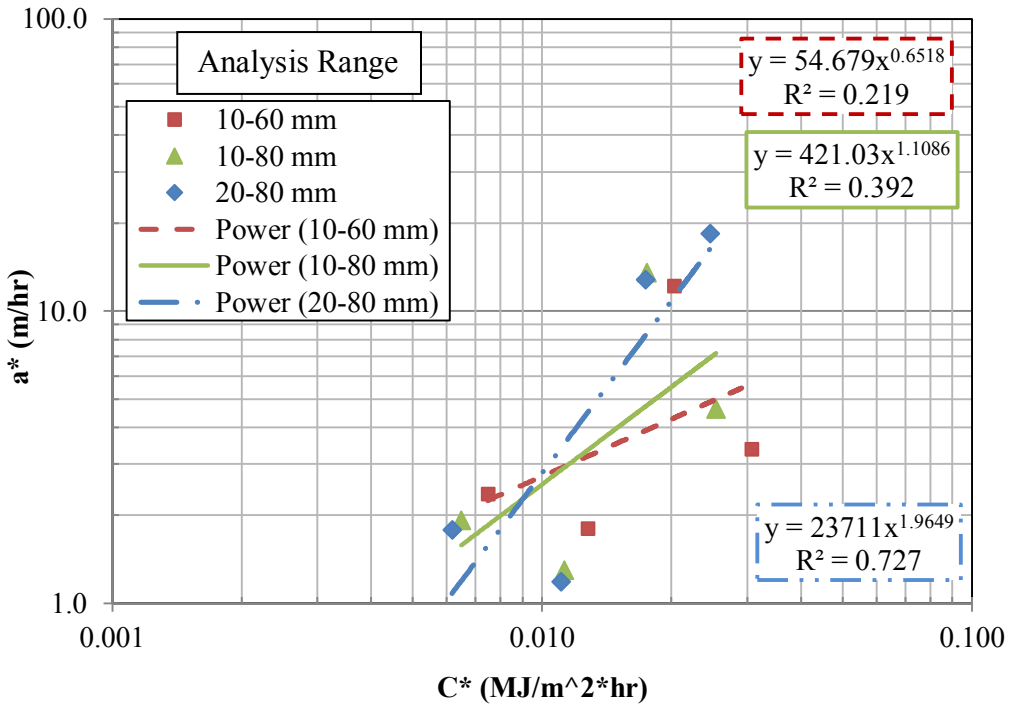

Figure 55 Data analysis range comparison of Evergreen Fiber-2 mixture.

4.7.4 Final Recommendation of Data Analysis Range

Based on the aforementioned analysis and discussion, a final recommendation of data analysis ranges for the 150 x 50 mm is 20-80 millimeters and 10-50 millimeters for the 100 diameter specimens. These conclusions are based on dense graded mixtures tested at various temperatures. The range also appears valid for the Swedish gap-graded mixtures. However, additional gap-graded mixtures should be tested to support these conclusions.

4.8 Experimental Results –Geometric Study

C* and crack growth rate (a*) data were obtained for all test and geometric conditions described in the geometric study portion of the experimental plan shown in Table 4. For samples tested at 21°C, it was found that loading rates between 0.15 mm/min and 0.45 mm/min produced crack propagation rates easily captured and analyzed using the video camera technique. Table 16 presents the CFT results for 150 x 50 mm specimens tested at 21°C using two replicate series. Recall that multiple specimens are required in order to obtain C* values. In this case, each replicate series consisted of one specimen tested at each displacement rate for a total of five specimens per replicate series. C* and a* data were collected between 20 and 80 millimeters based on the recommended data analysis range.

Table 16 CFT results for 150 x 50 mm specimens at 21°C.

Parameter	Replicate Series	Displacement Rate (mm/min)				
		0.15	0.228	0.30	0.378	0.45
C* (MJ/m2-hr)	1	0.010	0.017	0.023	0.031	0.041
	2	0.011	0.019	0.026	0.035	0.044
	Average	***0.010***	***0.018***	***0.025***	***0.033***	***0.042***
	St. Dev.	***0.00085***	***0.00123***	***0.00178***	***0.00253***	***0.00259***
Crack Growth Rate, a* (m/hr)	1	1.12	1.27	2.61	2.16	4.07
	2	1.13	1.82	2.12	4.30	4.37
	Average	***1.13***	***1.54***	***2.37***	***3.23***	***4.22***
	St. Dev.	***0.008***	***0.395***	***0.352***	***1.509***	***0.211***

Crack growth rate data at displacement rates of 0.15, 0.228, 0.30 and 0.45 mm/min resulted in the lowest variability ($s < 0.40$) whereas the standard deviation increased significantly to 1.509 at the 0.378 mm/min displacement rate. Typically, the potential for more variable crack growth rates were observed at higher displacement rates since more power was input to specimen resulted in crack branching. Also, the presence of an aggregate at the beginning of the crack path may influence the material tensile strength which allowed additional storage of potential energy. This energy was subsequently released through more rapid crack growth that replicate specimens tested at the same displacement rate.

Figure 56 and Figure 57 present the C*-Δ* and a*- Δ* plots, respectively. Both data sets are best fit a power trend with high coefficient of determination values. Again, a majority of the variability in the data comes from crack growth rates observed in the replicates.

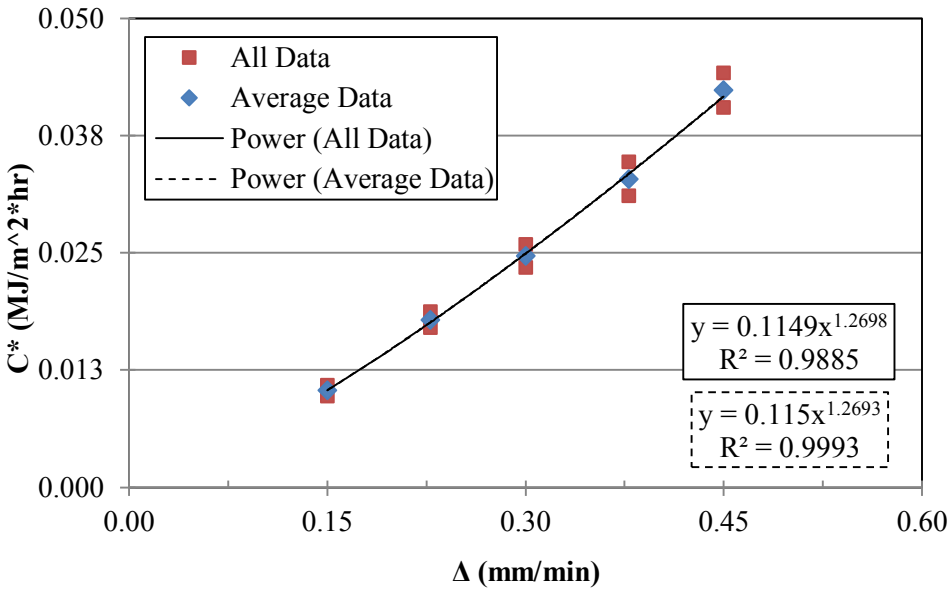

Figure 56 C* versus displacement rate for 21°C (150 x 50 mm).

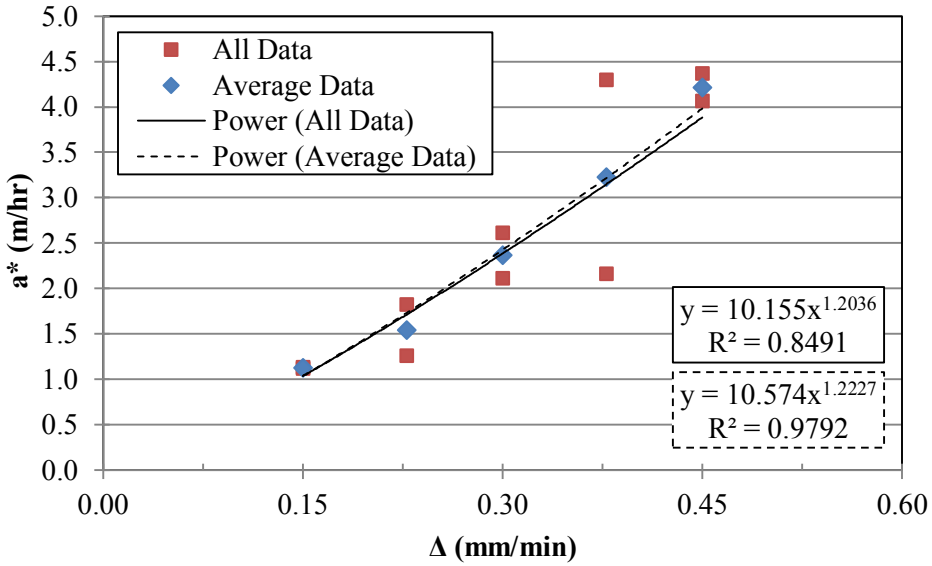

Figure 57 a* versus displacement rate for 21°C (150 x 50 mm).

Figure 58 shows the final plot of a* versus C* for 150 x 50 mm specimens tested at 21°C. For comparison, the two replicate series data were plotted and fitted with a power trend and also the average of the C* and a* data were fitted with a power trend.

Data shows that the models fit the data well and that crack growth rate is related to the C* parameter in power model form.

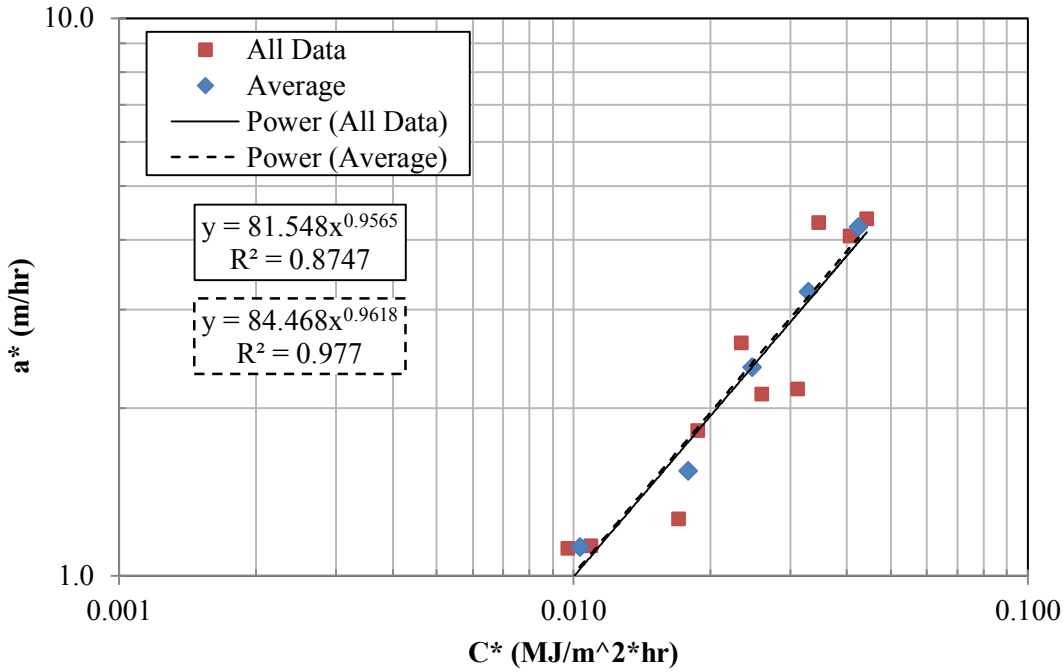

Figure 58 a* versus C* plot for 21°C (150 x 50 mm)

Table 17 shows the C* and crack growth rate data for the 150 x 25 mm specimens. Based on standard deviation values, there is very low variability in the C* parameter for the replicates at each displacement rate. However, as displacement rate increases from 0.15 mm/min to 0.45 mm/min, the variation in crack growth rate increases as indicated by larger standard deviation values.

Table 17 CFT results for 150 x 25 mm specimens at 21°C.

Parameter	Replicate Series	Displacement Rate (mm/min)				
		0.15	0.228	0.30	0.378	0.45
C* (MJ/m2-hr)	1	0.012	0.019	0.027	0.034	0.042
	2	0.010	0.015	0.020	0.026	0.033
	Average	***0.011***	***0.017***	***0.023***	***0.030***	***0.037***
	St. Dev.	***0.00153***	***0.00309***	***0.00475***	***0.00555***	***0.00584***
Crack Growth Rate, a* (m/hr)	1	1.06	1.11	3.59	4.83	4.62
	2	1.38	1.77	2.72	5.78	5.66
	Average	***1.22***	***1.44***	***3.15***	***5.31***	***5.14***
	St. Dev.	***0.225***	***0.462***	***0.616***	***0.669***	***0.735***

Figure 59 and Figure 60 graphically present the C*-Δ* and a*- Δ* relationships, respectively. Both replicate and average data are provided to show variability across the range of displacement rates.

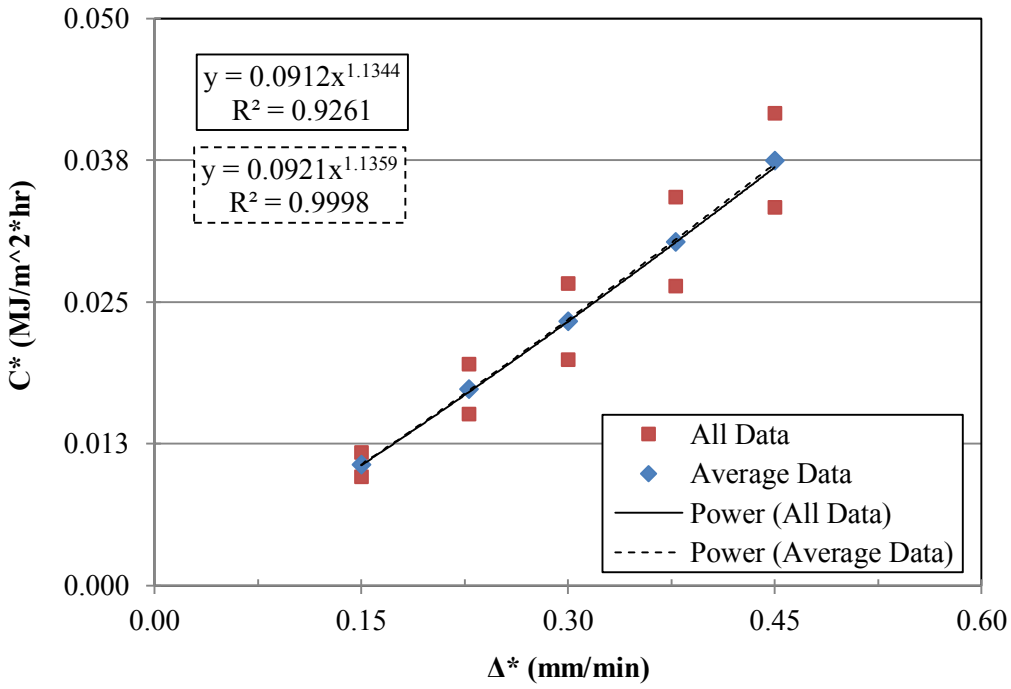

Figure 59 C* versus displacement rate for 21°C (150 x 25 mm).

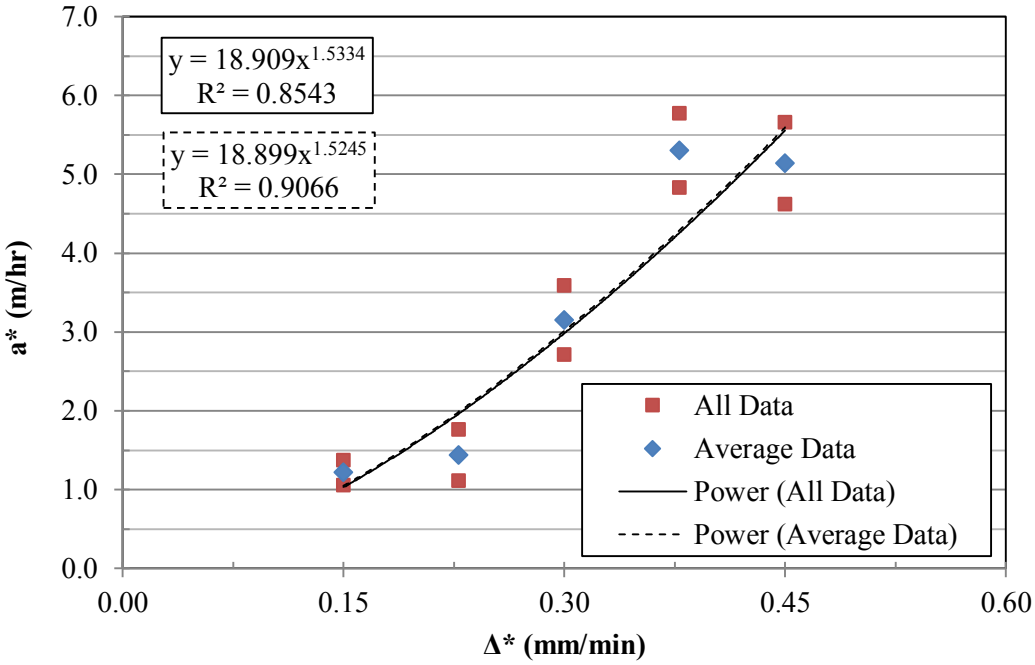

Figure 60 a* versus displacement rate for 21°C (150 x 25 mm).

Figure 61 displays the final CFT test results for the 150 x 25 mm samples. All data and average data are presented in the plot along with fitted power trends. Compared to the CFT results from the 150 x 50 mm specimens, there is more variability in the 150 x 25 mm data as indicated by the R^2-values.

Table 18 shows the C* and crack growth rate data for the 100 x 50 mm specimens. Based on standard deviation values, there is very low variability in the C* parameter for the replicates at each displacement rate. However, as displacement rate increases from 0.15 mm/min to 0.45 mm/min, the variation in crack growth rate generally increases as indicated by standard deviation values between 0.111 and 0.689.

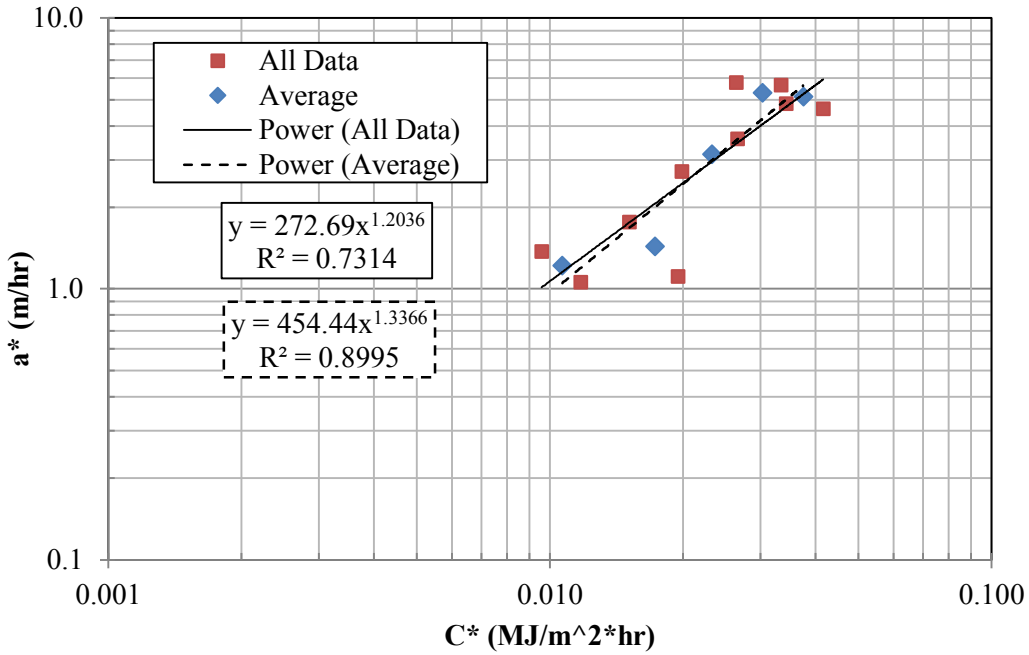

Figure 61 a* versus C* plot for 21°C (150 x 25 mm)

Table 18 CFT results for 100 x 50 mm specimens at 21°C.

Parameter	Replicate Series	Displacement Rate (mm/min)				
		0.15	0.228	0.30	0.378	0.45
C* (MJ/m2-hr)	1	0.014	0.023	0.030	0.038	0.045
	2	0.010	0.017	0.024	0.033	0.041
	Average	***0.012***	***0.020***	***0.027***	***0.035***	***0.043***
	St. Dev.	***0.00295***	***0.00410***	***0.00410***	***0.00343***	***0.00306***
Crack Growth Rate, a* (m/hr)	1	0.68	2.20	2.90	3.74	3.31
	2	1.12	1.62	3.05	2.77	2.70
	Average	***0.90***	***1.91***	***2.98***	***3.26***	***3.00***
	St. Dev.	***0.311***	***0.411***	***0.111***	***0.689***	***0.435***

Figure 62 and Figure 63 graphically show the relationship between C*-Δ* and a*-Δ* relationships, respectively. Both replicate and average data are presented to show variability across the range of displacement rates.

Figure 64 displays the final CFT test results for the 100 x 50 mm samples. All data and average data are presented in the plot along with fitted power trends. Compared

to the CFT results from the 150 x 50 mm specimens, there is more variability in the 100 x 50 mm data as indicated by the R^2-values. Also it appears that there is a departure from a true power fit of the data as test displacement rate increases, which could be the result of subjecting smaller diameter specimens to the CFT at similar displacement rates used for 150 mm diameter specimens.

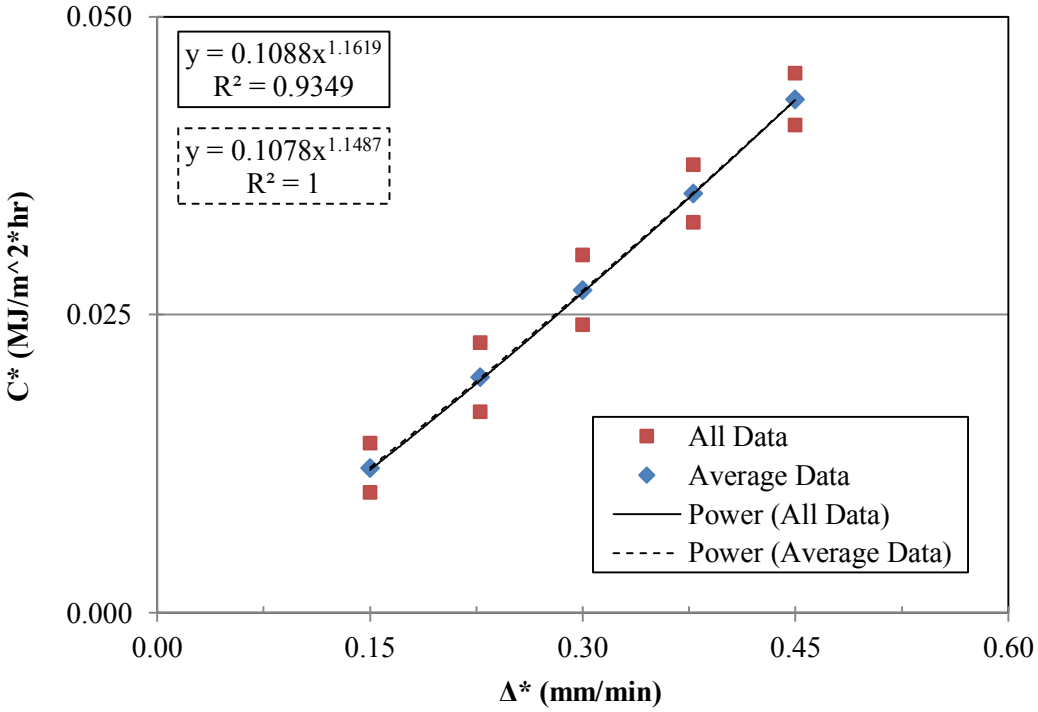

Figure 62 C* versus displacement rate for 21°C (100 x 50 mm).

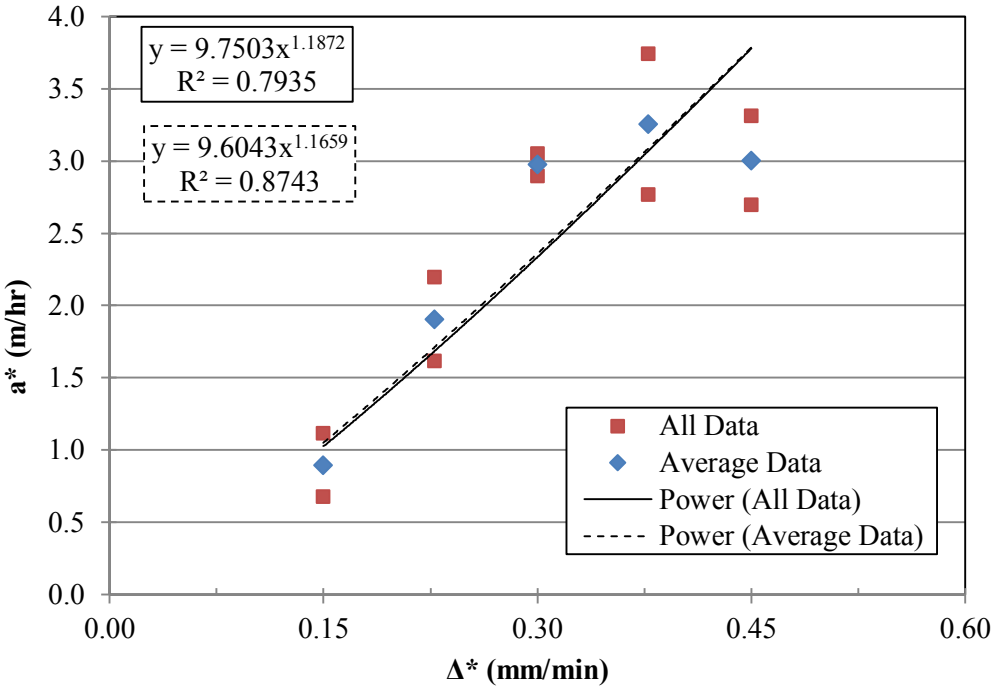

Figure 63 a* versus displacement rate for 21°C (100 x 50 mm).

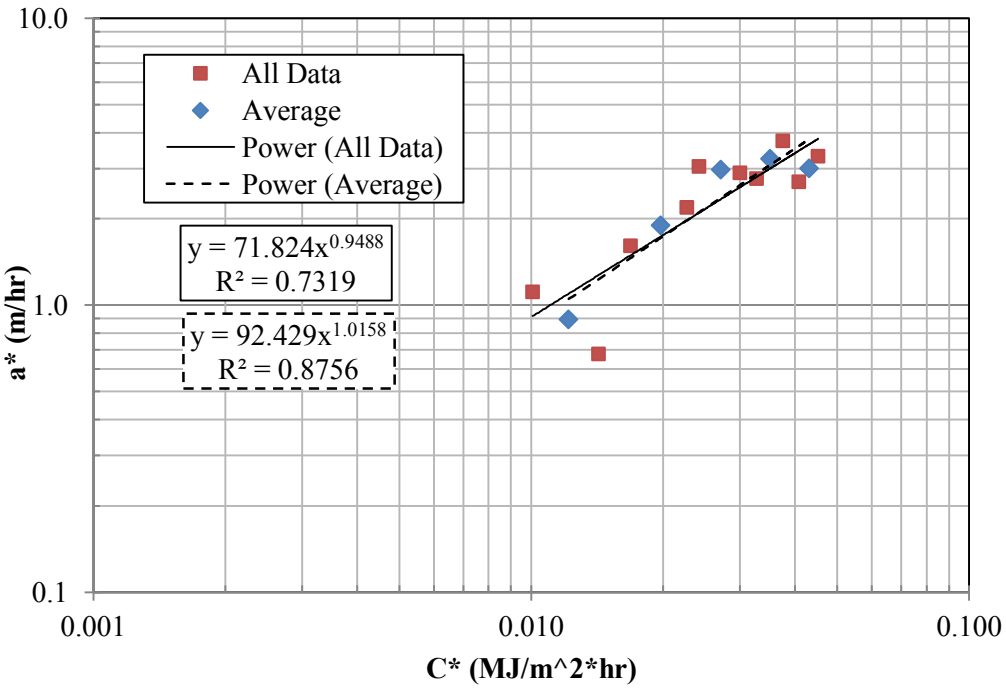

Figure 64 a* versus C* plot for 21°C (100 x 50 mm)

Table 19 provides a summary of all C* and a* data from the geometric study.

Table 19 C* Summary CFT data from geometric study at 21°C.

Dimensions	Test Temperature	Disp. Rate (mm/min)	Crack Growth Rate (m/hr)[1]	C* (MJ/m^2-hr)[1]
150 mm x 50 mm	21°C	0.15	1.13	1.032E-02
		0.228	1.54	1.787E-02
		0.30	2.37	2.468E-02
		0.378	3.23	3.290E-02
		0.45	4.22	4.237E-02
150 mm x 25 mm	21°C	0.15	1.22	1.067E-02
		0.228	1.44	1.731E-02
		0.30	3.15	2.327E-02
		0.378	5.31	3.030E-02
		0.45	5.14	3.747E-02
100 mm x 50 mm	21°C	0.15	0.90	1.217E-02
		0.228	1.91	1.975E-02
		0.30	2.98	2.709E-02
		0.378	3.26	3.515E-02
		0.45	3.00	4.307E-02

[1]*Data based on two replicates at each displacement rate.*

Data obtained from the C* Fracture Test appears reasonable in that for all specimen geometries, the C* parameter increased as a function of increased loading rate. Higher loading rates result in more power input to the specimen that must eventually be released. Given finite specimen dimensions, the release rate (C*) must increase to achieve equilibrium at the termination of cracking. Figure 65 presents a graphical summary of C* values as a function of displacement rates for all specimen geometries at 21°C. It is evident that a slight specimen size effect exists on the C* parameter. The 100 mm diameter samples expressed the highest C*-parameter at all loading rates, followed by the 150 mm x 50 mm and 150 mm x 25 mm specimens.

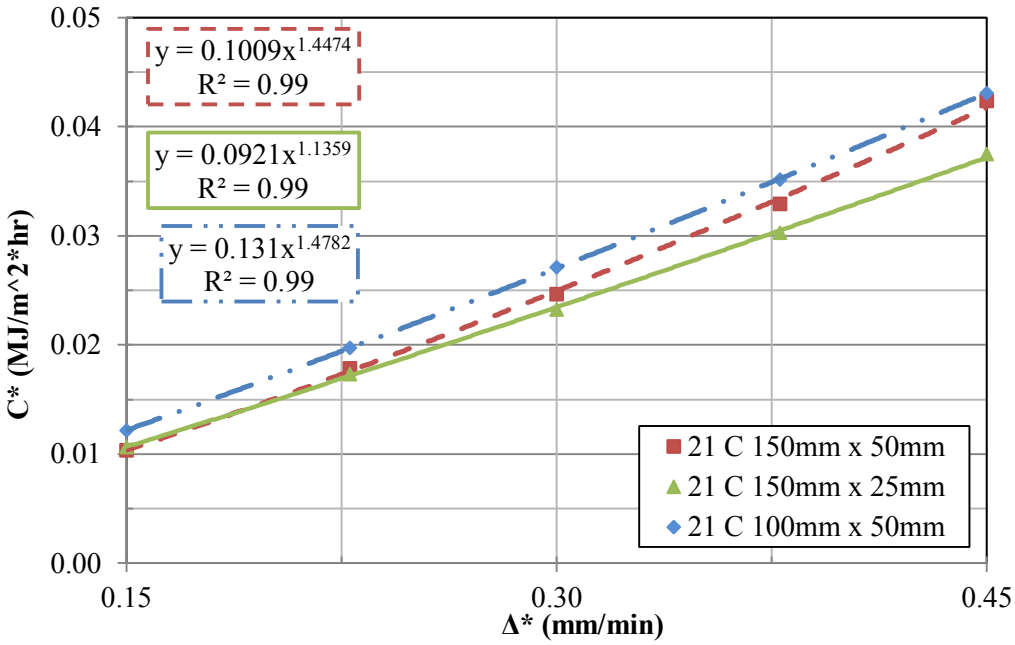

Figure 65 C* versus Δ* relationship at 21°C for all specimen sizes.

Average crack growth rates generally tend to increase as a function of larger displacement rate as expressed in Figure 66. However, instances exist when crack growth rates are similar or slightly less for different displacement rates. This is evident in the 150 x 25 mm and 100 x 50 mm specimens tested at 21°C (Δ = 0.378 and 0.45). This may be the result of the crack path deviation from the centerline or crack branching due to quicker energy dissipation. Also, the presence of large aggregates in the specimen required the cracks to travel longer paths and thus; crack growth rate expressed a tendency to decrease. It appears that specimen thickness slightly affects crack growth rate in that a thinner specimen allows the crack to propagate more rapidly. Thicker specimens expose the crack front to additional material thickness that potentially can result in a non-uniform crack front across the specimen thickness.

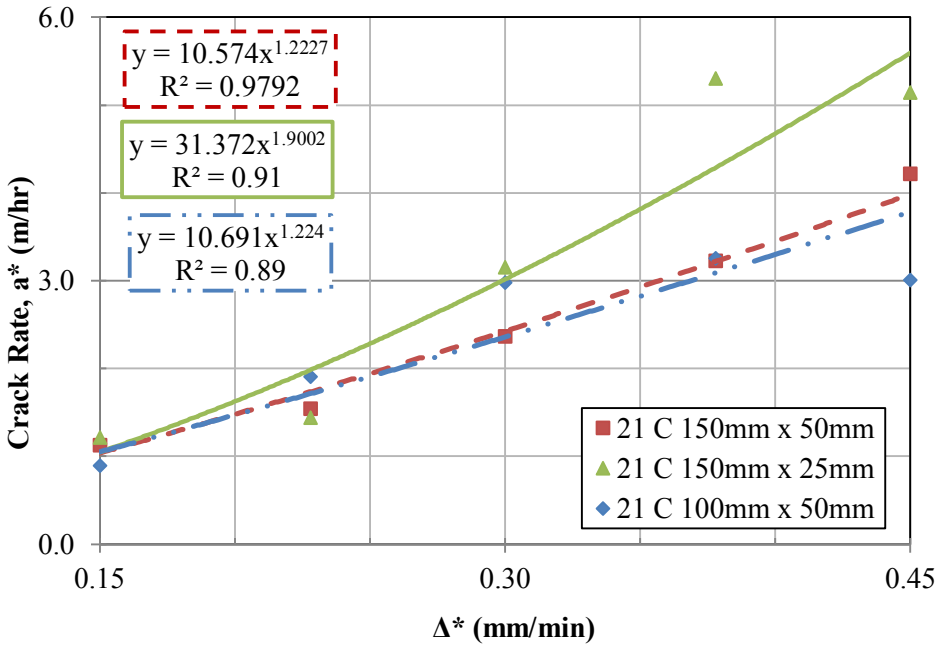

Figure 66 a*-Δ* relationship at 21°C for all specimen sizes.

The final step in C* analysis requires plotting the crack growth rate (a*) versus the C* parameter on a log-log scale which is shown in Figure 67. This unique relationship can be used to describe crack growth rate as a function of the C* parameter. At 21°C, the 100 mm diameter specimens expressed the slowest crack growth rate for a given C*-value followed by the 150 x 50 mm and 150 x 25 mm specimens. The slopes of the lines indicate that for increasing C*, the crack propagation rate increases much more rapidly in the 150 x 25 mm specimens when compared to the 150 x 50 mm and 100 x 50 mm specimens. Thus, crack growth rate appears more dependent on specimen thickness than diameter. Overall, the power fit of these data have R^2-values greater than 0.88 which, indicate a good fit of the data and thus a power model can be used effectively to represent C* data obtained on asphalt concrete. This is in agreement with literature in which the crack growth rate is uniquely related to C* according to a power model

(Anderson, 2005). Recall that data analysis was performed in the 20-80 mm and 10-50 mm ranges for the 150 mm and 100 mm diameter specimens, respectively.

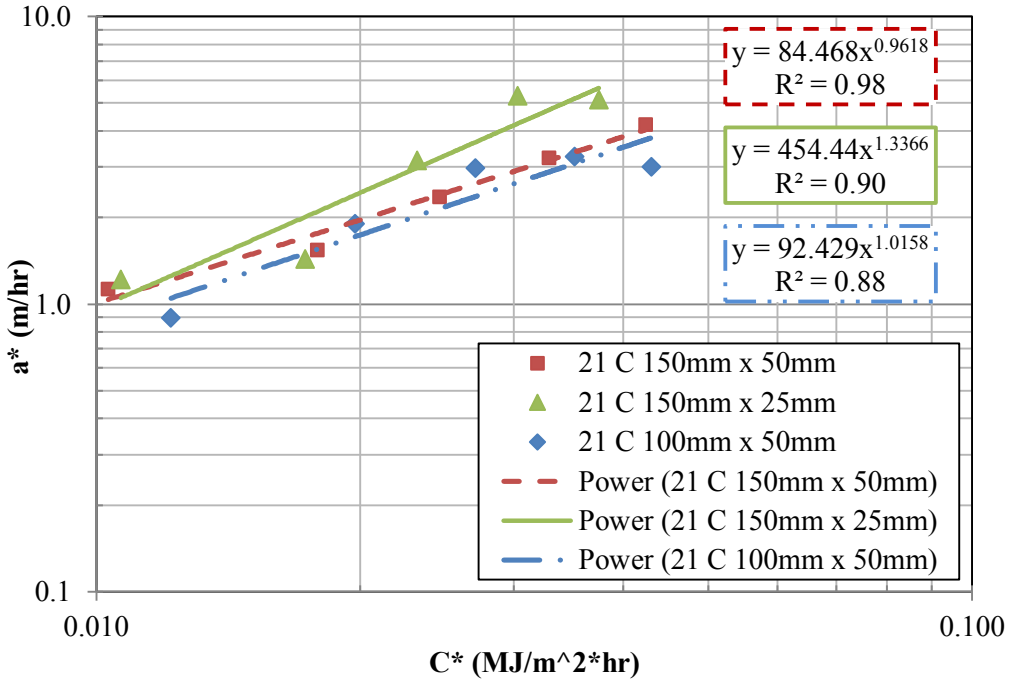

Figure 67 a*-C* relationship comparison at 21°C for all specimen sizes.

4.9 Statistical Comparison of CFT Results

Statistical comparison was performed in order to determine if the crack growth rate versus C* trends (Figure 67) obtained from different size specimens produced statistically different trends. A log transformation was required in order to use linear regression techniques and the assumption of equal variance and normality was also verified. Two data sets were compared at a time by fitting Equation 4.4 to the combined data set. An indicator variable was required in this analysis in order to distinguish between the trends obtained from the two different data analysis ranges being compared (Neter et al, 1996).

$$\log a^* = \alpha + \beta \log C^* + \gamma Size + \delta \log C^* * Size \quad \textbf{4.4}$$

Where:

a* = crack growth rate (m/hr),

C* = power release rate parameter (MJ/m^2-hr),

Size = indicator variable (0 or 1) to distinguish specimen sizes, and

$\alpha, \beta, \gamma, \delta$ = regression parameters.

The hypothesis test for the comparison was as follows and statistical analysis was performed using level of significance of 0.05:

H_o: Both γ and $\delta = 0$

H_a: Not both γ and $\delta = 0$

Failure to reject the null hypothesis (H_o) indicated that specimen size was statistically insignificant and a*-C* trends produced from different size CFT specimens were not statistically different. In comparison, rejection of the null hypothesis indicated that specimen size has an impact on a*-C* trends and should not be disregarded. Minitab 16 statistical software was used for all statistical analyses.

4.9.1 Specimen Size Effect on CFT Results

Both crack growth rate and C* data were transformed into log scale in order to use linear regression techniques to compare a*-C* trends and statistically capture any potential effects of specimen size. Assumptions of normally distributed data and equal variances were verified and results are included in Appendix B along Minitab output. Table 20 presents the results of the statistical analysis for two levels of significance; 0.05 and 0.10. If the p-value is less than the level of significance, the null hypothesis (H_o) is rejected.

Table 20 Statistical analysis results considering specimen size.

Comparison (size, mm)	Parameter	p-value	α = 0.05 Decision	α = 0.10 Decision
150 x 50 vs. 150 x 25	γ	0.08	Accept H_o	***Reject H_o***
	δ	0.20		
150 x 50 vs. 100 x 50	γ	0.34	Accept H_o	Accept H_o
	δ	0.82		
150 x 25 vs. 100 x 50	γ	0.04	***Reject H_o***	***Reject H_o***
	δ	0.38		

At a level of significance of 0.05, there is a statistical difference between a*-C* trends obtained in the CFT using 150 x 25 mm and 100 x 50 mm specimen sizes. The "γ" parameter is significant indicating the y-intercept values are statistically different between the two trends and the combined dataset cannot be represented by a single regression function. At a level of significance of 0.10, a*-C* trends are statistically different between 150 x 50 mm and 150 x 25 mm as indicated by a p-value less than 0.10.

These results are in line with practical consideration of a*-C* trends presented in Figure 67. From this figure, it is evident that CFT results on 150 x 25 mm specimens produce a different a*- C* trend than from data extracted from CFT tests on 150 x 50 mm and 100 x 50 mm specimens. Also, it appears that 150 x 50 mm and 100 x 50 mm specimens produce similar a*-C* for the test conditions considered in the geometric study. These results agree with practical observation that specimen thickness plays a more significant role in the C* and crack growth rate data than specimen diameter.

4.9.2 Effect of CFT Replicates on a*-C* Trends

Typically, two specimens were tested at each displacement rate applied during the CFT. For comparison, a third replicate was added to tests conducted at 21°C using 150 x

50 mm specimens and the crack growth rate versus C* trends were compared using one, two and three replicates at each displacement rate.

Figure 68 provides a graphical comparison of a*-C* trends developed using one, two and three replicates at each displacement rate. It is evident that the R^2-value of the power data fit increases from 0.824 to 0.977 when a second test replicate is added. However, adding a third replicate only increases the R^2-value from 0.977 to 0.981. Also, a*-C* trends using average data from two and three CFT replicates are not substantially different.

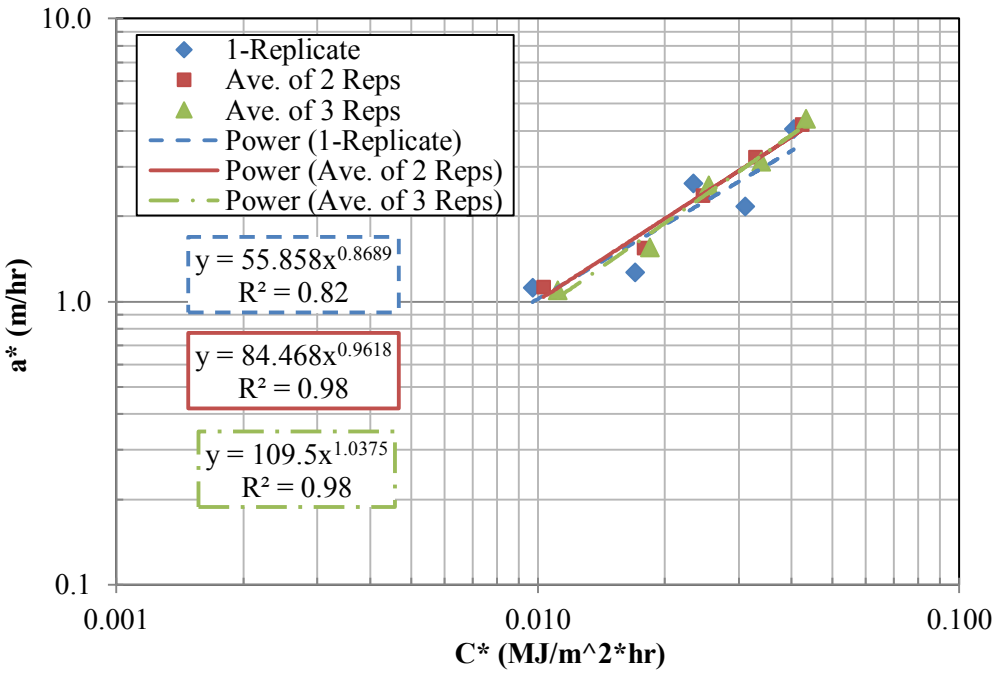

Figure 68 Effect of test replicates on a*-C* relationship at 21°C.

Statistical comparisons were performed to determine if there was a statistical difference between trend lines fitted using one, two and three replicates at each displacement rate as shown in Figure 68. Equation 4.4 was used to fit these data and with

the exception that the "size" variable was replaced with "replicates". The hypothesis test for the comparison at a 0.05 level of significance was:

H_o: Both γ and $\delta = 0$

H_a: Not both γ and $\delta = 0$

Table 21 presents the results of the statistical analysis to compare the effect of replicates on the a*-C* trends. All cases fail to reject the null hypothesis which indicate that the addition of replicates did not significantly affect the a*-C* relationship for the ADOT mixture tested at five displacement rates (21°C test temperature). Minitab output files can be found in Appendix B.

Table 21 Statistical analysis results considering number of replicates at each displacement rate.

Comparison (size, mm)	Parameter	p-value	$\alpha = 0.05$ Decision
1 replicate vs. 2 replicates	γ	0.68	Accept H_o
	δ	0.72	
1 replicate vs. 3 replicates	γ	0.51	Accept H_o
	δ	0.53	
2 replicates vs. 3 replicates	γ	0.59	Accept H_o
	δ	0.55	

It can be concluded that the two CFT replicates at each displacement rate should produce sufficient data to provide an accurate a*-C* trend for a given mixture when five displacement rates are used. If insufficient mixture is available and only one CFT can be conducted at any given displacement rate, it is recommended that at least five displacement rates be tested.

4.10 Experimental Results – Test Temperature Study

The test temperature study was previously outlined in Table 4 and expanded the geometric study to consider additional CFT temperatures of 0°C, 4.4°C, 10°C and 37.8°C using the recommended specimen size of 150 mm in diameter by 50 mm in thickness. The overall goal was to establish an effective temperature range for the CFT. All testing described in this section was conducted on the ADOT mixture using 150 x 50 mm specimens and a data analysis range of 20-80 millimeters.

CFT tests were conducted at 0°C in an effort to establish a lower temperature limit of the test. However, crack growth rates were extremely difficult to capture using the video camera method even at constant displacement rates as low as 0.042 mm/min. Table 22 provides example data from the CFT conducted at 0°C.

Table 22 CFT crack growth rates at 0°C.

Parameter	Replicate Series	Displacement Rate (mm/min)		
		0.042	0.078	0.15
Crack Growth Rate, a* (m/hr)	1	12.85	10.27	7411.8
	2	16.88	15.48	-
	Average	***14.87***	***12.88***	**-**
	St. Dev.	***2.85***	***4.68***	**-**

- Indicates test not performed.

Average crack growth does not increase as it should between displacement rates of 0.042 and 0.078 mm/min. Also, a crack growth rate of 7411.8 m/hr (Δ^* = 0.15 mm/min) is not a reasonable value to measure from the CFT. Given this upper limit on displacement rates for the CFT at 0°C, it is difficult to test at four displacement rates to develop a reasonable a*-C* trend.

Also, it was observed that the load cell on the IPC UTM-100 test apparatus did not respond fast enough to the rapid fracture at 0°C. A slight delay in response indicated

that unloading occurred after the entire specimen was cracked rather than unloading during fracture. Thus, it was nearly impossible to determine an accurate load at specified crack lengths, which underestimated the C* parameter. Given these challenges, the test results 0°C were eliminated from the remainder of the analyses and 4.4°C was considered the lowest practical limit for the CFT using the ADOT mixture.

Table 23 presents the CFT test results for a test temperature of 4.4°C. As the test temperature decreased, the crack growth rate (a*) tended to exhibit greater variability as indicated by higher standard deviation values.

Table 23 CFT results at 4.4°C.

Parameter	Replicate Series	Displacement Rate (mm/min)				
		0.03	**0.06**	**0.10**	**0.15**	**0.3**
C* (MJ/m^2-hr)	1	0.002	0.006	0.011	0.019	0.036
	2	0.003	0.006	0.012	0.017	0.025
	Average	***0.003***	***0.006***	***0.011***	***0.018***	***0.030***
	St. Dev.	***0.00038***	***0.00030***	***0.00034***	***0.00096***	***0.00752***
Crack Growth Rate, a* (m/hr)	1	2.88	5.19	19.17	35.38	222.68
	2	1.34	7.96	14.21	36.24	76.04
	Average	***2.11***	***6.57***	***16.69***	***35.81***	***149.36***
	St. Dev.	***1.086***	***1.960***	***3.508***	***0.611***	***103.689***

At a CFT displacement rate of 0.3 mm/min, the crack growth rate was extremely variable and very difficult to observe using the video recording technique utilized. Typically, the crack propagated through the specimen in less than one second which complicated efforts to obtain accurate data. In Table 23, the crack growth rate standard deviation of 103.7 at a displacement rate of 0.30 mm/min was much greater than standard deviation values at slower displacement rates. Given this variability which may have been the result of inaccurate crack length measurement readings during the CFT, data at a

displacement rate of 0.30 mm/min was eliminated from the analysis. Figure 69 provides a graph of a*-C* trends for the CFT at 4.4°C.

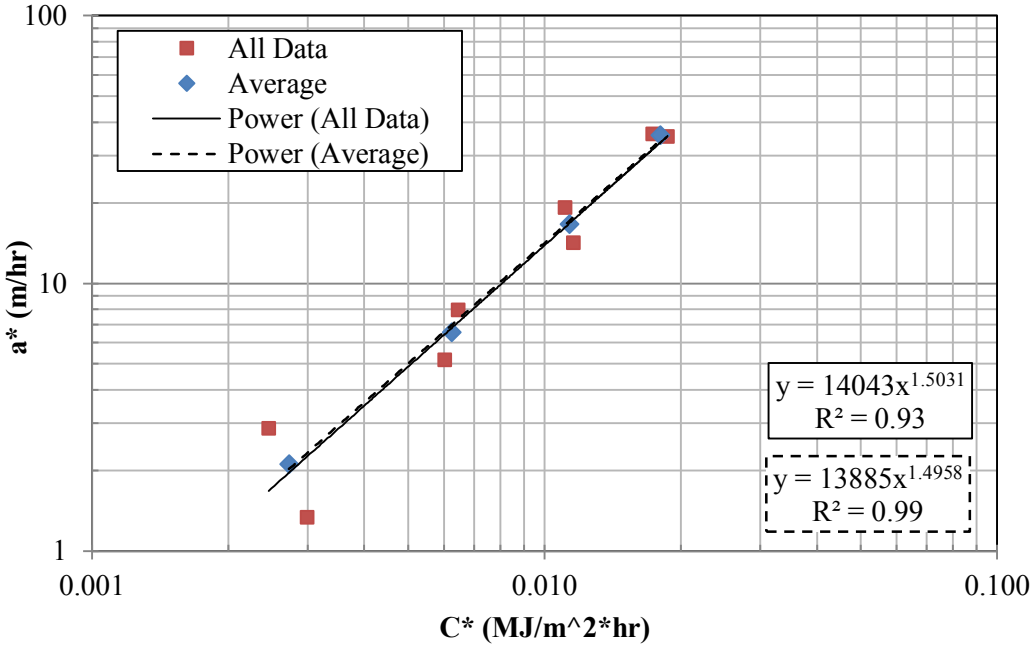

Figure 69 a* versus C* plot for 4.4°C.

Table 24 provides test CFT test results at 10°C. Based and the standard deviation values, crack growth rates expressed variability consistent with other temperatures included in this study except at a displacement rate of 0.23 mm/min. In this case, the standard deviation was considerably higher at a value of 5.68. For comparison, Figure 70 presents a*-C* trends graphically.

Table 24 CFT results at 10°C.

Parameter	Replicate Series	Displacement Rate (mm/min)			
		0.072	0.15	0.23	0.3
C* (MJ/m^2-hr)	1	0.008	0.020	0.030	0.037
	2	0.006	0.015	0.026	0.034
	Average	***0.007***	***0.018***	***0.028***	***0.035***
	St. Dev.	***0.00141***	***0.00363***	***0.00245***	***0.00259***
Crack Growth Rate, a* (m/hr)	1	1.89	3.94	13.70	13.24
	2	2.07	5.42	5.67	11.72
	Average	***1.98***	***4.68***	***9.68***	***12.48***
	St. Dev.	***0.130***	***1.049***	***5.677***	***1.076***

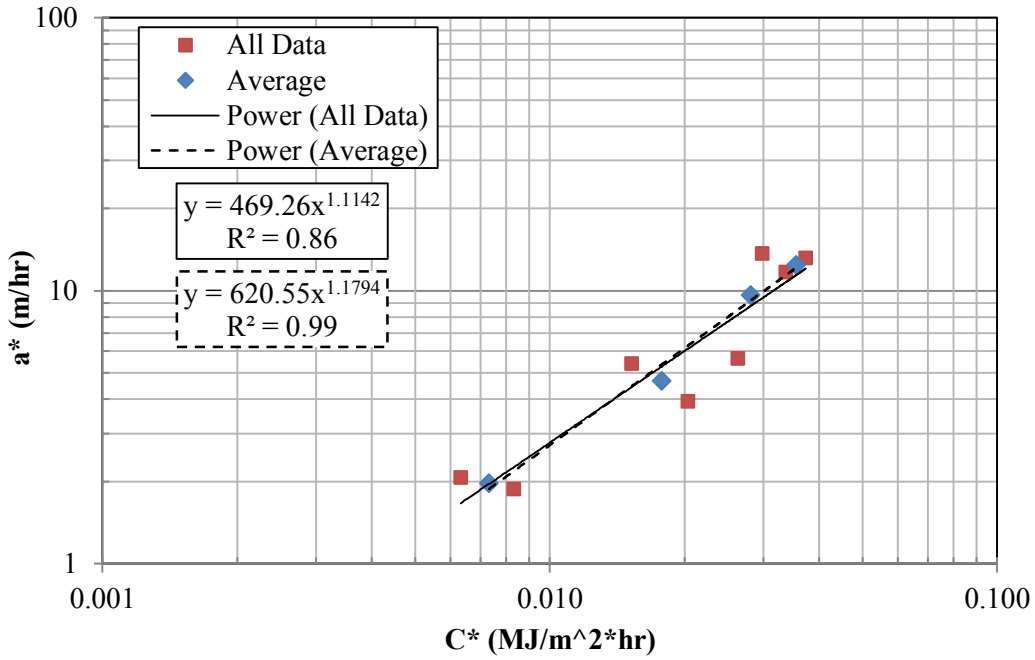

Figure 70 a* versus C* plot for 10°C.

Table 25 presents CFT test results at 37.8°C. Based and the standard deviation values, crack growth rates expressed low variability consistent with other temperatures included in this study. Figure 71 presents a*-C* trends graphically.

Table 25 CFT results at 37.8°C.

Parameter	Replicate Series	Displacement Rate (mm/min)				
		0.378	**0.6**	**0.90**	**1.2**	**1.5**
C* (MJ/m^2-hr)	1	0.016	0.029	0.047	0.064	0.085
	2	0.018	0.032	0.047	0.070	0.094
	Average	***0.017***	***0.030***	***0.047***	***0.067***	***0.089***
	St. Dev.	***0.00155***	***0.00195***	***0.00020***	***0.00392***	***0.00694***
Crack Growth Rate, a* (m/hr)	1	1.50	2.10	5.41	6.65	8.22
	2	1.18	1.98	3.88	7.34	8.20
	Average	***1.34***	***2.04***	***4.64***	***7.00***	***8.21***
	St. Dev.	***0.226***	***0.085***	***1.085***	***0.492***	***0.017***

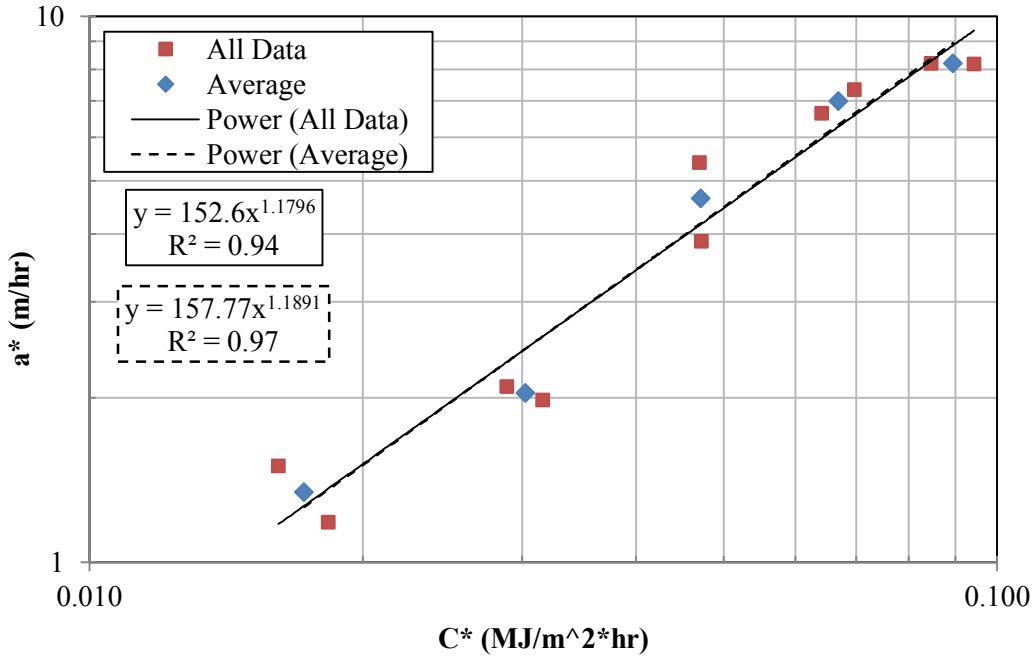

Figure 71 a* versus C* plot for 37.8°C.

Table 26 provides summary CFT data collected at 4.4, 10, 21 and 37.8°C for the ADOT dense graded mixture. Figure 72 presents a summary C* plot for data collected at all four temperatures in the geometric study and test temperature study. The plot is rational in that colder test temperature resulted in higher crack growth rates.

Table 26 Summary of CFT results for the Test Temperature Study.

Test Temperature	Displacement Rate (mm/min)	Crack Growth Rate (m/hr)	C* MJ/m^2-hr
4.4°C	0.03	2.11	2.724E-03
	0.06	6.57	6.242E-03
	0.102	16.69	1.135E-02
	0.15	35.81	1.804E-02
10°C	0.072	1.98	7.314E-03
	0.15	4.68	1.779E-02
	0.228	9.68	2.809E-02
	0.3	12.48	3.550E-02
21°C	0.15	1.13	1.032E-02
	0.228	1.54	1.787E-02
	0.3	2.37	2.468E-02
	0.378	3.23	3.290E-02
	0.45	4.22	4.237E-02
37.8°C	0.378	1.34	1.725E-02
	0.6	2.04	3.022E-02
	0.9	4.64	4.713E-02
	1.2	7.00	6.683E-02
	1.5	8.21	8.948E-02

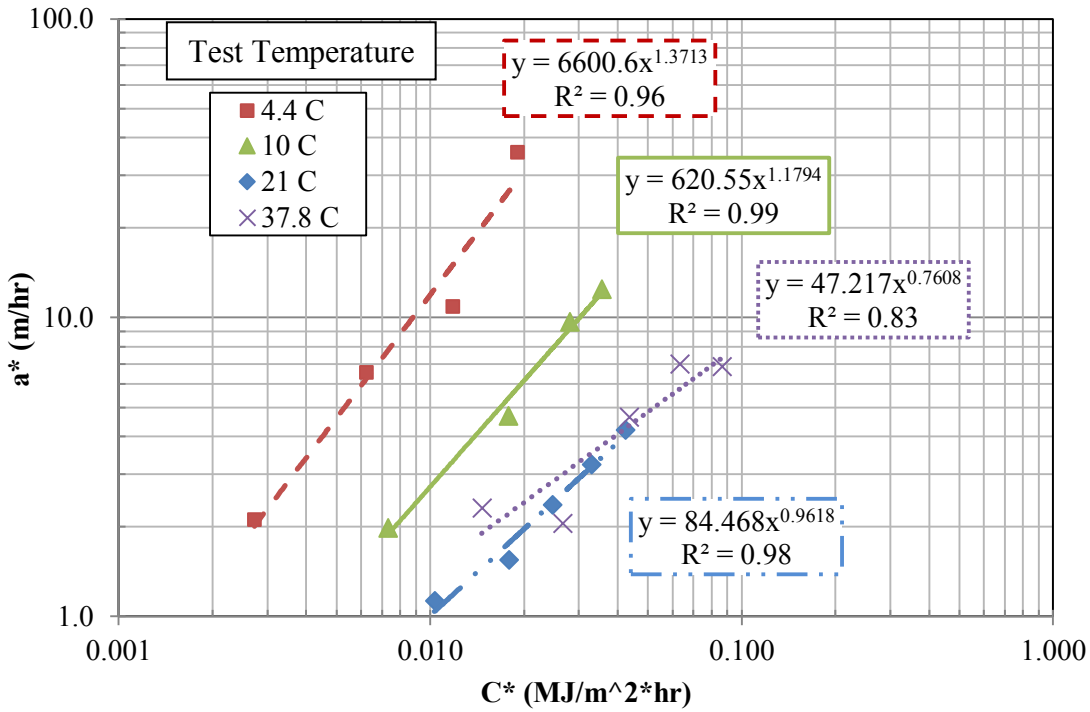

Figure 72 a* versus C* plot comparison for all CFT test temperatures.

An interesting finding was that the crack growth rate versus C* trend at 37.8°C was nearly the same as the trend observed at 21°C. This observation is reasonable given the fact that more deformation is typical in asphalt concrete at higher temperatures as viscous behavior dominates. Thus, energy released through crack growth becomes less dominant compared to energy released through deformation or softening. For the temperatures considered in this study and the ADOT mixture properties, it appears that 21°C is the threshold to consider creep dominated crack growth that can effectively be describe using the C*-parameter.

Data presented in this section provides evidence that the CFT can effectively be conducted in the temperature range of 4.4°C to 21°C and crack growth rates can be captured. At a temperature of 0°C, asphalt concrete behaves in a more elastic and brittle

manner, and crack growth rates were difficult, if not impossible to capture since crack growth under elastic conditions is very rapid. It may be the case that softer binder or modifiers such as rubber will allow the CFT to be conducted at lower temperatures than 4.4°C. However, after a certain temperature, the importance of the crack growth rate diminishes as a rapid crack can propagate a layer quickly. In the low temperature range, perhaps fracture energy and/or tensile strength may be more important parameters in characterizing crack resistance. It is anticipated that the CFT can be effective at capturing crack growth in the intermediate pavement temperature range.

4.11 Recommended Specimen Geometry

According to the geometric and test condition study and review of literature, the recommended test geometry is a specimen of 150 mm diameter and 50 mm thickness. The right angle notch length shall be 25 mm and an initial crack of 3 mm deep by 1.6 mm wide shall be cut at the bottom of the notch. The following provides support for selection of the recommended specimen size.

1. 150 mm diameter specimen can easily be obtained from the Superpave gyratory compactor or field specimens,
2. Specimen diameter of 150 mm produces a dimension of four times the nominal maximum aggregate size for typical Superpave mixtures.
3. Specimen thickness of 50 mm provides a dimension of four times the 12.5 nominal maximum aggregate for typical Superpave surface course mixtures.
4. Numerical simulation using ABAQUS (Chapter 5) indicated that horizontal tensile stress was developed at the crack tip in the 150 mm diameter specimens.

5. Numerical simulation indicated that crack growth in the 150 mm diameter specimens remained linear over a larger range when compared to 100 mm diameter specimens.
6. Development of indirect tensile stress within the sample was not evident through ABAQUS simulations.
7. Specimen size provides large surface area for crack propagation.
8. Data analysis indicated that 150 x 50 mm specimens produced the best fit of a*-C* data trends (highest R^2-values).
9. Can obtain multiple notched disk specimens from a single gyratory specimen.

4.12 Recommended Data Analysis Procedure

Based on data analysis methods described in the previous section, the following modifications are proposed to the graphical data analysis method proposed by Landes and Begley (1976) and shown in Figure 12. These modifications are based on the C* Fracture test and asphalt concrete.

Step 1: For static loading, plot load (P) and crack length (a) as a function of time Determine the crack propagation rate using a linear fit of data between 20-80 mm.

Step 2: Use Step 1 data to plot normalized load (P/t) versus displacement rate (Δ^*) for each incremental crack length (a) between 20-80 mm increments. The area under each P-Δ^* curve per incremental crack length represents the power or energy rate (U*). Determine the area utilizing the average end area method. The first area increment shall be multiplied by a factor of 0.8.

Step 3: Plot U* as a function of crack length for each displacement rate between 20-80 mm crack length intervals. The C*-parameter is taken as the slope a linear fit of these data.

Step 4: Plot C* and a* as a function of displacement rate (Δ*) and model using a power relationship.

Step 5: Plot crack growth rate (a*) versus C* on a log-log plot and use a power model to represent the data.

4.13 Effect of Dynamic Loading

The C* Fracture Test was carried out using dynamic loading to initially explore effects on crack propagation. Initial testing was carried out using a constant load amplitude dynamic load on the ADOT mixture. To simulate creep loading, a 0.4 second square wave load was applied followed by a 0.6 second rest period. The load magnitude was kept constant at 5 kN and testing was carried out at 20°C. Figure 73 presents crack length as a function of load cycles for specimens from the ADOT mixture. A video camera recorded crack length as a function of time, which was converted to number of cycles (N).

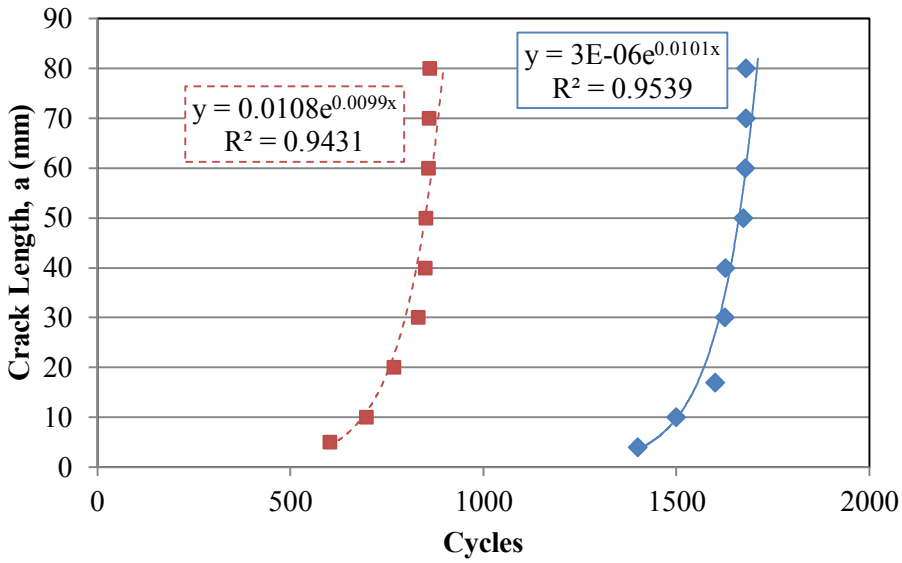

Figure 73 Crack length versus number of load cycles.

It is evident that the number of cycles to initiate the crack varies significantly but the crack growth through the specimen after initiation appears similar. Figure 74 shows a plot of incremental crack growth per cycle (da/dN) as a function of a/W. These data indicate similar crack growth rates through the specimen at all a/W values despite the differences in number of cycles to initiate crack growth. These initial results are promising in that crack propagation rates in CFT specimens are similar and should be considered independently of crack initiation.

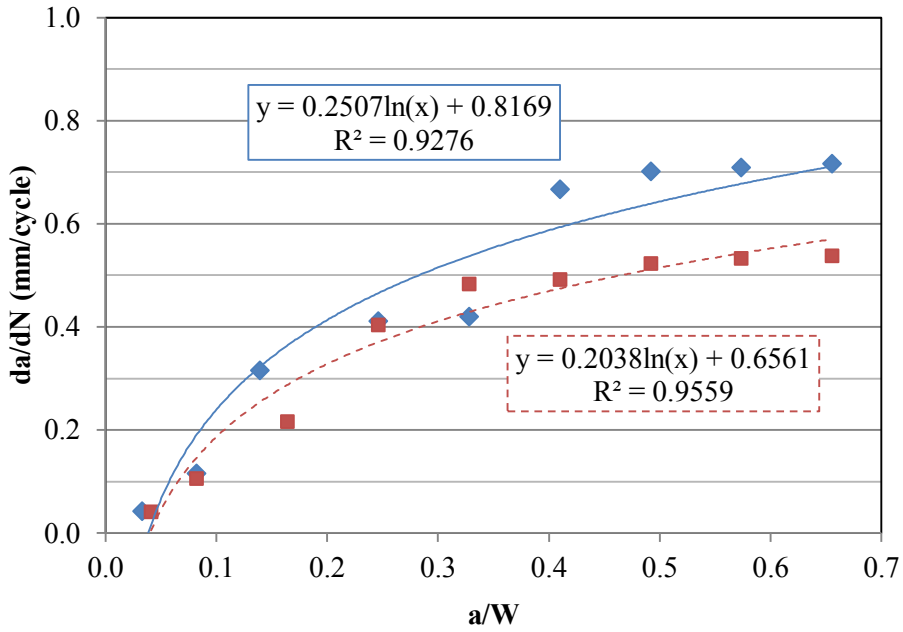

Figure 74 Incremental crack growth per cycle versus a/W.

Future testing should consider a different range of frequencies and load magnitudes. Also, it is recommended that the crack be initiated using static loading to a length of 5 millimeters prior to beginning the dynamic CFT. Next, explore and/or validate the concept presented by Nikbin and Webster (1988). This literature presents a comparison of a*-C* relationships obtained by static and dynamic loading conditions. Authors report the a*-C* relationship from dynamic loaded tests corresponds with static test results, above a threshold frequency. This can be attributed to the fact that dynamic loading with higher frequency acts as a static or creep load. Authors suggests that crack propagation is driven by a creep mechanism rather than a purely fatigue phenomenon.

4.14 Summary

This chapter presented a study to evaluate specimen geometries and test conditions for the C* Fracture Test. A dense graded mixture (ADOT) was tested at 21°C using three different sample geometries (diameter x thickness): 150 x 50 mm, 150 x 25

mm and 100 x 50 mm. Based on the initial results for the given mixture, a specimen size of 150 x 50 mm was recommended. Specimens were then subjected to the CFT at 0, 4.4, 10 and 37.8°C using different loading rates to evaluate the effect of temperature on CFT results.

In addition, modifications to the original graphical data analysis technique proposed by Landes and Begley (1976) are proposed based on the C* Fracture Test geometry, asphalt concrete material and analysis conducted at ASU. For dense graded mixtures, the recommended data analysis range was determined to be 20-80 mm and 10-50 mm for the 150 mm and 100 mm diameter specimens, respectively. Statistical comparison between a*-C* trends indicated that the 150 x 25 mm specimens produced statistically different a*-C* trends than 150 x 50 mm and 100 x 50 mm specimens; indicating that thickness had a greater effect on test results than diameter for the ADOT mixtures used in this study.

CFT test results were presented for the different temperatures included in the test temperature study. Results are rational in that crack growth rate increases as test temperature decreases. For 4.4°C, crack growth rates are higher at all C* values when compared to results at 21°C. Also, for the ADOT mixture, 21°C appears to be a threshold temperature after which no significant decrease in crack growth rates were observed for similar C* values. For a low temperature limit, tests conducted at 4.4 °C produced the most reasonable results. However, testing at 0°C was not recommended or even possible as crack growth rates were too rapid to provide rational results.

For future analysis at low temperatures, it is recommended that more advanced crack growth capture techniques be explored such as the use of higher resolution video

equipment or digital image correlation. For all temperatures, it is recommended to monitor crack growth on both sides of the CFT specimen to obtain an average crack growth rate in a test specimen.

Finally, CFT was carried out using dynamic loading conditions. A 5kN load controlled test was performed using a square waveform at 1 Hz (0.4s load, 0.6s rest). Initial results show similar crack growth rates (da/dN) through the specimens at all a/W values despite differences in number of cycles to initiate crack growth. These results are promising in crack propagation should be considered independently of crack initiation.

Chapter 5

5 FINITE ELEMENT MODELING OF C* FRACTRE TEST SPECIMENS

5.1 Objective

In order to access stress distributions and crack propagation within the 100 mm and 150 mm diameter C* Fracture Test (CFT) specimens, numerical simulation on specimen geometries was accomplished through Finite Element Analysis (FEA) using ABAQUS 6.10 software. The overall goal was to simulate the C* Fracture Test, analyze the stresses and deformations developing within the samples and to compare the simulation results to actual laboratory test data.

5.2 Model Description

A linear elastic model was used for all CFT simulations and the assumption of homogeneous and isotropic asphalt concrete material was used in all analysis. It is inherent that these assumptions are not completely valid, but they are acceptable to establish baseline modeling for the CFT test specimens. In addition, the assumption of plane stress was applied to the analysis as the thicknesses of the specimens were not sufficient to satisfy plane strain conditions. CPS4R (4-node bilinear plane stress quadrilateral) elements were selected and ABAQUS was used to automatically mesh all parts included in the analysis.

Extended Finite Element Analysis (XFEM) was used in order to allow a crack to propagate through the specimen. This is a powerful tool in ABAQUS that allows damage modeling and can be used simulate crack propagation. Damage modeling allows the degradation and failure of elements in the model without the need for re-meshing. This method requires user-defined damage criteria to be specified upfront which includes a

damage initiation criteria and damage evolution law. Damage initiation is assumed linear but the evolution law can be linear or non-linear as shown in the traction separation law schematic presented in Figure 75. It is important to note the assumption that damage does not occur in compression in this analysis.

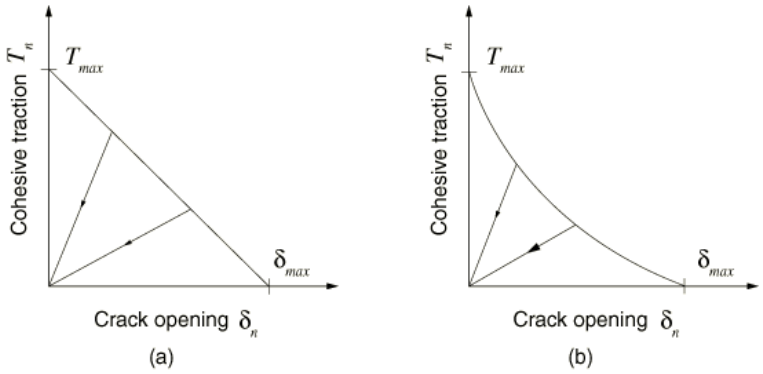

Figure 75 Examples of traction-separation, linear (a) and nonlinear (b) damage evolution laws (ABAQUS, 2009).

The maximum principal damage (Maxps Damage) option was selected from the traction-separation laws available in ABAQUS. This option requires the user to specify the maximum principal stress or (tensile strength) of the material. Once this user-defined tensile stress is exceeded, a crack develops in the associated element. The direction of crack propagation depends on the magnitude of tensile stress in the adjacent elements. Crack propagation (damage evolution) through the specimen occurs according to a user-defined damage evolution law which was selected to be the linear traction-separation law. Fracture energy or the area under the cohesive traction versus crack opening curve presented in Figure 75 was selected as a sub option of damage evolution. Thus, the crack was considered cohesive traction free once the crack opening reached a value such that the user-defined fracture energy input value was exceeded.

5.3 Geometric Assembly Used for Modeling

The assembly used in this analysis consisted of four main components: a base plate, CFT specimen, loading plates and loading head. The base plate and loading plates were assigned elastic properties of stainless steel (E= 200 Gpa, μ = 0.3) while the properties of asphalt concrete were varied during the analysis. To simplify the analysis, the loading head was created using an analytically rigid surface in which its only purpose was to apply a displacement similar to the laboratory test. Recall, the main objective was to simulate the CFT setup while maintaining a reasonable and practical model in ABAQUS. Figure 76 shows a schematic of the CFT model assembly employed in ABAQUS.

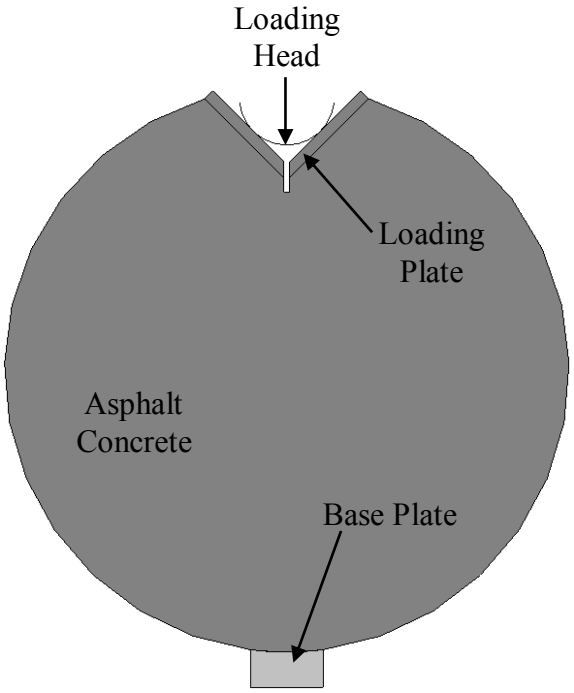

Figure 76 Assembly used for FEA modeling.

Another assumption involved modeling the loading plates. Initially, they were considered separate parts but the simulation time increased significantly as additional

surface interactions were included in the computation. An assumption was made to include the plates as part of the specimen and add a partition in the part to account for the loading plates. This partition allowed the plates to be assigned stainless steel properties and to be assigned a separate mesh size than the asphalt concrete specimen.

The contact between the loading plates and the loading head was considered to be frictionless while the contact between the specimen and the bottom plate was assigned a friction value of 0.1. Without friction, the specimen was not restrained at the base plate and rotation was observed during initial simulations. Applying a boundary with friction resolved this modeling concern.

In order to apply the constant displacement, loading was accomplished by applying a vertical displacement of two millimeters to the loading head as a boundary condition. This required the force to be varied as a function of displacement and, coupled with the traction-separation behavior, achieved a load-displacement curve similar to the laboratory data. The bottom of the base plate was assigned fixed "x" and "y" boundary conditions to simulate the fixed base in the actual test setup.

Figure 77 and Figure 78 present the meshed assembly used for numerical simulation in ABAQUS for the 150 mm and 100 mm diameter specimens, respectively. Smaller size elements were necessary at critical locations such as the loading points, initial crack location and at the base plate.

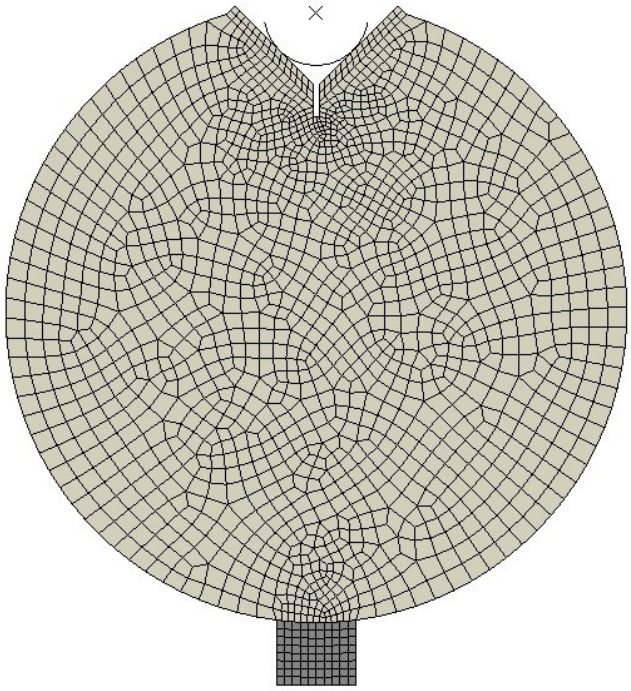

Figure 77 Meshed assembly for a 150 mm diameter CFT specimen.

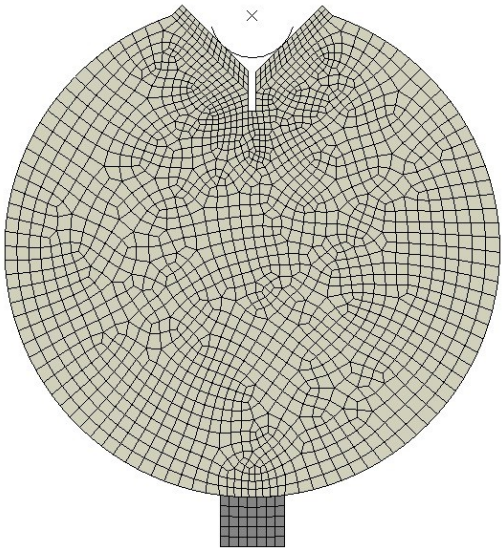

Figure 78 Meshed assembly for a 100 mm diameter CFT specimen.

5.4 Stress Analysis Results

This section presents numerical simulation input values for asphalt concrete CFT samples along with the results of the numerical simulations for both the 100 and 150 mm diameter specimens.

Numerical simulation in ABAQUS required the following input parameters: Young's modulus, Poisson's ratio, tensile strength and fracture energy. Table 27 presents the final input parameters used in numerical simulation of CFT specimens. Initial simulation was performed at 21°C so Poisson's ratio was fixed at 0.35. All other parameters were iterated until load-displacement curves obtained from simulation were similar to laboratory data. Laboratory data for the 150 mm and 100 mm diameter specimens were extracted from specimens tested at the same loading rate of 0.228 mm/min for comparison.

Table 27 Input parameters for numerical simulation.

Diameter (mm)	User Specified Input Values			
	E (MPa)	μ	S_t (MPa)	G_f (MJ)
150	700	0.35	2.08	2.10
100	725	0.35	2.30	1.38

Figure 79 presents a comparison of load-displacement plots between numerical simulation and laboratory results for a 150 mm and 100 mm specimen tested at a constant displacement loading rate of 0.228 mm/min.

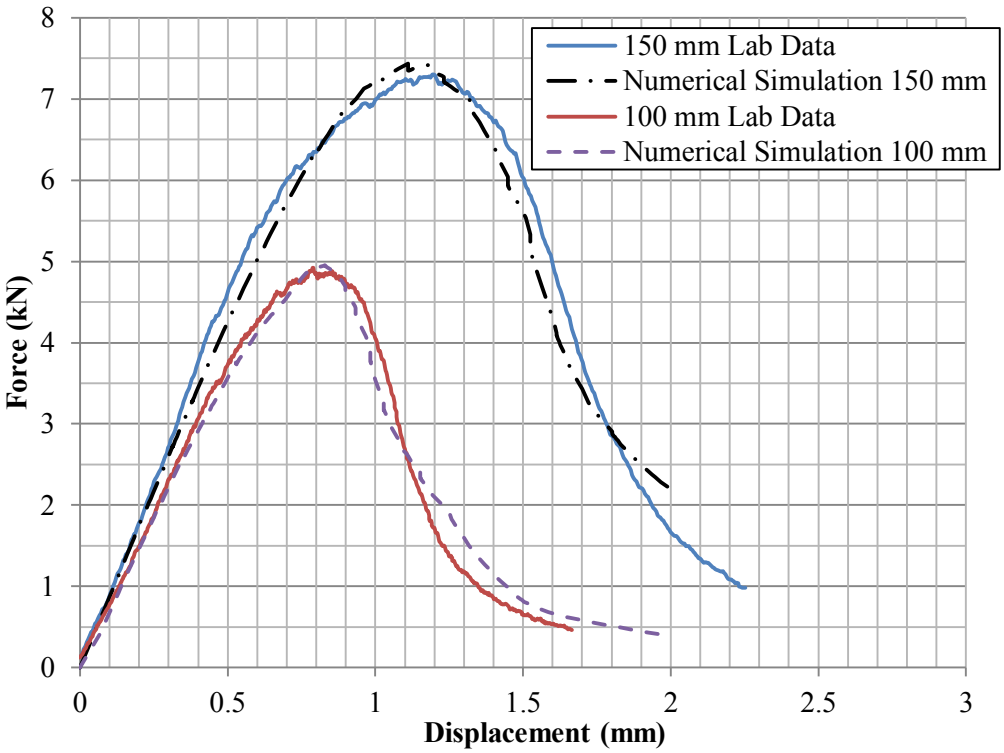

Figure 79 Force versus displacement comparison for 150 mm and 100 mm diameter samples.

Recall that crack propagation typically occurs at or just beyond the peak load. With this in mind, the 100 mm and 150 mm diameter specimens tested in the laboratory required approximately 4.8 kN and 7.3 kN of applied force to initiate crack propagation, respectively. For both specimen sizes, it appears that numerical simulation tends to overestimate the load in the tail of the curve. The assumptions of a linear-traction separation law or elastic analysis may be a factor in this observation.

Once laboratory load-displacement curves were replicated through numerical simulation, the stress development along the crack path was evaluated. Figure 80 and Figure 81 show the development of horizontal tensile stresses at the crack tip for 150 mm diameter and 100 mm diameter specimens, respectively. This stress state was early in the simulation at an applied displacement of 0.25 mm.

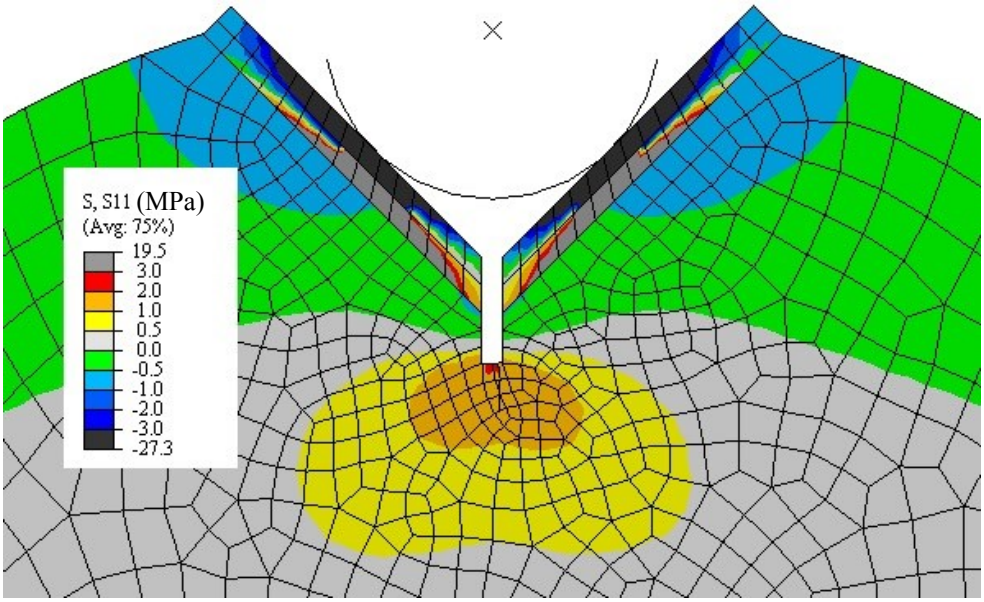

Figure 80 Horizontal stress development at crack tip for 150 mm diameter specimen (Δ = 0.25 mm)

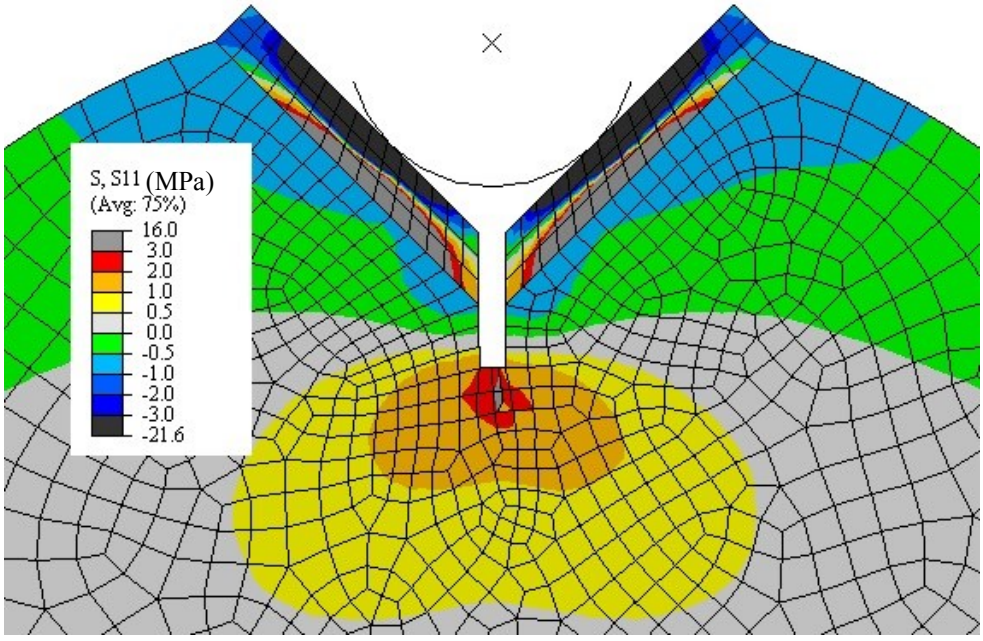

Figure 81 Horizontal stress development at crack tip for 100 mm diameter specimen (Δ = 0.25 mm)

Given the same displacement step, the horizontal tensile stress development surrounding the crack tip is between 2-3 MPa (290-435 psi) in the 100 mm diameter

specimen whereas the tensile stress ranges between 1-2 MPa (145-290 psi) in the crack tip region of the 150 mm diameter specimen. Thus, tensile stresses develop at the crack tip much quicker in the 100 mm diameter specimen.

Figure 82 presents numerically simulated crack growth and horizontal stress evolution within the 150 mm diameter CFT specimen for three arbitrarily selected applied displacements. Crack propagation throughout the specimen is consistent with laboratory test results in that propagation typically occurs through the specimen center. Horizontal tensile stress development occurs at the crack tip and the lag of the stress bulb is the result of traction which is based on the applied linear damage separation law. A zone of horizontal compressive stresses exists at the base of the specimen at the base plate which approaches a large value of 90 MPa (13,053 psi) at one of the nodes. This compressive zone was expected but the magnitude is very high and it was speculated to influence crack growth toward the bottom of the specimen. As the crack approaches the bottom of the specimen, it tends to deviate from centerline as shown in Figure 82 at an applied displacement of 2.0 mm.

One important observation is that indirect tensile stresses do not appear to develop in the specimen due to the presence of the bottom base plate. However, the inclusion of aggregate into the numerical simulation may alter the stress development within the sample and should be considered in future, more comprehensive analyses.

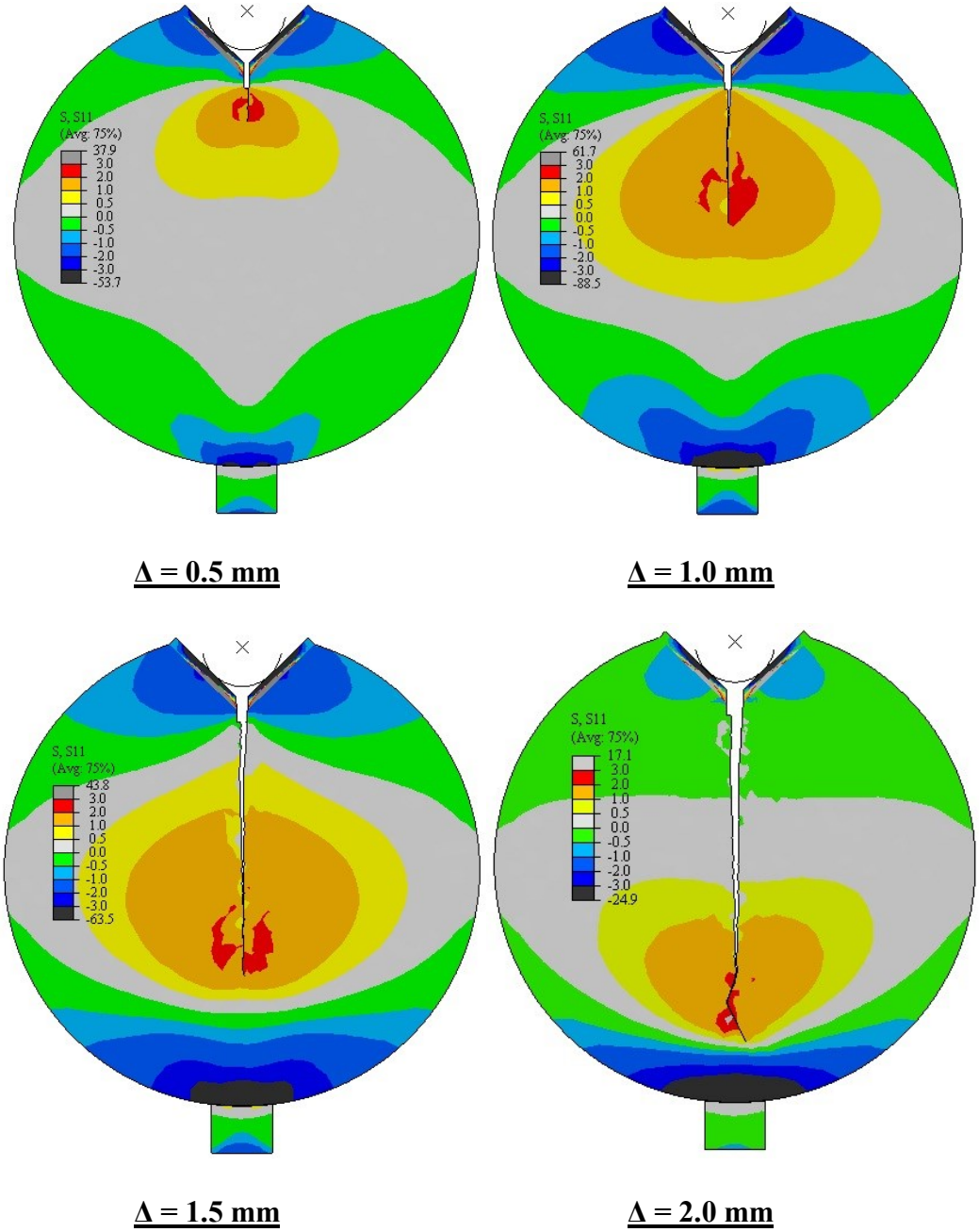

Figure 82 Crack growth and horizontal stress (MPa) evolution versus applied displacement (150 mm diameter)

Figure 83 shows similar numerical simulation results for crack growth and horizontal stress development in a 100 mm diameter specimen. Again, within the CFT sample, the maximum tensile stress development occurs at or just beyond the crack tip at

all crack lengths. The zone of compressive horizontal tensile stresses approaches a maximum value of 42 MPa (6,091 psi) for this given simulation and reduces in size and magnitude as the crack approaches the bottom of the specimen. Similar to the 150 mm diameter specimen, indirect tensile stresses are not observed in the specimen as a result of the base plate. Again, this observation should be confirmed with more extensive numerical simulation of CFT specimens with the presence of large aggregates.

It is an important observation that crack growth deviates from the centerline as the crack approaches the bottom of the specimen and enters the zone of compressive stresses. A more likely cause of crack path deviation may be due to a reduction in tensile stress transfer to the crack tip. In this case, stress development at the edges of the base plate can induce shear stresses which may be more pronounced than the tensile stresses. Thus, crack growth results from a combination of shear (Mode II) and tensile (Mode I) stresses and deviates from centerline if Mode II controls. Analysis of shear stress development is evaluated in the following paragraphs.

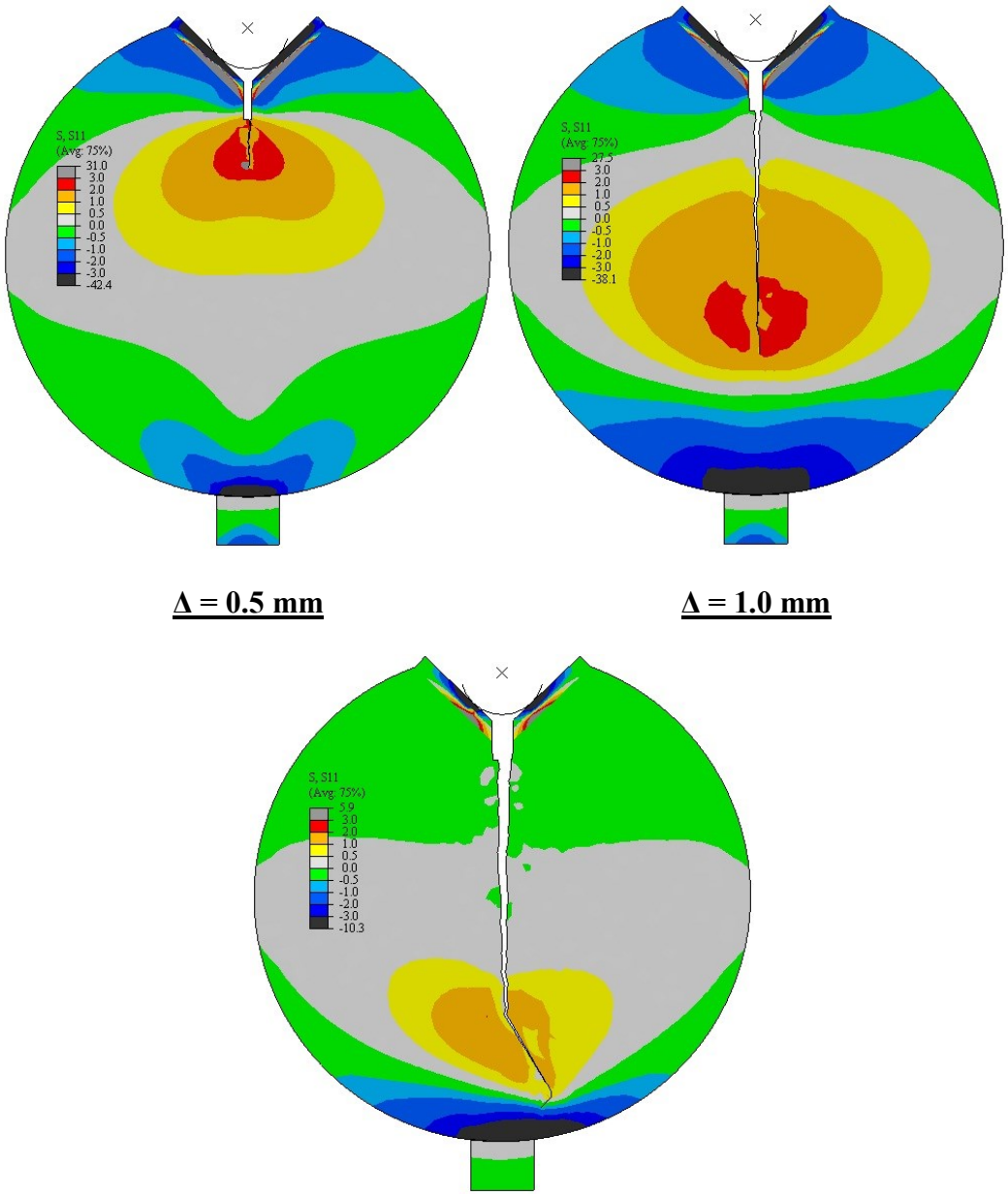

Δ = 0.5 mm **Δ = 1.0 mm**

Δ = 1.5 mm

Figure 83 Crack growth and horizontal stress (MPa) evolution versus applied displacement (Δ) (100 mm diameter)

Another consideration in fracture mechanics is Mode II crack growth due to shear forces acting along the crack face. Up until this point, only Mode I crack growth has been discussed in analysis. Thus, shear stress development as a function of applied displacement was evaluated as part of the numerical simulation. Figure 84 and Figure 85 present the shear stress evaluation in 150 mm and 100 mm diameter specimens, respectively. In both cases, shear stress within the specimen is uniform until the crack approaches the bottom of the specimen. At these crack lengths, non-uniform shear stress develops in the sample adjacent to the crack path. Thus, shear stress potentially contributes to crack growth as the crack path deviates from the centerline of the specimen.

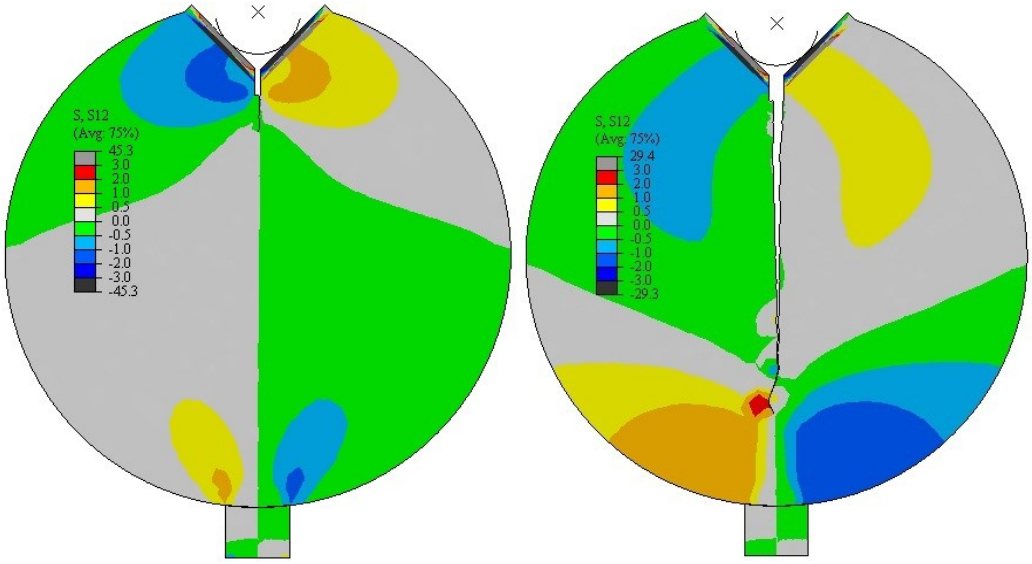

Δ = 0.5 mm **Δ = 1.75 mm**

Figure 84 Shear stress evolution (MPa) versus applied displacement (Δ) (150 mm diameter)

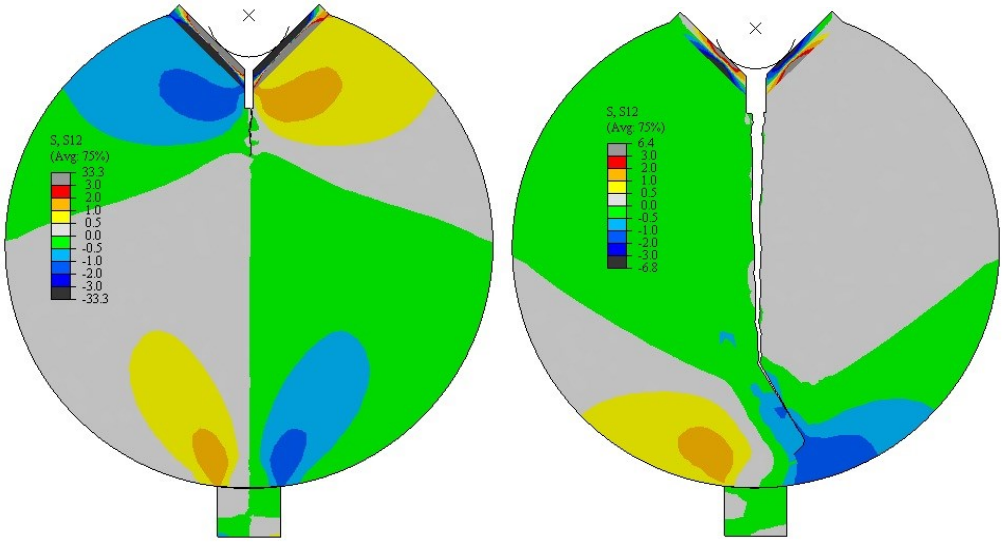

Δ = 0.5 mm **Δ = 1.50 mm**

Figure 85 Shear stress evolution (MPa) versus applied displacement (Δ) (100 mm diameter)

5.5 Analysis of Specimen Deformation

Another factor to consider was deformation of the specimen under the notched wedge loading configuration. It was anticipated that the majority of the vertical displacement was translated into the x-direction which caused the sample to split along the center line. Figure 86 and Figure 87 present the numerical simulation results for vertical deformation observed in the 150 mm and 100 mm diameter specimens, respectively. Units are in millimeters and it can be observed in both sample sized that the vertical deformation under the load apparatus is less than 0.5 mm for selected applied displacements. It is observed that the CFT loading setup results in 0.5 to 1.0 mm of vertical deformation at the outer portion of the CFT specimens for the test conditions considered.

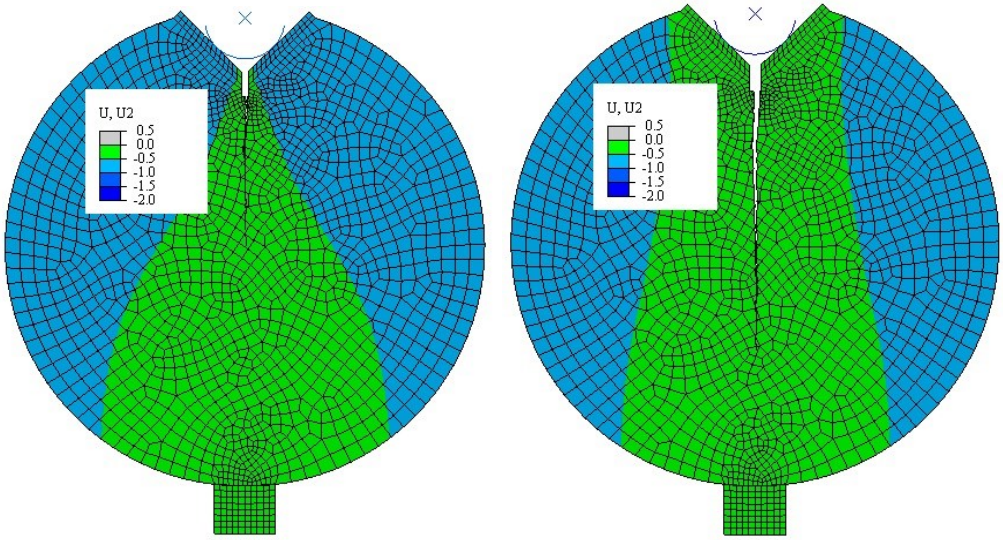

Δ = 1.0 mm **Δ = 1.50 mm**

Figure 86 Vertical displacement (mm) versus applied displacement (Δ) (150 mm diameter)

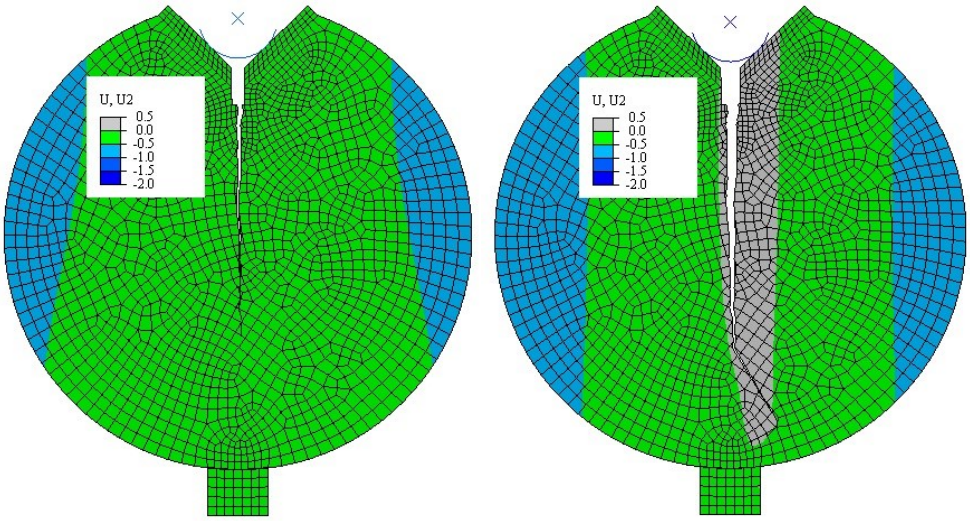

Δ = 1.0 mm **Δ = 1.50 mm**

Figure 87 Vertical displacement (mm) versus applied displacement (Δ) (100 mm diameter)

In order to further evaluate the horizontal and vertical deformation experienced by a CFT specimen, deformation was plotted for a node located at the tip of the initial crack (introduced notch). Figure 88 depicts a typical mesh and location of the point of analysis.

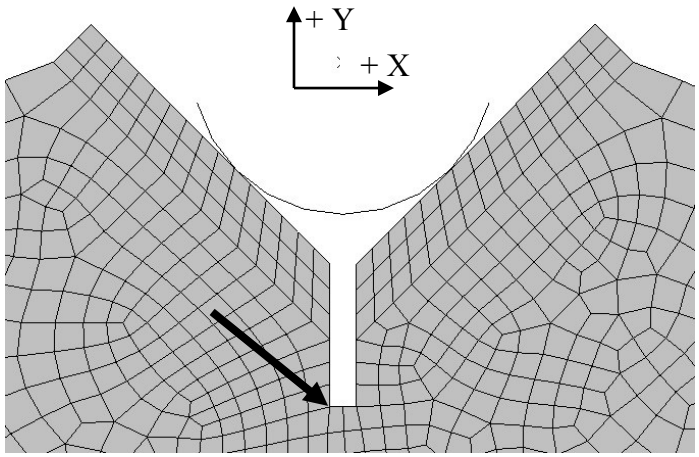

Figure 88 Initial crack notch location selected for displacement analysis.

Vertical and horizontal deformation was plotted as a function of applied actuator displacement to determine if the CFT setup was splitting the sample (x-direction), compressing the sample (y-direction) or a combination of both. Figure 89 and Figure 90 present the results of the vertical and horizontal displacement analysis for 150 mm and 100 mm diameter specimens, respectively. In both sample sizes, the majoring of the deformation at the initial crack tip is in the x-direction which is desirable. However, there is a small component in the y-direction as the specimen experiences some vertical deformation (less than 0.5 mm) until macro cracking occurs. At this point, the vertical deformation is recovered due to the linear elastic assumption applied to this numerical simulation. The recovery of the vertical deformation in the 100 mm diameter specimen was quicker which can be explained by the more rapid crack growth discussed in the following section.

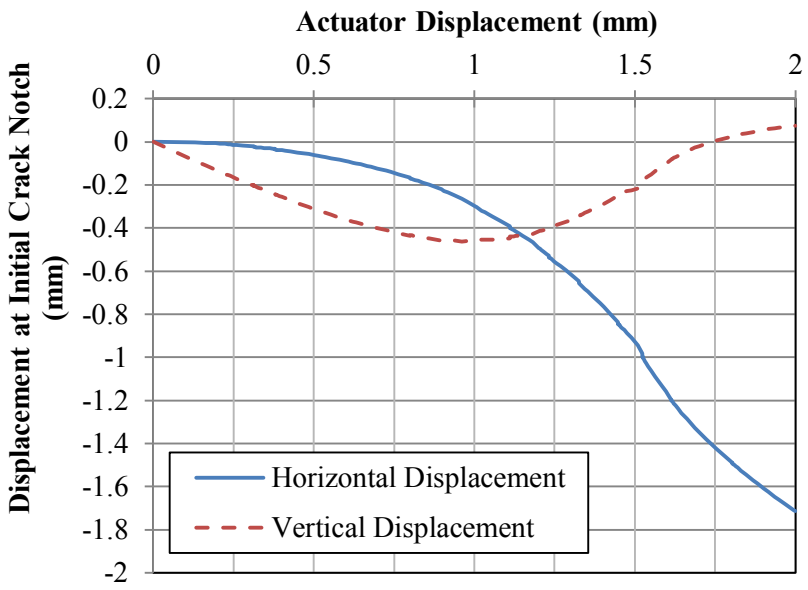

Figure 89 Spatial displacement at initial crack notch (150 mm diameter)

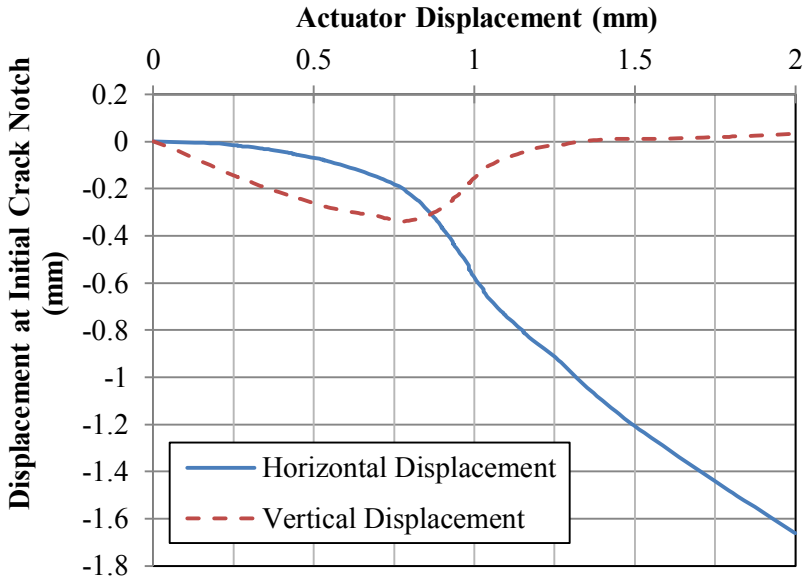

Figure 90 Spatial displacement at initial crack notch (100 mm diameter)

In order to experimentally observe that the CFT load application did not result in excessive vertical, on-specimen deformation, two specimens were instrumented with vertical linear variable displacement transducers (LVDT's). The LVDT's measured vertical, on-specimen displacement during a test and data were averaged. Due to the

mounting configuration of the LVDT's, the instrumentation had to be offset ±25 mm from the center of the specimen to accommodate the loading head. Figure 91 provides an example of LVDT's mounted on a 150 mm diameter CFT specimen.

Figure 91 Vertical LVDT's mounted on CFT specimen

Figure 92 shows the on-specimen vertical deformation recorded by the two LVDT's. The laboratory test was conducted at 21°C at a loading rate of 0.228 mm/min. The maximum vertical deformation of 0.34 mm occurs at an actuator displacement of 1.55 mm and then is reduced as crack front advanced.

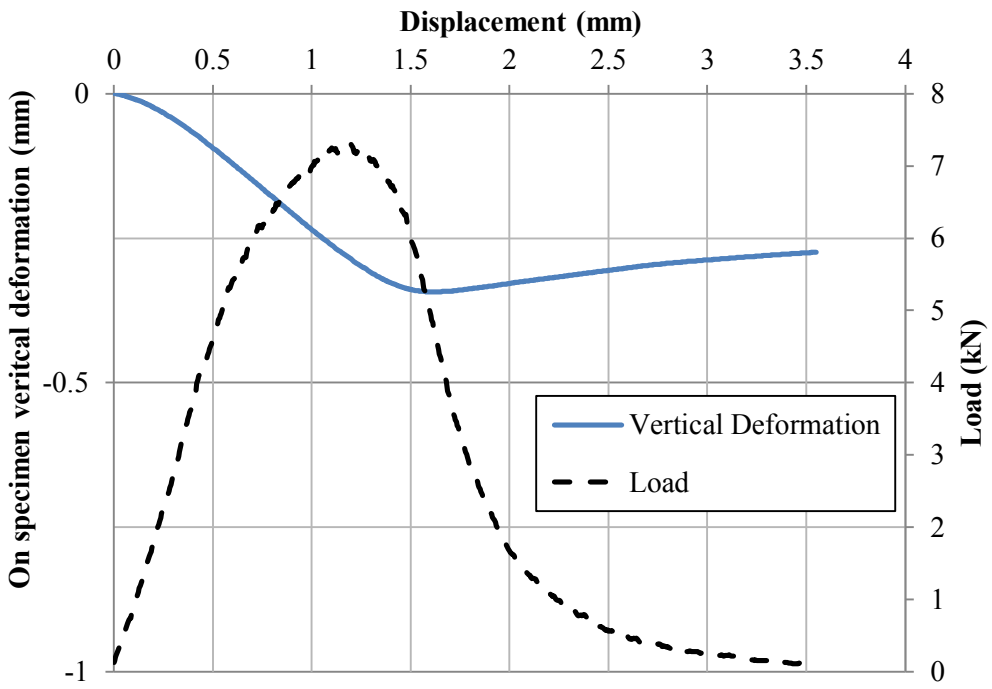

Figure 92 On-specimen vertical displacement from CFT at 21°C.

Very little of the vertical deformation was recovered which can be considered non-recoverable deformation. In comparison, the purely elastic numerical simulation showed full recovery of vertical deformation. Finally, the load-displacement plot was included to show that vertical displacement reached a maximum at a point just past peak load. This point typically signifies the onset of crack growth through the specimen.

5.6 Crack Growth Modeling Results

Crack length data was extracted from numerical analysis in order to compare crack growth in the 150 mm and 100 mm diameter specimens. Recall the earlier observation that a much lower vertical force was required to initiate cracking in the smaller diameter specimen. The crack tip location (y-direction) at various stages of applied displacement was recorded and data are presented graphically in Figure 93.

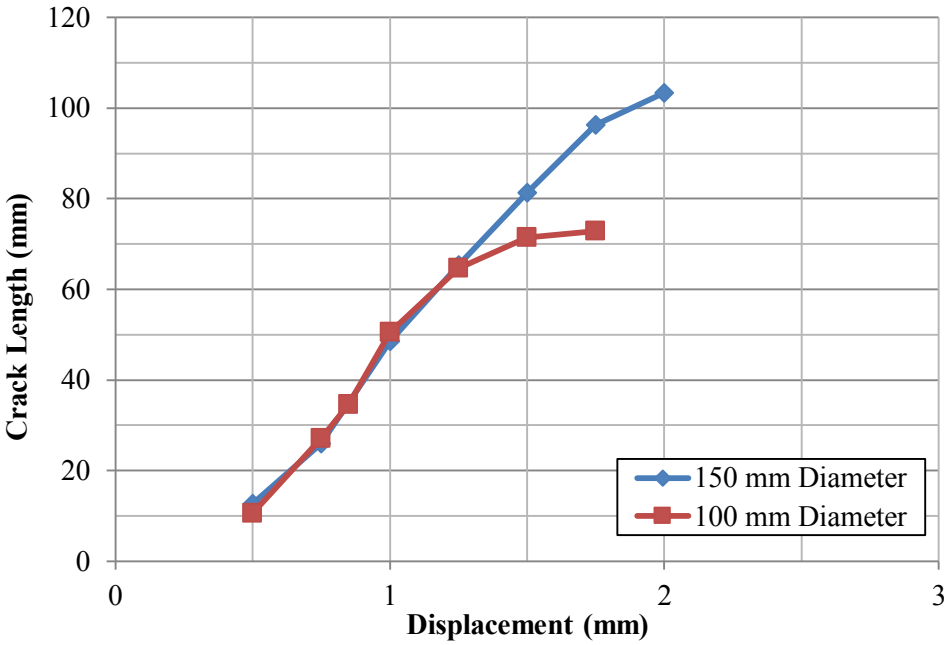

Figure 93 Crack tip location versus applied displacement (numerical simulation).

Numerical simulation of 150 mm and 100 mm specimens produce similar crack growth as a function of applied displacement. However, crack growth becomes non-linear sooner in the smaller diameter specimen as the crack approaches the bottom of the specimen. As discussed earlier, this may be the result of the crack entering the zone of compressive stresses at the bottom, a reduction of stress transfer to the crack tip or a combination of both. Considering the numerical simulation results provided in Figure 82 and Figure 83, the horizontal stress at the crack tip is reduced as the crack approachs the bottom of the specimen.

Based on these results, the 150 mm diameter specimen provides a much larger area for crack growth. This is supported by the fact that crack length as a function of displacement remains linear over a much larger region than observed for the 100 mm diameter specimen. However, the location of the crack tip versus applied displacement in numerical simulations does not appear to be rational since the crack growth begins at

small displacements, prior to attainment of maximum load as shown graphically in Figure 94

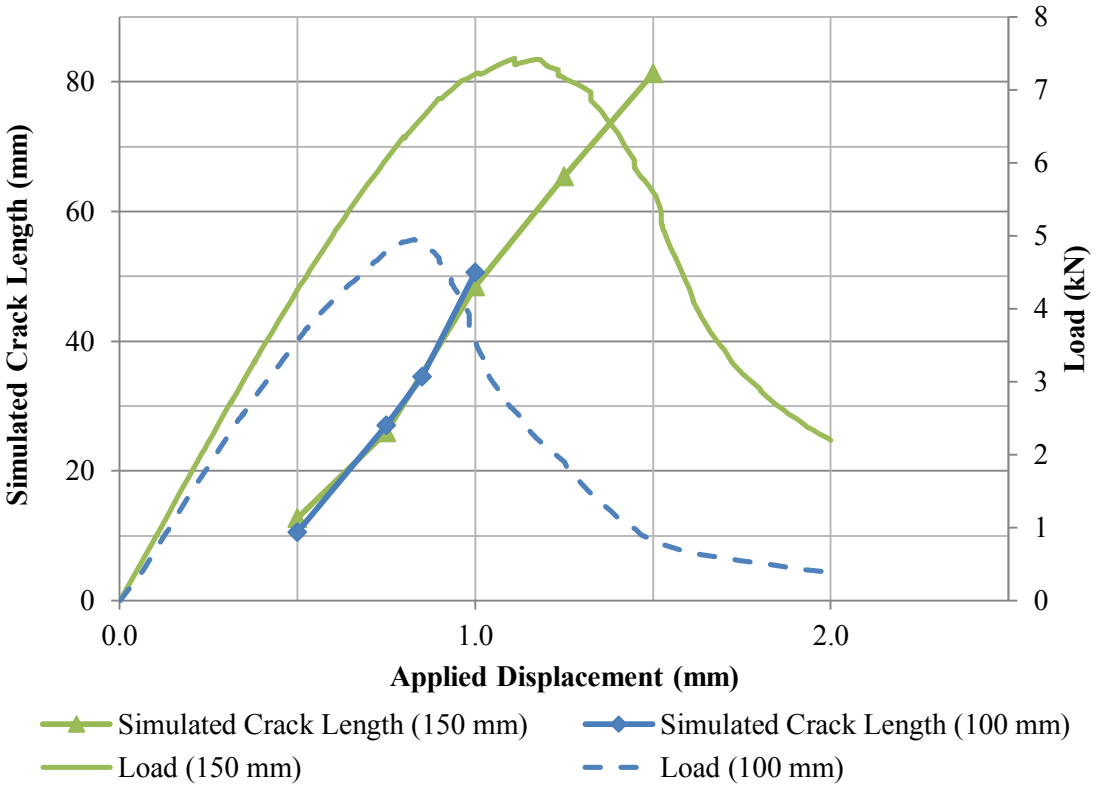

Figure 94 Numerical simulation crack length and applied load data

In comparison, Figure 95 presents laboratory crack length and load data for the specimens used in numerical simulations. In both the 150 mm and 100 mm diameter samples, the crack reaches 10 mm at or just beyond the point of maximum load.

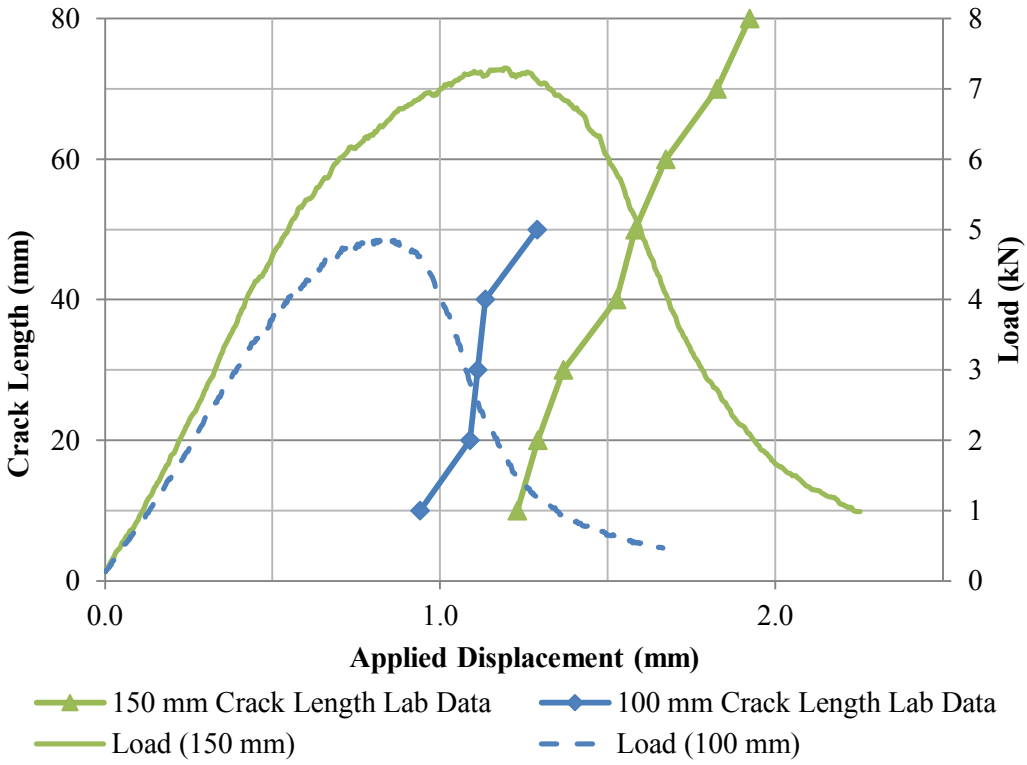

Figure 95 Experimental crack length and applied load data

Thus, the crack tip observed in the numerical simulation can be considered a micro crack which cannot be observed by the camera or human eye. Figure 82 and Figure 83 indicate that traction exists behind the crack front based on the user-specified traction-separation law. Thus, the macro crack in the numerically simulated specimen is at some distance behind the actual visible crack tip. This difference in simulated crack tip and actual crack tip can be considered the fracture process zone (FPZ) commonly discussed in fracture analysis of asphalt concrete.

Thus, an adjustment to crack length was necessary in order to match laboratory data. It was assumed that a macro-crack was visible once the displacement in the x-direction of a node adjacent to specified crack lengths (e.g. 10 mm, 20 mm, etc.) reached a user-selected value. Thus, recorded length of the macro crack would be shorter than the

location of the crack tip. Displacement values of 0.4 mm (150 mm diameter) and 0.2 mm (100 mm diameter) were found as suitable crack length adjustments to simulate laboratory data for the modeled specimens. A crack length comparative plot for both diameter specimens is provided in Figure 96.

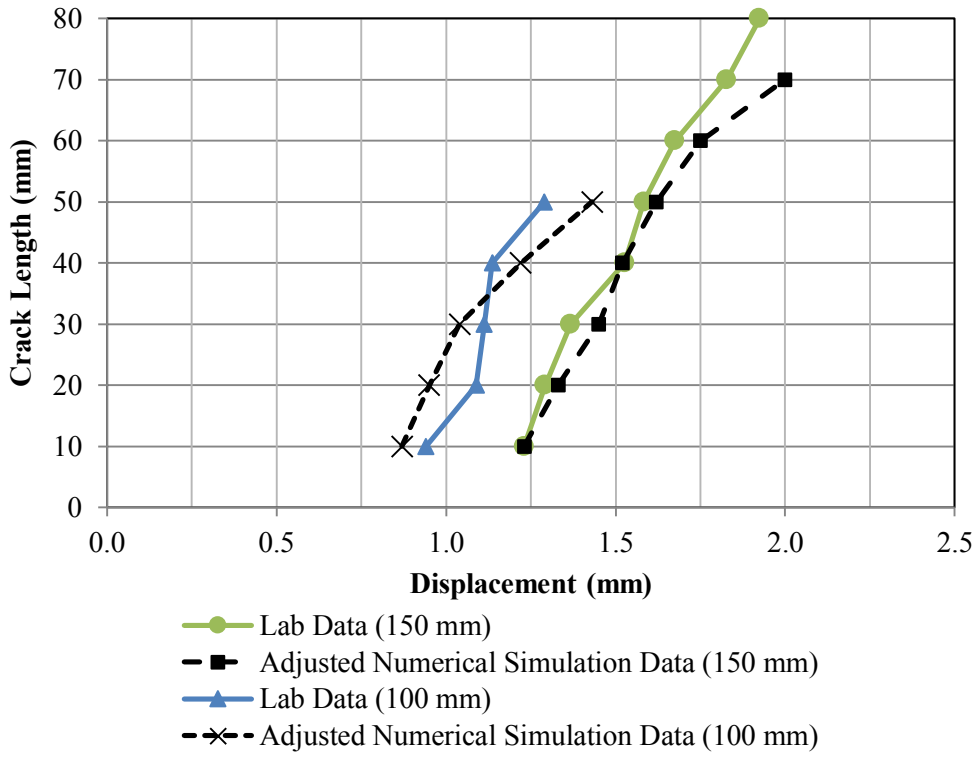

Figure 96 Adjusted crack length from simulations versus actual crack length.

Overall, the adjusted simulated crack lengths versus displacement match the laboratory data well. Given the non-linear crack length trends at longer crack lengths, it is evident that the common node displacement values of 0.4 and 0.2 mm are not practical. This illustrates the fact that the fracture process zone size is reduced as the crack approaches the bottom of the specimen. This may be the result of the complex stress state that can exist near the base plate.

5.7 Summary

Numerical simulations on 100 and 150 mm diameter CFT specimens were carried out and described in detail in this chapter. Notable findings are summarized as follows:

- Numerical simulations on both CFT specimen diameters were able to replicate laboratory load-displacement curves for a loading rate of 0.228 mm/min (21°C). The 100 mm diameter specimen required about 66% of the peak load of the 150 mm diameter to initiate crack growth. However, in both cases, simulations overestimated the load in the tail end of the curve. This may have been caused by applying assumptions of linear damage or purely elastic analysis.
- CFT load configuration results in horizontal tensile stress development at the crack tip. Crack tip stress development is more rapid in the 100 mm diameter specimens. Simulations show that the base plate does not induce noticeable indirect tensile stresses within the specimen. However, this should be further examined with the inclusion of large aggregate in the model.
- A zone of horizontal compressive stresses exists at the base plate which could potentially hinder crack growth towards the bottom of the specimen. The magnitude can be rather large but is reduced as crack length increases.
- Non-uniform shear stress was observed at the crack tip as the crack approached the bottom of the specimen. It was concluded that the effect of crack tip tensile stress (Mode I) on crack growth diminished toward the bottom of the specimen and Mode II crack growth was evident.
- Simulation indicated that the majority of the deformation at the original crack tip location was horizontal which was desirable. A vertical deformation component

does exist but appears to be small in comparison to horizontal deformation for the material properties in consideration. LVDTs mounted on a test specimen confirmed that small vertical deformation occurred.

- Crack growth occurred prior to peak load in numerical simulations which does not match laboratory data. The crack tip observed in numerical simulation could be considered a micro-crack. Crack length was defined as the location where an adjacent node experienced a given horizontal deformation (macro-crack). After applying this adjustment, simulated crack growth appeared reasonable in comparison to actual crack growth observed in the laboratory specimens tested at the same conditions.
- Since fracture occurred at a lower maximum load in the 100 mm diameter specimen, less potential for non-recoverable deformation exists when compared to the 150 mm diameter specimen. However, less area was available for crack growth in the 100 mm diameter specimen and a more non-linear crack growth trend was observed in comparison to the 150 diameter specimen.
- The 150 mm diameter specimen is the preferred diameter for the CFT since it provides ample area for crack growth. Stress and deformation analysis appeared reasonable and similar for both diameter specimens.

Chapter 6

6 DEVELOPMENT OF A CRACK GROWTH RATE MASTER CURVE

6.1 Objective

Using the concept of reduced crack growth rate presented by Seo et al (2004) and the time-temperature superposition principle, the potential for a crack growth rate master curve was explored using C* Fracture Test data from the ADOT mixture tested at 4.4°C, 10°C, 21°C and 37.8°C. Data at these four temperatures allows the relationship between temperature and shift factor (a_T) to be established. The benefit of the master curve lies in the fact that crack growth rates can be predicted at temperature and loading ranges where laboratory testing is difficult or not practical, such as the case of 0°C for the ADOT mixture. One of the most beneficial aspects of a crack growth rate master curve is that it can be incorporated into design software such as Pavement ME in order to predict crack propagation rates as a function of different pavement temperatures and C* values.

6.2 Master Curve Development

The procedure to develop a crack growth rate master curve was presented by Seo et al (2004) and discussed in Section 3.14. This procedure was established through time-temperature superposition and utilizes shift factors (a_T) from dynamic modulus tests. In summary, reduced crack growth rate is related to measured crack growth rate according to the relationship presented in Equation 6.1.

$$\dot{a}_\xi = \frac{da}{dt} * a_T \qquad \textbf{6.1}$$

Where:

a_ξ = reduced crack growth rate,

da/dt = crack growth rate, and

a_T = linear visco-elastic shift factor for temperature (T) from the complex modulus test.

Crack growth rate as a function of C* and test temperature are shown graphically in Figure 97. Observation of the data indicates the potential to shift these data vertically and obtain a single crack growth rate master curve for the ADOT mixture.

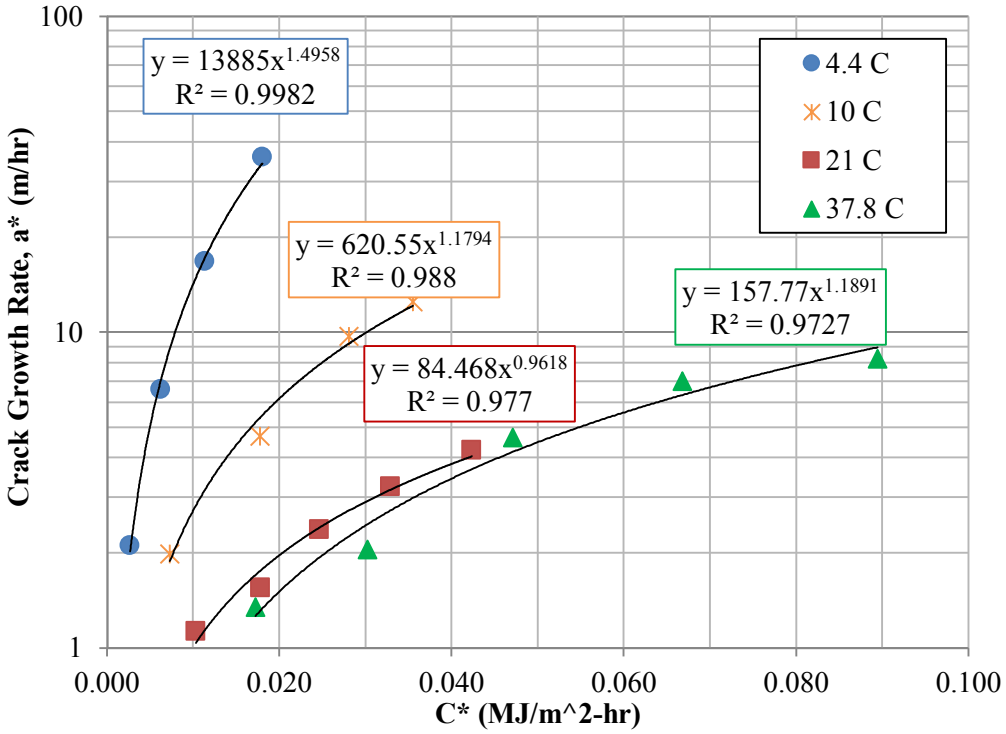

Figure 97 Crack growth rate as a function of temperature (ADOT mixture)

Shifting of data was accomplished by minimizing the summation of squared error between the observed and predicted data through a spreadsheet developed in Microsoft Excel. Master curves were developed using actual crack growth and C* data in addition

to log transformed data. Results of these analyses are presented in the following two sections.

6.2.1 Master Curve using Actual Data

Using a reference temperature of 21°C (and validated at 4.4°C), crack growth rate data were shifted and fit with a power model presented in Equation 6.2. The solver function in Microsoft Excel 2010 was used to estimate the parameters (a, b) by minimizing the squared error between actual and predicted reduced crack growth rates.

$$\dot{a}_{\xi} = a * (C^*)^b \qquad \textbf{6.2}$$

Where:

a_{ξ} = reduced crack growth rate,

C* = power release rate parameter (MJ/m^2-hr), and

a, b = regression parameters.

Figure 98 presents the results of the crack growth rate master curve fitted using a power function. The reduced crack growth rate data was vertically and the corresponding fit of the data is very good with adjusted R^2 value of 0.97 and S_e/S_y of 0.174. These values indicate excellent model accuracy according to the categories adopted and described in the NCHRP 465 report (Witczak et al, 2002).

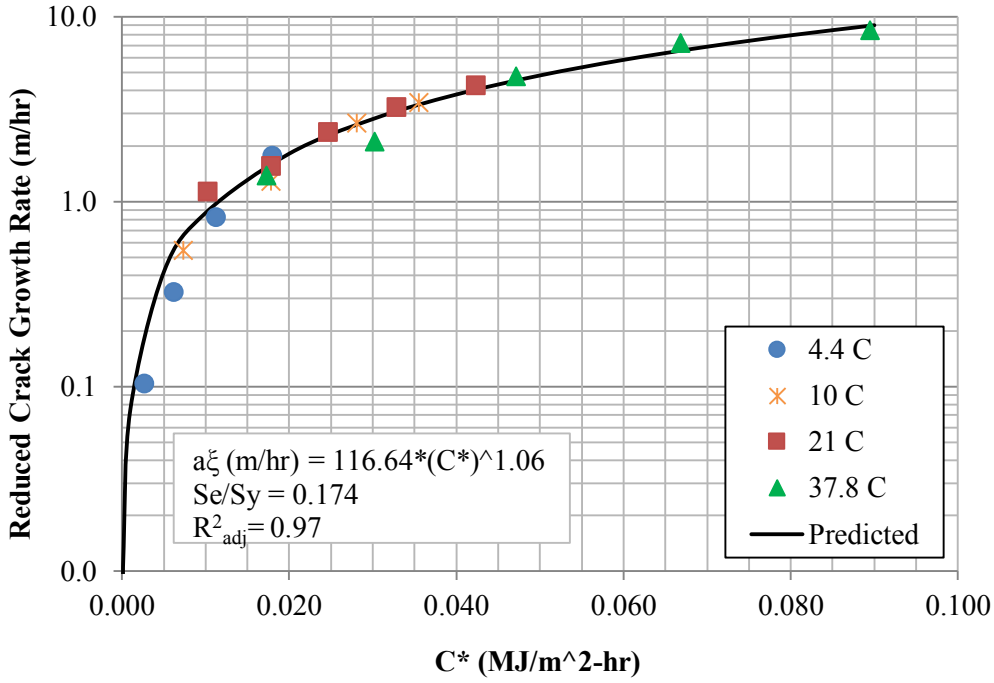

Figure 98 Crack growth rate master curve for ADOT mixture.

The log shift factors (log a_T) corresponding to the data presented in Figure 98 are shown in Table 28. C* data obtained at 37.8°C was nearly identical to 21°C test data which is reflected in the small shift factor for 37.8°C. It was found that a plot of log shift factor versus temperatures can be fit using a hyperbolic tangent (tanh) function which is plotted in Figure 99. This contradicts the earlier statement that dynamic modulus master curve shift factors can be used. A summary of all dynamic modulus master curve shift parameters can be found in Appendix C.

Table 28 Crack growth rate master curve shift factors (actual data).

Temp °C	log a_T
4.4	-1.3100
10	-0.5607
21	0.0000
37.8	0.0127

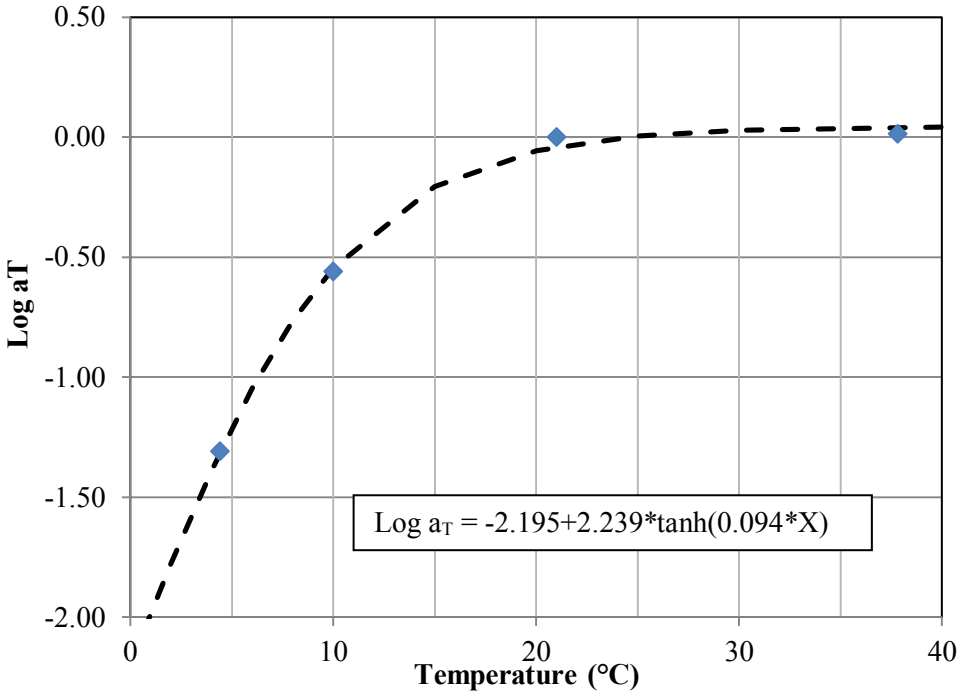

Figure 99 Shift factors as a function of test temperature (actual data).

Figure 100 presents a comparison of the predicted reduced crack growth rate versus measured reduced crack growth rate. These data appear to lie near the line of equality which indicates the power model fit of reduced crack growth rate data is suitable. Next, predicted reduced crack growth rate data was converted to actual crack growth rate data and plotted against measured crack growth rate data in Figure 101. Data for 10°C, 21°C and 37.8°C follows the line of equality nicely. However, it appears the power model tends to overestimate the predicted crack growth rate data at a test temperature of 4.4°C.

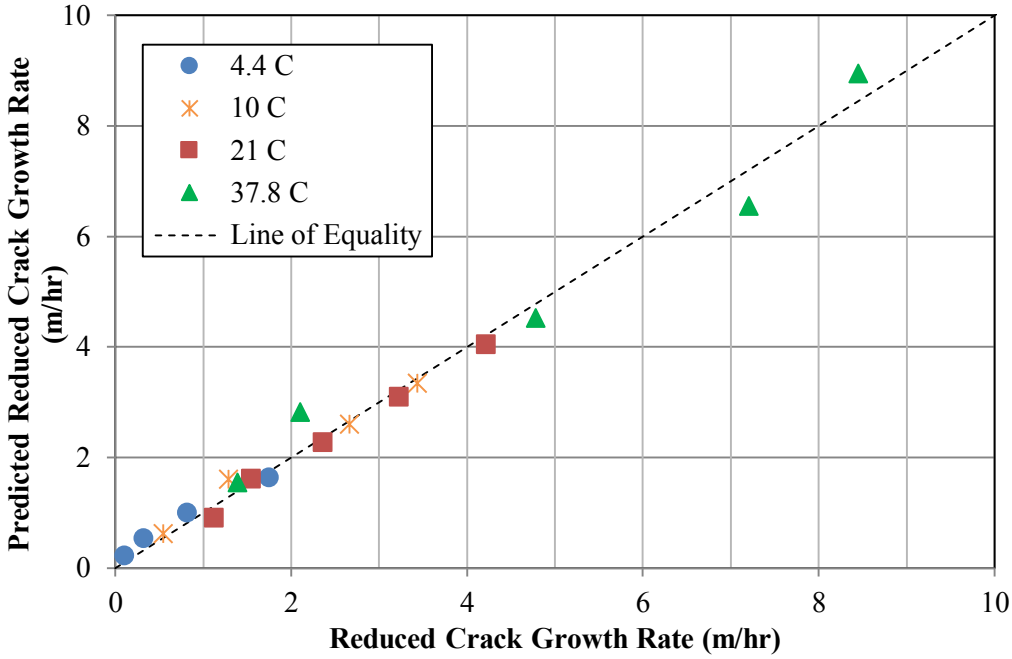

Figure 100 Predicted versus measured reduced crack growth rate.

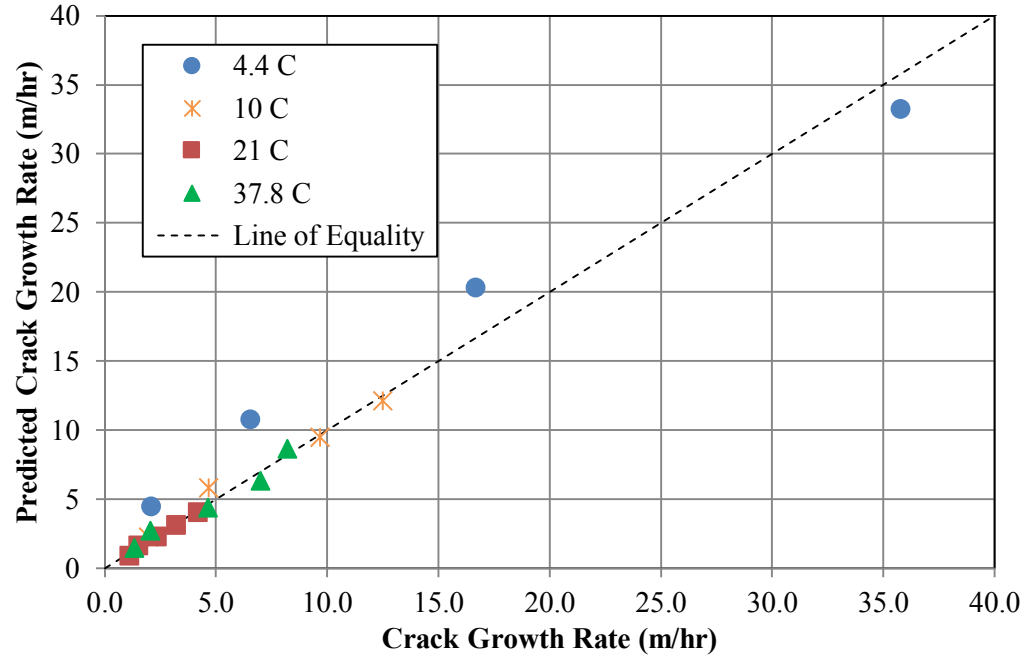

Figure 101 Predicted versus measured crack growth rate.

6.2.2 Master Curve using Log Transformed Data

In order to improve the predication of actual crack growth from reduced crack growth rate master curve data, log transformed data were considered. Using a reference temperature of 21°C, crack growth rate data were shifted and fit with a linear model presented in Equation 6.3. The solver function in Microsoft Excel 2010 was used to estimate the parameters (a, b) by minimizing the squared error between actual and predicted reduced crack growth rates.

$$\log \dot{a}_{\xi} = \log a + b * \log(C^{*}) \qquad \textbf{6.3}$$

Where:

a_{ξ} = reduced crack growth rate,

C* = power release rate parameter (MJ/m^2-hr), and

a, b = regression parameters.

Figure 102 presents the results of the log transformed crack growth rate master curve fitted using a linear function. The reduced crack growth rate data was vertically and the corresponding fit of the data is very good with adjusted R^2 value of 0.95 and S_e/S_y of 0.219. These values indicate excellent model accuracy according to the categories adopted and described in the NCHRP 465 report (Witczak et al, 2002).

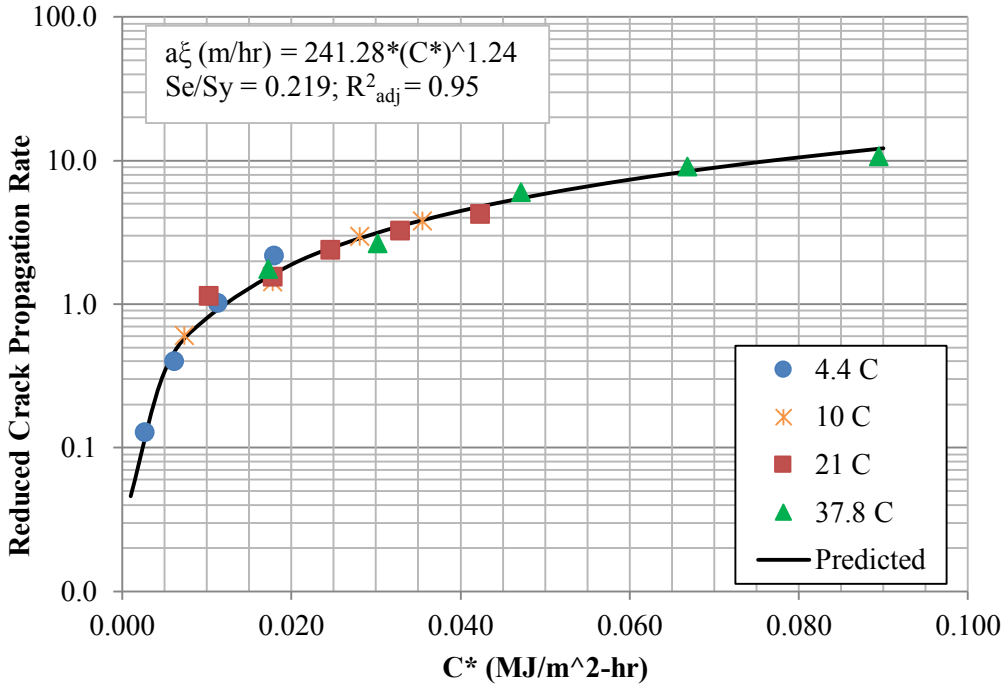

Figure 102 Crack growth rate master curve for ADOT mixture (log reduced data).

The log shift factors (log a_T) corresponding to the data presented in Figure 102 are shown in Table 29. It appears that the prediction better encompasses the 4.4°C data. Again, it was found that a plot of log shift factor versus temperatures can be fit using a hyperbolic tangent (tanh) function which is plotted in Figure 103.

Table 29 Crack growth rate master curve shift factors (log reduced data).

Temp °C	log aT
4.4	-1.2188
10	-0.5144
21	0.0000
37.8	0.1152

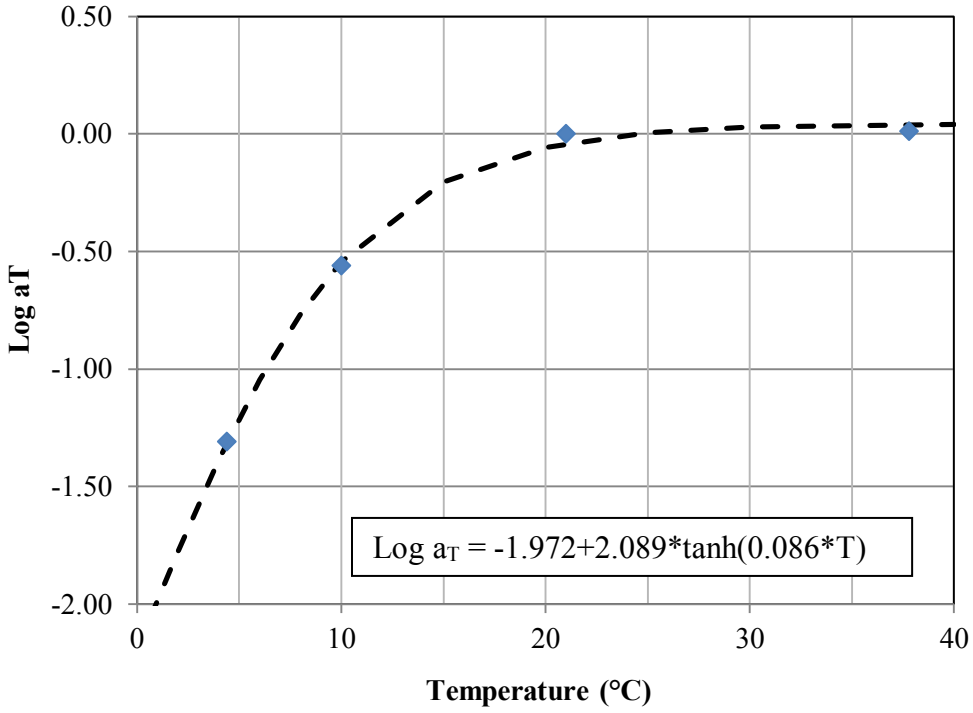

Figure 103 Shift factors as a function of test temperature.

Figure 104 presents a comparison of the predicted crack growth rate versus measured reduced crack growth rate. These data appear to lie near the line of equality which indicates the linear fit of log reduced crack growth rate data is suitable. Next, predicted reduced crack growth rate data was converted to actual crack growth rate data and plotted against measured crack growth rate data in Figure 105. Data for all temperatures follow the line of equality nicely except for the largest crack growth rate at a temperature of 4.4°C.

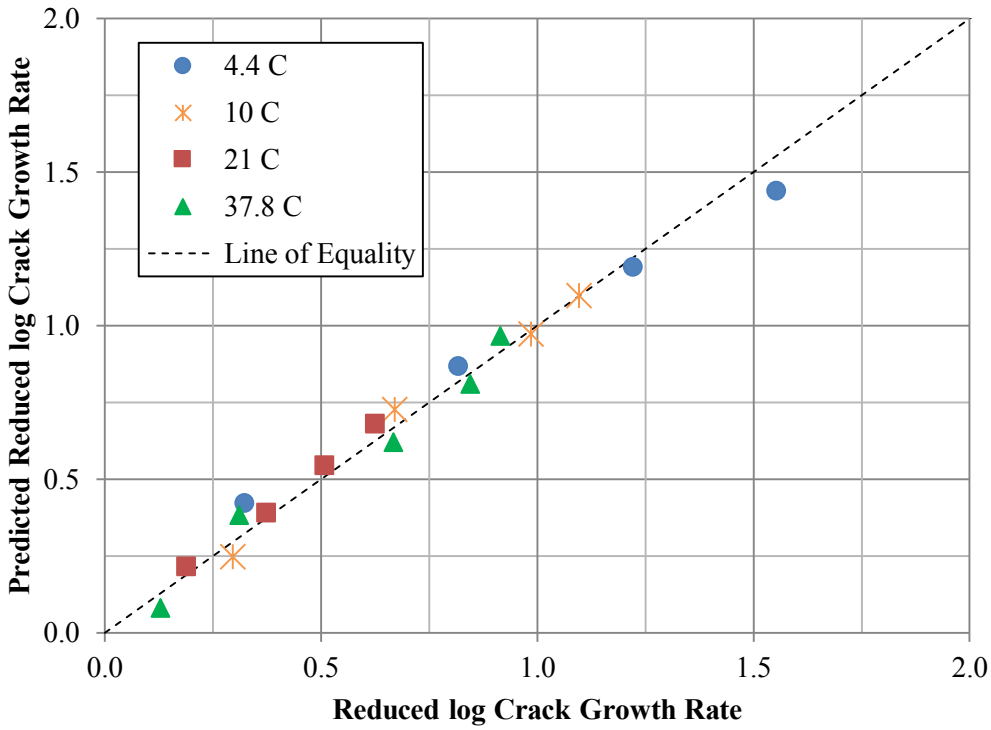

Figure 104 Predicted versus measured reduced log crack growth rate.

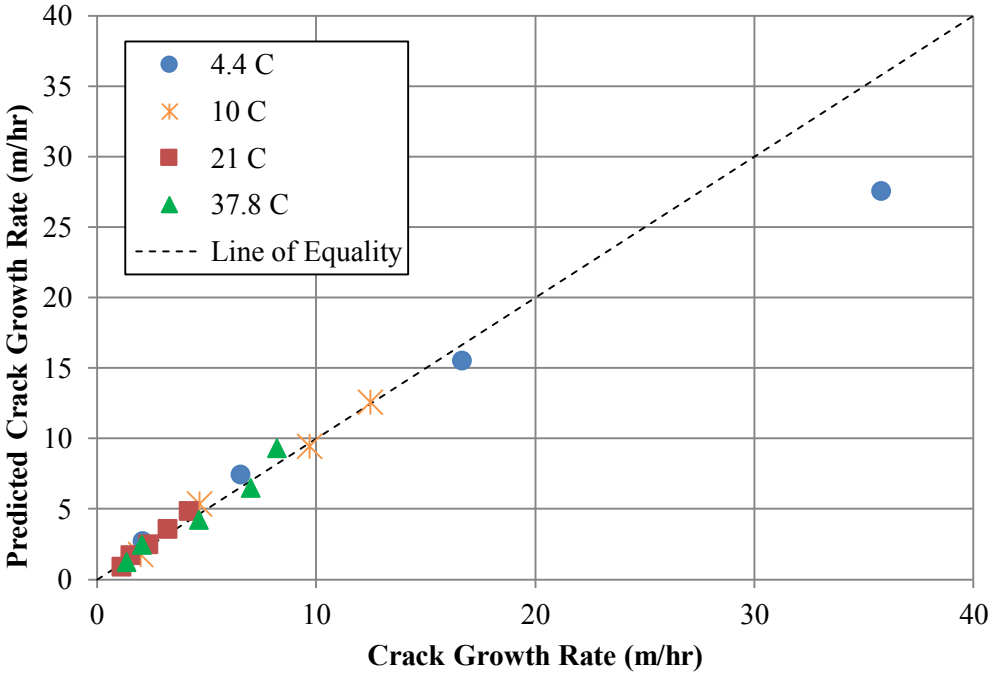

Figure 105 Predicted versus measured crack growth rate.

6.3 Summary

This chapter described the construction of a reduced crack growth rate master curve using C* and crack growth rate data obtained from the C* Fracture Test for the ADOT mixture. Based on the results described herein, the concept of a reduced crack growth rate master curve is feasible. For comparison, reduced crack growth rate data were fitted using a power function and log transformed data were fit using a linear function. Both methods gave excellent adjusted R^2-values and S_e/S_y values, however; the linear fit of log transformed data method provided better prediction of measured crack growth rate data with an R^2_{adj}-value of 0.95 and S_e/S_y equal to 0.219.

Plots of log shift factor versus temperature take the form of a hyperbolic tangent (tanh) function since minimal shifting is required from 37.8°C to the reference temperature of 21°C. This is rational since, at 37.8°C, no significant increase in crack growth rate is observed for an increase in C* when compare to data at 21 °C. At higher temperatures, the effect of energy release on crack growth rate diminishes as creep deformation becomes a more significant factor. This corresponds with a discussion provided by Saxena (1980) when conducting C* tests on metals at high temperatures. For the same displacement rate, crack length and specimen size, creep deformation rate will be greater for a sample tested at a higher temperature. Thus, in order to maintain the same displacement rate, the crack growth rate must be lower.

Also, it appears that the shift factors do not correspond with the dynamic modulus master curve shift factors used in the process described by Seo et al (2004). The crack growth rate master curve shift factors do not follow the typical polynomial trend

observed in plots of dynamic modulus master curve (log) shift factors and test temperature.

Development of the crack growth rate master curve can be beneficial to predict crack propagation in asphalt concrete as a function of pavement temperature and C* values. In the future, a crack growth rate master curve can be incorporated into pavement design software such as Pavement ME to evaluate cracking. More discussion on this concept is presented in a later Chapter. It is recommended that master curves should be developed for additional asphalt concrete mixtures to validate this concept.

Chapter 7

7 DEVELOPMENT OF ASU C* DATABASE

7.1 Background

C* line integral fracture testing was initially carried out at Arizona State University (ASU) in 2007 and 2009 on dense graded (Evergreen Drive) and gap-graded mixtures (Swedish Stockholm), respectively. In both projects, the intent of C* testing was to evaluate crack resistance of the modified mixtures compared to the control or unmodified mixtures. However, these tests were carried out prior to this dissertation reserach, which improved upon the existing C* Line Integral Test.

After C* Fracture Test modifications recommended in this dissertation, several additional field mixtures were analyzed and presented in this chapter to develop an ASU CFT database. For the original two mixtures, (Evergreen Drive and Swedish Stockholm) data were re-analyzed using the recommended data analysis procedure and included in this database. Four additional mixtures were subjected to the CFT and included in this database in addition to the ADOT mixture discussed in Chapter 4. These four additional mixtures, summarized in Table 30, were obtained from field construction projects in Pennsylvania (PA).

Table 30 Summary of field produced mixtures tested.

Name	Binder	Gradation	Modification
PA Cranberry Twp.	PG 64-22	Dense	None
PA Cranberry Twp.	PG 64-22	Dense	Fiber – 1lb/ton
PennDOT I-78	PG 76-22	Dense	Evotherm
PennDOT I-78 AR	PG 64-22 AR	Gap	Evotherm + Crumb Rubber

7.2 Mixture Characterization

Dynamic modulus testing was conducted on all four mixtures tested in this project in order to provide data for future Pavement ME evaluation of the mixture performance and to be used to investigate any potential relationships between dynamic modulus master curve parameters and the fracture parameters obtained from the CFT. Testing on mixtures presented in Table 30 was carried out according to AASHTO TP 62-07 using IPC UTM-25 test equipment. Tests were conducted at five temperatures (-10, 4.4, 21, 37.8 and 54.4°C) and six frequencies at each temperature (25, 10, 5, 1, 0.5 and 0.1 Hz). Test results and data are presented in Appendix C. In addition, indirect tensile strength tests were conducted according to ASTM D6931-07 and are also included in Appendix C.

7.3 C* Fracture Test Data Evaluation

Evaluation of C*Fracture Test (CFT) data was accomplished using the graphical method presented by Landes and Begley (1976) including modifications recommended in previous chapters. The following sections present the C* analysis and discussion of crack resistance of several field mixtures analyzed as part of this research study.

7.3.1 Evergreen Drive Mixtures

The Evergreen Drive project involved a dense graded mixture which was placed on Evergreen Drive in Tempe, Arizona. The field test section consisted of a control mixture and mixtures modified with different dosages of a blend of polypropylene and aramid fibers. The base binder was PG 70-10 and the target air void level in the field was 7%. Table 31 and Table 32 show a summary of the mixture properties and gradation. The fiber blend was provided by the FORTA Corporation and was added at dosages of

one pound of fibers per ton on asphalt (1lb/ton) and two pounds of fibers per ton of asphalt (2 lb/ton).

Table 31 Evergreen Drive mixture properties.

Mix	Binder Content (%)	Air Voids (%)	G_{mm}
C-3/4 Control	5	7	2.428
C-3/4 1 lb/ton	5	7	2.458
C-3/4 2 lb/ton	5	7	2.471

Table 32 Evergreen Drive gradation.

Sieve Size (US)	Percent Passing
	C-3/4 Mix
1	100
0.75	95
0.5	85
0.375	75
No. 4	58
No. 8	44
No. 30	24
No. 200	4

Figure 106 Fiber blend incorporated into the Evergreen Drive mixture (Kaloush et al, 2008).

The CFT was performed in 2007 on the control, 1 lb/ton and 2 lb/ton mixtures using IPC UTM-25 test equipment. It is important to note that this testing was carried out prior to modifications recommended in this project. Data were re-analyzed using the recommended analysis method for inclusion in this ASU database. All testing was carried out at 21°C and crack length was monitored both visually and with video equipment. Figure 107 presents the U* versus displacement rate data which shows a good linear trends between energy release rate and crack length. Table 33 presents a tabulation of Evergreen Drive mixture C*-values and crack growth rates as a function of mixture type and displacement rates.

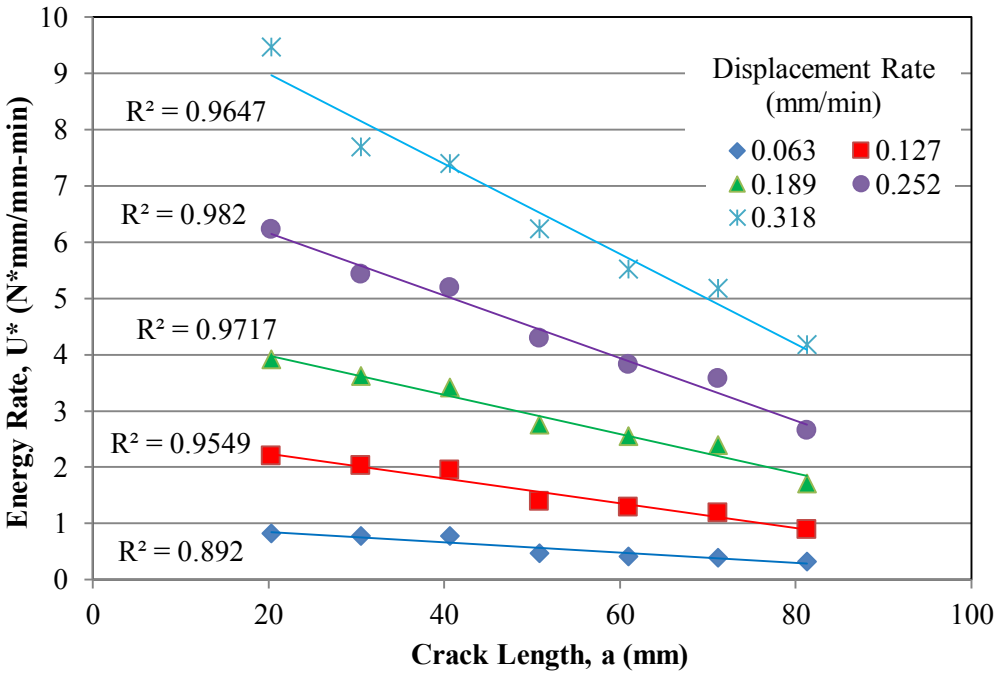

Figure 107 Example U*-crack length relationship for Evergreen Drive control mixture.

Table 33 C* and crack growth data for Evergreen Drive mixtures.

Mixture	Displacement Rate (mm/min)	Crack Growth Rate (m/hr)	C* MJ/m^2-hr
Control	0.063	0.76	5.56E-04
	0.127	1.85	1.32E-03
	0.189	4.73	2.10E-03
	0.252	6.48	3.34E-03
	0.318	4.40	4.81E-03
1 lb/ton	0.063	0.18	8.22E-04
	0.126	0.45	2.60E-03
	0.189	1.19	5.63E-03
	0.252	4.32	9.67E-03
	0.318	6.38	1.33E-02
2 lb/ton	0.126	1.79	6.18E-03
	0.189	1.18	1.11E-02
	0.252	12.80	1.74E-02
	0.318	18.47	2.47E-02

From Table 33 it is evident that C* increases and crack growth rates tend to increase as a function of higher displacement rates. These trends are reasonable given the fact that more power is input into the specimen at higher loading rates and must be released through cracking or plastic deformation. Thus the rate of energy release will be greater and lead to a higher crack propagation rate.

Figure 108 and Figure 109 show the C*-Δ and a*-Δ relationships, respectively. C*-Δ relationships for the control, 1 lb/ton and 2 lb/ton mixtures can be modeled using a power function with excellent R^2-values of 0.99. The 2 lb/ton mixture exhibited the highest energy release followed by the 1 lb/ton and control mixtures. This ranking appears logical since the addition of fiber to the mixture adds tensile strength and thus more power input is required to propagate a crack through the mixture.

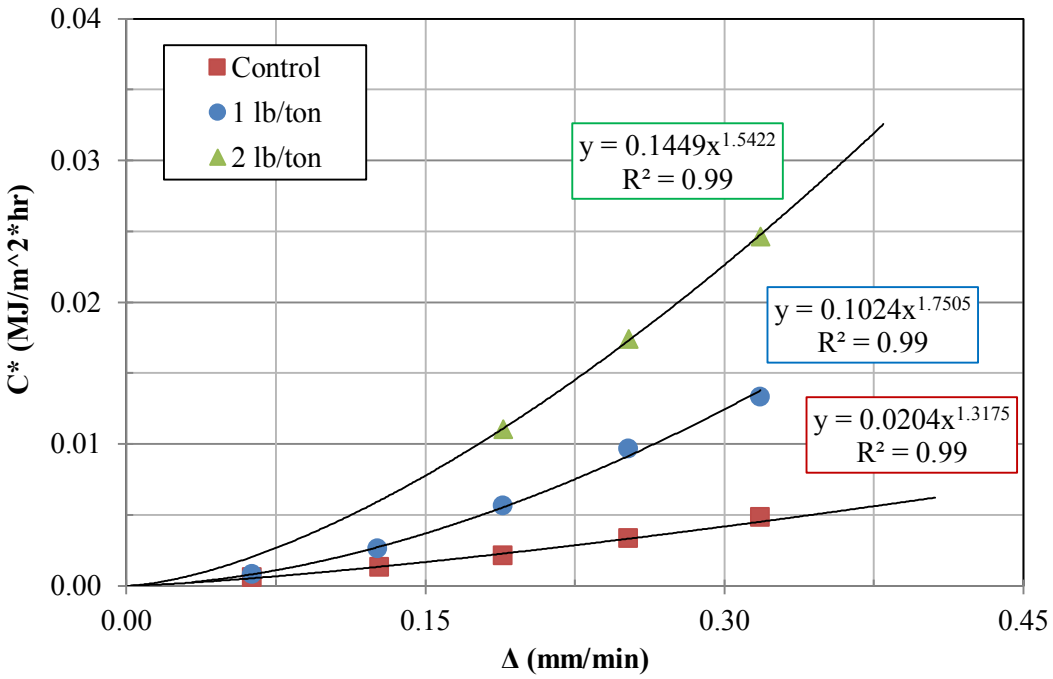

Figure 108 C*-Δ relationship for Evergreen Drive mixtures.

The a*-Δ relationships for the three mixture can also be modeled using a power model with R^2-values ranging between 0.71 and 0.97. The control mixture shows the least resistance to cracking followed by the 2 lb/ton and 1 lb/ton mixtures. A plot of crack growth rates graphically exhibits the variability in the data for the control and fiber reinforced mixtures. Thus, ranking of mixtures according to crack growth rates is difficult for the Evergreen Drive mixtures.

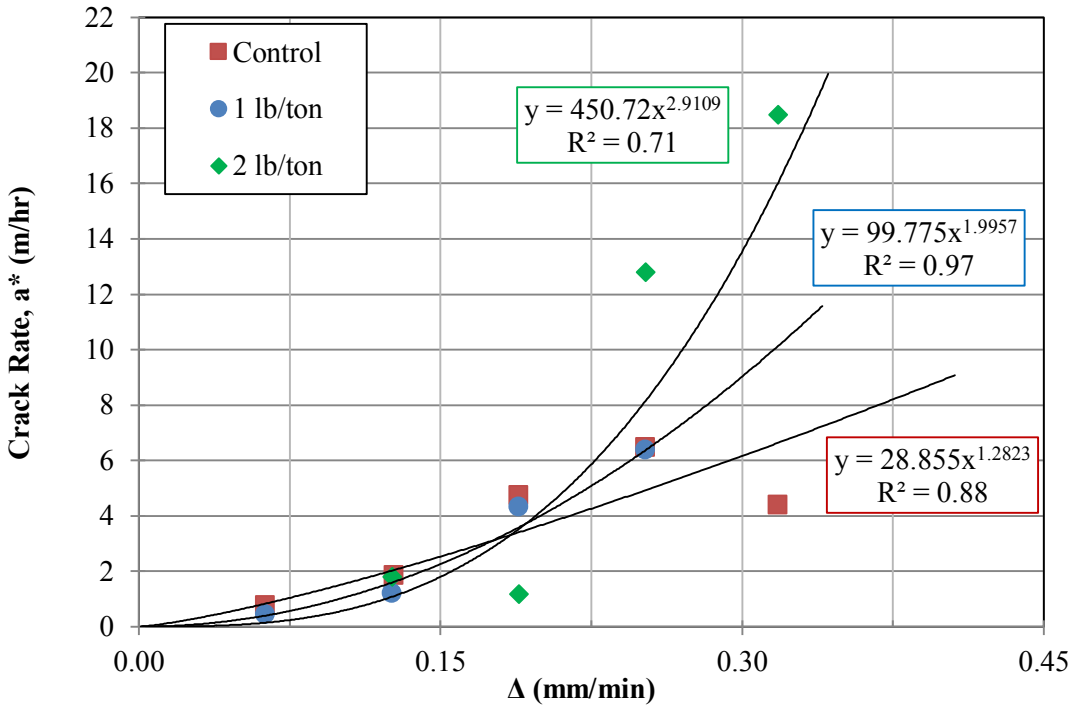

Figure 109 a*-Δ relationship for Evergreen Drive mixtures.

Finally, the crack growth rate was plotted as a function of C* for each mixture and is presented in Figure 110 and modeled using a power function. The control mixture shows the least resistance to crack propagation indicated by the greater y-intercept value. The slopes of the trends are essentially the same which is logical since the mixtures have the same gradation, binder content and air voids. Thus, a given C* value will result in a higher crack propagation rate in the control mixture compared to the fiber reinforced mixtures. This ranking matches a field survey of field sections conducted by Kaloush et al (2010) approximately two years after construction. In this field survey, it was observed that the control mixtures exhibited approximately three times more low-severity cracks compared to the fiber reinforced mixtures. Also, given the trends in Figure 110, a fiber dosage of 2 lb/ton does not appear to provide any additional benefit to crack resistance as compared to the 1 lb/ton fiber dosage rate.

The 1 lb/ton mixture showed the best correlation (R^2=0.96) followed by the control (R^2=0.84) and 2 lb/ton (R^2=0.73) mixtures. It is important to note that only one replicate was tested at each loading rate which in itself could contribute to the variability associated with the control and 2 lb/ton mixtures.

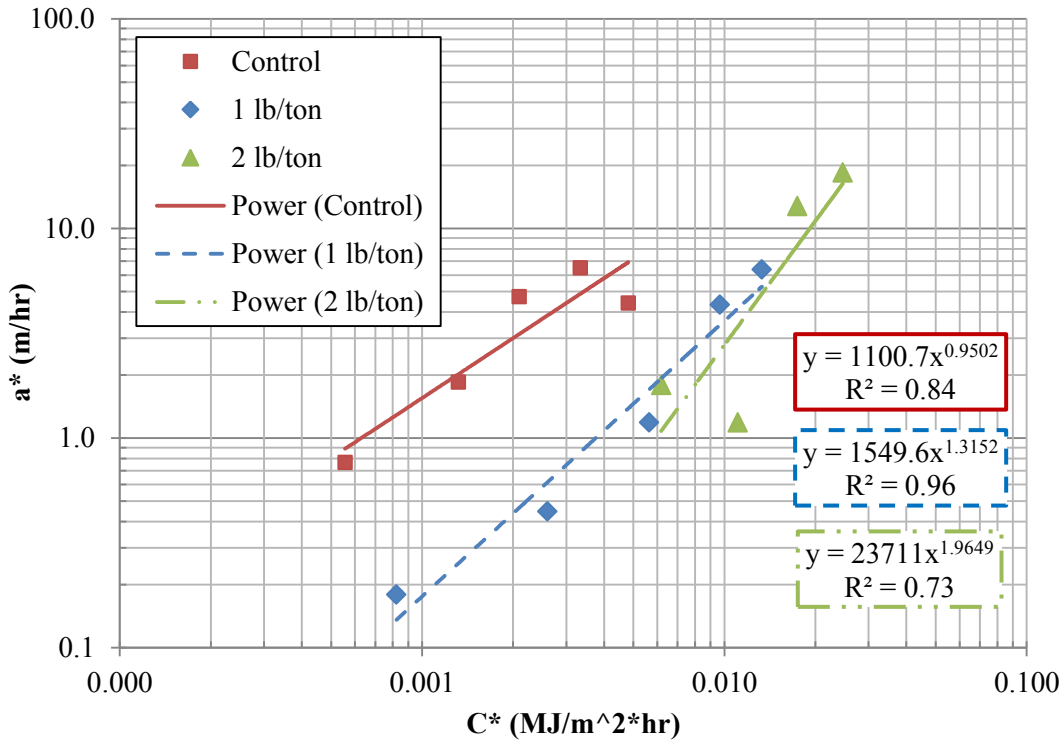

Figure 110 a*- C* relationship for Evergreen Drive mixtures

Statistical comparison of the a*-C* trends were carried out using the technique described in Section 4.9 which the exception that the "Size" variable was replaced with mixture "Type". The hypothesis test for the comparison was as follows and statistical analysis was performed using level of significance of 0.05:

H_o: Both γ and δ = 0

H_a: Not both γ and δ = 0

Table 34 present the results of the statistical comparisons which indicate the mixture modified with a dosage rate of 1 lb/ton of fibers was statistically different than the control mixture with no fibers. All other comparisons indicate no statistical difference at a level of significance of 0.05. However, it is evident in Figure 110 that the mixture modified with a 2 lb/ton dosage rate appears different from the control mixture. Failure to reject the null hypothesis in this case may be due to the variability in the a*-C* trend for the mixture modified with a 2 lb/ton dosage rate of fibers.

Table 34 Statistical comparison of Evergreen Drive mixture performance.

Comparison (size, mm)	Parameter	p-value	$\alpha = 0.05$ Decision
Control vs. 1 lb/ton Fibers	γ	<0.001	***Reject H_o***
	δ	0.247	
Control vs. 2 lb/ton Fibers	γ	0.056	Accept H_o
	δ	0.220	
1 lb/ton vs. 2 lb/ton Fibers	γ	0.686	Accept H_o
	δ	0.373	

A pavement condition survey, conducted approximately two years after construction, found that the Evergreen Drive control section had approximately three times the amount of low severity cracking as the fiber modified sections (Kaloush et al, 2010). Thus, the CFT was able to capture differences in crack resistance in the laboratory which corresponded well to field performance.

7.3.2 Swedish Stockholm Mixtures

The Swedish project consisted of a gap-graded mixture placed on the E18 highway near Stockholm, Sweden. Field test sections included unmodified reference, polymer modified and asphalt-rubber mixtures. This was a Marshall mixture design with

a target air void level of approximately 3%. The base binder was Pen 70/100 and polymer and rubber modifications were made to this binder. Table 35 and Table 36 present the mixture properties and gradation of the Swedish mixtures included in C* testing (Kaloush et al, 2010b).

Table 35 Swedish mixture properties.

Mix	Binder Content (%)	Air Voids (%)	G_{mm}
Reference ABS 16 70/100	5.9	2.6	2.464
Polymer ABS 16 Nypol 50/100-75	5.9	2.6	2.456
Rubber GAP 16	8.7	2.4	2.359

Table 36 Swedish gradation.

Sieve Size (mm)	Percent Passing		
	Reference	Polymer	Rubber
22.4	100	100	100
16	98	98	98
11.2	65	65	68
8	38	38	44
4	23	23	24
2	21	21	22
0.063	10.5	10.5	7.5

C* Fracture Tests were carried out in 2009 on the Swedish reference, polymer modified and asphalt-rubber mixtures using IPC UTM-25 test equipment. It is important to note that this testing was carried out prior to modifications recommended in this project. Data were re-analyzed using the recommended analysis method for inclusion in this ASU database. All testing was carried out at 4°C and crack length was monitored visually. Figure 111 shows and example of U* versus crack length data for the Swedish

reference mixture. These data are modeled very well using a linear fit with R^2-values greater than 0.94.

Table 37 presents a tabulation of Swedish mixture C*-values and crack growth rates as a function of mixture type and displacement rates. C* values increase with higher loading rates which is expected. Crack growth rates also tend to increase but variability is observed due to crack tortuosity and specimen deformation.

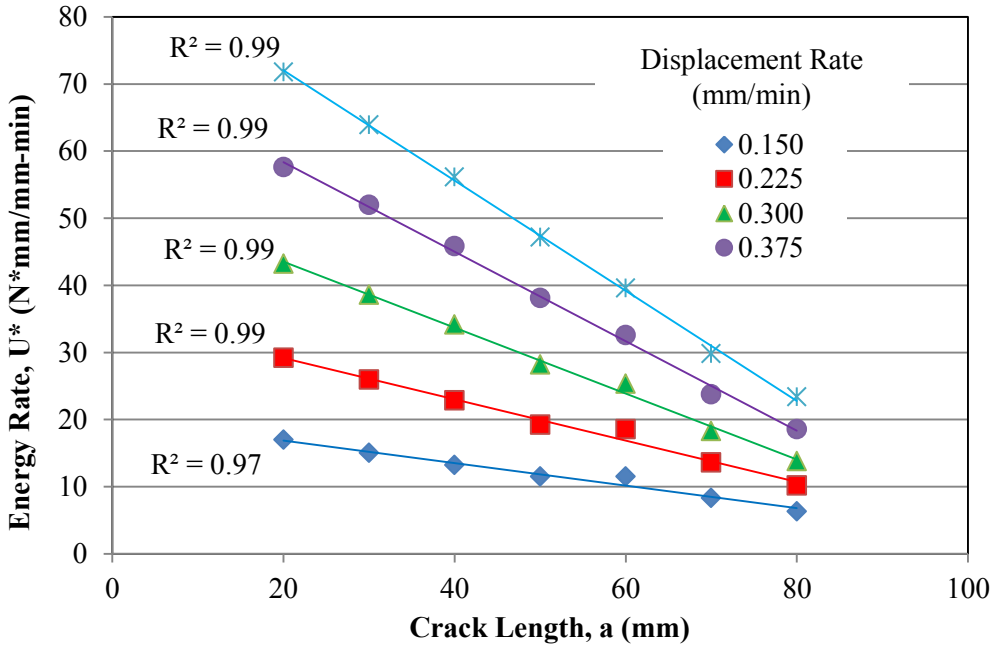

Figure 111 Example U*-crack length relationship for Swedish reference mixture.

Table 37 C* and crack growth data for Swedish mixtures.

Mixture	Displacement Rate (mm/min)	Crack Growth Rate (m/hr)	C* MJ/m^2-hr
Reference	0.15	0.60	1.01E-02
	0.225	0.61	1.84E-02
	0.3	0.83	2.95E-02
	0.375	1.05	4.00E-02
	0.45	3.85	4.93E-02
Polymer	0.15	1.04	1.72E-02
	0.225	1.32	2.85E-02
	0.3	2.71	4.22E-02
	0.375	1.89	5.74E-02
	0.45	5.33	7.13E-02
Rubber	0.15	0.37	1.17E-02
	0.225	0.94	1.87E-02
	0.3	0.53	2.67E-02
	0.375	1.02	3.56E-02
	0.45	1.25	4.54E-02

Figure 112 and Figure 113 show the C*-Δ and a*-Δ relationships, respectively. C*-Δ relationships for the three Swedish mixtures can be modeled using a power function with excellent R^2-values of 0.99. The polymer-modified mixture showed the highest energy release followed by the control and rubber-modified mixtures. This ranking appears logical since the addition of polymer adds stiffness to the mixture; resulting in more energy released in the form of cracking. Rubber-modification results in increased elasticity and thus less energy release is observed through crack extension.

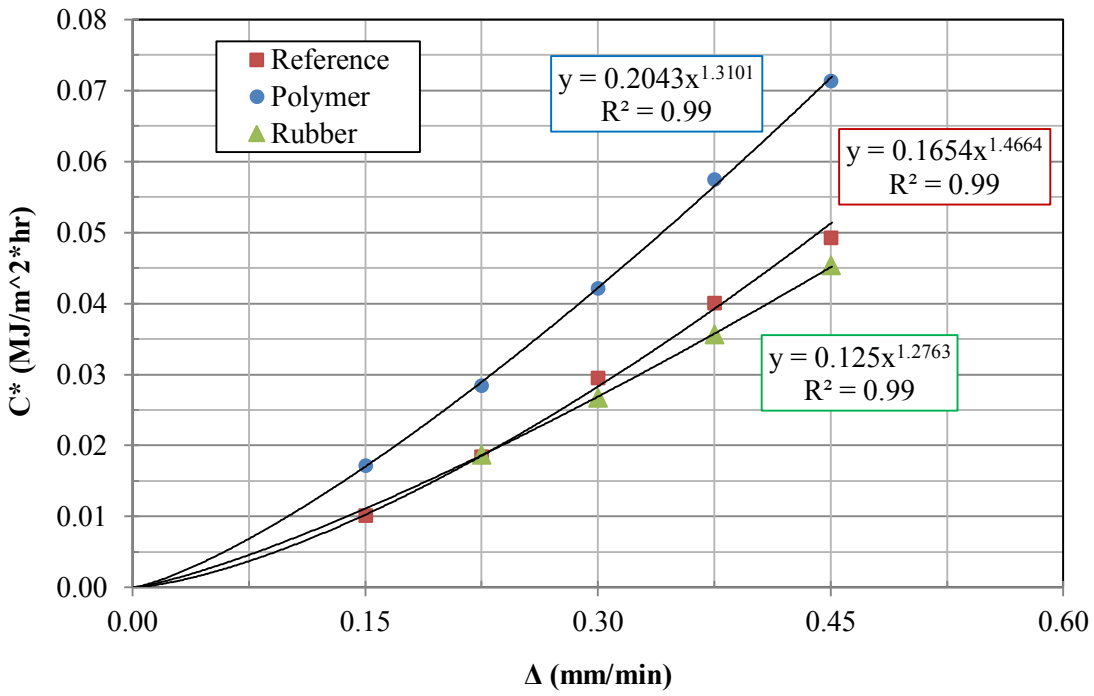

Figure 112 C*-Δ relationship for Swedish mixtures.

The a*-Δ relationships for the Swedish mixtures can also be modeled using a power model with R^2-values ranging between 0.63 and 0.66. The polymer-modified mixture shows the highest crack propagation rate followed by reference and asphalt-rubber mixtures. This ranking appears logical since the stiffer polymer mixture provide little resistance to crack growth whereas the addition of rubber particles requires the crack to follow a very tortuous path. Also, reduced crack growth rate observed in the rubber mixture may be the result of the more elastic properties of the rubber mixture.

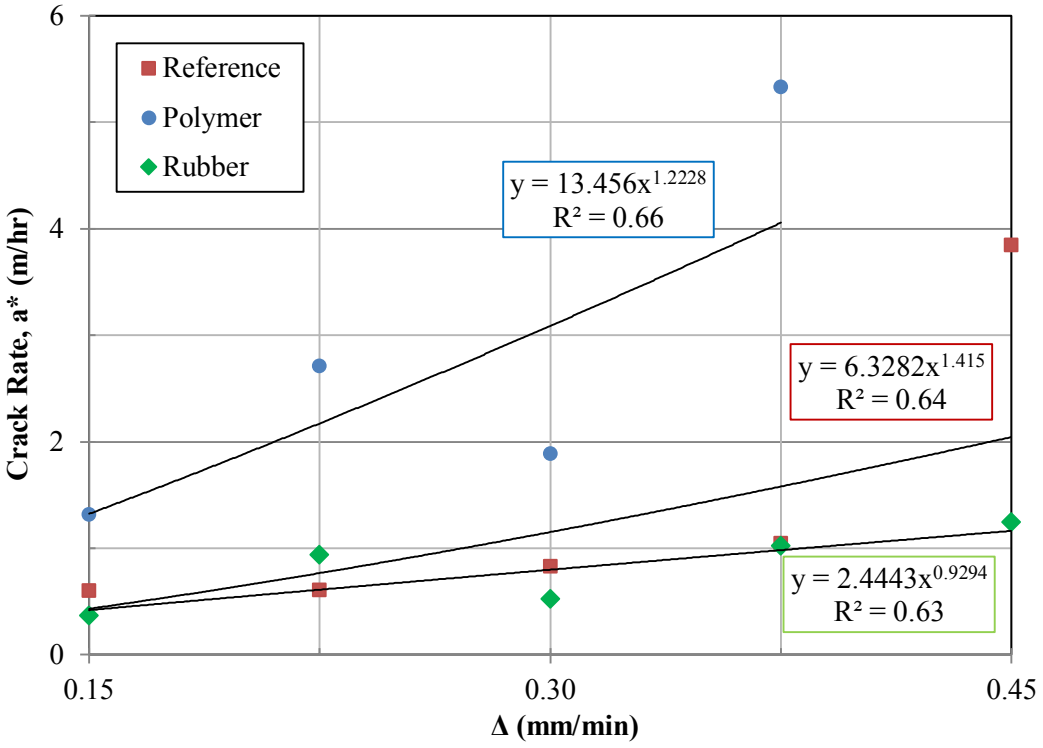

Figure 113 a*-Δ relationship for Swedish mixtures.

Finally, the crack growth rate was plotted as a function of C* for each mixture and is presented in Figure 114 and modeled using a power function. The polymer-modified mixture shows the least resistance to crack propagation indicated by the greater slope value. Thus, for the same C* values, a higher crack propagation rate will be observed in the polymer-modified mixture compared to the reference and asphalt-rubber mixtures. The asphalt-rubber mixture appears to have slightly better crack resistance than the reference mixture but given the variability in the test data, the mixtures may actually have similar resistance to crack propagation. Also, large variability in test results may be due to the fact that testing was performed prior to development and refinement of the C* Fracture Test procedure.

In addition, high variability within each mixture may have been the result of only one specimen tested at each loading rate or the higher air voids of the Swedish mixture specimens.

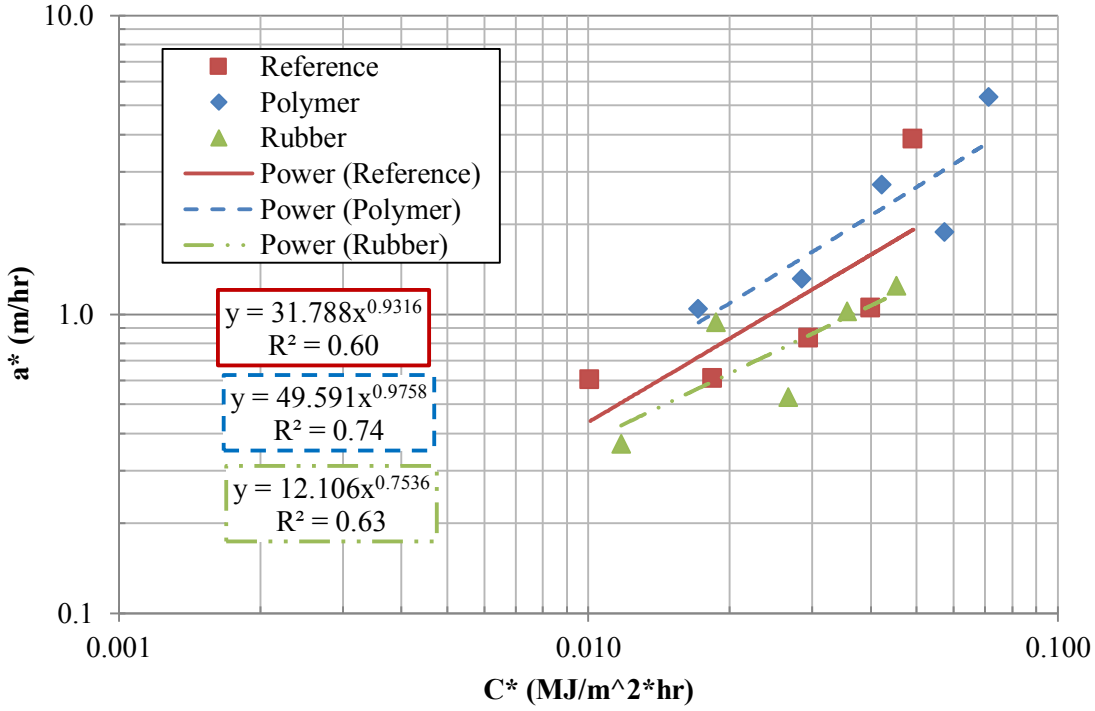

Figure 114 a*-C* relationship for Swedish mixtures.

Statistical comparison of the a*-C* trends were carried out using the technique described in Section 4.9 which the exception that the "Size" variable was replaced with mixture "Type". The hypothesis test for the comparison was as follows and statistical analysis was performed using level of significance of 0.05:

H_o: Both γ and δ = 0

H_a: Not both γ and δ = 0

Table 38 present the results of the statistical comparisons which indicate the polymer modified mixture was statistically different than the asphalt rubber mixture. All

other comparisons indicate no statistical difference at a level of significance of 0.05. Failure to reject the null hypothesis in this case may be due to the variability in the a*-C* trends for the reference and rubber modified mixtures.

Table 38 Statistical comparison of Swedish mixture performance.

Comparison (size, mm)	Parameter	p-value	α = 0.05 Decision
Reference vs. Polymer	γ	0.399	Accept H_o
	δ	0.940	
Reference vs. Rubber	γ	0.337	Accept H_o
	δ	0.767	
Polymer vs. Rubber	γ	0.046	***Reject H_o***
	δ	0.653	

7.3.3 PA Cranberry Township Mixtures

The Pennsylvania (PA) Cranberry Township mixtures consisted of a dense-graded mixture designed for a medium traffic level of 3 to 10 million ESAL's using Marshall mixture design. The base binder was PG64-22 and the asphalt content was 5.9%. Fiber modification at a dosage of 1 lb/ton was added to mixture without modifying the design.

The maximum specific gravity measured in the ASU laboratory was 2.397 and 2.394 for the control and fiber mixtures, respectively and target air voids for specimens were set to 7 ± 0.7%. Table 39 presents the gradation used for both mixtures. It is important to note that this mixture was actually sampled from a different project being constructed from similar mixture at the same asphalt plant.

C* Fracture Tests were carried out on the control and fiber modified mixtures using IPC UTM-100 test equipment at 21°C and 10°C. Figure 115 shows an example of

U* versus crack length data for the control mixture. These data are modeled very well using a linear fit with R^2-values greater than 0.96.

Table 39 Cranberry Township gradation.

Sieve Size (US)	Percent Passing
	Both Mixes
1/2”	100
3/8”	96
No. 4	55
No. 8	38
No. 16	26
No. 30	17
No. 50	9
No. 100	5
No. 200	4.1

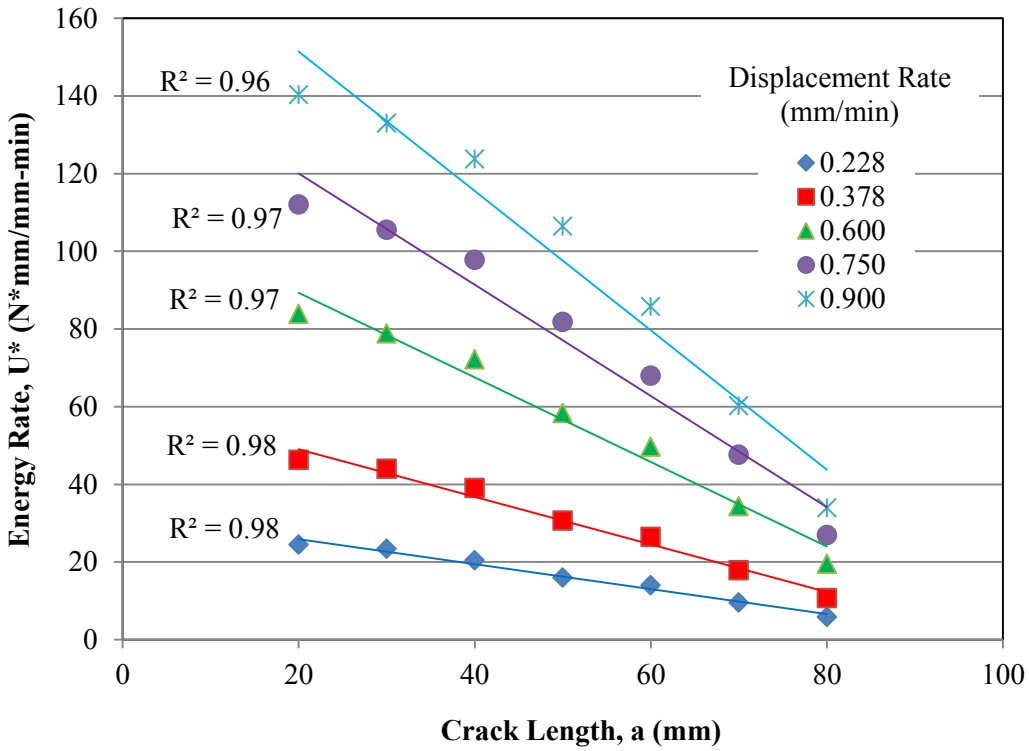

Figure 115 Example U*-crack length relationship for Cranberry Township control mixture (10°C).

Table 40 presents a tabulation of C*-values and crack growth rates as a function of mixture type and displacement rates. C* values increase with higher loading rates which is expected.

Table 40 C* and crack growth data for Cranberry Township mixtures.

Temp. (°C)	Mixture	Displacement Rate (mm/min)	Crack Growth Rate (m/hr)	C* MJ/m^2-hr
10	Control	0.228	0.62	1.926E-02
		0.378	1.03	3.673E-02
		0.600	1.84	6.528E-02
		0.750	2.68	8.592E-02
		0.900	6.42	1.077E-01
	Fiber Modified	0.450	1.04	3.872E-02
		0.600	1.77	5.715E-02
		0.750	2.21	7.647E-02
		0.900	3.44	9.785E-02
		1.200	3.76	1.406E-01
21	Control	0.378	0.54	1.481E-02
		0.450	0.78	1.789E-02
		0.600	1.00	2.498E-02
		0.828	1.61	3.758E-02
	Fiber Modified	0.378	0.55	1.357E-02
		0.600	0.77	2.323E-02
		0.828	1.01	3.552E-02

Figure 116 and Figure 117 show the C*-Δ and a*-Δ relationships, respectively. C*-Δ relationships for the two mixtures at both temperatures can be modeled using a power function with excellent R^2-values of 0.99. The fiber modified mixture exhibits lower energy release followed by the control mixture for both test temperatures. This ranking does not appear logical since the addition of fibers adds stiffness and tensile strength to the mixture; resulting in more energy released in the form of cracking.

Again, it is important to note that the asphalt concrete mixture tested for this project was not sampled from the PA Cranberry Township project rather from mixture prepared for a similar project on a different production day. The effectiveness of fiber in this mixture is questionable because of indication that virgin binder may have been contaminated with polymer and also that fibers were introduced by automatic feeder rather than by whole bags as done in the successful Evergreen Drive project. Observations and CFT results support these suspicions that fiber addition was not effective in this specific mixture.

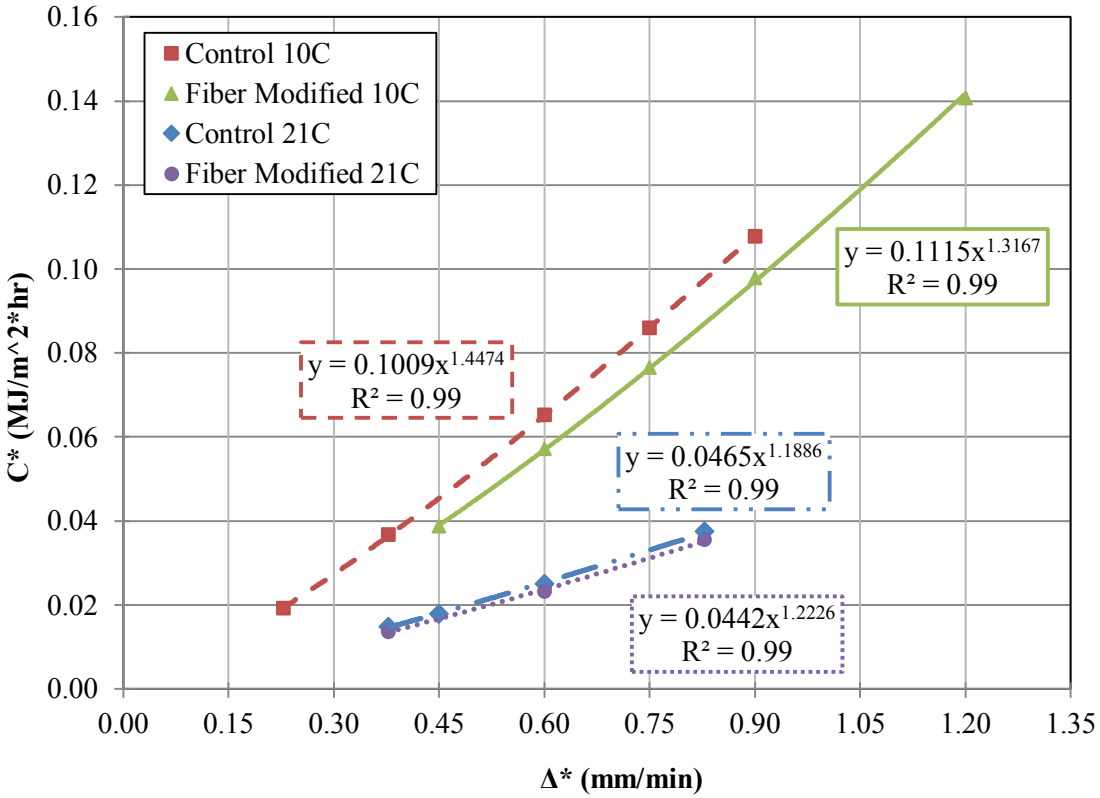

Figure 116 C*-Δ relationship for Cranberry Township mixtures.

The a*-Δ relationships for the mixtures can also be modeled using a power model with R^2-values greater than 0.91. The control mixture shows the highest crack

propagation rate followed by the fiber modified mixture at both test temperatures. This ranking appears logical since the addition of aramid fiber adds resistance to crack propagation.

Finally, the crack growth rate was plotted as a function of C* for each mixture and is presented in Figure 118 and modeled using a power function. From these data, it appears that the mixtures have similar resistance to crack propagation. This finding is interesting as the addition of polypropylene and aramid fibers should provide additional resistance to crack propagation. Again, these results support the fact that fiber addition was not successful in this asphalt concrete mixture as discussed previously.

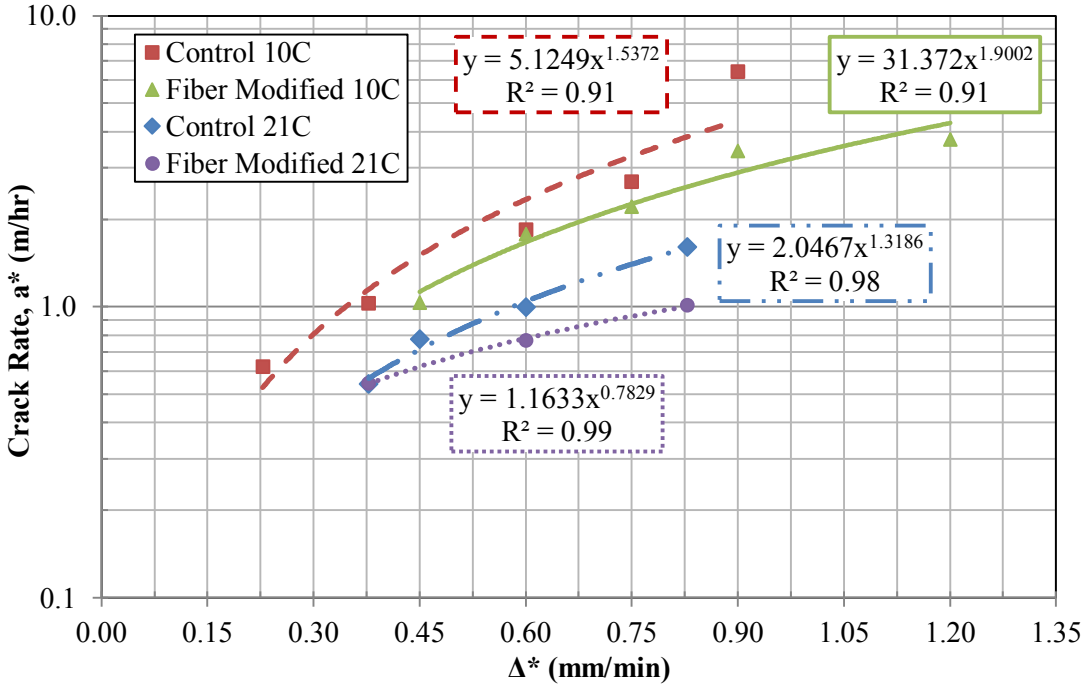

Figure 117 a*-Δ relationship for Cranberry Township mixtures.

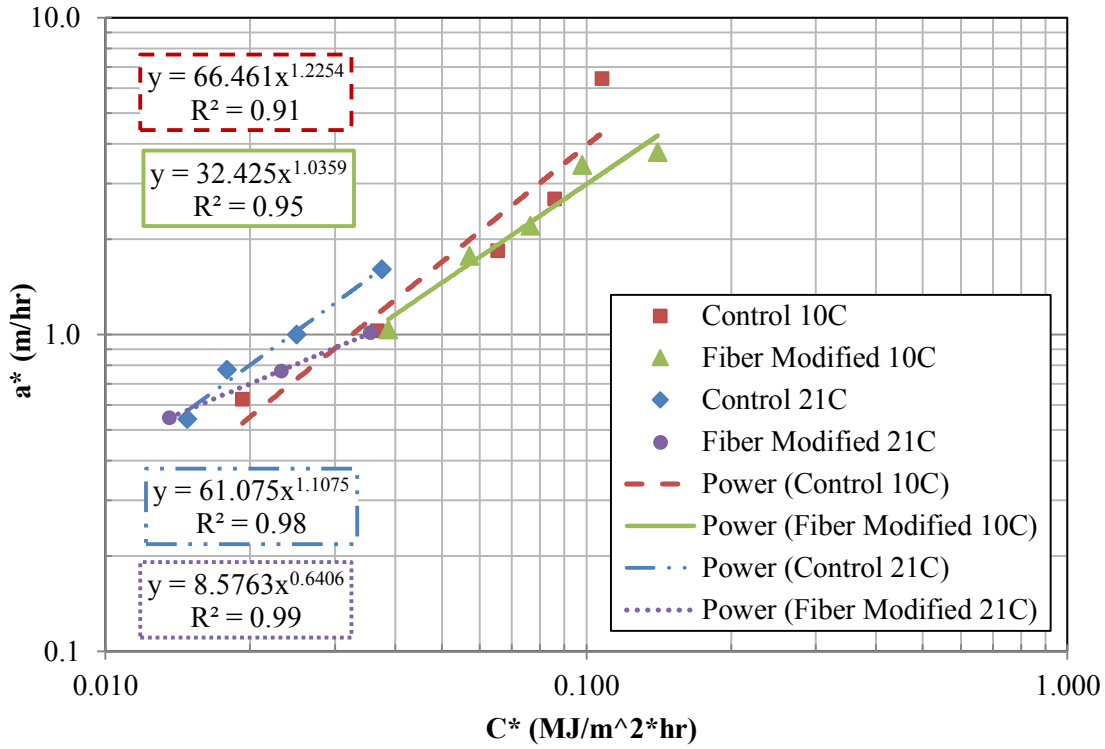

Figure 118 a*-C* relationship for Cranberry Township mixtures.

However, it is expected that the a*-C* relationships at 21°C should be equivalent or shift slightly to the right of the data at colder temperatures where higher crack growth rates are expected. For these mixtures, a test temperature of 21°C may be outside of the practical range of the CFT for the associated mixture stiffness. At this temperature, energy release may be in the form of vertical specimen deformation which may underestimate the C* parameter. Table 41 shows a summary of the dynamic modulus values (0.1 Hz) at each CFT test temperature.

Table 41 |E*| values (0.1 Hz) at CFT test temperature.

Mixture	|E*| 0.1 Hz (MPa)	
	10°C	21°C
Control	6053	2417
Fiber	5955	2278

The dynamic modulus (0.1 Hz) values of the control and fiber modified mixtures are essentially the same at both test temperatures. These data further indicate that fiber modification was not successful. However, the low modulus value at 21°C may cause the unexpected CFT results at this temperature. This concept will be further explored in a subsequent section.

Statistical comparison of the a*-C* trends were carried out using the technique described in Section 4.9 which the exception that the "Size" variable was replaced with mixture "Type". The hypothesis test for the comparison was as follows and statistical analysis was performed using level of significance of 0.05:

H_o: Both γ and $\delta = 0$

H_a: Not both γ and $\delta = 0$

Figure 116 presents the results of the statistical comparisons which indicate no significant statistical difference between a*-C* trends for the control and fiber modified mixtures at 10°C. However, a the control and fiber modified mixtures are statistically different at 21°C

Table 42 Statistical comparison of PA Cranberry Township mixture performance.

Comparison (size, mm)	Temp. °C	Parameter	p-value	$\alpha = 0.05$ Decision
Control vs. Fiber Modified	10	γ	0.248	Accept H_o
		δ	0.550	
Control vs. Fiber Modified	21	γ	0.031	***Reject H_o***
		δ	0.037	

7.3.4 PenDOT I-78 Warm Mix Asphalt Mixtures

The PennDOT I-78 mixtures consisted of two warm-mix asphalt mixtures designed for >30 million ESAL's; a 9.5mm control section (PG76-22) and a 12.5 mm, gap-graded, asphalt-rubber (PG64-22 AR) section. Binders for both mixtures were blended with 0.5% Evotherm. The control mixture targeted 5.7% of PG76-22 whereas the rubber modified mixture targeted 8.1% of PG64-22 binder and contained 18% crumb rubber. Both mixtures were used as wearing courses and placed to a final thickness of 1.5 inches. The in-place air voids of the control and rubber modified mixtures were between 3-5% and 5-7%, respectively.

The maximum specific gravity measured in the ASU laboratory was 2.498 and 2.407 for the control and rubber modified, respectively. A target air void level of 6.5 ± 0.65% set for all specimens tested in the laboratory. Table 43 presents the gradation used for both mixtures.

Table 43 PennDOT I-78 gradations.

Sieve Size (US)	% Passing	
	9.5 mm Wearing	12.5 mm Gap (18% crumb rubber)
3/4"	100	100
1/2"	100	97
3/8"	95	84
No. 4	59	30
No. 8	45	22
No. 16	27	14
No. 30	17	9
No. 50	12	7
No. 100	8	6
No. 200	5.5	5

C* Fracture Tests were carried out on the control and rubber modified mixtures using IPC UTM-100 test equipment at 4.4°C and 10°C. Figure 119 shows an example of

U* versus crack length data for the control mixture. These data are modeled very well using a linear fit with R^2-values of 0.98. Table 44 presents a tabulation of C*-values and crack growth rates as a function of mixture type and displacement rates. C* values increase with higher loading rates which is expected.

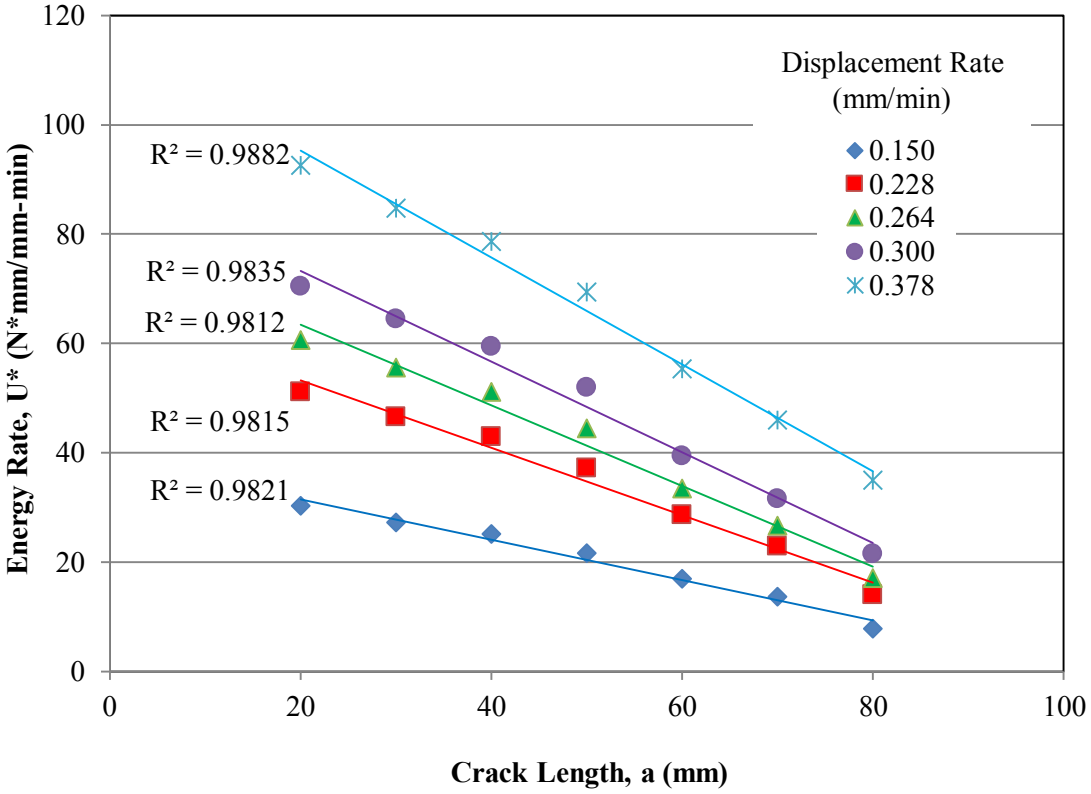

Figure 119 Example U*-crack length relationship for PennDOT I-78 PG76-22 (4.4C)

Table 44 C* and crack growth data for PennDOT I-78 mixtures.

Temp. (°C)	Mixture	Displacement Rate (mm/min)	Crack Growth Rate (m/hr)	C* MJ/m^2-hr
4.4	PG76-22 WMA	0.150	1.13	2.207E-02
		0.228	1.41	3.705E-02
		0.264	4.46	4.420E-02
		0.300	5.62	4.981E-02
		0.378	8.17	5.861E-02
	PG64-22 AR WMA	0.300	0.81	3.282E-02
		0.450	1.18	5.215E-02
		0.600	1.30	7.301E-02
		0.750	1.86	9.537E-02
		0.900	3.62	1.179E-01
10	PG76-22 WMA	0.300	1.26	4.297E-02
		0.450	2.04	6.831E-02
		0.750	3.50	1.179E-01
		1.200	8.00	1.847E-01
	PG64-22 AR WMA	0.600	0.93	4.012E-02
		0.750	2.64	5.230E-02
		0.900	2.39	5.942E-02
		1.050	3.80	6.682E-02
		1.200	3.60	8.051E-02

Figure 120 and Figure 121 show the C*-Δ and a*-Δ relationships, respectively. C*-Δ relationships for the three mixtures can be modeled using a power function with excellent R^2-values of 0.99. The PG64-22AR, rubber modified mixtures have the lowest C*-value trends for both temperatures which is reasonable given the highly elastic behavior of the mixture; less applied load is required during crack propagation. For the PG76-22 mixture, a higher C*-value trend is observed at 4.4°C which indicates that more energy is released through crack propagation; a higher load is required to propagate the crack.

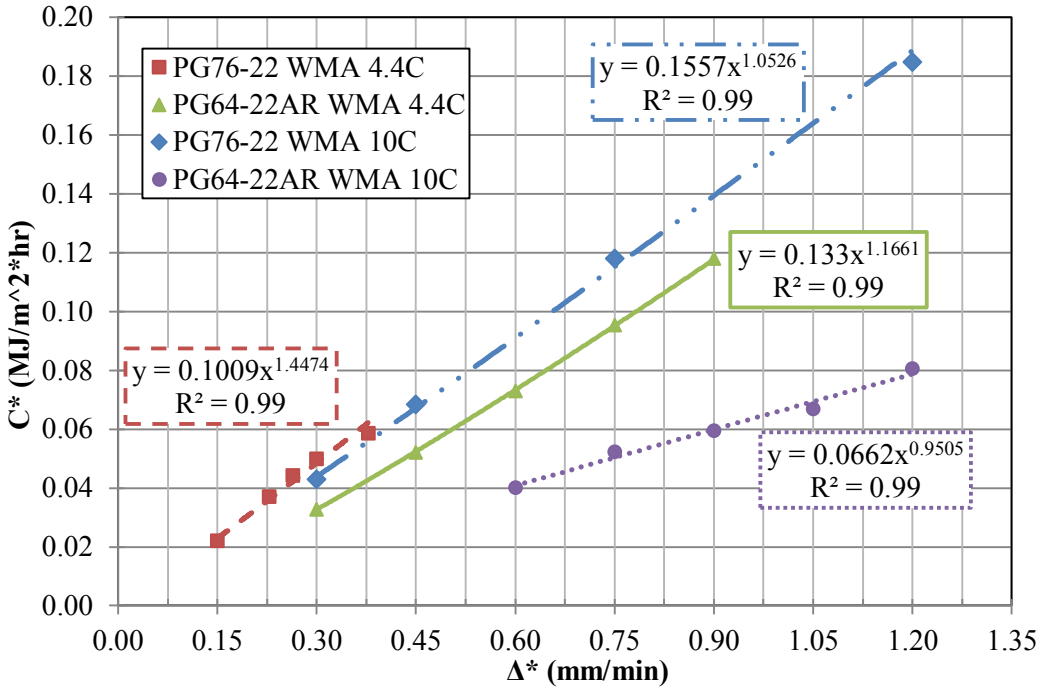

Figure 120 C*-Δ relationship for PennDOT I-78 mixtures.

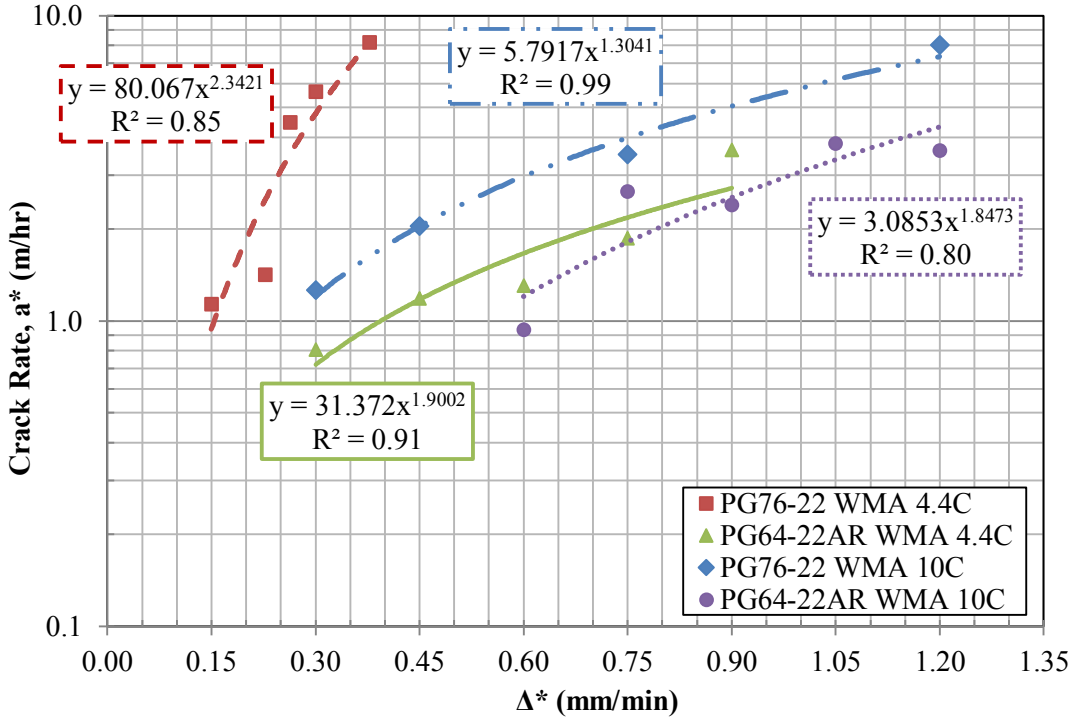

Figure 121 a*-Δ relationship for PennDOT I-78 mixtures

The a*-Δ relationships for the mixtures can also be modeled using a power model with R^2-values greater than 0.80. The PG64-22AR mixture has the highest resistance to crack growth compared to the PG76-22 mixture at all loading rates. The trends appear reasonable for all mixtures in that crack growth rates are higher at 4.4°C than 10°C. This effect is more pronounced in the PG76-22 mixtures than in the PG64-22AR mixture. The crack resistance of the rubber modified mixture appears to be less susceptible to temperature changes which are expected behavior of this type of modified mixture.

Finally, the crack growth rate was plotted as a function of C* for each mixture and is presented in Figure 122 and modeled using a power function. From these data, the PG64-22AR mixture has better resistance to crack propagation than the PG76-22 mixture at 4.4°C; however, the trend is opposite at 10°C.

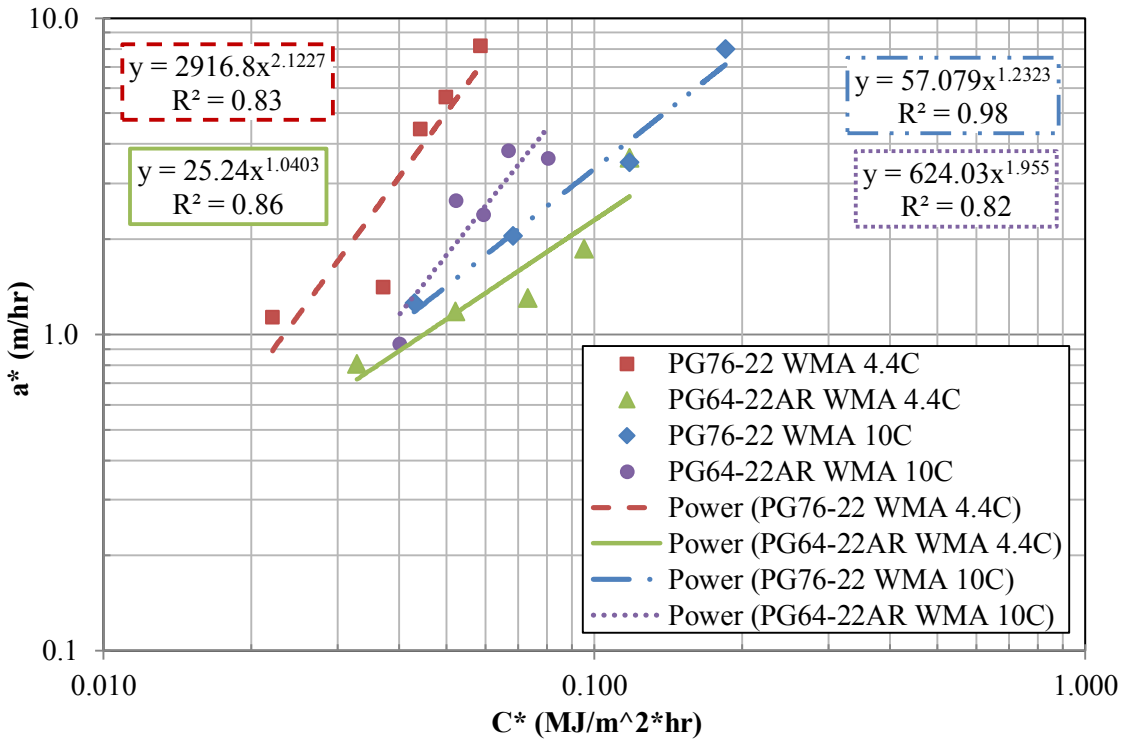

Figure 122 a*-C* relationship for PennDOT I-78 mixtures.

The a*-C* trend for PG64-22AR does not appear rational in that the mixture has less resistance to crack propagation at 10°C than 4.4°C. It may be the case that the C* value is underestimated when the stiffness of the mixture is low enough to allow vertical unrecoverable deformation the specimen in the CFT prior to crack growth or that crack growth mechanism is more micro-cracking or branch cracking than a single vertical crack. In this situation, energy is released through specimen deformation which results in a lower C*-value and/or crack growth rate. Table 45 shows a summary of the dynamic modulus values (0.1 Hz) at each CFT test temperature.

Table 45 |E*| values (0.1 Hz) at CFT test temperature.

Mixture	|E*| 0.1 Hz (MPa)	
	4.4°C	10°C
PG76-22	10902	7037
PG64-22 AR	5861	3590

The dynamic modulus (0.1 Hz) values of the rubber modified mixture are approximately 50% of the unmodified PG76-22 mixture. Also, the PG64-22 AR mixture has a very low value of 3590 MPa at 10°C. Perhaps the test temperature of 10°C for the highly elastic rubber modified mixture is above a threshold temperature to capture crack growth in the C* Fracture Test. This concept will be further explored in a subsequent section.

Statistical comparison of the a*-C* trends were carried out using the technique described in Section 4.9 which the exception that the "Size" variable was replaced with mixture "Type" and then "Temperature" in a secondary comparison. The hypothesis test for both comparisons was as follows and statistical analysis was performed using a level of significance of 0.05:

H_o: Both γ and δ = 0

H_a: Not both γ and δ = 0

Table 46 and Table 47 presents the results of the statistical comparisons across mixture type and test temperature, respectively. Results indicate that all a*-C* trends are all statistically significant (different) except for the mixture type comparison at 10°C. These conclusions correspond well with the aforementioned discussion regarding the PG64-22AR mixture results at 10°C.

Table 46 Statistical comparison of PennDOT I-78 mixture performance across mixture type.

Comparison (size, mm)	Temp. °C	Parameter	p-value	α = 0.05 Decision
PG76-22 vs. PG64-22AR	4.4	γ	0.001	***Reject H_o***
		δ	0.103	
PG76-22 vs. PG6422AR	10	γ	0.077	Accept H_o
		δ	0.204	

Table 47 Statistical comparison of PennDOT I-78 mixture performance across test temperature.

Comparison (size, mm)	Mixture	Parameter	p-value	α = 0.05 Decision
4.4°C vs. 10°C	PG76-22	γ	0.008	***Reject H_o***
		δ	0.160	
4.4°C vs. 10°C	PG64-22AR	γ	0.009	***Reject H_o***
		δ	0.153	

CFT results from the PennDOT I-78 mixtures indicate that the test can characterize crack growth in modified and unmodified mixtures. Although field crack survey data are not currently available, the a*-C* trends across mixture type and temperature appear to match expected behavior of the two types of mixtures tested.

7.4 Temperature Range of CFT

CFT results on mixtures included in the ASU CFT database along with CFT data from the ADOT mixture in Chapter 4 indicate that mixture stiffness may be an important parameter to assess crack propagation. There were several previously discussed cases when the a*-C* trends did not follow logical order. This may have been due to vertical deformation in the specimen, excessive branch cracking or a combination of both. In other cases, crack growth rates were too fast to capture with common video recording equipment.

In order to evaluate and recommended a stiffness range to assess crack propagation in the CFT, dynamic modulus values (0.1 Hz) were tabulated for all mixtures tested in this research study and are summarized in Table 48. This frequency was selected as it can simulate a load that could potentially induce creep fracture in a pavement layer. The values range from 18,694 to 1,477 MPa (2,711 to 214 ksi) with the majority of the values falling in the range of 5,000 to 16,000 MPa (725 to 2,321 ksi). Test temperatures where crack growth was difficult to observe because it was too fast or excessive deformation and branch cracking was observed are enclosed in parenthesis. Figure 123 provides an example of PennDOT I-78 asphalt rubber specimens tested below and within this recommended stiffness range. A noticeable difference can be observed between a single macro crack and branch cracking.

Table 48 |E*| values (0.1 Hz) at CFT test temperatures.

Mixture	Type	|E*| 0.1 Hz (MPa)				
		0°C	4.4°C	10°C	21°C	37.8°C
ADOT	Unmodified	(18694)	16337	12205	6383	(1477)
PA Cranberry Twp.	Control	-	-	6053	(2417)	-
	Fiber	-	-	5955	(2278)	-
PennDOT I-78	PG76-22	-	10902	7037	-	-
	PG64-22 AR	-	5861	(3590)	-	-

- Indicated tests were not performed
( ) Indicates that crack growth was difficult to observe

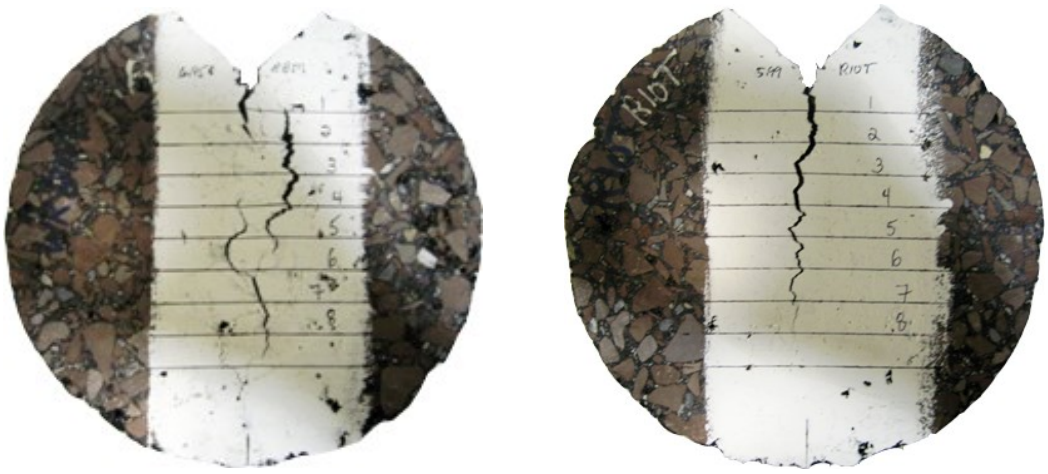

a) **b)**

Figure 123 Crack pattern observed a) below b) within stiffness range.

Figure 124 presents a graphical summary of the dynamic modulus values (0.1 Hz) versus test temperatures for all mixtures. The two thresholds present an initial range of dynamic modulus values (0.1 Hz) where crack propagation can be captured by the CFT. Above a value of approximately 17,000 MPa (2,466 ksi), crack growth is too fast to be observed with common video recording techniques. In comparison, specimens tested at temperatures corresponding to dynamic modulus (0.1 Hz) below approximately 5,000 MPa (725 ksi) typically exhibit vertical deformation and excessive branch cracking.

An initial recommendation, mixtures should be subjected to the CFT at temperatures where the dynamic modulus value (0.1 Hz) falls between 5,000 MPa (725 ksi) and 17,000 MPa (2,466 ksi). If dynamic modulus data are not available, predictive equations can be used or initial tests should be conducted at a temperature of 10°C. If excessive branch cracking is observed, test temperature should be lowered to 4.4°C as a starting point.

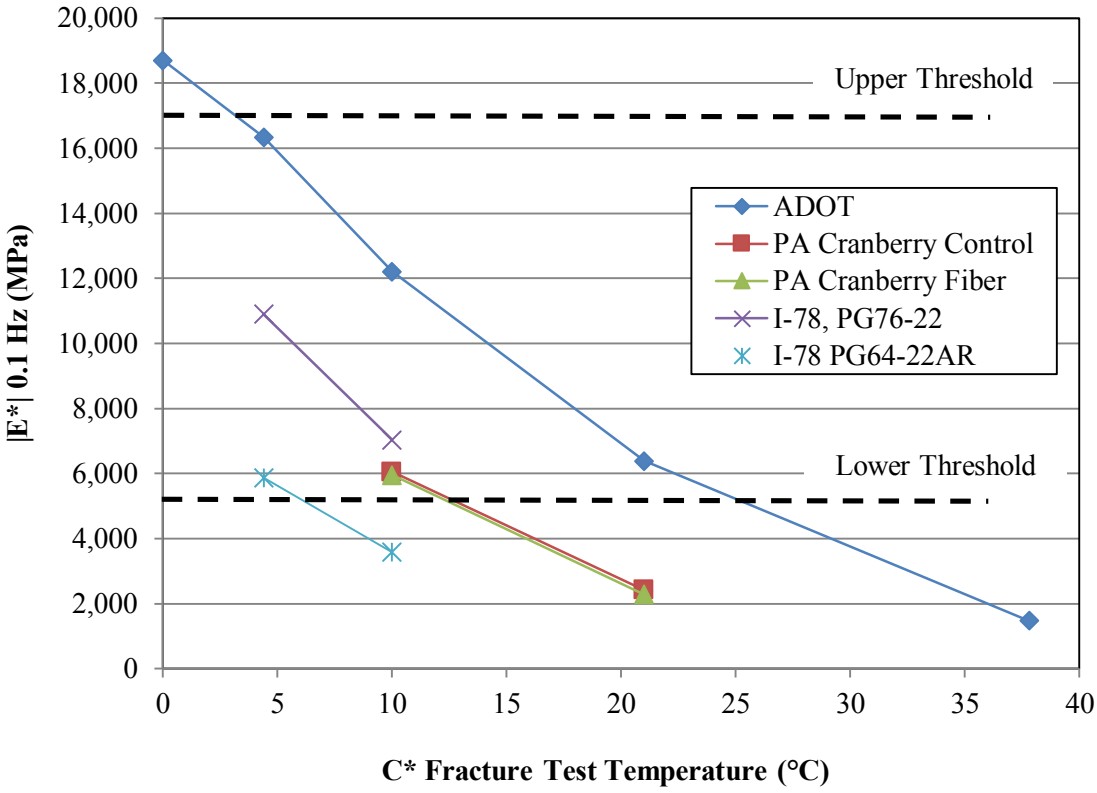

Figure 124 a*-C* relationship for PennDOT I-78 mixtures.

Dynamic modulus data were also used to provide guidance for choosing an initial displacement rate of the CFT. Selection of an initial displacement rate can be challenging and guidance was necessary to supplement a comprehensive CFT test protocol. Equation 7.1 presents a relationship between initial displacement rate, Δ^*_i of the CFT and mixture stiffness at CFT temperature and 0.1 Hz load frequency, $|E^*_{01}|$.

$$\dot{\Delta}_i = 3.3945 * e^{-0.0003*(E^*_{01})} \qquad R^2 = 0.97$$

For: 5,000 MPa < E^*_{01} < 17,000 MPa **7.1**

For: $\dot{\Delta}_i$ between 0.06 - 1.2 mm/min

(Target a* = 2.0 m/hr @ Δ^*_i)

Where:

Δ^*_i = initial displacement rate of test sequence (mm/min), and

$|E^*_{01}|$ = dynamic modulus value at test temperature (0.1 Hz).

This initial relationship was established using the ADOT, PA Cranberry Township, PennDOT I-78: PG76-22 and PennDOT I-78: PG64-22AR mixtures. Temperatures included 4.4 and 10˚C which yielded mixture stiffness values within the aforementioned stiffness range. Displacement rates were plotted versus crack growth rates and fit using a power function. Displacement rates, corresponding to a crack growth rate of 2.0 m/hr, were calculated and related to corresponding mixture stiffness as presented in Equation 7.1. Typically, a crack growth rate in the range of 1.0 - 2.0 m/hr was targeted in CFT testing and thus 2.0 m/hr was selected as the initial target crack growth rate. It is important to note that this equation should be limited to initial displacement rates between 0.06 and 1.2 mm/min and modified as additional mixtures are evaluated using the CFT.

7.5 Summary

This chapter provided a summary of C* Fracture Test data from mixtures that were previously tested at ASU along with additional unmodified and modified mixtures that were tested during this research study. Overall, it was found that the CFT is able to capture differences in resistance to crack propagation for several types of mixtures and

test temperatures. Table 49 provides a summary of the test conditions and crack growth rates for mixtures included in the database.

Table 49 Summary CFT temperature, loading rates and crack growth rates.

Mixture	Modification	Temp (°C)	Δ* (mm/min)	a* (m/hr)
Evergreen	Control	21	0.063-0.318	0.76-6.48
	Fiber 1 lb/ton			0.18-6.38
	Fiber 2 lb/ton			1.18-18.47
Swedish Stockholm	Unmodified	4	0.15-0.45	0.60-3.85
	Polymer			1.04-5.33
	Asphalt Rubber			0.37-1.25
ADOT	Unmodified	4.4	0.03-0.15	2.11-35.81
		10	0.072-0.30	1.98-12.48
		21	0.15-0.45	1.13-4.22
		37.8	0.378-1.50	1.34-8.21
PA Cranberry Twp.	Unmodified	10	0.228-0.90	0.62-6.42
	Fiber 1lb/ton		0.45-1.20	1.04-3.76
	Unmodified	21	0.378-0.828	0.54-1.61
	Fiber 1lb/ton		0.378-0.828	0.55-1.01
PennDOT I-78	Unmodified WMA	4.4	0.15-0.378	1.13-8.17
	Asphalt Rubber WMA		0.30-0.90	0.81-3.62
	Unmodified WMA	10	0.30-1.20	1.26-8.0
	Asphalt Rubber WMA		0.60-1.20	0.93-3.80

It was observed that mixture stiffness at CFT temperature plays in important role in observing crack growth. As an initial recommendation, mixtures should be subjected to the CFT at several temperatures where the dynamic modulus value (0.1 Hz) falls between 5,000 MPa (725 ksi) and 17,000 MPa (2,466 ksi). If dynamic modulus data are not available, initial tests should be conducted at a temperature of 10°C. If excessive branch cracking is observed, test temperature should be lowered to 4.4°C. In addition, mixture stiffness was used to develop guidance to select the initial displacement rate of the CFT.

Chapter 8

8 DEVELOPMENT OF C* AND a* PREDICTION MODELS

8.1 Overview

The overall goal of this chapter is to develop and present models which can be used to predict crack growth rate (a*) and the C* parameter. These models utilize mixture properties, volumetric and test data from laboratory performance tests. The Δ* prediction model will be of immediate benefit is it can be used to determine the loading rates for the CFT for different temperatures and mixture types. The C* and a* prediction models can potentially be used in pavement design and analysis software such as Pavement ME to describe crack propagation as a function of the C* parameter, traffic and temperatures; if CFT test data is not available. The final section presents a conceptual approach to incorporate the a*-C* relationship into pavement analysis and design procedures.

8.2 Independent Variables

Crack growth rate (a*) and C* prediction models were developed using five dense graded, unmodified mixtures: ADOT, PA Cranberry Township, PennDOT I-78, Swedish Stockholm and Evergreen Drive. The total data set included 69 data points crack growth rate measurements and test temperatures ranges from 4.4°C to 37.8°C. All material properties were obtained from laboratory test results and associated mixture design information. It is important to note that the viscosity at test temperature parameter (η) was estimated for the PA Cranberry Township and PennDOT I-78 mixtures from typical Mechanistic-Empirical Pavement Design Guide (MEPDG) values since Ai and VTSi

parameters were not available for these mixtures. Modeling efforts considered the following parameters.

- Loading rate of CFT (Δ), mm/min
- C* Parameter (C), MJ/m^2-hr
- Temperature of CFT (T), °C
- Slope of linear portion of dynamic modulus master curve (m)
- Dynamic modulus value at 0.1 Hz at CFT test temperature (E^*_{01}), MPa
- Specimen air voids (AV), %
- Percent binder (%B), %
- Nominal maximum aggregate size (n_{max}), mm
- Percent retained about 9.5mm (3/8") sieve ($\rho_{9.5}$), %
- Percent retained about 4.76 mm (No. 4) sieve ($\rho_{4.76}$), %
- Percent passing 0.074 mm (No. 200) sieve size ($P_{0.074}$), %
- Binder viscosity at CFT temperature (η), p x 10^6

Table 50 summarizes maximum, minimum, average and standard deviation values for each of the prediction parameters along with crack growth rate dependent variable. The performance parameters (m, E^*_{01}, η) were selected because they can easily be obtained from MEPDG calculations and predictive equations. This association can allow the C* and a* parameters to be predicted easily without the need for additional laboratory performance testing.

Table 50 Descriptive statistics for prediction parameters.

Parameter	Max	Min	Average	St. Dev.
Δ (mm/min)	1.50	0.03	0.40	0.338
a* (m/hr)	36.24	0.54	4.96	6.533
C* (MJ/m^2-hr)	0.185	0.001	0.034	0.0315
T (°C)	37.8	4.0	16.4	11.13
m-value	0.345	0.247	0.328	0.0279
E^*_{01} (MPa)	16337	1477	8215	4991.6
AV (%)	7.77	3.13	6.03	0.944
%B	5.9	4.7	5.1	0.53
n_{max} (mm)	19.0	9.5	16.3	4.14
$\rho_{9.5}$ (%)	48.5	4.0	20.8	11.59
$\rho_{4.76}$ (%)	77.0	40.0	43.6	9.55
$P_{0.074}$ (%)	10.6	4.0	5.2	1.57
η (P)	8385.09	0.61	1411.62	2642.713

8.3 Crack Growth Rate Prediction Model

A crack growth rate (a*) model was developed to predict the relationship between a* and C*. Linear regression techniques were used to develop a crack growth prediction model since a log transformation of the power relationship between crack growth rate and the C* yielded a linear equation shown in Equation 8.1.

$$\log a^* = \log a + b * logC^* \qquad \textbf{8.1}$$

Where:

a* = crack growth rate (m/hr),

C* = C* parameter (MJ/m^2-hr), and

a, b = material constants.

Spearman correlation coefficients were calculated to initially identify parameters with different levels of correlation to crack growth rate. This non-parametric technique is

applicable since several variables are not normally distributed; a requirement of the more common Pearson correlation analysis (Neter et al, 1996). Table 51 provides a summary of the Spearman correlation coefficients. A value close to zero indicates no correlation between parameters whereas a value approaching -1 or 1 has high correlation.

Table 51 Spearman correlation coefficients.

	log a	*log C*	*T*	*m*	E_{01}	*AV*	*%B*	n_{max}	$\rho_{9.5}$	$\rho_{4.76}$	$P_{0.074}$	η
log a	1.00											
log C	0.28	1.00										
T	-0.04	0.10	1.00									
m	0.33	-0.05	0.21	1.00								
E_{01}	0.19	-0.23	-0.88	0.21	1.00							
AV	-0.14	-0.09	0.30	-0.50	-0.49	1.00						
%B	-0.43	0.21	-0.39	-0.90	-0.05	0.27	1.00					
n_{max}	0.35	-0.42	0.42	0.74	-0.01	-0.22	-0.90	1.00				
$\rho_{9.5}$	0.07	-0.43	0.01	0.29	0.19	-0.38	-0.33	0.64	1.00			
$\rho_{4.76}$	-0.44	0.11	-0.37	-0.91	-0.06	0.26	0.98	-0.80	-0.17	1.00		
$P_{0.074}$	0.02	0.33	-0.47	0.27	0.53	-0.60	0.02	-0.20	0.13	-0.04	1.00	
η	0.28	-0.11	-0.90	0.09	0.92	-0.33	0.04	-0.16	-0.06	-0.01	0.44	1.00

The criteria presented in Table 52 (Rodezno, 2010) were used to determine which prediction parameters were most correlated with crack growth rate. Some parameters are highly correlated to each other and thus both parameters may not be necessary in the final model.

Table 52 Correlation ranking categories.

Very High	0.61-1.00
High	0.36-0.60
Medium	0.16-0.35
Low	0.06-0.15
None	0.00-0.05

Based on these ranking categories, the following correlation levels to crack growth rate (a*) were assigned to each of the prediction parameters.

High: %B, n_{max} and $\rho_{4.76}$

Medium: log C, m, E^*_{01}, η

Low: AV, $\rho_{9.5}$

None: T, $P_{0.074}$

Minitab statistical software package was used to perform linear regression analysis. The stepwise procedure (forward and backward selection) was used to determine the best crack growth rate prediction model for parameters in the medium and high correlation categories. The first two models considered numerical values and log transformed values, respectively and the third model considered both numerical and log transformed values. Recall that crack growth rate and the C* parameters were log transformed in both cases given the relationship presented in Equation 8.1. Table 53 shows the stepwise regression results for the first three models in the analysis. Models 1 and 2 had adjusted R^2-values of 0.865 and 0.693, respectively whereas the combination of terms in Model 3 only improved the R^2-value to 0.8848.

Figure 125 shows a plot of predicted versus measured crack growth rate values for Model 1. It is evident that the data do not follow the line of equality and thus the model does not accurately predict crack growth rates for the mixture data included in the analysis. It appears that the model underestimates crack growth rates above a value of approximately 7 m/hr, which is typically associated with colder temperatures. All terms considered in Models 1-3 affect the intercept of the relationship in Equation 8.1 with the exception of log C*.

Table 53 Initial stepwise regression model terms.

Parameter	Model		
	1	2	3
Constant	11.9828	5.3764	2.9790
%B	-0.968	-11.06	-0.961
Log %B			
n_{max}			
Log n_{max}			
$\rho_{4.76}$			
Log $\rho_{4.76}$			
Log C	1.101	0.816	1.143
m	-15.9		
Log m		-7.8	-11.73
E^*_{01}	0.00004		0.00009
Log E^*_{01}			-0.59
η	0.00008		0.00006
Log η		0.228	
$R^2_{(adj)}$	86.48	67.26	88.48

Thus, no additional predictors influence the slope of the log a*-log C* relationship. Practical observation of data indicates that the slope of the line changes across mixture type and at different CFT test temperatures and thus includes of interaction terms with log C* in the model is necessary.

In addition, review of the Spearman correlation matrix in Table 51 indicates that percent binder (%B) is highly correlated to the m-value and also that E_{01} value is highly correlated to binder viscosity (η). Inclusion of covariates can produce misleading modeling results. Removal of either set of highly correlated terms from the model reduces the R^2-value significantly below the current value. Review of Model 2 and Model 3 data produce similar observations and development of a crack growth rate model should consider additional predictors.

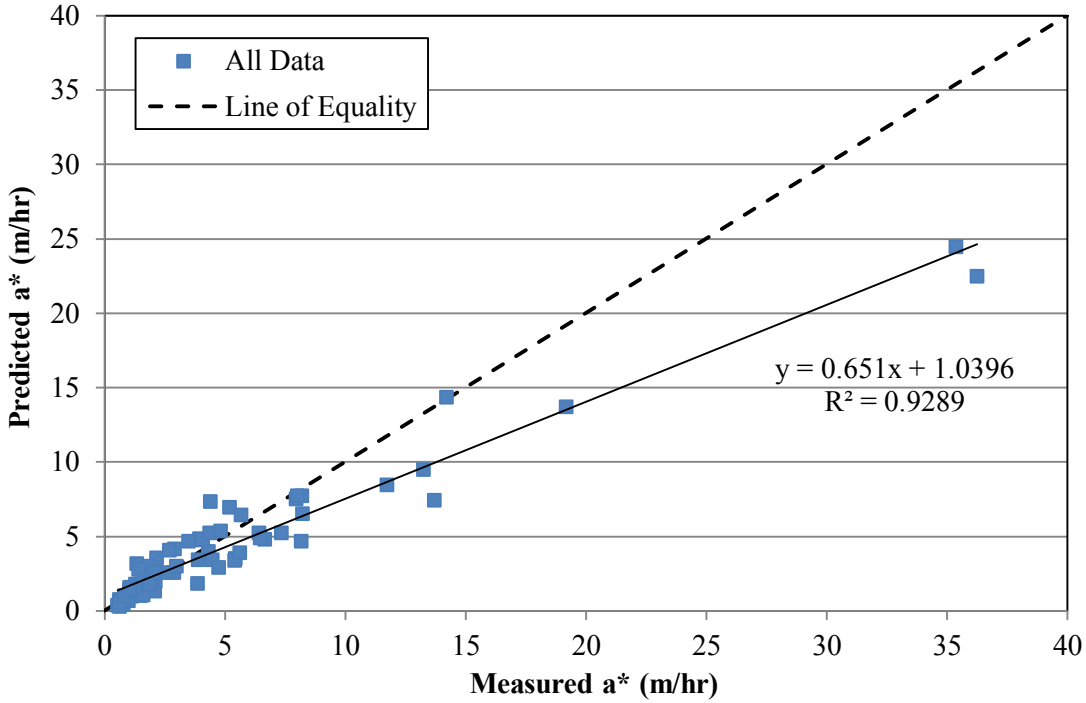

Figure 125 Comparison of Model 1 predicted versus measured a* values.

Final modeling efforts included numerical terms, interaction terms with log C, squared terms and log transformed terms. Again, the stepwise regression function in Minitab was used to develop a model for crack growth rate. Table 54 shows the steps in the model and improvement in adjusted R^2-value. The final model (Step 7) was selected and evaluated for to determine the effectiveness of predicting the a*-C* relationships for mixtures considered in this analysis.

Table 54 Final stepwise regression model steps.

Step	Variables	$R^2_{(adj)}$
1	Log C	3.02
2	Log C, η	31.53
3	Log C, η, $\%B^2$	51.91
4	Log C, η, $\%B^2$, log m	77.50
5	Log C, η, $\%B^2$, log m, E_{01}^2	88.10
6	Log C, η, $\%B^2$, log m, E_{01}^2, ηxC	89.72
7	Log C, η, $\%B^2$, log m, E_{01}^2, ηxC, log %B	90.72

The final model used to predict crack growth rate as a function of the C* parameter is presented in Equation 8.2 with all terms previously defined. The model has an overall adjusted R^2-value of 0.91 and S_e/S_y equal to 0.30.

$$\log a^* = 26.5848 + 0.97764 * \log C^* + 2.53324\,x\,10^{-5} * \eta + 0.34335 * \%B^2 + 0.00366\,(\eta * C) + 2.45468\,x\,10^{-9} * E_{01}^2 - 11.6053 * \log m - 56.0271 * \log \%B \qquad R^2_{adj} = 0.91 \quad Se/Sy = 0.30 \qquad \textbf{8.2}$$

Residual plots of the final model, generated from Minitab, are shown in Figure 126. This plots indicate the final log a* distribution is normally distributed and that the lack of systematic pattern in the residual plot indicated that a linear model is appropriate for these data. Figure 127 displays a comparison plot of predicted versus actual crack growth rate values from the final model. Data fall nicely along the line of equality indicating the ability of the model to predict crack growth rates for several types of mixtures and different CFT test conditions.

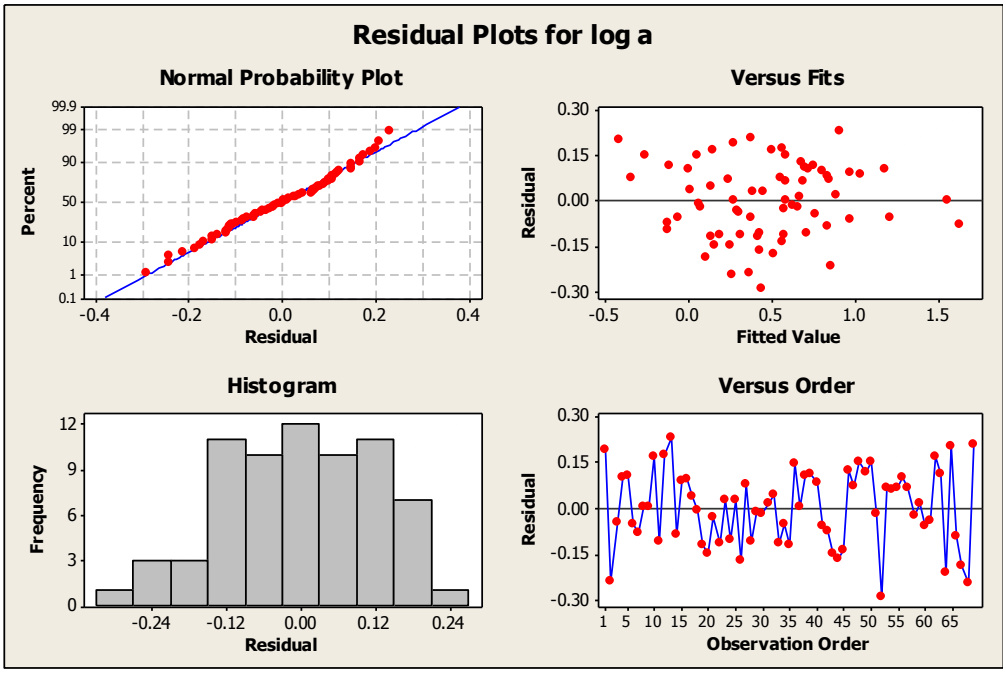

Figure 126 Residual plots for final crack growth rate prediction model.

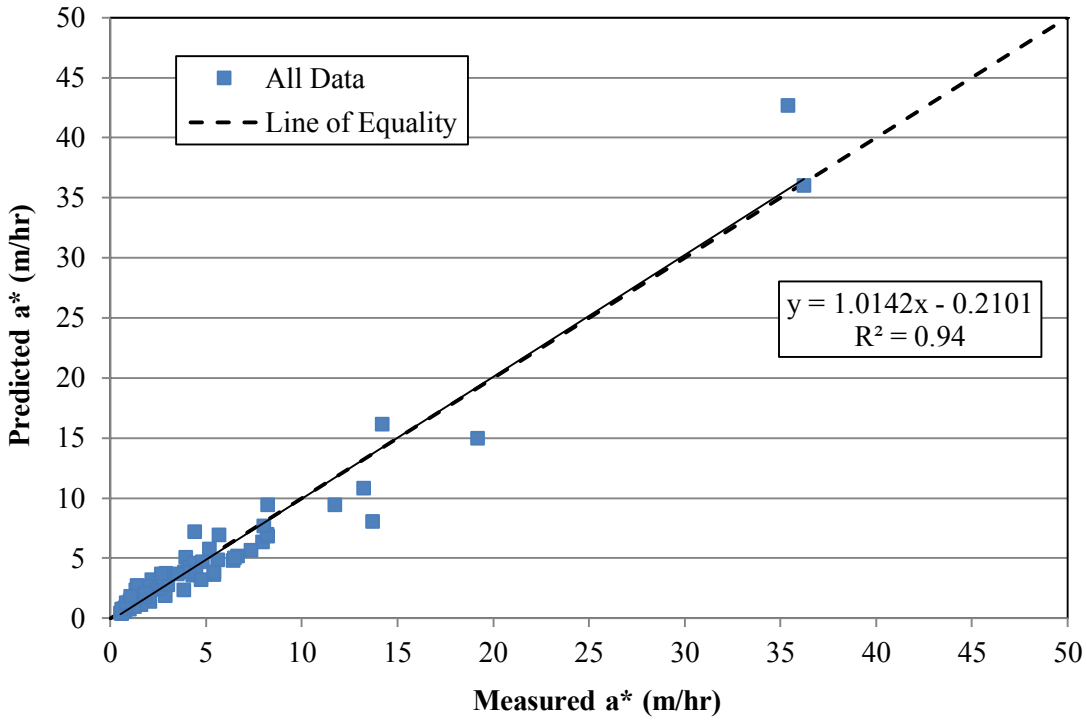

Figure 127 Comparison of predicted versus measured a* values for final model.

8.3.1 Crack Growth Rate Model Verification

The crack growth rate prediction model was used to predict a*-C* relationships for all dense graded, unmodified mixtures included in this study. Crack growth rate data were predicted for each mixture and then fitted using a power relationship in Microsoft Excel. Actual versus predicted trends were plotted on the same graphs which are shown below in Figure 128 and Figure 129 for the ADOT mixture, Figure 130 for the PA Cranberry Township mixture and Figure 131 for the PennDOT I-78 mixture. In addition, Figure 132 and Figure 133 present these relationships for the Evergreen Drive and Swedish Stockholm mixtures, respectively.

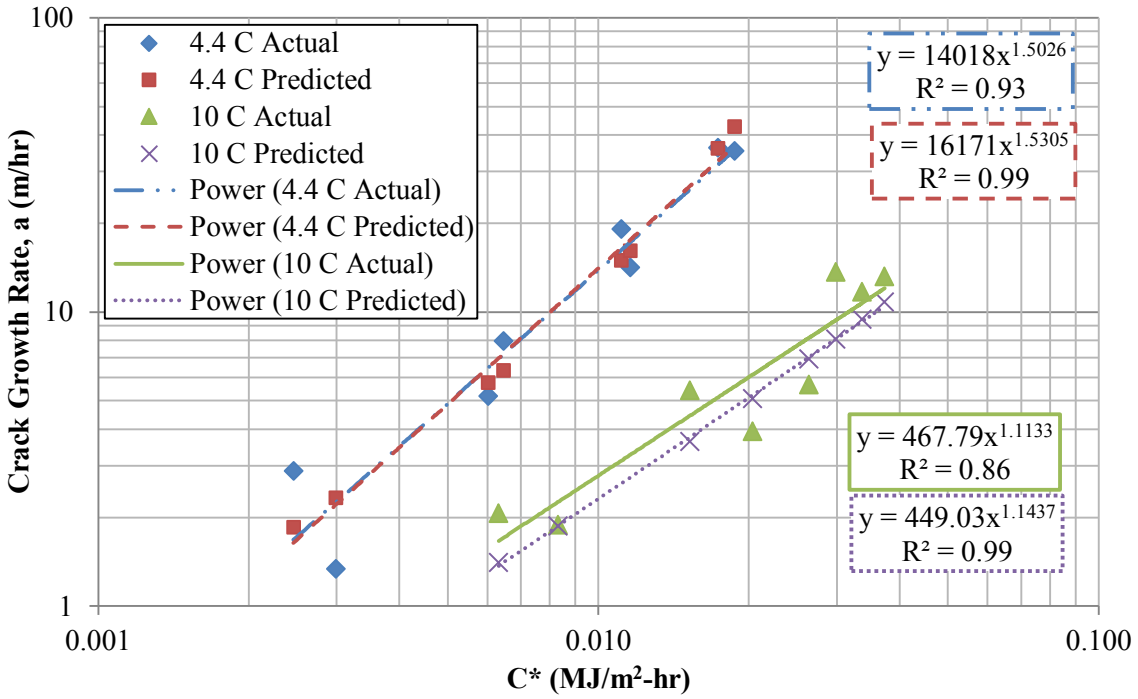

Figure 128 Actual and predicted crack growth rates (ADOT, 4.4°C & 10°C).

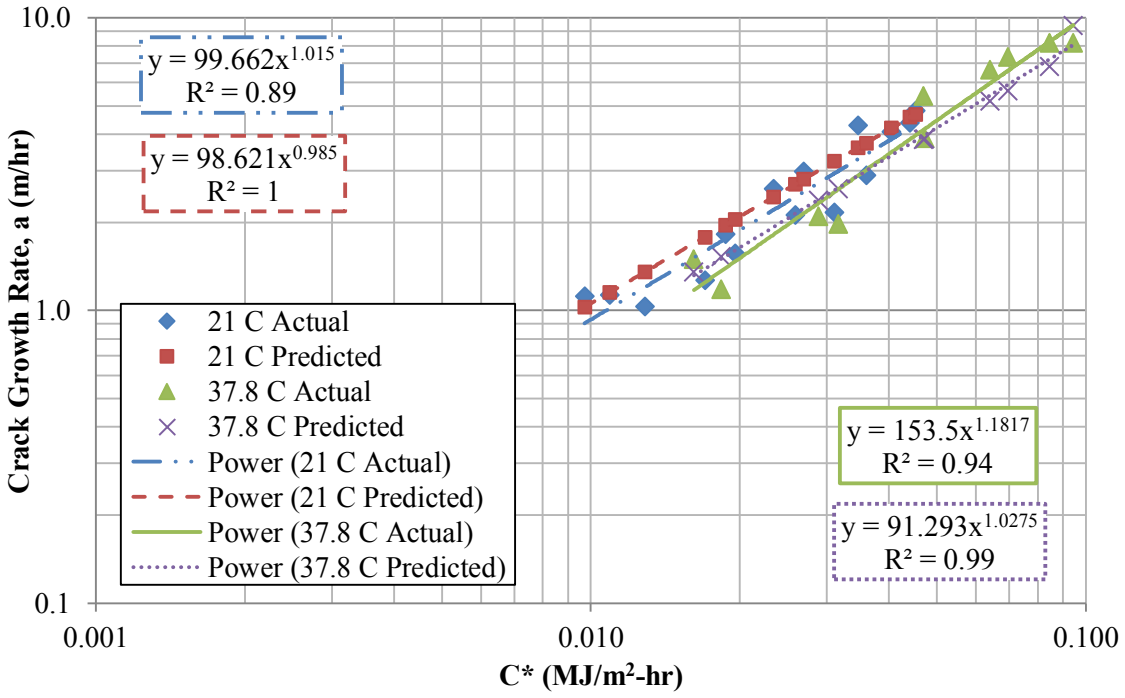

Figure 129 Actual and predicted crack growth rates (ADOT, 21°C & 37.8°C).

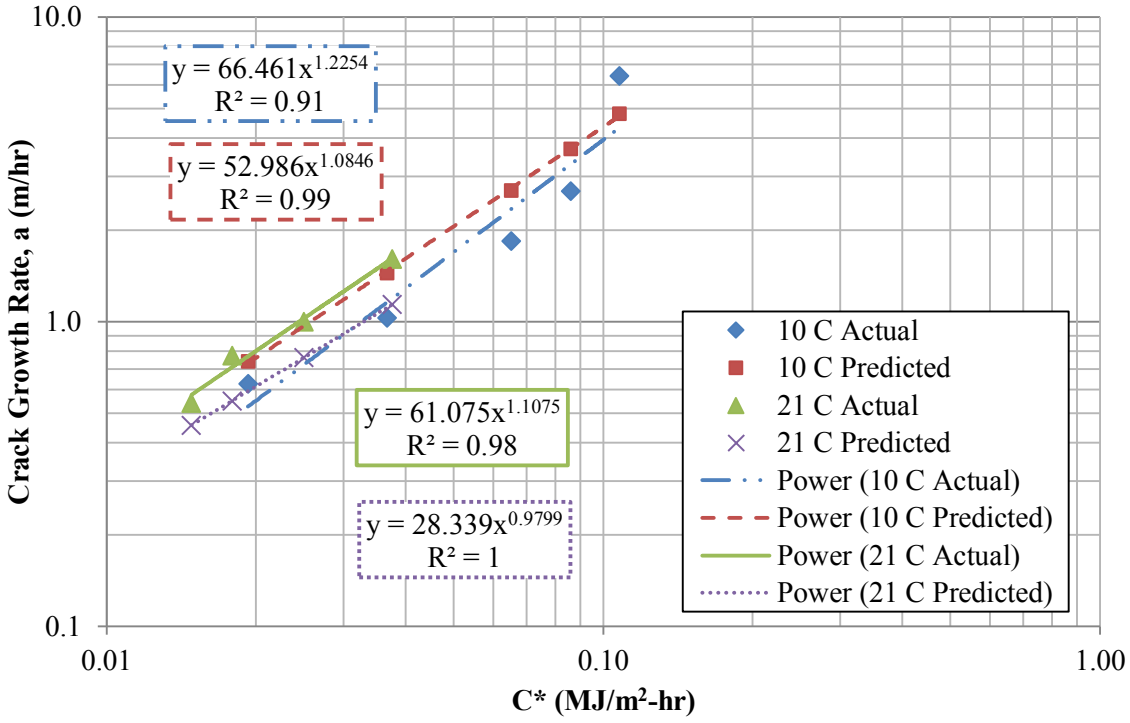

Figure 130 Actual and predicted crack growth rates (PA Mix, 10°C & 21°C).

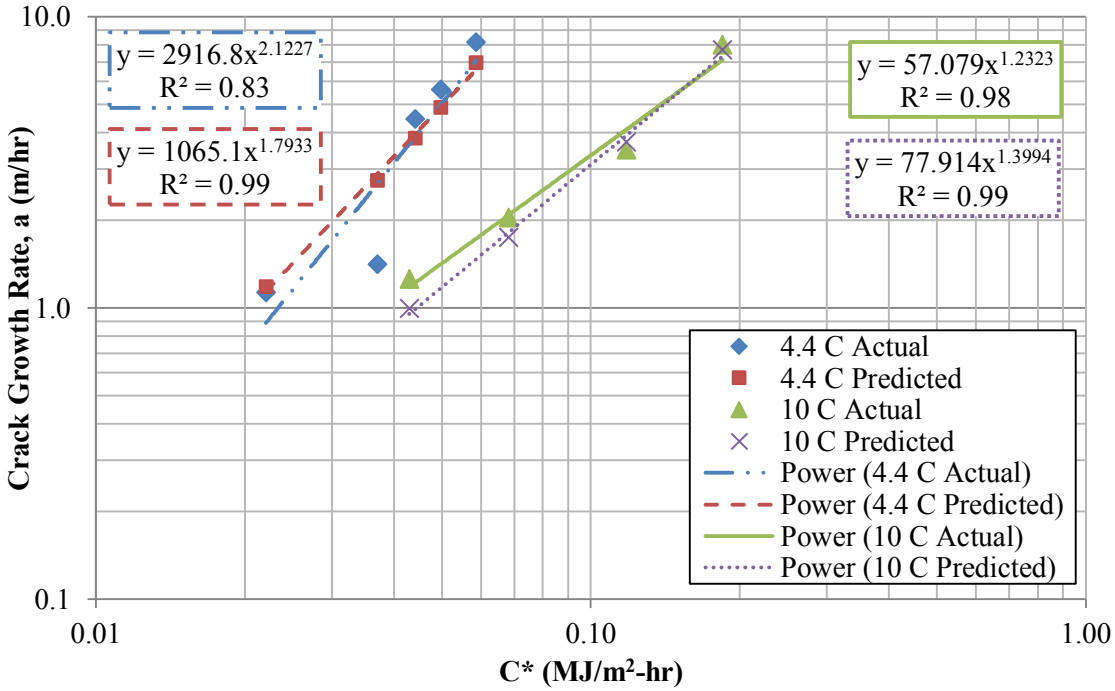

Figure 131 Actual and predicted crack growth rates (I-78 Mix, 4.4°C & 10°C).

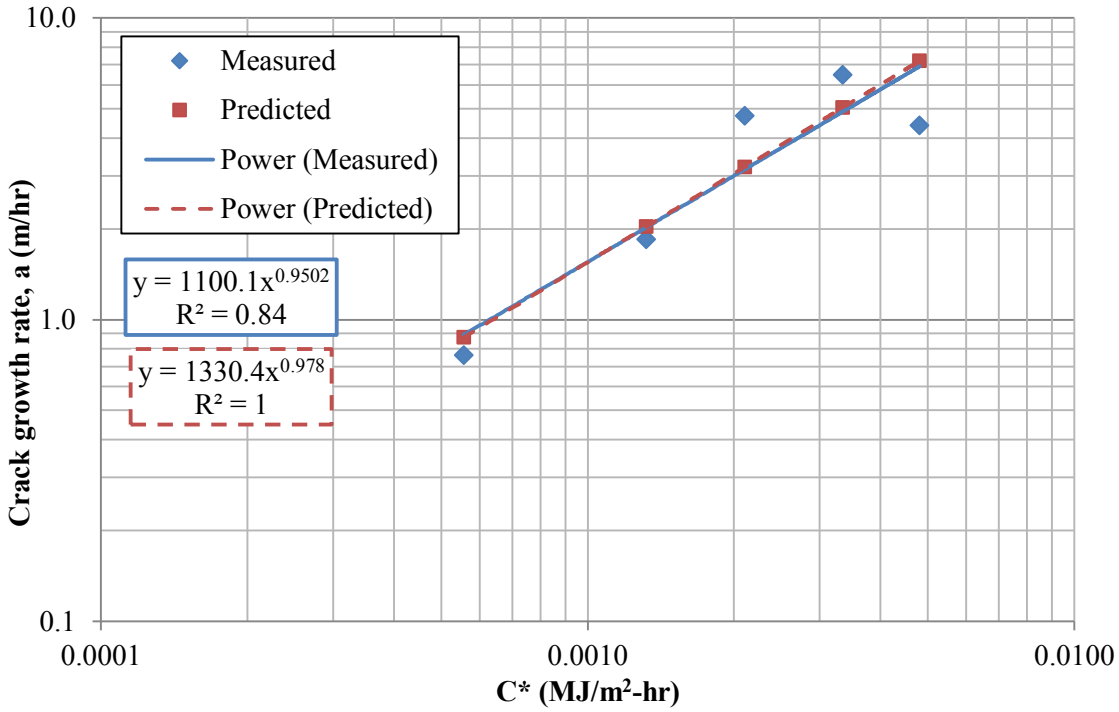

Figure 132 Actual and predicted crack growth rates (Evergreen Drive, 21°C).

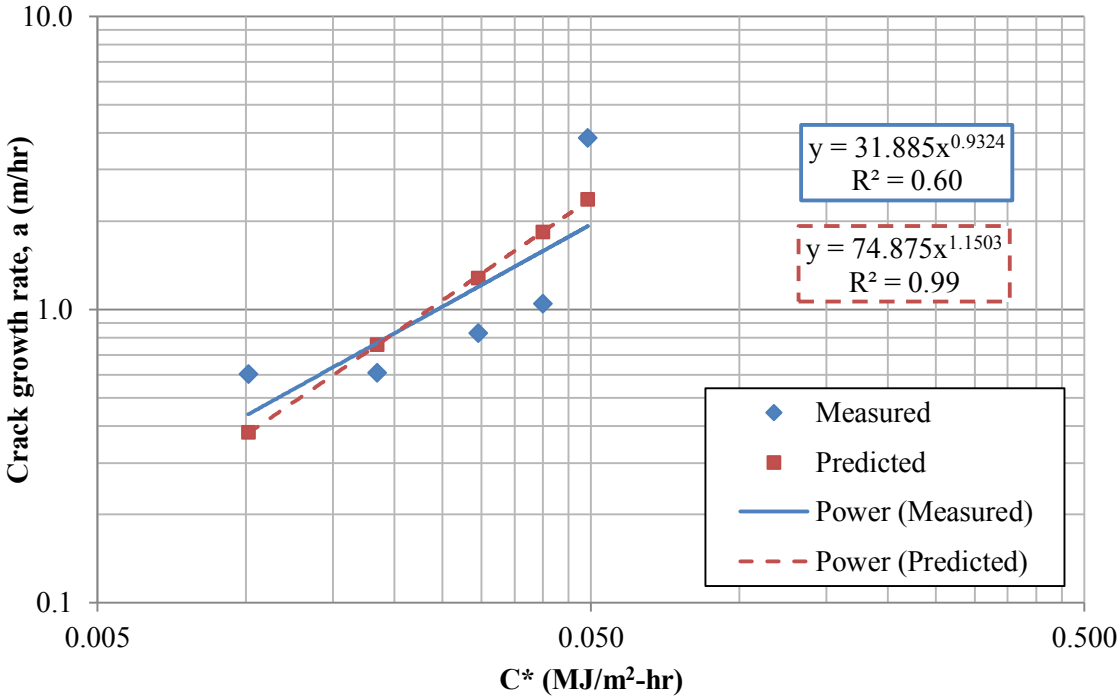

Figure 133 Actual and predicted crack growth rates (Swedish Stockholm, 4°C).

All cases appear the predict the a*-C* relationships well except the PA Cranberry township mixture at 21°C which is slightly under predicted. This under prediction may be due to the fact that the viscosity at CFT test temperature for this mixture was estimated from standard MEPDG Ai and VTSi for PG64-22 binder. However, for the other types of mixtures, the model is able to capture changes in the slope and intercept of the a*-C* relationships.

This modeling effort presents an initial model that can be used to predict crack growth rate as a function of the C* parameter and mixture properties. However, additional mixtures should be added to the database to verify the model form and prediction parameters. In addition, separate models can be developed for asphalt rubber mixtures and fiber reinforced mixtures when CFT test results become available in the future. Models developed using unmodified mixtures were not able to predict values for mixtures modified with fibers or asphalt rubber.

8.4 C* Prediction Model

Next, a model was developed to predict the relationship between the C* parameter and the CFT loading rate (Δ*). Linear regression techniques were used to develop a crack growth prediction model since a log transformation of the power relationship between crack growth rate and the C* yielded a linear equation shown in Equation 8.1.

$$\log C^* = \log a + b * log\Delta \quad \textbf{8.3}$$

Where:

Δ = displacement rate of CFT (mm/min),

C* = C* parameter (MJ/m^2-hr), and

a, b = material constants.

Spearman correlation coefficients were calculated to initially identify parameters with different levels of correlation to crack growth rate. Table 55 provides a summary of the Spearman correlation coefficients. A value close to zero indicates no correlation between parameters whereas a value approaching -1 or 1 has high correlation.

Table 55 Spearman correlation coefficients.

	log C	*log* Δ	*T*	*m*	E_{01}	*AV*	*%B*	n_{max}	$\rho_{9.5}$	$\rho_{4.76}$	$P_{0.074}$	η
log C	1.00											
log Δ	0.82	1.00										
T	0.10	0.50	1.00									
m	-0.05	-0.14	0.21	1.00								
E_{01}	-0.23	-0.65	-0.88	0.21	1.00							
AV	-0.09	0.11	0.30	-0.50	-0.49	1.00						
%B	0.21	0.22	-0.39	-0.90	-0.05	0.27	1.00					
n_{max}	-0.42	-0.30	0.42	0.74	-0.01	-0.22	-0.90	1.00				
$\rho_{9.5}$	-0.43	-0.34	0.01	0.29	0.19	-0.38	-0.33	0.64	1.00			
$\rho_{4.76}$	0.11	0.16	-0.37	-0.91	-0.06	0.26	0.98	-0.80	-0.17	1.00		
$P_{0.074}$	0.33	-0.03	-0.47	0.27	0.53	-0.60	0.02	-0.20	0.13	-0.04	1.00	
η	-0.11	-0.58	-0.90	0.09	0.92	-0.33	0.04	-0.16	-0.06	-0.01	0.44	1.00

The criteria previously presented in Table 52 were used to determine which prediction parameters were most correlated with crack growth rate. Some parameters were highly correlated to each other and thus both parameters may not be necessary in the final model. Based on these ranking categories, the following correlation levels to crack growth rate (a*) were assigned to each of the prediction parameters.

Very High: log Δ

High: n_{max}, $\rho_{9.5}$

Medium: E^*_{01}, %B, $P_{0.074}$

Low: T, AV, $\rho_{4.76}$, η

None: m

Minitab statistical software package was used to perform linear regression analysis. The stepwise procedure (forward and backward selection) was used to determine the best C* prediction model for parameters in the medium, high and very high correlation categories. Based on crack growth rate modeling efforts in the previous section, models containing interaction parameters were considered in the initial models as it was found that models with only numerical or log transformed terms were unable to accurately predict C*-Δ relationships for the mixtures included in this modeling effort. Table 56 presents the steps in development of the C* prediction model. The additional terms in Models 6 and 8 resulted in essentially no improvement in R^2-value. Model 7 was selected because of the high R^2-value, inclusion of interaction terms and that predicted values matched experimental data well.

Table 56 Final stepwise regression model steps.

Step	Variables	$R^2_{(adj)}$
1	Log Δ	62.80
2	Log Δ, m x Log Δ	83.89
3	Log Δ, m x Log Δ, log E_{01}	92.48
4	Log Δ, m x Log Δ, log E_{01}, ($\rho_{9.5}$ x log Δ)	96.53
5	Log Δ, m x Log Δ, log E_{01}, ($\rho_{9.5}$ x log Δ), log m	97.61
6	Log Δ, m x Log Δ, log E_{01}, ($\rho_{9.5}$ x log Δ), log m, log $\rho_{9.5}$	98.83
7	Log Δ, log E_{01}, ($\rho_{9.5}$ x log Δ), log m, log $\rho_{9.5}$	98.85
8	Log Δ, log E_{01}, ($\rho_{9.5}$ x log Δ), log m, log $\rho_{9.5}$, log P_{200}	98.89

The final model used to predict C* as a function of the CFT displacement rate is presented in Equation 8.4 with all terms previously defined. The model has an overall adjusted R^2-value of 0.99 and S_e/S_y equal to 0.11.

$$\log C^* = -0.339753 + 1.15875 * \log \Delta + 0.61069 * \log E_{01} + 0.00492 * (\rho_{9.5} * \log \Delta) + 5.26501 * \log m - 0.32401 * \log \rho_{9.5} \quad \textbf{8.4}$$

$R^2_{adj} = 0.99$

$Se/Sy = 0.11$

Residual plots of the final model, generated from Minitab, are shown in Figure 134. This plots indicate the final log C* distribution is normally distributed and the lack of systematic pattern in the residual plot indicated that a linear model is appropriate for these data. Figure 135 displays a comparison plot of predicted versus actual crack growth rate values from the final model. Data fall nicely along the line of equality indicating the ability of the model to predict C* values for several types of mixtures and different CFT test conditions.

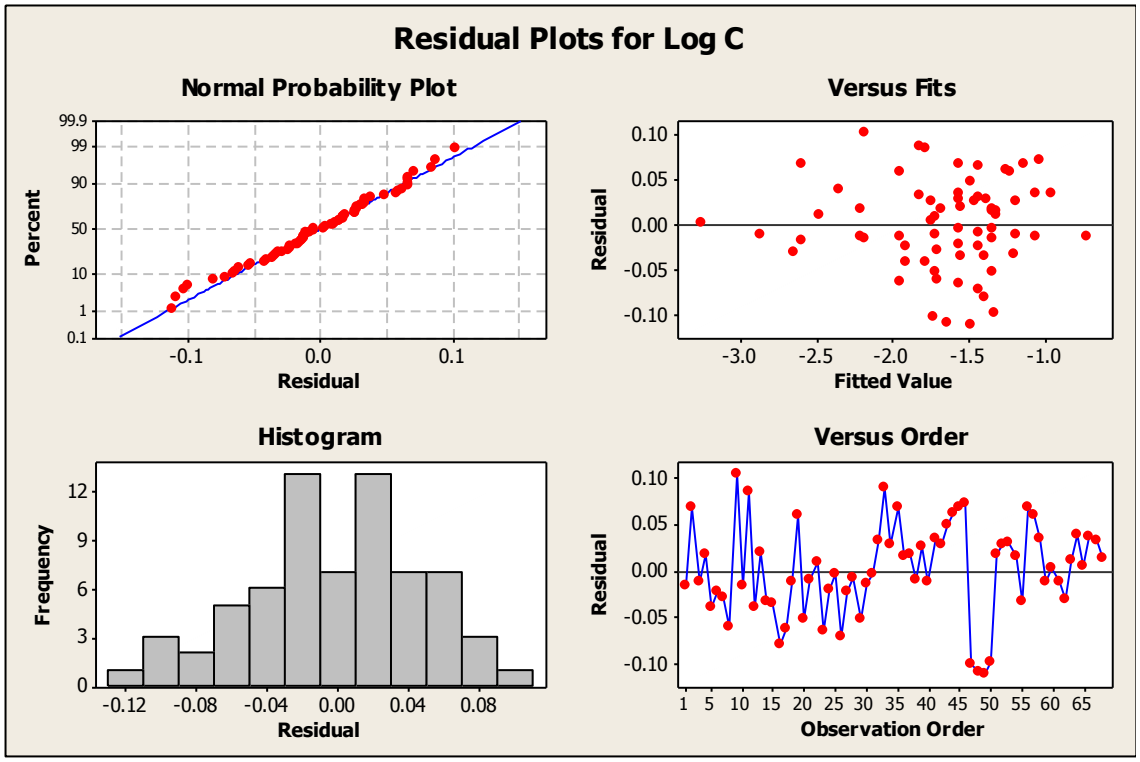

Figure 134 Residual plots for final C* prediction model.

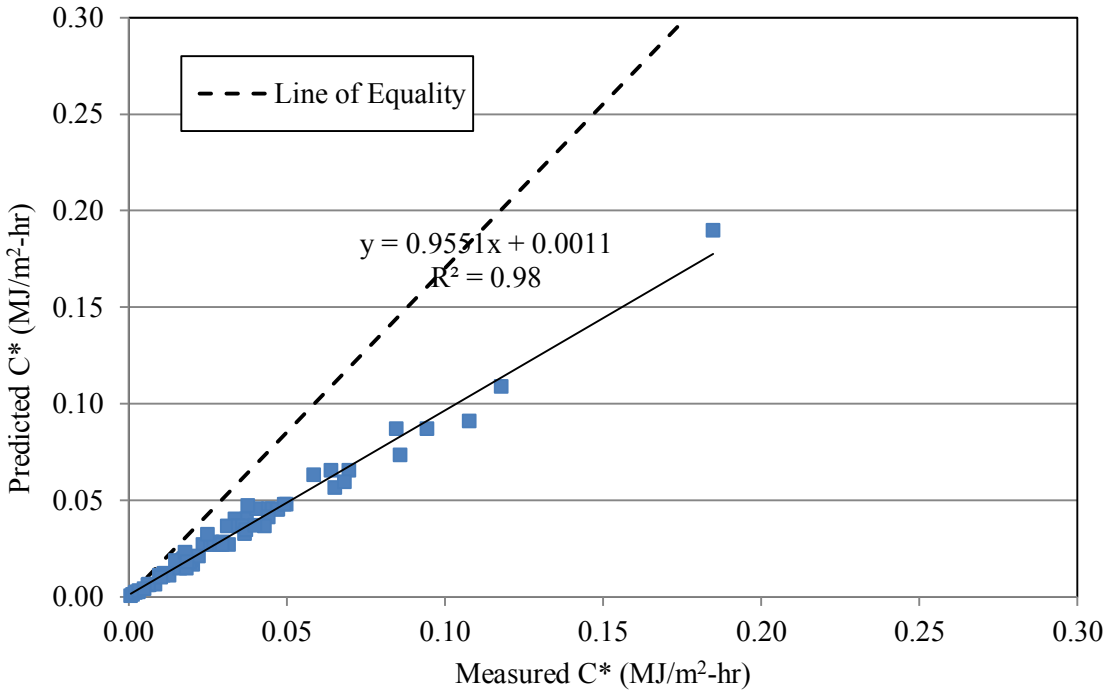

Figure 135 Comparison of predicted versus measured C* values for final model.

8.4.1 C* Model Verification

The C* prediction model was used to predict C*-Δ* relationships for all dense graded, unmodified mixtures included in this study. To verify the model, C* values were predicted for each mixture and then fitted using a power relationship in Microsoft Excel. Actual versus predicted trends were plotted on the same graphs which are shown below in Figure 136 and Figure 137 for the ADOT mixture, Figure 138 for the PA Cranberry Township mixture and Figure 139 for the PennDOT I-78 mixture. In addition, Figure 140 and Figure 141 present these relationships for the Evergreen Drive and Swedish Stockholm mixtures, respectively.

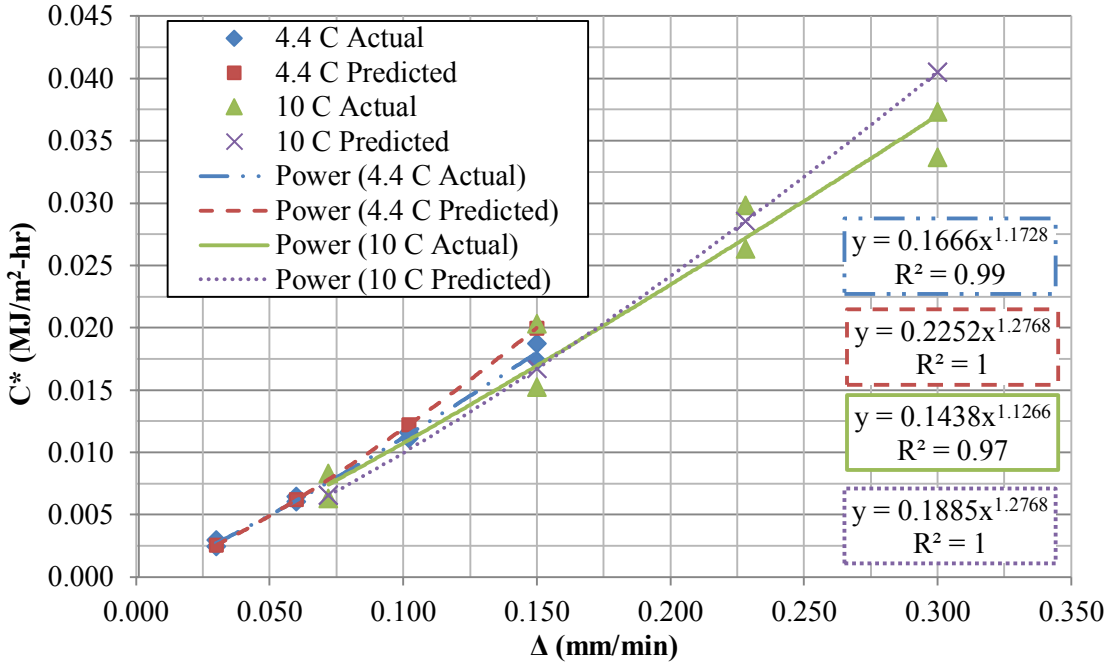

Figure 136 Actual and predicted C* values (ADOT, 4.4°C & 10°C).

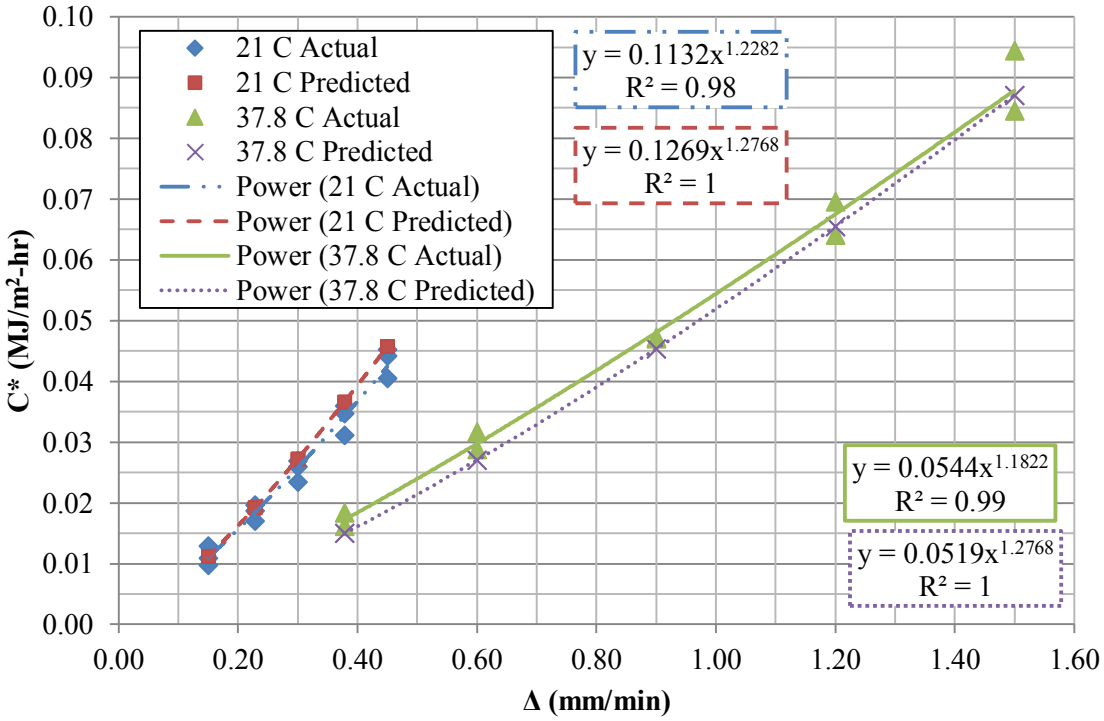

Figure 137 Actual and predicted C* values (ADOT, 21°C & 37.8°C).

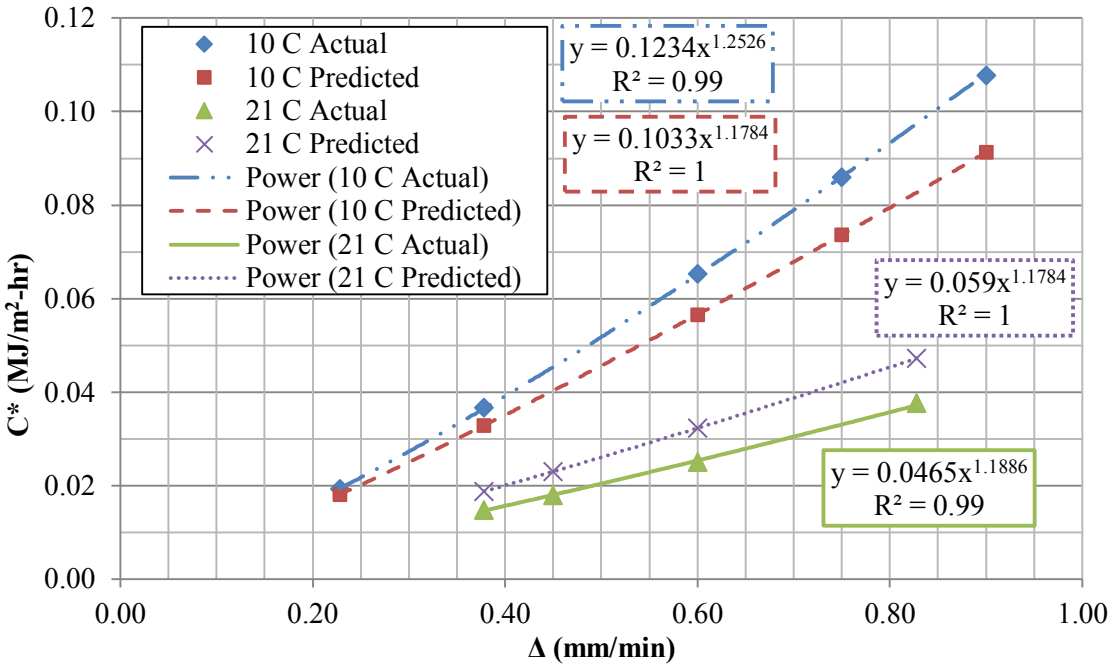

Figure 138 Actual and predicted C* values (PA Mix, 10°C & 21°C).

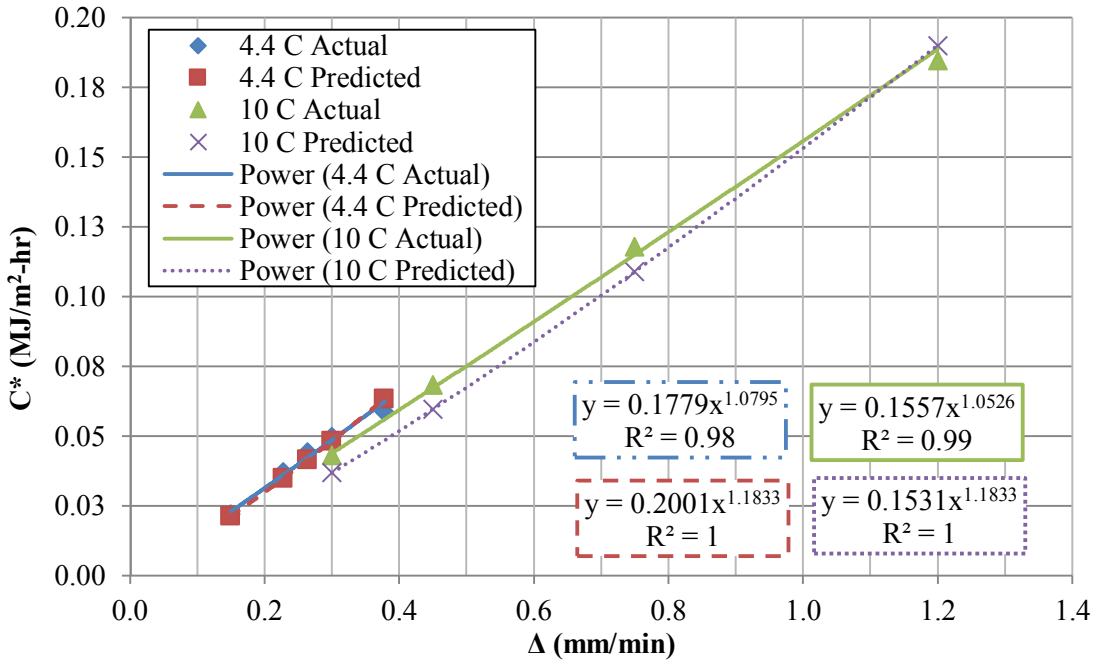

Figure 139 Actual and predicted C* values (I-78 Mix, 4.4°C & 10°C).

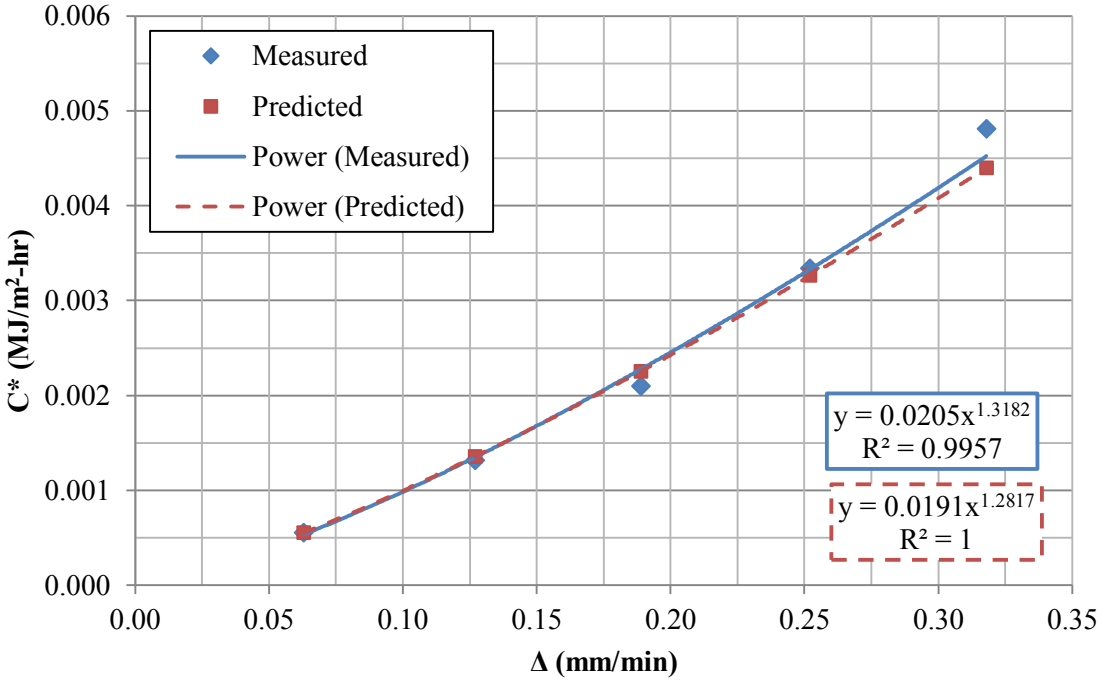

Figure 140 Actual and predicted C* values (Evergreen Drive, 21°C).

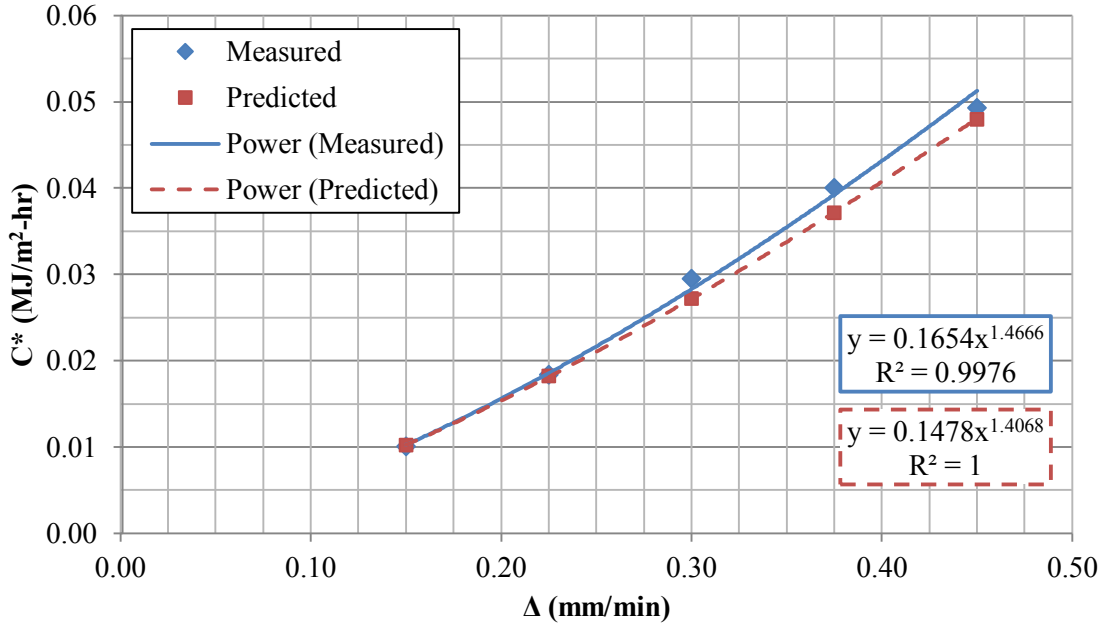

Figure 141 Actual and predicted C* values (Swedish Stockholm, 4°C).

All cases appear the predict the C*-Δ* relationships well except the PA Cranberry township mixture at 10°C and 21°C which is slightly under predicted. This under prediction may be due to the fact that the viscosity at CFT test temperature for this mixture was estimated from standard MEPDG Ai and VTSi for PG64-22 binder. However, for the other types of mixtures, the model is able to capture changes in the slope and intercept of the C*-Δ* relationships.

This modeling effort presents an initial model that can be used to predict crack growth rate as a function of the C* parameter and mixture properties. However, additional mixtures should be added to the database to verify the model form and prediction parameters. In addition, separate models can be developed for asphalt rubber mixtures and fiber reinforced mixtures when CFT test results become available in the future.

8.5 Method to Calculate the C* Parameter

The existing C* value from the CFT was calculated based on constant vertical displacement loading. Thus, a unique relationship between displacement rate and C* can be established for an asphalt concrete material as shown in Figure 142. Calculating the C* parameter as a function of traffic loading is a more challenging task and will require further research and evaluation of existing relationships between C* and stresses and strains surrounding the crack tip. However, as an intermediate step, a relationship between traffic load, frequency of load, layer stiffness (age), existing crack length and the vertical displacement rate (Δ*) can potentially be established as shown schematically in Figure 143.

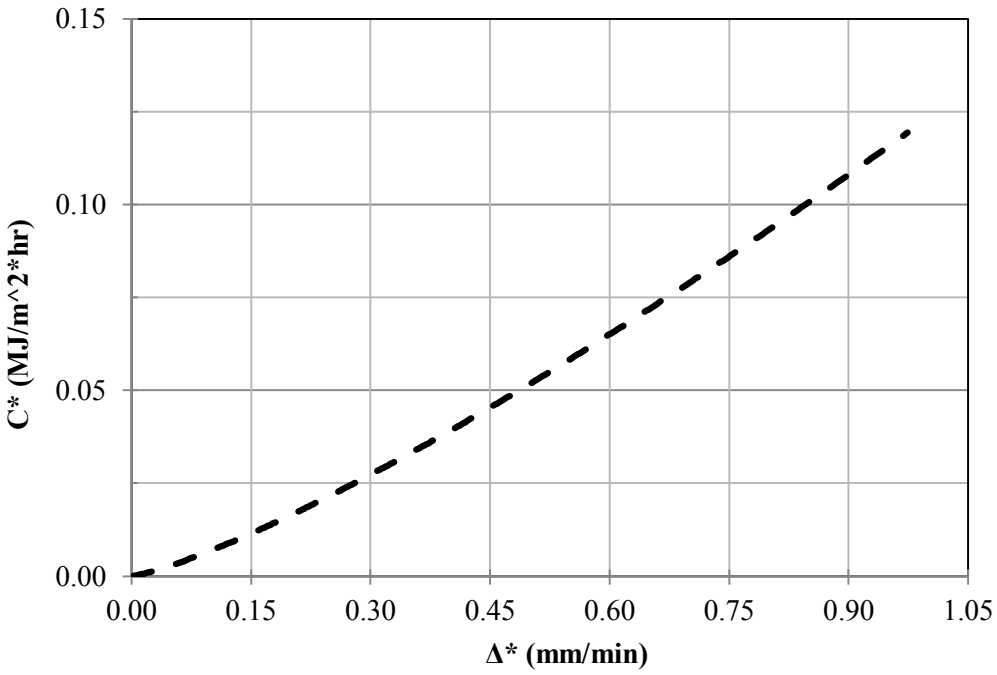

Figure 142 Example C* relationship to CFT displacement rate.

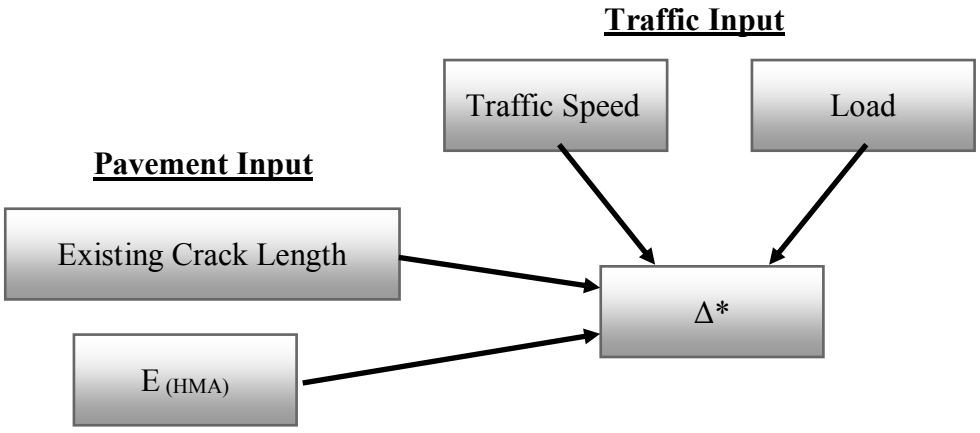

Figure 143 Schematic of intermediate method to determine Δ*.

8.6 Method to Calculate Crack Growth Rate

Once the C* parameter is determined for any given traffic conditions, the crack growth rate master curve can be used to determine the expected crack growth rate in a pavement layer for different seasonal temperature conditions. Thus, during colder

temperatures, the crack will propagate quicker than during warmer temperatures for a given C* value. Ideally, a crack growth rate master curve can be determined from the C* Fracture Test prior to design. However, if test data are not available or feasible, a predicted crack growth rate master curve can be developed using C* and a* prediction models. Figure 144 provides an example of a crack growth rate master curve for a dense graded, unmodified HMA.

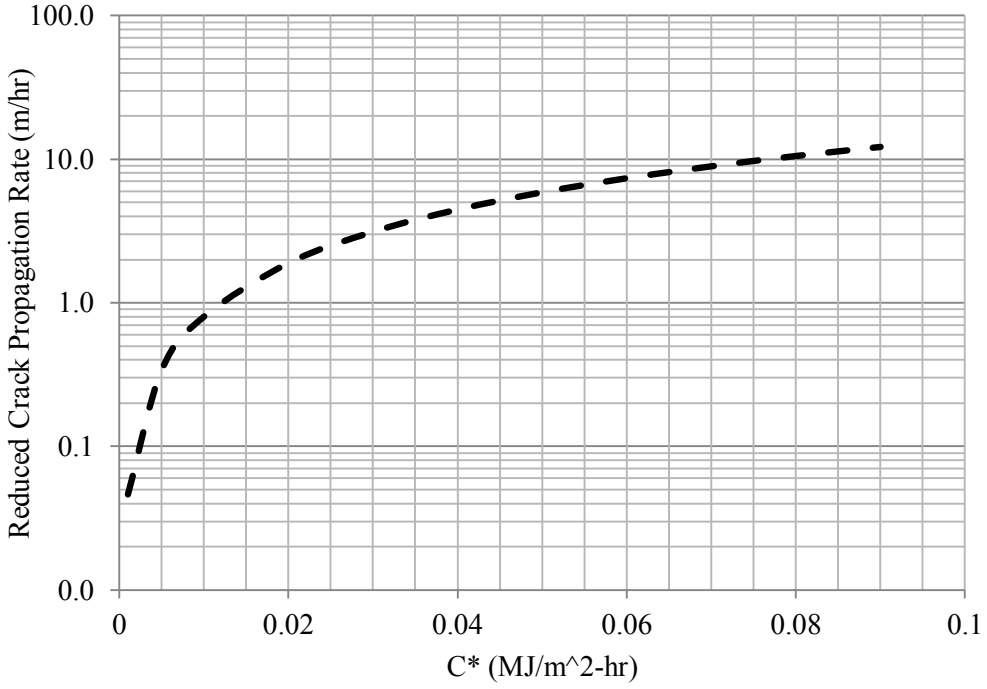

Figure 144 Example crack growth rate master curve (Ref =21°C).

The actual crack growth rate through a pavement layer for a given temperature and C* value can be extracted from the crack growth rate master curve according to Equation 8.5.

$$\frac{da}{dt} = \frac{\dot{a}_\xi}{a_T} \qquad \textbf{8.5}$$

Where:

a_ξ = reduced crack growth rate (m/hr),

da/dt = crack growth rate (m/hr), and

a_T = shift factor for temperature (T) from the CFT.

8.7 Method to Calculate Crack Propagation

Once a crack has initiated in a pavement layer, propagation of the crack based on creep fracture can be described according to Equation 8.6. Here, time-dependent crack growth rate is transformed to crack growth per load cycle using the loading frequency. This transformation concept, described in Section 2.6, needs to be verified as part of future research. The crack growth rate master curve shift factor (a_T) is included in this equation in order to determine the actual crack growth at the pavement temperature of interest.

$$\left(\frac{\mathrm{da}}{\mathrm{dN}}\right)_{\mathrm{creep}} = \mathrm{a}(\mathrm{C}^*)^{\mathrm{b}} * \left(\frac{1}{36 * \mathrm{f} * a_T}\right) \qquad \textbf{8.6}$$

Where:

$\frac{da}{dN}$ = creep crack growth per load cycle (mm/cycle),

C* = power release rate (MJ/m^2-hr),

f = loading frequency (Hz),

a_T = crack growth rate master curve shift parameter,

a, b = material constants.

Once this relationship has been established, crack growth rate can be determined for any traffic loading conditions and pavement temperatures and cumulative crack

length can be obtained by summing the incremental crack growths over selected seasonal time periods as shown in Equation 8.7.

$$a = \sum_{i=1}^{n} \left(\frac{da}{dN_{creep}} \right)_i * N_i \qquad \textbf{8.7}$$

Where:

i = incremental time period used to determine da/dt, and

n = n^{th} time period of analysis.

Once cumulative crack length (a) in Equation 8.7 reaches the thickness of the layer (t), the corresponding cumulative number of cycles to propagate a crack through a pavement layer (N_p) can be determined by summing corresponding N_i-values. This type of concept can be developed in the form of a fracture mechanics based initiation and propagation model.

8.8 Flow Chart Summary

The flowchart shown in Figure 145 provides a summary of the concept presented in the previous sections including descriptions of notations and terms.

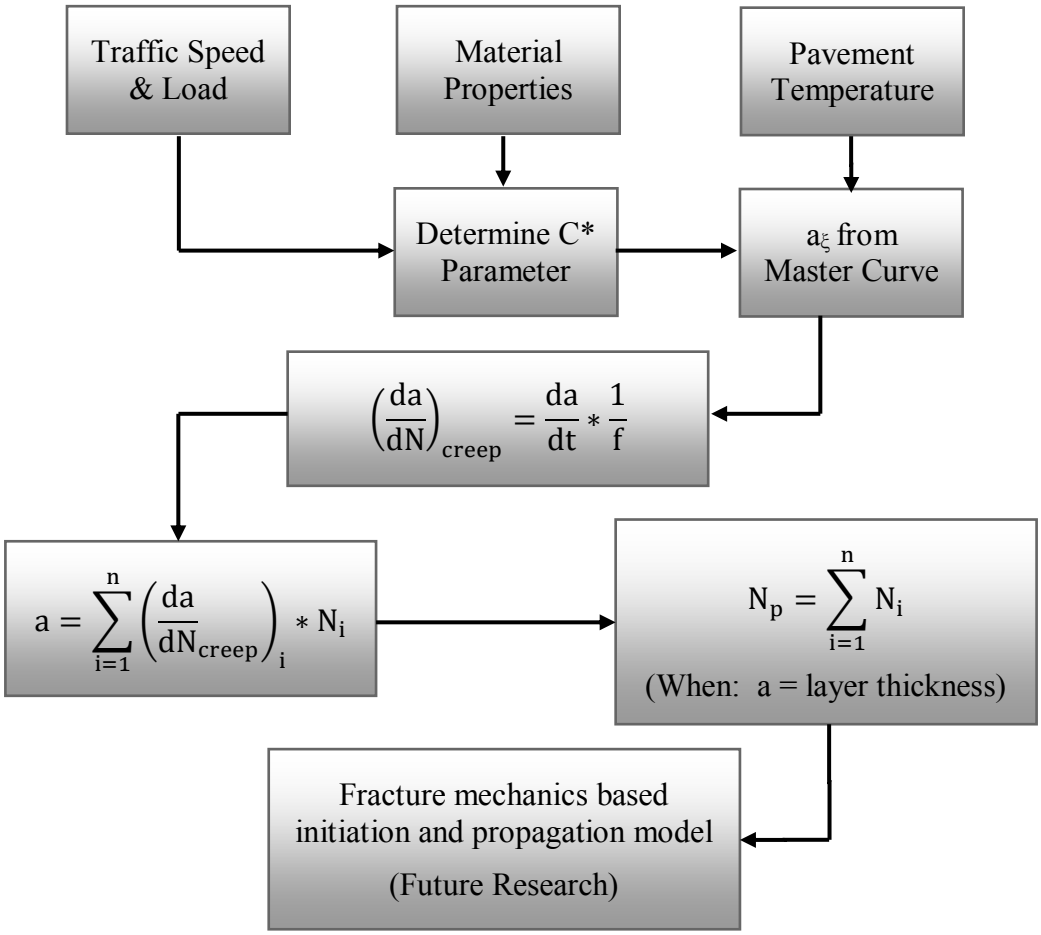

Figure 145 Flowchart showing concept to incorporate crack propagation into pavement analysis and design.

8.9 Summary

This chapter presented development of prediction models which can be used to determine crack growth rate (a*) and the C* parameters. Model development was based on five dense graded, unmodified mixtures: ADOT, PA Cranberry Township, PennDOT I-78, Swedish Stockholm and Evergreen Drive. The total data set included 69 data points crack growth rate measurements and test temperatures ranges from 4.4°C to 37.8°C. These models utilized mixture properties and laboratory performance test data. The C* and a* prediction models can potentially be used in pavement design and analysis

software such as Pavement ME to describe crack propagation as a function of the C* parameter, traffic and temperatures if CFT test data is not readily available. The models were able to accurately predict a*-C* and C*-Δ* relationships for the five different mixtures in the database; however, these models should be verified and improved as additional CFT test data become available. Finally, models should be developed for modified mixtures such as fiber reinforced and asphalt rubber mixtures.

In addition, the final section of this chapter presented a conceptual approach to incorporate the a*-C* relationship into pavement analysis and design procedures. This method uses a crack growth rate master curve, obtained from CFT tests, to determine different crack growth rates as a function of traffic speed and load, material properties and pavement temperatures. Creep crack growth is summed over the analysis period or design life to determine the propagated crack length as function of load cycles. This conceptual approach potentially can provide better analysis of crack behavior in asphalt pavement structures if included in a fracture mechanics based initiation and propagation model.

Chapter 9

9 SUMMARY, CONCLUSIONS AND RECOMMENDATIONS

9.1 Summary

The main objective of this research study was to develop and document a standard test procedure for a fracture mechanics based, C* Fracture Test (CFT) to assess crack resistance and propagation in asphalt concrete in the laboratory. Unlike other common fracture mechanics based tests, the unique notched disk specimen provides a simple geometry and allows the splitting tensile stress to be directly applied to the crack tip region. In addition, the C* parameter considers the time-dependent behavior of asphalt concrete and does not require the assumption of linear elasticity. This work builds on the application of the C* Line Integral test to asphalt concrete in the early 1980's by Abdulshafi (1983) at The Ohio State University. This test has shown promise to capture crack resistance along with crack propagation within asphalt concrete.

Using a laboratory produced mixture in this research; a study was conducted at 21°C to recommend a specimen size for the CFT. A 150 x 50 mm size was proposed as the standard specimen size as it was easily produced from a gyratory specimen and also provided ample area for crack growth and monitoring. Using this specimen size, additional tests were carried out at 0, 4.4, 10 and 37.8°C to evaluate the effect of test temperature on CFT results for the ADOT mixture. In addition, modifications were recommended to the test procedure to improve the easy and quality of data from the test.

Finite element analysis was conducted on the CFT specimen to analyze the stress distributions and location of the tensile stresses and crack location under creep loading. Two diameters, 150 mm and 100 mm, were considered in the analysis which assumed

elastic conditions for simplicity. Numerical simulations captured the tensile stress development at the crack tip region and numerical simulations corresponded well with laboratory test results.

Using the concept of time-temperature superposition, a reduced crack growth rate master curved was developed using CFT data at different temperatures. This concept of a reduced crack growth rate master curve can potentially useful in design to describe crack growth behavior under different loading and temperature conditions.

A proposed C* Facture Test standard was drafted as part of this research and includes all findings of this study. This test standard can be used as part of future CFT research and can serve as a basis to standardize the CFT.

Several field mixtures were subjected to the CFT in order to assess the test's ability to distinguish between several modified asphalt concrete mixtures' resistance to crack growth and to begin development of an ASU CFT results database. Field mixtures included the following: two dense graded, HMA mixtures, two dense graded HMA mixtures modified with fiber reinforcement, one dense graded WMA and one gap-graded WMA with asphalt rubber modification.

The final task involved development of C* and crack growth rate prediction models which can potentially be implemented in Pavement ME or other pavement design or analysis procedures. In addition, a proposed method of incorporating the C* parameter and crack growth rate data into pavement analysis and design was presented.

9.2 Conclusions

The following sections describe the conclusions from this study.

9.2.1 CFT Test Method Development

The existing C* Line Integral test method was evaluated and recommendations were presented to improve the ease of the test and data acquisition methods. Modifications included use of a video camera to record crack growth as a function of time, a recommended crack growth rate analysis range of 20-80 mm for improved data quality and recommendations for specimen preparation. Finally a detailed C* Fracture Test protocol was prepared which outlines specimen preparation, test procedure, data analysis techniques and data reporting.

The simplicity of this CFT makes it an attractive laboratory test to characterize resistance to crack propagation. First, the required jig can be produced by a simple modification to a standard Lottman breaking head or IPC AMPT Indirect Tensile Jig used for the Indirect Tensile Test (IDT). Second, high quality video recording equipment are widespread on the market and can easily be obtained. Finally, the test procedure requires only load and time data to be collected during the test by data acquisition software. Thus, the CFT can be performed on essentially any type of load frame with environmental controls and necessary load capacity. For example, the IPC Global, Asphalt Mixture Performance Tester (AMPT) could be candidate equipment to perform the CFT with minor modifications. This type of equipment is quickly becoming popular laboratory equipment because of its capabilities to run dynamic modulus tests. The AMPT can accommodate the recommended test temperature of 10°C and 4.4°C if necessary and the clear chamber should allow recording of crack length with no disruption to specimen

temperature. However, the maximum load typically required to initiate crack growth in dense graded specimens at 10°C approaches or exceeds 15 kN. Thus, modifications to specimen thickness would have to be considered in order to reduce the maximum load required to initiate crack growth.

9.2.2 Specimen Size and Test Condition Study

Three specimen sizes were evaluated using the CFT (diameter x thickness): 150 x 50 mm, 150 x 25 mm and 100 x 50 mm. Statistical comparisons of the results found that specimen thickness had a greater effect on test results than diameter as the 150 x 50 mm, 100 x 50 mm specimens produced similar results which were found to be statistically insignificant. However, a 150 x 50 mm specimen provides a larger area for crack growth and thus was recommended as the standard specimen size for the CFT. These conclusions were based on a 19 mm, dense graded mixture and should be verified for smaller nominal maximum aggregate sizes.

CFT test results were presented for the different temperatures included in the test temperature study. Results were rational in that crack growth rate increased as test temperature decreased. For 4.4°C, crack growth rates are higher at all C* values when compared to results at 21°C. For the ADOT mixture, there appeared to be an upper threshold temperature (21°C) after which no significant decrease in crack growth rates was observed in the CFT. The lower limit temperature was 4.4 °C as testing at 0°C produced crack growth rates too rapid to provide rational results with the video recording equipment. It can be concluded that there is an optimal mixture stiffness range where crack propagation is an important parameter to consider.

9.2.3 Finite Element Modeling of CFT Specimens

Numerical simulations on both diameter CFT specimens were able to replicate laboratory load-displacement curves for a loading rate of 0.228 mm/min (21°C). The 100 mm diameter specimen required about 66% of the peak load of the 150 mm diameter to initiate crack growth. However, in both cases, simulations overestimated the load in the tail end of the curve. This may have been caused by applying assumptions of linear damage or purely elastic analysis.

CFT load configuration resulted in horizontal tensile stress development at the crack tip. Crack tip stress development was more rapid in the 100 mm diameter specimens. Simulations show that the base plate did not induce noticeable indirect tensile stresses within the specimen. However, this should be further examined with the inclusion of large aggregate in the model.

A zone of horizontal compressive stresses exists at the base plate which could potentially hinder crack growth towards the bottom of the specimen. The magnitude can be rather large but is reduced as crack length increases.

Non-uniform shear stress was observed at the crack tip as the crack approached the bottom of the specimen. It was concluded that the effect of crack tip tensile stress (Mode I) on crack growth diminished toward the bottom of the specimen and Mode II crack growth was evident which allowed continual propagation of the crack through the specimen.

Simulation indicated that the majority of the deformation at the original crack tip location was horizontal which was desirable. A vertical deformation component does exist but appears to be small in comparison to horizontal deformation for the material

properties in consideration. LVDTs mounted on an actual test specimens subjected to the CFT confirmed that small vertical deformation occurred.

Crack growth occurred prior to peak load in numerical simulations which does not match laboratory data. The crack tip observed in numerical simulation could be considered a micro-crack which is not visible to the human eye in a CFT specimen. Crack length in numerical simulations was defined as the location where an adjacent node experienced a given horizontal deformation (macro-crack). After applying this adjustment, simulated crack growth appeared reasonable in comparison to actual crack growth observed in laboratory specimens tested at the same conditions.

Since fracture occurred at a lower maximum load in the 100 mm diameter specimen, less potential for unrecoverable deformation exists when compared to the 150 mm diameter specimen. However, less area was available for crack growth in the 100 mm diameter specimen and a more non-linear crack growth trend was observed in comparison to the 150 diameter specimen. In addition, the presence of large aggregate (19 mm or greater) can further reduce the area available for fracture and complicate crack growth patterns.

Numerical simulations confirmed that the 150 mm diameter specimen is the preferred diameter for the CFT. Stress and deformation analysis appeared reasonable and similar for both diameter specimens yet the 150 mm diameter specimen provides larger area for crack growth.

9.2.4 Development of a Crack Growth Rate Master Curve

The concept of the reduced crack rate master curve, presented by Seo et al (2004) was applied to C* and crack growth rate data from the CFT. For comparison, reduced

crack growth rate data were fitted using a power function and log transformed data were fit using a linear function. Both methods gave excellent adjusted R^2-values and S_e/S_y values, however; the linear fit of log transformed data method provided better prediction of measured crack growth rate data (R^2_{adj} =0.95; S_e/S_y=0.219).

Plots of log shift factor versus temperature take the form of a hyperbolic tangent (tanh) function since minimal shifting is required from 37.8°C to the reference temperature of 21°C. This is rational for the ADOT mixture since, at 37.8°C, no significant increase in crack growth rate is observed for an increase in C* when compare to data at 21 °C. At higher temperatures, the effect of energy release on crack growth rate diminishes as creep deformation becomes a more significant factor. This corresponds with a discussion provided by Saxena (1980) when conducting C* tests on metals at high temperatures. For the same displacement rate, crack length and specimen size, creep deformation rate will be greater for a sample tested at a higher temperature. Thus, in order to maintain the same displacement rate, crack growth rate must be lower.

It appears that the shift factors do not correspond with the dynamic modulus master curve shift factors used in the process described by Seo et al (2004). The crack growth rate master curve shift factors do not follow the typical polynomial trend observed in plots of dynamic modulus master curve (log) shift factors and test temperature.

Development of the crack growth rate master curve can be beneficial to evaluate seasonal differences in crack propagation rates in asphalt concrete as a function of pavement temperature and C* values. In the future, a crack growth rate master curve can

be incorporated into pavement design software such as Pavement ME to evaluate cracking as a function of different loading rates and pavement temperatures.

9.2.5 Development of ASU C* Database

The ASU C* database was developed to provide a summary of ASU CFT test results for plant mixtures and laboratory produced mixtures. Mixtures were dense and gap-graded and contained different binder types, air voids and modifiers such as rubber and fiber reinforcement. Specimens included both hot mix asphalt (HMA) and warm mix asphalt (WMA). Overall, it was found that the CFT is able to capture differences in resistance to crack propagation for several types of mixtures and test temperatures.

At certain temperatures, CFT test results did not follow expected trends and excessive deformation and branch cracking was observed. This led to the observation that mixture stiffness at CFT temperature plays in important role in observing single macro-crack growth. For an initial recommendation, mixtures should be subjected to the CFT at temperatures where the dynamic modulus value (0.1 Hz) falls between 5,000 MPa (725 ksi) and 17,000 MPa (2,466 ksi). If dynamic modulus data are not available, initial tests should be conducted at a temperature of 10°C. If excessive branch cracking or specimen deformation is observed, test temperature should be lowered to 4.4°C. In addition, a stiffness based relationship is presented to provide guidance on selecting the initial displacement rate of the CFT.

Finally, test data available in this database can be used in future analysis and to correlate laboratory test results to field cracking data collected at the respective field sites were the mixtures were placed.

9.2.6 Prediction Model Development

Using data from the CFT database, crack growth rate (a*) and C* prediction models were developed. Model development was based on four dense graded (one gap-graded), unmodified mixtures: ADOT, PA Cranberry Township, PennDOT I-78, Swedish Stockholm (gap-graded) and Evergreen Drive. The total data set included 69 data points crack growth rate measurements and test temperatures ranges from 4.4°C to 37.8°C.

The final crack growth rate model (Equation 9.1) has an $R^2_{(adj)}$ value of 0.91 and was verified by accurately predicting a*-C* trends for the unmodified mixtures in the CFT database, with the exception of the PA Cranberry Township mixture where crack growth rates were under predicted.

$$\log a^* = 26.5848 + 0.97764 * \log C^* + 2.53324\,x\,10^{-5} * \eta + 0.34335 * \%B^2 + 0.00366\,(\eta * C) + 2.45468\,x\,10^{-9} * E_{01}^2 - 11.6053 * \log m - 56.0271 * \log \%B \qquad \textbf{9.1}$$

R^2_{adj}= *0.91*
S_e/S_y =*0.30*

The final C* model (Equation 9.2) has an $R^2_{(adj)}$ value of 0.99 and was verified by accurately predicting C*-Δ* trends for the unmodified mixtures in the CFT database, with the exception of the PA Cranberry Township mixture where C* values were under predicted.

$$\log C^* = -0.339753 + 1.15875 * \log \Delta + 0.61069 * \log E_{01} + 0.00492 * (\rho_{9.5} * \log \Delta) + 5.26501 * \log m - 0.32401 * \log \rho_{9.5} \qquad \textbf{9.2}$$

R^2_{adj}= *0.99*
S_e/S_y =*0.11*

These models can potentially be used in pavement design and analysis software such as Pavement ME to describe crack propagation as a function of the C* parameter, traffic and temperatures if CFT test data is not readily available. However, models should be verified and improved as additional CFT test data become available. In

addition, models should be developed for modified mixtures such as fiber reinforced and asphalt rubber mixtures once data becomes available.

9.2.7 Potential Method to Incorporate C* and a* into Pavement Design and Analysis

A conceptual approach to incorporate the a*-C* relationship into pavement analysis and design procedures was presented. This method uses the concept of a crack growth rate master curve, obtained from CFT tests, to determine different crack growth rates as a function of traffic speed and load, material properties and pavement temperatures. Once this relationship is established, creep crack growth can be calculated and summed over the analysis period or design life to determine the crack length as a function of load cycles. The a*-C* relationship can be potentially used in future thermal cracking or top-down cracking models to describe a fracture mechanics based crack propagation phase.

9.3 Recommendations for Future Work

The following sections describe recommendations for future work regarding the CFT.

9.3.1 Dynamic Loading

Expand initial dynamic CFT results using different load magnitudes and frequencies. These results should be used to determine if a relationship exists between static and dynamic CFT results (as a function of test frequency), similar to the concept presented in Section 2.6. Obtaining crack growth per cycle from static CFT results will significantly reduce the laboratory testing effort required by dynamic tests. However, the following need to be resolved prior to performing the CFT in dynamic conditions:

1. Constant load control should be evaluated and compared to other potential modes of loading such as constant displacement CMOD. The potential issue with load control is that the crack growth is very minimal for a large number of cycles. However, once the crack approaches the 40-50 mm reference lines, it takes a relatively small number of cycles to drive the crack through the remainder of the specimen. Alternatively, an endurance limit may exist where constant dynamic loading below this level does not result in crack propagation. A confining mechanism on the notched disk specimen may be used to better simulate in-place confinement experienced in pavements.
2. Development of geometric correction factors necessary to compute the C* parameter according to the method presented in Nikbin and Webster (1988). This will require numerical simulation of the CFT specimens in order to compute the correction factor necessary in the referenced C* calculation method. Once, the C* values are computed for dynamic conditions a relationship between static and dynamic CFT results can be explored.

9.3.2 Explore Additional Methods to Calculate C*

Several closed form solutions to calculate the C* parameter are available in the literature. However, applicability of these equations to the notch disk specimen is not yet fully understood. Assumptions presented in development of these equations should be further investigated prior to use in the analysis of C* from notched disk asphalt concrete specimens.

The use of a closed form solution is desirable because it calculates a C* parameter which is independent of other specimens in the multi-specimen test sequence. In the

graphical method, the value of C* is highly dependent on test results from specimens tested a lower displacement rates in the sequence. Thus, it is possible to have a poor test at the initial displacement rate that can affect all C* calculations at the given crack length.

Development of a closed form solution will help determine different C* values as a crack propagates through a specimen. Recall that the graphical method assumes a linear fit of U* versus crack length. At times, this relationship followed a non-linear s-curve which indicated slower crack growth rates at short and long crack lengths. Considering this concept, it is possible that the C* parameter could be used to describe slow or no crack growth after a certain depth in thick pavements.

9.3.3 SIF Calculation using the CFT Results

The stress intensity factor (K) has widely been applied to fracture analysis of asphalt concrete and can also be obtained from the CFT. However, the geometric correction factor, a necessary part of the calculation, has not yet been derived for the 150 mm diameter, notched disk specimen. Future numerical simulation should be used to determine this factor which will allow the relationship between stress intensity factor and crack propagation rate to be determined using the notched disk specimen and compared with results from already standardized asphalt concrete fracture tests.

9.3.4 Consideration of Anisotropy

In the current CFT, specimens are compacted vertically but cut and tested in the horizontal direction (90° from direction of compaction). Future analysis and testing should consider specimens cut axially in the same direction as compaction and compare results to those cut horizontally. This analysis will help to determine the effects of anisotropy on CFT results.

9.3.5 Viscoelastic Numerical Simulation of CFT

Numerical simulation of CFT specimens using ABAQUS should consider viscoelastic behavior of the materials. Although the elastic assumptions applied to the modeling provided verification of the CFT, difficulties arose in modeling when vertical and/or horizontal creep deformation became a more pronounced factor during the test. The elastic simulations were unable to match laboratory data when there was a poorly defined peak load (longer time at peak load on the load-deformation plot) during the CFT. Figure 146 presents an example of typical results when elastic simulation did not match laboratory test data.

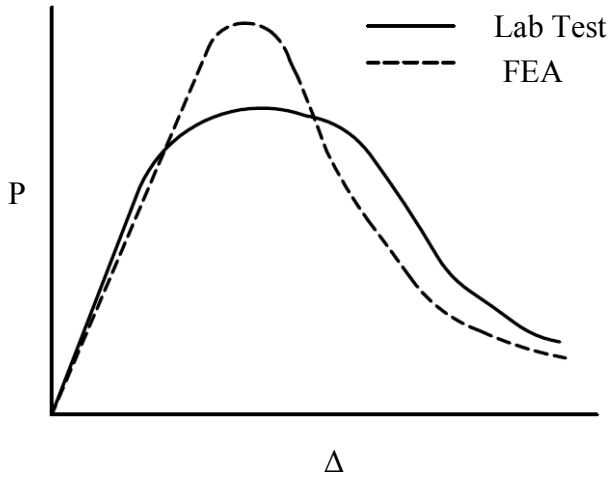

Figure 146 Example of FEA and laboratory comparison.

9.3.6 Development of Simplified Performance Test

A simplified version of the CFT should be developed to serve as an assessment tool for resistance to crack propagation during the mixture design process. This simplified test could also serve as performance test to evaluate fracture or the presence and/or usefulness of modifies to the asphalt concrete such as asphalt rubber or fiber reinforcement. A potential performance test could consider three or four loading rates and

threshold limits for crack growth rate as a function of C* trends at those levels could be established. These thresholds could be established based on design reliability, size of project, local conditions, and so forth. Figure 147 shows an example when four test results fall within a specified acceptance region.

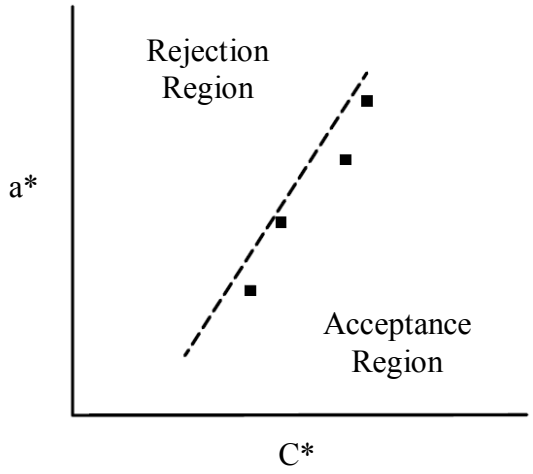

Figure 147 Example performance test acceptance criterion.

In addition, the existing CFT, which utilizes the IPC UTM-100 test equipment, should be conducted using more common laboratory load frames such as the IPC AMPT equipment which is becoming more widely used in laboratories. Use of this type of equipment will allow for a more practical use of the CFT for performance evaluation during the mixture design process.

9.3.7 Future CFT Test Modifications

In order to ensure uniform specimen notches, a jig to cut the right-angle notch should be fully designed and manufactured. The jig should be designed in a way that it can be mounted to a saw table in a fixed location and that one edge of the notch can be cut vertically. The jig should allow the specimen to be rotated so that other notch edge can be cut vertically without moving the fixed base.

Another recommended improvement would be the use of the IPC AMPT Indirect Tensile Jig. Unlike the Lottman breaking head, this jig has guide rods are rotated from the specimen centerline which will allow unobstructed views of the specimen face on both sides.

While the video recording equipment provides a suitable measure of crack growth during the CFT, future research should consider two permanently mounted cameras capable of transferring video to an adjacent computer with on-screen video capture. This will simplify data transfer and streamline testing. It is recommended that a second camera be added to the test setup to capture crack growth on both sides of the specimen and the average growth rate computed.

9.3.8 Digital Image Correlation

To complement recommended numerical simulation on the CFT specimen, a study of the specimen behavior and crack front during the test should be studied using the digital image correlation (DIC) technique. This image analysis will also allow vertical and horizontal deformation to be observed along with the crack behavior.

9.3.9 Consideration of Additional Mixtures, Field Validation and Design Implementation

Conclusions drawn herein are based on limited mixture testing and volumetrics and thus; additional mixtures should be analyzed using the CFT to confirm and supplement research findings. Field and laboratory mixtures, subjected to the test should vary by gradation, binder type and content, air-voids and mixture modification. Data should be used to supplement existing prediction models and recommended test

conditions. Also, within laboratory and across laboratory variability should be addressed and acceptable limits for two tests established.

In order to support the laboratory CFT conclusions, test data from the CFT should be correlated to field crack measurements. This could include measurement of crack type and depths on mixtures already included in the ASU database or through coring pavements and testing field cores using the CFT. In addition, prediction models developed herein should also be validated and calibrated by comparing predicted C* and crack growth rates for pavements with known properties and crack depths.

The final recommendation is to explore ways to incorporate the crack growth relationship to the C* parameter in current pavement analysis and design methods. This task will require a significant research effort and fundamental understanding of both fracture mechanics and pavement design practices. The final product would be a fracture mechanics based crack initiation and propagation model that could be incorporated into current pavement design software such as Pavement ME.

REFERENCES

ABAQUS 6.9 User's Manual. Available online at: http://abaqusdoc.ucalgary.ca/v6.9/, Dassault Systèmes, 2009.

Abdulshafi, O. "Rational Material Characterization of Asphaltic Concrete Pavements," Ph.D. Dissertation, The Ohio State University, 1983.

Abdulshafi, A. and Kaloush, K. "Modifiers for Asphalt Concrete, ESL-TR-88-29", Air Force Engineering and Technical Services Center, Tyndall Air Force Base, Florida, 1988.

Abdulshafi, O. "Effect of Aggregate on Asphalt Mixture Cracking Using Time-Dependent Fracture Mechanics Approach". *Effects of aggregate and Mineral Fillers on Asphalt Mixture Performance, ASTM STP1147-EB, American Society for Testing and Materials*, Philadelphia, 1992.

Anderson, T.L. *Fracture Mechanics 3rd Edition, Fundamentals and Applications.* Boca Raton, FL: Taylor and Francis, 2005.

AASHTO T322-07, *Standard Method of Test for Determining the Creep Compliance and Strength of Hot-Mix Asphalt (HMA) Using the Indirect Tensile Test Device.* American Association of State and Highway Transportation Officials, 2007.

ASTM D7313-07a, *Standard Test Method for Determining Fracture Energy of Asphalt-Aggregate Mixtures Using the Disk-Shaped Compact Tension Geometry.* Annual Book of ASTM Standards, 04-03. ASTM International, West Conshohocken, PA, 2010: 991-997.

ASTM D6931-07, *Standard Test Method for Indirect Tensile (IDT) Strength of Bituminous Mixtures.* Annual Book of ASTM Standards, 04-03. ASTM International, West Conshohocken, PA, 2007.

ASTM E1457-07e4, *Standard Test Method for Measurement of Creep Crack Growth Times in Metals.* Annual Book of ASTM Standards, 03-01. ASTM International, West Conshohocken, PA, 2007.

Arbani, M. and Ferdwoski, B., "Evaluating the Semi-Circular Bending Test for HMA Mixtures." *International Journal of Engineering, Transactions A, 22* (1), 2009: 47-58.

Broek, D. *Elementary Engineering Fracture Mechanics, 4th ed*. Netherlands: Springer, Netherlands, 1986.

Christensen, D.W. and Bonaquist, R.F. *NCHRP Report 530: Evaluation of Indirect Tensile Test (IDT) Procedures for Low-Temperature Performance of Hot Mix Asphalt.* Transportation Research Board– National Research Council, Washington, D.C.: National Academy Press, 2004.

European Standard FprEN 12697-44. *Bituminous Mixtures – Test Methods for Hot Mix Asphalt – Part 44: Crack Propagation by Semi-Circular Bending Test.* European Committee for Standardization, Brussels, Belgium, 2010.

FHWA, (2001). Highway Statistics. Federal Highway Administration, Washington, D.C.

Goldman, N.L. & Hutchinson, J.W. "Fully Plastic Crack Problems: The Center-Cracked Strip under Plane Strain." *International Journal of Solids and Structures, 11*, 1975: 575-591.

Harper, M.P. & Ellison, E.G., "The use of the C* Parameter in Predicting Crack Propagation Rates." *Journal of Strain Analysis, 12* (3), 1977: 167-179.

Haigh, J.R. & Richards, C.E., *Yield Point Loads and Compliance Functions of Fracture Mechanics Specimens, C.E.G.B, C.E.R.L, Report RD/L/M461*, 1994.

Hofman, R., Oosterbaan, S., Erkens, J. & van der Kooij, J., "Semi-Circular Bending Test to Assess the Resistance Against Crack Growth." *Proceedings: Sixth International RILEM Symposium on Performance Testing and Evaluation of Bituminous Materials.* RILEM Publications SARL, 2003: 257-263.

Huang, B., Shu, X. & Tang, Y., (2005) Comparison of semi-circular bending and indirect tensile strength tests for HMA mixtures. *Proceedings of the Sessions of the ASCE Geo-Frontiers - Advances in Pavement Engineering, GSP 130*, 155-169.

Huang, Y., *Pavement Analysis and Design, 2nd Edition*. New Jersey: Pearson Prentice Hall, 2004.

Hutchinson, J.W., "Singular Behavior at the End of a Tensile Crack Tip in a Hardening Material." *Journal of the Mechanics and Physics of Solids, 16*, 1968: 13-31.

Ioannides, A. M., "Fracture Mechanics in Pavement Engineering: The specimen-size effect." *Transportation Research Record, 1568*, 1997: 10-16.

Jacobs, M., Hopman, P., Molenaar, A., "Application of Fracture Mechanics Principles to Analyze Cracking in Asphalt Concrete." *Journal of the Association of Asphalt Paving Technologists, 65*, 1996: 1–39.

Jacobs MMJ. *Crack Growth in Asphaltic Mixes*, Ph.D. Dissertation, Technical University Delft, Netherlands, 1995.

Janssen, M., Zuidema, J. and Wanhill, R. *Fracture Mechanics*, New York: Spon, 2002.

Kaloush, K., Biligiri, K., Zeiada, W., Rodezno, M., & Reed, J., "Evaluation of Fiber-Reinforced Asphalt Mixtures Using Advanced Material Characterization Tests." *ASTM Journal of Testing and Evaluation, 38*(4), 2010: 1-12.

Kaloush, K., Biligiri, K., et al., *Laboratory Evaluation of Rubber and Polymer Modified Bituminous Mixtures Constructed in Stockholm (E18 Highway between Järva Krog & Bergshamra Interchanges)*. Arizona State University, 2010b.

Kim, H., Wagoner, M. and Buttlar, W., "Numerical Fracture Analysis on the Specimen Size Dependency of Asphalt Concrete using a Cohesive Softening Model." *Construction and Building Materials, 23*, 2009: 2112-2120.

Kim, Y.R. and Wen, H., "Fracture Energy from Indirect Tension Testing." *Journal of the Association of Asphalt Paving Technologists, 71*, 2002: 779-793.

Kleemans, C., Zuidema, J., Krans, R., Molenaar J. and Tolman, F. "Fatigue and Creep Crack Growth in Fine Sand Asphalt Materials." *ASTM Journal of Testing and Evaluation*, *25*(4), 1997: 424-428.

Krans, R.L., Tolman, F. & Van de Ven, M.F.C., "Semi-Circular Bending Test: A Practical Crack Growth Test using Asphalt Concrete Cores. *Reflective Cracking in Pavements,* RILEM, London: E& FN Spon, 1996: 123-132.

Kuai, H., Lee, H.J., Zi, G. and Mun, S., "Application of Generalized *J*-Integral to Crack Propagation Modeling of Asphalt Concrete Under Repeated Loading." *Transportation Research Record, 2127*, 2009: 72-81.

Landes, J.D. & Begley, J., "A Fracture Mechanics Approach to Creep Crack Growth." *Mechanics of Crack Growth; Proceedings of the Eighth National Symposium on Fracture Mechanics, 590*, 1976: 128-148.

Lee, N.K. and Hesp, S.A.M., "Low Temperature Fracture Toughness of Polyethylene-Modified Asphalt Binders, *Transportation Research Record 1436*, 1994: 54-59.

Lee, N.K., Morrison, G.R. and Hesp, S.A.M, Low Temperature Fracture Toughness of Polyethylene-Modified Asphalt Binders and Asphalt Concrete Mixes. *Journal of the Association of Asphalt Paving Technologists, 64*, 1995: 534-574.

Li, X. and Marasteanu, M., "The Fracture Process Zone in Asphalt Mixture at Low Temperature." *Engineering Fracture Mechanics, 77,* 2010: 1175-1190.

Li, X. and Marasteanu, M., "Using Semi Circular Bending Test to Evaluate Low Temperature Fracture Resistance for Asphalt Concrete." *Experimental Mechanics, 50*(7), 2009: 867-876.

Li, X. and Marasteanu, M., "Investigation of Low Temperature Cracking in Asphalt Mixtures by Acoustic Emission." *International Journal of Road Materials and Pavement Design, 7*(4), 2006: 491-512.

Li, X. and Marasteanu, M., "Evaluation of the Low Temperature Fracture Resistance of Asphalt Mixtures using the Semi-Circular Bend Test." *Journal of the Association of Asphalt Paving Technologists, 73*, 2004: 401–426.

Lytton, R., Uzan, J. and Fernando, E., et al. *Development and Validation of Performance Prediction Models and Specifications for Asphalt Binders and Paving Mixtures. Report SHRP-A-357.* Strategic Highway Research Program, National Highway Research Program, Washington D.C., 1993.

Majidzadeh, K., E.M. Kauffmann, D.V. Ramsamooj, and Chan, A.T. (1970). *Analysis of Fatigue and Fracture of Bituminous Paving Mixtures, Report No. 2546.* U.S. Bureau of Public Roads. Research and Development, 1970.

Marasteanu, M., et al, Investigation of Low Temperature Cracking in Asphalt Pavements, National Pooled Fund Study 776. University of Minnesota, 2007.

Mobasher, B., Mamlouk, M and Lin, H-M. "Evaluation of Crack Propagation Properties of Asphalt Mixtures." *ASCE Journal of Transportation Engineering*, *123*(5) 1997: 405-413.

Molenaar, A., Scarpas, A., Liu, X. & Erkens, G., "Semi-Circular Bending Test; Simple but Useful?" *Journal of the Association of Asphalt Paving Technologists, 71*, 2002: 794-815.

Molenaar, A.A.A., *Structural Performance and Design of Flexible Road Constructions and Asphalt Overlays.* Ph.D. Dissertation, Delft University of Technology, Netherlands, 1983.

Mull, M.A., Othman, A., & Mohammad, L. "Fatigue Crack Propagation Analysis of Chemically Modified Crumb Rubber-Asphalt Mixtures." *Journal of Elastomers and Plastics, 37*, 2005: 73-87.

Neter, J., Kutner, M., Nachtsheim, C. and Wasserman, W. *Applied Linear Regression, Third Edition.* Chicago: IRWIN, 1996.

Nikbin, K.M. and Webster, G.A., "Prediction of Crack Growth under Creep-Fatigue Loading Conditions." *Low Cycle Fatigue, ASTM STP 942, H.D.* Solomon, G.R. Halford, L.R. Kaisand, and B.N Leis, Eds., American Society for Testing and Materials, Philadelphia, 1988: 281-292.

Paris, P.C. and Erdogan, F., "A Critical Analysis of Crack Propagation Laws." *Transactions of the ASME, Journal of Basic Engineering, Series D, 85*(3), 1963: 528-534.

Pérez-Jiménez, F., Valdés, G., Miró, R., Marínez, A, and Botella, R. "Fénix Test Development of a New Test Procedure for Evaluating Cracking Resistance in Bituminous Materials." *Transportation Research Record, 2181*, 36-43, 2010.

Rice, J.R., "A Path Independent Integral and the Approximate Analysis of Strain Concentration by Notches and Cracks." *Journal of Applied Mechanics, 35*, 1968: 379-386.

Rice J.R., Rosengren, G.F., "Plane Strain Deformation near a Crack Tip in a Power-Law Hardening Material." *Journal of the Mechanics and Physics of Solids, 16*, 1968: 1-12.

Rodezno, M.C., Kaloush, K. and Corrigan, M. "Development of a Flow Number Predictive Model." *Transportation Research Record, 2181*, 79-87, 2010.

Roque, R., Zhang, Z. and Sankar, B., "Determination of Crack Growth Rate Parameters of Asphalt Mixtures Using the Superpave IDT." *Journal of the Association of Asphalt Paving Technologists, 68*, 1999: 404-433.

Saxena, A. *Crack Growth, Temperature-Fatigue Interaction*, Editors: L. Remy and J. Petit, ESIS Publication 29, Elsevier Science Ltd, 2002.

Saxena, A., "Evaluation of C* for the Characterization of Creep Crack Growth Behavior in 304 Stainless Steel. *Fracture Mechanics: 12th Conference, ASTM STP 700, American Society for Testing and Materials,* 1980: 131-151.

Schapery, R.A., *Time-Dependent Fracture: Continuation Aspects of Crack Growth.* Encyclopedia of Materials Science and Engineering, M.B., Bever (ed.), New York: Pergamon Press, 1986: 5043-5053.

Schapery, R.A., "Corrspondence Principles and a Generalized J Integral for Large Deformation and Fracture Analysis of Viscoelastic Media." *International Journal of Fracture, 25,* 1984: 195-223.

Schwartz, C.W., Gibson, N. and Schapery, R.A. Time-temperature superposition for asphalt concrete at large compressive strains. *Transportation Research Record, 1789*, 101-112, 2002.

Seo, Y., Kim, Y.R., Schapery, R.A., Witczak, M.W., and Bonaquist, R., "A Study of Crack-Tip Deformation and Crack Growth in Asphalt Concrete using Fracture Mechanics. *Journal of the Association of Asphalt Paving Technologists, 73*, 2004: 697-730.

Tschegg, E.K., Jamek, M. & Lugmayr. R., "Fatigue Crack Growth in Asphalt and Asphalt-Interfaces." *Engineering Fracture Mechanics 78*, 2011: 1044-1054.

Uzan, J., "Evaluation of Fatigue Cracking." *Transportation Research Record, 1570,* 1997: 89-95.

Vinson, T.S, Janoo, V. & Haas, R., *SHRP-A-306 - Low Temperature and Thermal Fatigue Cracking SR-OSU-A-003A-89-1.* Transportation Research Board, Washington D.C. Accessed online at: http://onlinepubs.trb.org/onlinepubs/shrp/SHRP-A-306.pdf, 1989.

Vinson, T.S., Janoo, V.C. and Haas, R.C.G., *Low Temperature and Thermal Fatigue Cracking*, SHRP Summary Report No. A-003A, 1989b.

Von Quintus, H.L. *Performance Prediction Models in the Superpave Mix Design System.* SHRP Report No. A-699. 1994.

Walubita, L., Jamison, B., Das, G. Scullion, T., Martin, A.E., Rand, D., Mikhail, M., "HMA Crack Characterization: Search for Laboratory Test to Evaluate HMA Mixture Crack Resistance. *Transportation Research Record, 2210,* 2011: 73-80.

Wagoner, M.P. *Fracture Tests for Bituminous-Aggregate Mixtures: Laboratory and Field Investigations*, Ph.D. Dissertation, University of Illinois at Urbana-Champaign, Urbana, IL, 2006.

Wagoner, M.P., Buttlar, W. & Paulino, G., "Disk-Shaped Compact Tension Test for Asphalt Concrete Fracture." *Society for Experimental Mechanics, 45*(3), 2005a: 270-277.

Wagoner, M.P., Buttlar, W., Paulino, G. & Blankenship, P., "Investigation of the Fracture Resistance of Hot-Mix Asphalt Concrete using a Disk-Shaped Compact Tension Test." *Transportation Research Record, 1929,* 2005b: 183-192.

Wagoner, M.P., Buttlar, W., Paulino, G. & Blankenship, P., "Development of a Single-Edge Notched Beam Test for Asphalt Concrete Mixtures. *ASTM Journal of Testing and Evaluation, 33*(6), 2005c: 1-9.

Witczak, M.W. et al., *Simple Performance Test for Superpave Mix Design, NCHRP Report 465*. Transportation Research Board– National Research Council, Washington, D.C.: National Academy Press, 2002.

Wu, D., Christian, E.M. & Ellison E.G., "Evaluation of Creep Crack C* Integrals." *Journal of Strain Analysis, 19* (3), 1984: 185-195.

Zborowski, A. and Kaloush, K, "A Fracture Energy Approach to Model the Thermal Cracking Performance of Asphalt Rubber Mixtures." *Road Materials and Pavements Design Journal, 12*(2), 2011: 377-395.

Zborowski, A., *Development of a Modified Superpave Thermal Cracking Model for Asphalt Concrete Mixtures Based on the Fracture Energy Approach.* Ph.D. Dissertation, Arizona State University, 2007.

Zhang, Z., Roque, R. and Birgisson, B., "Evaluation of Laboratory Measured Crack Growth Rate for Asphalt Mixtures." *Transportation Research Record, 1767*, 2001: 67-75.

APPENDIX A

A. CFT TEST DATA AND RAW DATA SUMMARY

Table A.1 ADOT CFT Data at 4.4°C (10-60 mm interval)

Parameter	Replicate Series	Displacement Rate (mm/min)				
		0.03	0.06	0.10	0.15	0.3
C* (MJ/m^2-hr)	1	0.001	0.003	0.007	0.017	0.041
	2	0.001	0.004	0.007	0.012	0.018
	Average	*0.001*	*0.003*	*0.007*	*0.014*	*0.030*
	St. Dev.	*0.00003*	*0.00008*	*0.00015*	*0.00351*	*0.01599*
Crack Growth Rate, a* (m/hr)	1	1.95	1.70	18.22	21.00	62.68
	2	1.00	6.51	10.01	26.85	4.58
	Average	*1.47*	*4.11*	*14.12*	*23.93*	*33.63*
	St. Dev.	*0.671*	*3.405*	*5.803*	*4.141*	*41.084*

Table A.2 ADOT CFT Data at 4.4°C (10-80 mm interval)

Parameter	Replicate Series	Displacement Rate (mm/min)				
		0.03	0.06	0.10	0.15	0.3
C* (MJ/m^2-hr)	1	0.002	0.006	0.011	0.019	0.036
	2	0.003	0.006	0.012	0.017	0.025
	Average	*0.003*	*0.006*	*0.011*	*0.018*	*0.030*
	St. Dev.	*0.00038*	*0.00030*	*0.00034*	*0.00096*	*0.00752*
Crack Growth Rate, a* (m/hr)	1	2.45	2.30	20.11	27.97	84.37
	2	1.18	7.33	12.24	32.55	6.11
	Average	*1.81*	*4.82*	*16.18*	*30.26*	*45.24*
	St. Dev.	*0.895*	*3.557*	*5.566*	*3.235*	*55.341*

Table A.3 ADOT CFT Data at 4.4°C 20-80 mm interval)

Parameter	Replicate Series	Displacement Rate (mm/min)				
		0.03	0.06	0.10	0.15	0.3
C* (MJ/m^2-hr)	1	0.002	0.006	0.011	0.019	0.036
	2	0.003	0.006	0.012	0.017	0.025
	Average	*0.003*	*0.006*	*0.011*	*0.018*	*0.030*
	St. Dev.	*0.00038*	*0.00030*	*0.00034*	*0.00096*	*0.00752*
Crack Growth Rate, a* (m/hr)	1	2.88	5.19	19.17	35.38	222.68
	2	1.34	7.96	14.21	36.24	76.04
	Average	*2.11*	*6.57*	*16.69*	*35.81*	*149.36*
	St. Dev.	*1.086*	*1.960*	*3.508*	*0.611*	*103.689*

Table A.4 ADOT CFT Data at 10°C (10-60 mm interval)

Parameter	Replicate Series	Displacement Rate (mm/min)			
		0.072	0.15	0.23	0.3
C* (MJ/m^2-hr)	1	0.007	0.017	0.024	0.028
	2	0.004	0.009	0.015	0.018
	Average	*0.006*	*0.013*	*0.019*	*0.023*
	St. Dev.	*0.00153*	*0.00526*	*0.00691*	*0.00756*
Crack Growth Rate, a* (m/hr)	1	2.14	2.75	9.59	16.32
	2	4.00	5.27	4.30	25.24
	Average	*3.07*	*4.01*	*6.95*	*20.78*
	St. Dev.	*1.320*	*1.783*	*3.738*	*6.307*

Table A.5 ADOT CFT Data at 10°C (10-80 mm interval)

Parameter	Replicate Series	Displacement Rate (mm/min)			
		0.072	0.15	0.23	0.3
C* (MJ/m^2-hr)	1	0.008	0.019	0.028	0.035
	2	0.006	0.014	0.024	0.030
	Average	*0.007*	*0.017*	*0.026*	*0.033*
	St. Dev.	*0.00116*	*0.00354*	*0.00299*	*0.00317*
Crack Growth Rate, a* (m/hr)	1	1.93	3.26	11.10	13.71
	2	2.26	5.25	4.73	13.01
	Average	*2.09*	*4.25*	*7.92*	*13.36*
	St. Dev.	*0.234*	*1.411*	*4.504*	*0.493*

Table A.6 ADOT CFT Data at 10°C (20-80 mm interval)

Parameter	Replicate Series	Displacement Rate (mm/min)			
		0.072	0.15	0.23	0.3
C* (MJ/m^2-hr)	1	0.008	0.020	0.030	0.037
	2	0.006	0.015	0.026	0.034
	Average	*0.007*	*0.018*	*0.028*	*0.035*
	St. Dev.	*0.00141*	*0.00363*	*0.00245*	*0.00259*
Crack Growth Rate, a* (m/hr)	1	1.89	3.94	13.70	13.24
	2	2.07	5.42	5.67	11.72
	Average	*1.98*	*4.68*	*9.68*	*12.48*
	St. Dev.	*0.130*	*1.049*	*5.677*	*1.076*

Table A.7 ADOT CFT Data at 21°C (150 x 50 mm, 2 replicates, 10-60 mm interval)

Parameter	Replicate Series	Displacement Rate (mm/min)				
		0.15	0.228	0.30	0.378	0.45
C* (MJ/m^2-hr)	1	0.012	0.019	0.025	0.032	0.039
	2	0.008	0.013	0.017	0.023	0.031
	Average	*0.010*	*0.016*	*0.021*	*0.028*	*0.035*
	St. Dev.	*0.00296*	*0.00451*	*0.00600*	*0.00650*	*0.00614*
Crack Growth Rate, a* (m/hr)	1	1.20	1.43	2.76	3.14	2.56
	2	1.18	1.42	2.68	4.58	4.10
	Average	*1.19*	*1.43*	*2.72*	*3.86*	*3.33*
	St. Dev.	*0.019*	*0.010*	*0.059*	*1.016*	*1.093*

Table A.8 ADOT CFT Data at 21°C (150 x 50 mm, 2 replicates, 10-80 mm interval)

Parameter	Replicate Series	Displacement Rate (mm/min)				
		0.15	0.228	0.30	0.378	0.45
C* (MJ/m^2-hr)	1	0.010	0.017	0.023	0.031	0.039
	2	0.010	0.017	0.023	0.031	0.040
	Average	*0.010*	*0.017*	*0.023*	*0.031*	*0.040*
	St. Dev.	*0.00017*	*0.00020*	*0.00013*	*0.00016*	*0.00031*
Crack Growth Rate, a* (m/hr)	1	1.17	1.32	2.54	2.27	3.03
	2	1.18	1.52	2.19	4.41	4.06
	Average	*1.18*	*1.42*	*2.36*	*3.34*	*3.55*
	St. Dev.	*0.008*	*0.140*	*0.249*	*1.515*	*0.727*

Table A.9 ADOT CFT Data at 21°C (150 x 50 mm, 2 replicates, 20-80 mm interval)

Parameter	Replicate Series	Displacement Rate (mm/min)				
		0.15	0.228	0.30	0.378	0.45
C* (MJ/m^2-hr)	1	0.010	0.017	0.023	0.031	0.041
	2	0.011	0.019	0.026	0.035	0.044
	Average	*0.010*	*0.018*	*0.025*	*0.033*	*0.042*
	St. Dev.	*0.00085*	*0.00123*	*0.00178*	*0.00253*	*0.00259*
Crack Growth Rate, a* (m/hr)	1	1.12	1.27	2.61	2.16	4.07
	2	1.13	1.82	2.12	4.30	4.37
	Average	*1.13*	*1.54*	*2.37*	*3.23*	*4.22*
	St. Dev.	*0.008*	*0.395*	*0.352*	*1.509*	*0.211*

Table A.10 ADOT CFT Data at 21°C (150 x 50 mm, 3 replicates, 10-60 mm interval)

Parameter	Replicate Series	Displacement Rate (mm/min)				
		0.15	0.228	0.3	0.378	0.45
C* (MJ/m^2-hr)	1	0.012	0.019	0.025	0.032	0.039
	2	0.008	0.013	0.017	0.023	0.031
	3	0.009	0.015	0.021	0.030	0.036
	Average	*0.010*	*0.016*	*0.021*	*0.028*	*0.035*
	St. Dev.	*0.00214*	*0.00322*	*0.00425*	*0.00472*	*0.00442*
Crack Growth Rate, a* (m/hr)	1	1.20	1.43	2.76	3.14	2.56
	2	1.18	1.42	2.68	4.58	4.10
	3	0.90	1.14	3.70	4.21	4.71
	Average	*1.09*	*1.33*	*3.05*	*3.98*	*3.79*
	St. Dev.	*0.169*	*0.166*	*0.568*	*0.747*	*1.111*

Table A.11 ADOT CFT Data at 21°C (150 x 50 mm, 3 replicates, 10-80 mm interval)

Parameter	Replicate Series	Displacement Rate (mm/min)				
		0.15	0.228	0.3	0.378	0.45
C* (MJ/m^2-hr)	1	0.010	0.017	0.023	0.031	0.039
	2	0.010	0.017	0.023	0.031	0.040
	3	0.011	0.018	0.024	0.033	0.042
	Average	*0.010*	*0.017*	*0.023*	*0.032*	*0.040*
	St. Dev.	*0.00089*	*0.00047*	*0.00068*	*0.00115*	*0.00119*
Crack Growth Rate, a* (m/hr)	1	1.17	1.32	2.54	2.27	3.03
	2	1.18	1.52	2.19	4.41	4.06
	3	0.98	1.42	3.19	3.09	4.85
	Average	*1.11*	*1.42*	*2.64*	*3.26*	*3.98*
	St. Dev.	*0.118*	*0.099*	*0.508*	*1.080*	*0.911*

Table A.12 ADOT CFT Data at 21°C (150 x 50 mm, 3 replicates, 20-80 mm interval)

Parameter	Replicate Series	Displacement Rate (mm/min)				
		0.15	0.228	0.3	0.378	0.45
C* (MJ/m^2-hr)	1	0.010	0.017	0.023	0.031	0.041
	2	0.011	0.019	0.026	0.035	0.044
	3	0.013	0.020	0.027	0.036	0.045
	Average	*0.011*	*0.018*	*0.025*	*0.034*	*0.043*
	St. Dev.	*0.00159*	*0.00132*	*0.00182*	*0.00253*	*0.00248*
Crack Growth Rate, a* (m/hr)	1	1.12	1.27	2.61	2.16	4.07
	2	1.13	1.82	2.12	4.30	4.37
	3	1.03	1.57	2.99	2.89	4.82
	Average	*1.09*	*1.55*	*2.57*	*3.12*	*4.42*
	St. Dev.	*0.056*	*0.280*	*0.438*	*1.085*	*0.377*

Table A.13 ADOT CFT Data at 21°C (150 x 25 mm specimens, 10-60 mm interval)

Parameter	Replicate Series	Displacement Rate (mm/min)				
		0.15	0.228	0.30	0.378	0.45
C* (MJ/m^2-hr)	1	0.012	0.019	0.024	0.029	0.034
	2	0.007	0.010	0.013	0.020	0.026
	Average	*0.009*	*0.014*	*0.019*	*0.025*	*0.030*
	St. Dev.	*0.00387*	*0.00616*	*0.00761*	*0.00645*	*0.00551*
Crack Growth Rate, a* (m/hr)	1	0.93	1.11	3.88	3.65	5.43
	2	1.24	1.48	2.20	3.97	7.44
	Average	*1.08*	*1.30*	*3.04*	*3.81*	*6.44*
	St. Dev.	*0.225*	*0.267*	*1.186*	*0.229*	*1.418*

Table A.14 ADOT CFT Data at 21°C (150 x 25 mm specimens, 10-80 mm interval)

Parameter	Replicate Series	Displacement Rate (mm/min)				
		0.15	0.228	0.30	0.378	0.45
C* (MJ/m^2-hr)	1	0.011	0.018	0.024	0.031	0.038
	2	0.008	0.013	0.018	0.024	0.031
	Average	*0.010*	*0.016*	*0.021*	*0.028*	*0.034*
	St. Dev.	*0.00194*	*0.00347*	*0.00491*	*0.00525*	*0.00521*
Crack Growth Rate, a* (m/hr)	1	1.03	1.11	3.65	3.96	4.66
	2	1.33	1.68	2.54	4.95	5.77
	Average	*1.18*	*1.40*	*3.09*	*4.46*	*5.21*
	St. Dev.	*0.214*	*0.402*	*0.783*	*0.702*	*0.789*

Table A.15 ADOT CFT Data at 21°C (150 x 25 mm specimens, 20-80 mm interval)

Parameter	Replicate Series	Displacement Rate (mm/min)				
		0.15	0.228	0.30	0.378	0.45
C* (MJ/m^2-hr)	1	0.012	0.019	0.027	0.034	0.042
	2	0.010	0.015	0.020	0.026	0.033
	Average	*0.011*	*0.017*	*0.023*	*0.030*	*0.037*
	St. Dev.	*0.00153*	*0.00309*	*0.00475*	*0.00555*	*0.00584*
Crack Growth Rate, a* (m/hr)	1	1.06	1.11	3.59	4.83	4.62
	2	1.38	1.77	2.72	5.78	5.66
	Average	*1.22*	*1.44*	*3.15*	*5.31*	*5.14*
	St. Dev.	*0.225*	*0.462*	*0.616*	*0.669*	*0.735*

Table A.16 ADOT CFT Data at 21°C (100 x 50 mm specimens, 10-40 mm interval)

Parameter	Replicate Series	Displacement Rate (mm/min)				
		0.15	0.228	0.30	0.378	0.45
C* (MJ/m^2-hr)	1	0.016	0.024	0.031	0.039	0.045
	2	0.010	0.017	0.024	0.030	0.037
	Average	*0.013*	*0.020*	*0.027*	*0.035*	*0.041*
	St. Dev.	*0.00393*	*0.00499*	*0.00528*	*0.00626*	*0.00536*
Crack Growth Rate, a* (m/hr)	1	0.66	3.10	2.90	5.17	5.83
	2	1.05	1.77	3.32	2.49	2.59
	Average	*0.86*	*2.43*	*3.11*	*3.83*	*4.21*
	St. Dev.	*0.274*	*0.941*	*0.296*	*1.890*	*2.295*

Table A.17 ADOT CFT Data at 21°C (100 x 50 mm specimens, 10-50 mm interval)

Parameter	Replicate Series	Displacement Rate (mm/min)				
		0.15	0.228	0.30	0.378	0.45
C* (MJ/m^2-hr)	1	0.014	0.023	0.030	0.038	0.045
	2	0.010	0.017	0.024	0.033	0.041
	Average	*0.012*	*0.020*	*0.027*	*0.035*	*0.043*
	St. Dev.	*0.00295*	*0.00410*	*0.00410*	*0.00343*	*0.00306*
Crack Growth Rate, a* (m/hr)	1	0.68	2.20	2.90	3.74	3.31
	2	1.12	1.62	3.05	2.77	2.70
	Average	*0.90*	*1.91*	*2.98*	*3.26*	*3.00*
	St. Dev.	*0.311*	*0.411*	*0.111*	*0.689*	*0.435*

Table A.18 ADOT CFT Data at 21°C (100 x 50 mm specimens, 20-50 mm interval)

Parameter	Replicate Series	Displacement Rate (mm/min)				
		0.15	0.228	0.30	0.378	0.45
C* (MJ/m^2-hr)	1	0.015	0.025	0.032	0.040	0.049
	2	0.012	0.018	0.025	0.036	0.046
	Average	*0.013*	*0.021*	*0.029*	*0.038*	*0.048*
	St. Dev.	*0.00256*	*0.00466*	*0.00501*	*0.00256*	*0.00180*
Crack Growth Rate, a* (m/hr)	1	0.61	1.93	2.72	3.31	2.76
	2	1.05	1.71	2.87	3.61	2.27
	Average	*0.83*	*1.82*	*2.79*	*3.46*	*2.51*
	St. Dev.	*0.308*	*0.158*	*0.101*	*0.214*	*0.344*

Table A.19 ADOT CFT Data at 37.8°C (150 x 50 mm specimens, 10-60 mm interval)

Parameter	Replicate Series	Displacement Rate (mm/min)				
		0.378	0.6	0.90	1.2	1.5
C* (MJ/m^2-hr)	1	0.018	0.029	0.043	0.059	0.077
	2	0.017	0.028	0.044	0.066	0.089
	Average	*0.018*	*0.029*	*0.044*	*0.063*	*0.083*
	St. Dev.	*0.00098*	*0.00075*	*0.00096*	*0.00477*	*0.00888*
Crack Growth Rate, a* (m/hr)	1	1.21	2.45	3.91	4.89	8.06
	2	1.43	2.22	3.72	6.97	9.70
	Average	*1.32*	*2.33*	*3.82*	*5.93*	*8.88*
	St. Dev.	*0.151*	*0.164*	*0.132*	*1.471*	*1.158*

Table A.20 ADOT CFT Data at 37.8°C (150 x 50 mm specimens, 10-80 mm interval)

Parameter	Replicate Series	Displacement Rate (mm/min)				
		0.378	0.6	0.90	1.2	1.5
C* (MJ/m^2-hr)	1	0.016	0.027	0.043	0.060	0.080
	2	0.017	0.029	0.045	0.066	0.090
	Average	*0.016*	*0.028*	*0.044*	*0.063*	*0.085*
	St. Dev.	*0.00099*	*0.00145*	*0.00106*	*0.00447*	*0.00733*
Crack Growth Rate, a* (m/hr)	1	1.41	2.26	4.35	5.50	7.84
	2	1.26	2.11	3.69	7.11	8.44
	Average	*1.34*	*2.19*	*4.02*	*6.31*	*8.14*
	St. Dev.	*0.106*	*0.110*	*0.471*	*1.135*	*0.425*

Table A.21 ADOT CFT Data at 37.8°C (150 x 50 mm specimens, 20-80 mm interval)

Parameter	Replicate Series	Displacement Rate (mm/min)				
		0.378	0.6	0.90	1.2	1.5
C* (MJ/m^2-hr)	1	0.016	0.029	0.047	0.064	0.085
	2	0.018	0.032	0.047	0.070	0.094
	Average	*0.017*	*0.030*	*0.047*	*0.067*	*0.089*
	St. Dev.	*0.00155*	*0.00195*	*0.00020*	*0.00392*	*0.00694*
Crack Growth Rate, a* (m/hr)	1	1.50	2.10	5.41	6.65	8.22
	2	1.18	1.98	3.88	7.34	8.20
	Average	*1.34*	*2.04*	*4.64*	*7.00*	*8.21*
	St. Dev.	*0.226*	*0.085*	*1.085*	*0.492*	*0.017*

Table A.22 CFT test data for ADOT mixture (21°C; 150 x 50 mm)

Sample	Δ* (mm/min)	Time (T) Force (P)	Crack Length (mm)							
			10	20	30	40	50	60	70	80
CS17T	0.15	T (min)	11.64	11.81	12.43	12.93	13.43	14.02	14.63	14.97
		P (kN)	6.26	5.92	4.55	3.60	2.77	2.21	1.85	1.63
CS21B	0.15	T (min)	11.38	11.98	12.17	12.43	12.80	14.03	14.36	14.62
		P (kN)	6.85	6.48	6.31	6.11	5.77	3.53	3.08	2.56
CS48T	0.15	T (min)	9.56	10.49	10.98	11.70	12.58	12.76	13.09	14.04
		P (kN)	7.70	7.54	7.29	6.74	5.23	4.78	3.94	2.25
CS45B	0.228	T (min)	5.52	5.80	6.14	6.83	7.08	7.49	8.18	8.61
		P (kN)	7.20	7.11	6.85	5.81	5.17	4.07	2.72	2.10
CS15B	0.228	T (min)	3.90	4.88	5.28	5.53	5.75	5.95	6.65	6.81
		P (kN)	6.92	6.89	6.42	6.06	5.38	4.71	2.06	1.70
CS51T	0.228	T (min)	6.48	7.06	7.64	8.23	8.82	8.89	8.97	9.05
		P (kN)	8.53	8.35	7.93	7.26	6.04	5.87	5.58	5.31
CS6T	0.3	T (min)	5.32	5.75	5.91	6.03	6.26	6.45	6.62	7.16
		P (kN)	6.17	4.59	3.99	3.56	2.61	1.91	1.50	0.82
CS2B	0.3	T (min)	4.27	4.49	4.99	5.04	5.18	5.23	5.88	6.23
		P (kN)	6.55	6.39	5.39	5.23	4.73	4.52	2.34	1.61
CS47T	0.3	T (min)	5.93	6.00	6.22	6.30	6.46	6.73	6.98	7.18
		P (kN)	8.44	8.23	7.54	7.14	6.00	3.88	2.50	1.78
CS16B	0.378	T (min)	2.99	3.40	3.57	3.63	3.76	4.01	4.26	5.03
		P (kN)	8.38	7.68	6.99	6.57	5.51	3.71	2.67	1.54
CS15T	0.378	T (min)	2.76	2.88	2.96	3.17	3.31	3.36	3.50	3.73
		P (kN)	8.94	8.54	8.05	6.23	4.94	4.49	3.18	1.96
CS48B	0.378	T (min)	5.26	5.43	5.52	5.68	5.80	5.99	6.27	6.65
		P (kN)	6.92	5.69	4.87	3.67	3.02	2.27	1.63	1.14
CS16T	0.45	T (min)	1.85	2.47	2.53	2.76	2.88	3.00	3.11	3.35
		P (kN)	8.77	8.79	8.67	7.60	6.58	5.16	3.92	2.06
CS18B	0.45	T (min)	2.33	2.59	2.73	2.88	2.94	3.07	3.22	3.46
		P (kN)	8.21	8.03	7.56	6.76	6.23	4.65	2.95	1.87
CS49B	0.45	T (min)	3.59	3.70	3.83	3.95	4.10	4.22	4.36	4.41
		P (kN)	11.85	11.77	11.60	11.16	10.16	8.63	5.24	4.25

Table A.23 CFT test data for ADOT mixture (21°C; 100 x 50 mm)

Sample	Δ* (mm/min)	Time (T) Force (P)	Crack Length (mm)				
			10	20	30	40	50
CS20B	0.15	T (min)	6.33	6.65	8.19	8.61	9.62
		P (kN)	5.14	4.91	2.63	2.17	1.43
CS20T	0.15	T (min)	7.55	7.86	8.63	9.15	9.55
		P (kN)	4.21	4.04	3.10	2.20	1.68
CS3B	0.228	T (min)	5.53	5.73	5.88	6.12	6.62
		P (kN)	4.69	4.10	3.55	2.61	1.34
CS44M	0.228	T (min)	4.22	4.88	4.98	5.09	5.78
		P (kN)	4.59	2.83	2.54	2.30	1.20
CS3T	0.3	T (min)	2.78	2.98	3.08	3.41	3.58
		P (kN)	4.69	3.73	3.06	1.62	1.25
CS4B	0.3	T (min)	3.75	3.91	4.08	4.29	4.53
		P (kN)	5.97	5.65	4.82	3.34	2.08
CS4T	0.378	T (min)	2.51	2.62	2.75	2.85	3.15
		P (kN)	4.34	3.60	2.80	2.30	1.40
CS3M	0.378	T (min)	2.79	3.18	3.31	3.51	3.67
		P (kN)	7.16	7.16	6.91	5.40	3.76
CS19B	0.45	T (min)	2.57	2.65	2.73	2.88	3.25
		P (kN)	6.00	5.88	5.37	3.99	1.65
CS44T	0.45	T (min)	2.15	2.22	2.31	2.75	2.89
		P (kN)	5.31	4.80	4.01	1.87	1.51

Table A.24 CFT test data for ADOT mixture; (21°C; 150 x 25 mm)

Sample	Δ* (mm/min)	Time (T) Force (P)	Crack Length (mm)							
			10	20	30	40	50	60	70	80
CS23B1	0.15	T (min)	10.67	11.09	12.24	12.75	13.23	13.70	14.25	14.56
		P (kN)	3.49	3.40	2.95	2.54	1.95	1.42	1.21	1.01
CS13B	0.15	T (min)	11.28	11.87	12.33	12.83	13.43	13.57	13.70	14.62
		P (kN)	3.38	3.36	3.18	3.07	2.43	2.28	2.07	1.12
CS14TM	0.228	T (min)	5.11	5.74	6.21	6.58	7.16	7.93	8.48	8.75
		P (kN)	3.29	3.28	3.18	2.95	2.45	1.64	1.12	0.90
CS13MB	0.228	T (min)	6.84	7.18	7.83	8.20	8.48	8.75	9.02	9.27
		P (kN)	4.09	4.05	3.89	3.78	3.57	3.39	2.90	2.25
CS14MB	0.3	T (min)	4.44	4.58	4.78	4.94	5.09	5.17	5.33	5.65
		P (kN)	4.33	4.25	3.99	3.61	3.03	2.76	2.20	1.51
CS21B1	0.3	T (min)	4.11	4.37	4.81	4.98	5.24	5.42	5.51	5.74
		P (kN)	4.13	4.10	3.80	3.64	3.33	3.01	2.84	2.14
CS15B1	0.378	T (min)	2.38	2.79	2.88	2.99	3.11	3.18	3.35	3.55
		P (kN)	3.48	3.32	3.21	2.96	2.56	2.26	1.50	0.91
CS13MT	0.378	T (min)	4.60	4.80	4.98	5.19	5.23	5.29	5.34	5.38
		P (kN)	4.37	4.11	3.59	2.56	2.32	2.03	1.81	1.67
CS14T	0.45	T (min)	2.33	2.54	2.60	2.73	2.78	2.90	2.95	3.33
		P (kN)	4.37	4.09	3.93	3.43	3.15	2.54	2.28	1.04
CS17B1	0.45	T (min)	3.98	4.12	4.23	4.29	4.33	4.37	4.60	4.75
		P (kN)	3.86	3.64	3.39	3.16	2.86	2.71	1.50	1.17

Table A.25 CFT test data for ADOT mixture (4.4°C; 150 x 50 mm)

Sample	Δ* (mm/min)	Time (T) Force (P)	Crack Length (mm)							
			10	20	30	40	50	60	70	80
CS12B	0.03	T (min)	22.98	23.33	23.88	24.12	24.27	24.36	24.46	24.56
		P (kN)	13.04	12.98	12.51	11.85	11.28	10.61	8.60	6.84
CS9T	0.03	T (min)	28.09	28.86	29.88	30.18	30.47	31.08	31.29	31.59
		P (kN)	15.27	15.12	14.60	14.45	14.13	12.32	10.58	6.80
CS8B	0.06	T (min)	20.11	21.14	21.35	21.43	21.53	21.62	21.69	21.90
		P (kN)	14.99	14.22	13.75	13.43	12.92	11.93	10.94	4.66
CS23B	0.06	T (min)	26.68	26.81	26.88	26.98	27.07	27.14	27.19	27.24
		P (kN)	15.77	15.52	15.28	14.77	13.97	12.37	11.20	9.96
CS52T	0.102	T (min)	14.59	14.61	14.63	14.65	14.72	14.74	14.76	14.78
		P (kN)	17.13	16.82	16.42	16.00	14.27	12.45	12.45	11.34
CS7T	0.102	T (min)	9.85	9.93	10.01	10.06	10.10	10.15	10.16	10.17
		P (kN)	14.76	14.49	13.93	13.60	12.99	9.89	8.42	6.94
CS11B	0.15	T (min)	6.27	6.30	6.37	6.37	6.38	6.38	6.38	6.39
		P (kN)	16.41	16.22	6.86	6.86	6.86	4.65	4.65	4.65
CS41T	0.15	T (min)	8.55	8.58	8.61	8.63	8.65	8.66	8.67	8.67
		P (kN)	19.12	18.72	18.38	17.65	15.80	15.80	13.77	13.77

Table A.26 CFT test data for ADOT mixture (10°C; 150 x 50 mm)

Sample	Δ* (mm/min)	Time (T) Force (P)	Crack Length (mm)							
			10	20	30	40	50	60	70	80
CS39B	0.072	T (min)	19.06	19.38	19.66	19.85	20.12	20.53	20.95	21.23
		P (kN)	11.35	10.63	9.91	9.14	8.21	6.35	4.71	3.91
CS35B	0.072	T (min)	22.42	22.66	22.83	22.96	23.06	23.17	23.71	24.33
		P (kN)	10.32	9.38	8.57	7.92	7.48	7.00	4.84	3.43
CS36T	0.15	T (min)	10.08	10.43	10.77	10.87	10.98	11.16	11.28	11.37
		P (kN)	14.89	14.03	12.49	11.71	10.68	8.33	6.90	5.95
CS40B	0.15	T (min)	9.84	10.00	10.12	10.21	10.32	10.43	10.53	10.68
		P (kN)	15.19	15.12	14.84	14.46	13.90	13.08	11.79	8.41
CS38B	0.228	T (min)	6.00	6.13	6.19	6.23	6.27	6.32	6.36	6.39
		P (kN)	16.16	15.71	15.43	15.17	14.88	14.10	12.90	11.53
CS37B	0.228	T (min)	6.40	6.68	6.86	6.93	7.00	7.08	7.23	7.36
		P (kN)	17.22	16.61	15.73	15.14	14.54	13.66	10.92	6.95
CS35T	0.3	T (min)	6.13	6.18	6.20	6.23	6.28	6.31	6.36	6.45
		P (kN)	16.03	15.56	15.11	14.61	13.57	13.05	11.34	8.35
CS39T	0.3	T (min)	4.60	4.65	4.67	4.68	4.70	4.73	4.79	4.93
		P (kN)	16.87	16.68	16.61	16.54	16.51	16.46	16.09	14.21

Table A.27 CFT test data for ADOT mixture (37.8°C; 150 x 50 mm)

Sample	Δ* (mm/min)	Time (T) Force (P)	Crack Length (mm)							
			10	20	30	40	50	60	70	80
CS27T	0.378	T (min)	4.87	5.40	5.98	6.39	6.99	7.27	7.48	7.69
		P (kN)	3.72	3.58	3.13	2.58	1.71	1.43	1.21	1.07
CS57B	0.378	T (min)	5.18	5.51	5.79	6.09	6.53	7.32	7.81	8.38
		P (kN)	3.65	3.44	3.11	2.77	2.02	1.21	0.85	0.59
CS32B	0.6	T (min)	1.54	1.67	1.80	1.93	2.47	2.63	2.98	3.25
		P (kN)	3.46	3.53	3.44	3.46	2.37	1.86	1.11	0.82
CS26T	0.6	T (min)	2.78	2.97	3.11	3.28	3.74	4.08	4.34	4.65
		P (kN)	3.72	3.60	3.45	3.20	2.48	1.80	1.39	0.98
CS31B	0.9	T (min)	1.98	2.35	2.48	2.55	2.67	2.74	2.88	3.04
		P (kN)	4.89	4.58	4.18	3.83	3.16	2.75	2.17	1.70
CS26B	0.9	T (min)	2.56	2.80	2.98	3.15	3.26	3.34	3.52	3.79
		P (kN)	3.78	2.98	2.32	1.75	1.45	1.22	0.89	0.58
CS27B	1.2	T (min)	1.75	2.01	2.12	2.20	2.28	2.38	2.47	2.56
		P (kN)	4.56	4.09	3.58	3.19	2.75	2.29	1.85	1.49
CS32T	1.2	T (min)	1.24	1.37	1.44	1.51	1.57	1.70	1.77	1.84
		P (kN)	6.24	6.06	5.79	5.36	4.44	2.22	1.73	1.42
CS30B	1.5	T (min)	1.25	1.38	1.44	1.50	1.56	1.64	1.72	1.83
		P (kN)	6.10	5.79	5.57	5.16	4.53	3.50	2.61	1.87
CS54T	1.5	T (min)	1.54	1.62	1.67	1.75	1.79	1.85	1.91	2.08
		P (kN)	4.93	4.29	3.69	2.87	2.56	2.12	1.81	1.08

Table A.28 ADOT mixture specimen properties (21°C)

Specimen	Temp °C	Size (mm)	Air Voids (%)	Thickness Summary				
				T_1 (mm)	T_2 (mm)	T_3 (mm)	Average (mm)	St Dev (mm)
CS17T	21	150 x 50	5.96	51.85	51.91	52.22	51.99	0.1986
CS21B			6.43	48.91	49.14	48.94	49.00	0.1250
CS48T			6.15	48.90	48.67	49.69	49.09	0.5350
CS45B			6.52	50.75	51.02	50.52	50.76	0.2503
CS15B			5.78	50.57	49.77	50.22	50.19	0.4010
CS51T			5.93	49.95	50.76	50.26	50.32	0.4087
CS6T			6.08	53.57	52.01	53.48	53.02	0.8758
CS2B			6.40	50.72	49.77	49.83	50.11	0.5320
CS47T			6.25	50.06	49.71	50.12	49.96	0.2214
CS16B			6.03	51.48	51.26	51.50	51.41	0.1332
CS15T			5.54	50.23	49.89	50.04	50.05	0.1704
CS48B			6.42	50.67	51.13	50.81	50.87	0.2358
CS16T			5.83	50.00	50.06	50.26	50.11	0.1361
CS18B			5.85	49.04	48.40	49.34	48.93	0.4801
CS49B			6.35	51.95	52.45	51.89	52.10	0.3075
CS20B	21	100 x 50	5.72	51.86	50.82	51.28	51.32	0.5212
CS20T			5.70	49.75	49.35	48.60	49.23	0.5838
CS3B			6.42	51.76	50.38	50.52	50.89	0.7596
CS44M			5.84	49.08	48.49	49.55	49.04	0.5311
CS3T			5.54	49.92	50.41	50.36	50.23	0.2696
CS4B			6.65	52.68	52.82	53.26	52.92	0.3027
CS4T			6.34	49.81	49.33	49	49.38	0.4073
CS3M			5.38	48.56	49.79	49.05	49.13	0.6192
CS19B			5.98	50.8	50.43	50.84	50.69	0.2261
CS44T			6.12	51.65	51.65	51.84	51.71	0.1097
CS23B1	21	150 x 25	5.97	25.89	25.5	25.93	25.77	0.2376
CS13B			5.97	26.25	25.93	26.19	26.12	0.1701
CS14TM			5.87	26.44	27.34	26.73	26.84	0.4594
CS13MB			5.73	26.44	26.99	26.64	26.69	0.2784
CS14MB			6.09	27.74	26.91	28.46	27.70	0.7757
CS21B1			6.20	26.02	25.1	25.48	25.53	0.4623
CS15B1			5.92	24.9	25.3	25.04	25.08	0.2030
CS13MT			6.32	25.92	25.36	25.68	25.65	0.2810
CS14T			5.52	26.7	26.02	26.6	26.44	0.3672
CS17B1			5.94	25.41	25.33	25.67	25.47	0.1778

Table A.29 ADOT mixture specimen properties (4.4, 10, 37.8°C)

Specimen	Temp °C	Size (mm)	Air Voids (%)	Thickness Summary				
				T_1 (mm)	T_2 (mm)	T_3 (mm)	Average (mm)	St Dev (mm)
CS12B	4.4	150 x 50	5.41	50.1	50	49.69	49.93	0.2138
CS9T			5.72	51.7	51.08	50.54	51.11	0.5805
CS8B			6.26	49.48	49.82	50.19	49.83	0.3551
CS23B			6.68	47.86	48.01	48.78	48.22	0.4936
CS52T			6.08	50.83	50.78	51.56	51.06	0.4366
CS7T			5.32	50.97	50.59	50.24	50.60	0.3651
CS11B			5.59	49.86	49.94	49.77	49.86	0.0850
CS41T			5.91	50.58	49.65	49.7	49.98	0.5231
CS39B	10	150 x 50	6.04	50.19	49.04	49.4	49.54	0.5882
CS35B			5.86	51.03	51.2	51.59	51.27	0.2871
CS36T			5.60	50.77	49.86	51.12	50.58	0.6504
CS40B			5.55	49.63	50.12	49.66	49.80	0.2747
CS38B			6.23	50.64	51.27	50.72	50.88	0.3430
CS37B			5.95	51.55	51.54	51.49	51.53	0.0321
CS35T			5.64	51.13	50.26	50.83	50.74	0.4419
CS39T			5.44	49.9	50.99	50.57	50.49	0.5498
CS27T	37.8	150 x 50	6.61	49.92	49.9	50.8	50.21	0.5139
CS57B			6.55	51.64	51.34	52.08	51.69	0.3722
CS32B			5.30	50.34	50.91	50.66	50.64	0.2857
CS26T			5.92	49.41	48.26	48.83	48.83	0.5750
CS31B			6.18	48.28	49.48	49.28	49.01	0.6429
CS26B			6.27	49.71	48.87	50.02	49.53	0.5950
CS27B			5.80	48.45	49.35	47.87	48.56	0.7457
CS32T			5.86	52.57	52.46	52.04	52.36	0.2797
CS30B			6.03	49.43	49.93	50.33	49.90	0.4509
CS54T			6.07	49.55	48.35	48.33	48.74	0.6987

Table A.30 CFT test data for Swedish Stockholm Mixtures.

Mix	ID	A.V. (%)	T (mm)	Δ* (mm/ min)	Time (T) Force (P)	Crack Length (mm)							
						10	20	30	40	50	60	70	80
Reference	S7-4M	3.35	40	0.15	T (min)	13.37	16.37	17.37	18.37	19.37	19.37	21.37	22.37
					P (kN)	6.62	5.66	5.01	4.41	3.84	3.84	2.77	2.11
	S7-3B	3.13	40	0.225	T (min)	8.83	9.8	11	11.7	12.7	13.3	14.3	16.1
					P (kN)	7.51	7.37	6.66	5.87	4.38	3.68	2.87	2.01
	S7-2T	3.47	41	0.3	T (min)	6.39	7.34	7.74	8	8.49	9.39	10.8	11.2
					P (kN)	8.78	7.75	6.98	6.31	5.31	3.62	2.16	1.89
	S7-4T	3.17	41	0.375	T (min)	4.8	5.53	5.8	6.4	6.87	7.8	8.22	8.72
					P (kN)	8.54	8.02	7.64	6.46	5.55	4.31	3.85	3.32
	S7-2B	3.25	45	0.45	T (min)	4.72	5.15	5.43	5.52	5.58	5.72	5.85	6.18
					P (kN)	9.95	8.18	5.96	5.27	4.77	3.68	3.06	2.12
Polymer	S5-5M	2.83	42	0.15	T (min)	9.72	10.1	10.3	10.8	10.9	11	11.2	13.3
					P (kN)	8.56	7.89	7.43	5.94	5.19	4.61	3.91	1.34
	S5-7M	3.03	42	0.225	T (min)	9.9	10.4	11	11.4	11.6	12.4	12.7	13.2
					P (kN)	8.18	8.1	7.83	7.37	7.03	3.87	2.98	2.15
	S5-6B	2.86	43	0.3	T (min)	3.9	4.47	4.77	5.18	5.35	5.47	5.63	5.75
					P (kN)	11.2	11.3	10.9	8.21	5.93	4.75	3.82	3.34
	S5-5B	2.94	42	0.375	T (min)	3.42	3.7	3.97	4.1	4.2	4.32	4.57	5.6
					P (kN)	10.3	9.65	8.23	7.07	5.97	4.38	2.66	1.14
	S5-6M	3.09	41	0.45	T (min)	2.8	2.9	3.1	3.13	3.22	3.28	3.43	3.63
					P (kN)	10.7	10.5	9.04	8.71	7.42	6.47	4.66	3.35
Rubber	SA-3B	2.50	42	0.15	T (min)	12.33	14.17	15.47	16.33	17.97	19.80	21.00	24.07
					P (kN)	5.97	5.61	4.95	4.39	3.66	2.8	2.36	1.47
	SA-02	n/a	40	0.225	T (min)	7.75	8.73	9.93	10.67	11.15	11.60	12.17	12.70
					P (kN)	6.7	5.93	4.87	4.15	3.69	3.19	2.65	2.26
	SA-4M	2.64	46	0.3	T (min)	5.00	6.42	7.67	8.97	9.48	10.32	11.60	13.67
					P (kN)	6.94	7.06	6.59	5.42	4.73	3.69	2.55	1.38
	SA-3T	2.61	46	0.375	T (min)	3.80	4.67	5.00	5.65	5.83	6.13	6.37	8.27
					P (kN)	6.87	6.97	6.67	5.52	5.08	4.21	3.58	1.39
	SA-4B	2.51	40	0.45	T (min)	4.40	5.20	5.50	5.90	6.57	7.07	7.40	8.00
					P (kN)	7.81	7.66	7.27	6.49	4.86	3.72	3.14	2.22

Table A.31 CFT test data for Evergreen Drive Mixtures.

Mix	ID	A.V. (%)	T (mm)	Δ* (mm/min)	Time (T) Force (P)	Crack Length (mm)							
						10	20	30	40	50	60	70	80
Control	C22B	n/a	45.47	0.063	T (min)	25.70	25.70	25.80	25.80	27.60	28.00	28.50	30.00
					P (kN)	0.74	0.74	0.70	0.70	0.42	0.37	0.35	0.29
	C21B	6.96	48.77	0.127	T (min)	8.13	8.13	8.53	8.73	8.93	9.03	9.13	10.23
					P (kN)	1.30	1.30	1.15	1.03	0.95	0.94	0.84	0.55
	C21T	7.28	49.96	0.189	T (min)	3.38	3.40	3.43	3.47	3.53	3.67	3.70	4.12
					P (kN)	1.47	1.45	1.39	1.32	1.24	1.08	1.08	0.77
	C22M	7.12	43.30	0.252	T (min)	2.00	2.08	2.13	2.13	2.22	2.32	2.47	2.60
					P (kN)	3.72	1.92	1.29	1.29	1.03	0.81	0.69	0.62
	C23M	7.31	46.40	0.318	T (min)	2.08	2.50	3.02	3.05	3.08	3.12	3.13	3.17
					P (kN)	2.32	2.50	1.80	1.73	1.63	1.51	1.52	1.48
Fiber - 1 lb/ton	F120T	7.00	45	0.063	T (min)	34.00	40.07	40.10	40.20	42.00	46.40	51.00	57.50
					P (kN)	1.79	0.79	0.79	0.76	0.63	0.36	0.24	0.13
	F120B	7.04	44.3	0.128	T (min)	8.70	10.30	11.80	14.70	15.70	16.30	17.50	17.70
					P (kN)	3.61	3.25	2.68	1.70	1.60	1.57	1.39	1.35
	F121B	7.10	47	0.189	T (min)	4.48	4.93	5.28	5.35	5.40	5.78	6.73	7.77
					P (kN)	4.19	4.20	4.12	4.10	4.07	3.85	2.38	1.26
	F121M	7.00	37.1	0.252	T (min)	4.05	4.08	4.08	4.15	4.25	4.58	4.70	4.72
					P (kN)	3.21	3.09	3.09	2.76	2.36	1.14	0.90	0.88
	F120M	7.31	46.4	0.318	T (min)	3.98	4.05	4.12	4.22	4.25	4.27	4.53	4.58
					P (kN)	4.39	4.16	3.83	3.42	3.29	3.22	2.47	2.33
Fiber - 2 lb/ton	F222B	6.71	45.3	0.126	T (min)	8.80	9.00	9.20	9.50	9.70	10.10	10.20	11.10
					P (kN)	4.62	4.09	3.41	2.70	2.37	1.81	1.68	1.15
	F220M	7.30	47	0.189	T (min)	8.20	8.37	8.63	8.92	9.40	9.82	10.20	11.48
					P (kN)	5.10	4.87	4.40	3.69	2.25	1.54	1.23	0.75
	F222T	7.12	33.7	0.252	T (min)	5.10	5.10	5.20	5.20	5.30	5.30	5.30	5.40
					P (kN)	7.03	7.03	4.59	4.59	2.28	2.28	2.28	1.65
	F222M	6.84	42.1	0.318	T (min)	3.08	3.65	3.68	3.73	3.77	3.80	3.82	3.83
					P (kN)	7.45	6.02	4.87	3.05	1.98	1.64	1.50	1.42

Table A.32 CFT test data for PA Cranberry Township Mixtures.

Mix / Temp.	Sample	Δ* (mm/min)	Time (T) Force (P)	Crack Length (mm)							
				10	20	30	40	50	60	70	80
Control 10°C	PAC4M	0.228	T (min)	9.45	9.97	10.65	11.69	12.78	13.23	14.28	15.87
			P (kN)	6.81	6.68	6.39	5.58	4.35	3.83	2.60	1.60
	PAC2M	0.378	T (min)	5.70	6.60	7.39	7.72	8.38	8.78	9.39	10.28
			P (kN)	8.05	7.98	7.42	6.90	5.49	4.49	3.02	1.66
	PAC2T	0.600	T (min)	2.68	3.53	4.17	4.32	4.64	4.86	5.14	5.67
			P (kN)	9.12	9.38	8.67	8.39	7.32	6.24	4.58	2.39
	PAC4B	0.750	T (min)	2.80	3.13	3.38	3.55	3.67	3.99	4.20	4.50
			P (kN)	10.28	10.17	9.89	9.42	8.98	6.44	4.65	2.77
	PAC4T	0.900	T (min)	2.17	2.40	2.45	2.50	2.53	2.65	2.75	2.95
			P (kN)	10.30	9.21	8.89	8.40	7.93	5.76	3.96	2.04
Fiber 10°C	PAF4T	0.450	T (min)	4.39	5.34	5.83	6.24	7.28	7.66	7.87	8.80
			P (kN)	7.45	7.32	7.15	6.87	5.39	4.63	4.11	1.87
	PAF4B	0.600	T (min)	4.33	4.98	5.19	5.53	5.84	6.22	6.71	6.86
			P (kN)	8.62	8.18	7.95	7.28	6.06	4.28	2.38	1.98
	PAF6M	0.750	T (min)	2.90	3.17	3.61	3.96	4.13	4.32	4.61	4.87
			P (kN)	9.38	9.26	8.55	7.42	6.93	5.99	4.40	3.30
	PAF6B	0.900	T (min)	2.17	2.52	2.75	2.96	3.19	3.33	3.43	3.53
			P (kN)	11.46	11.55	11.12	10.51	8.96	7.09	5.06	3.58
	PAF4M	1.200	T (min)	2.66	2.85	2.98	3.18	3.33	3.51	3.68	3.75
			P (kN)	10.16	9.90	9.67	8.98	8.28	6.96	4.97	4.35
Control 21°C	PAC6B	0.378	T (min)	4.76	6.88	8.28	8.60	9.05	11.09	12.18	13.41
			P (kN)	2.86	3.00	2.68	2.51	2.28	1.29	0.93	0.63
	PAC2B	0.450	T (min)	4.73	6.23	6.90	7.64	7.96	9.28	10.12	10.64
			P (kN)	2.73	2.42	2.21	2.03	1.81	1.20	0.88	0.77
	PAC6M	0.600	T (min)	5.41	5.83	6.73	7.21	7.67	7.96	8.83	9.66
			P (kN)	4.03	3.92	3.56	3.22	2.69	2.35	1.63	1.00
	PAC6T	0.828	T (min)	2.92	3.48	4.02	4.26	4.43	4.96	5.28	5.82
			P (kN)	3.87	3.60	3.16	2.74	2.40	1.69	1.39	1.00
Fiber 21°C	PAF7T	0.378	T (min)	7.08	8.17	9.20	10.36	11.27	13.11	13.47	14.52
			P (kN)	3.17	3.24	3.13	2.86	2.43	1.69	1.53	1.17
	PAF7B	0.322	T (min)	4.76	5.29	7.04	7.38	7.94	8.45	9.49	10.33
			P (kN)	3.22	3.32	3.00	2.88	2.47	2.11	1.55	1.23
	PAF7M	0.374	T (min)	2.85	4.14	5.14	5.83	6.05	6.68	7.46	7.71
			P (kN)	3.74	4.11	3.93	3.62	3.38	2.50	1.39	1.11

Table A.33 PA Cranberry Township specimen properties.

Specimen	Temp °C	Air Voids (%)	Thickness Summary				
			T_1 (mm)	T_2 (mm)	T_3 (mm)	Average (mm)	Stdev
PAC4M	10	7.11	49.96	50.05	49.58	49.86	0.2495
PAC2M		7.46	50.56	51.28	50.54	50.79	0.4216
PAC2T		6.93	51.75	51.85	51.19	51.60	0.3557
PAC4B		6.48	52.55	52.38	52.91	52.61	0.2706
PAC4T		7.17	49.84	50.41	50.15	50.13	0.2854
PAF4T		7.51	49.86	48.73	48.88	49.16	0.6137
PAF4B		7.33	51.12	50.40	50.87	50.80	0.3656
PAF6M		6.93	49.21	48.86	50.32	49.46	0.7623
PAF6B		6.36	50.86	51.54	50.87	51.09	0.3897
PAF4M		7.55	50.46	50.73	49.47	50.22	0.6634
PAC6B	21	6.40	51.26	52.14	51.62	51.67	0.4424
PAC2B		6.30	49.56	49.15	50.03	49.58	0.4403
PAC6M		7.77	49.61	50.32	49.87	49.93	0.3592
PAC6T		7.18	50.77	50.73	50.11	50.54	0.3700
PAF7T		7.49	49.94	51.30	49.94	50.39	0.7852
PAF7B		6.62	50.61	50.50	50.50	50.54	0.0635
PAF7M		7.32	48.90	50.61	49.44	49.65	0.8741

Table A.34 CFT test data for PennDOT I-78 Mixtures (4.4°C).

Mix / Temp.	Sample	Δ* (mm/min)	Time (T) Force (P)	Crack Length (mm)							
				10	20	30	40	50	60	70	80
PG76-22 4.4°C	WC9T	0.150	T (min)	8.83	9.36	10.04	10.28	10.63	11.08	11.53	12.77
			P (kN)	13.43	12.97	11.64	10.74	9.24	7.25	5.83	3.33
	WC7T	0.228	T (min)	5.50	6.60	7.03	7.50	7.81	8.38	8.74	9.13
			P (kN)	13.75	14.07	13.62	12.50	11.07	7.93	6.27	4.79
	WC12B	0.264	T (min)	5.66	5.79	5.90	5.99	6.05	6.28	6.44	6.56
			P (kN)	13.83	13.10	12.08	10.88	9.71	6.00	4.48	3.74
	WC12T	0.300	T (min)	4.45	4.80	5.06	5.18	5.27	5.32	5.40	5.42
			P (kN)	15.71	15.18	13.59	12.91	11.71	11.06	9.56	9.30
	WC9B	0.378	T (min)	3.57	3.78	3.93	4.02	4.09	4.15	4.17	4.18
			P (kN)	14.66	14.20	13.27	12.62	11.52	10.13	9.51	8.55
PG64-22AR 4.4°C	WR8T	0.300	T (min)	4.09	4.69	5.18	6.25	6.81	7.18	8.43	9.06
			P (kN)	7.92	8.14	8.12	7.27	5.34	4.38	2.54	2.08
	WR9M	0.450	T (min)	2.69	3.10	3.33	3.56	3.78	4.40	5.30	5.89
			P (kN)	9.02	9.26	9.29	9.28	9.07	7.97	4.71	3.37
	WR10T	0.600	T (min)	2.26	2.91	3.12	3.38	4.39	4.62	5.00	5.40
			P (kN)	8.68	8.72	8.45	7.78	3.54	3.07	2.20	1.66
	WR8M	0.750	T (min)	1.98	2.33	2.68	3.03	3.43	3.73	3.97	4.22
			P (kN)	8.86	9.14	8.98	8.49	6.71	4.93	3.84	2.87
	WR8B	0.900	T (min)	1.68	1.82	1.96	2.23	2.30	2.37	2.57	2.86
			P (kN)	10.88	10.69	10.31	7.88	7.00	5.97	3.95	2.51

Table A.35 CFT test data for PennDOT I-78 Mixtures (10°C).

Mix / Temp.	Sample	Δ* (mm/min)	Time (T) Force (P)	Crack Length (mm)							
				10	20	30	40	50	60	70	80
PG76-22 10°C	WC2B	0.300	T (min)	5.58	6.51	7.63	7.91	8.18	8.56	8.86	9.68
			P (kN)	11.92	11.85	10.23	9.25	7.74	5.69	4.37	2.57
	WC1T	0.450	T (min)	3.98	4.70	5.33	5.69	5.86	6.10	6.29	6.51
			P (kN)	12.53	12.41	11.26	10.06	8.95	7.08	5.68	4.44
	WC1B	0.750	T (min)	2.85	3.12	3.40	3.65	3.80	3.90	3.99	4.18
			P (kN)	13.34	12.93	12.06	10.94	9.48	8.07	6.36	3.87
	WC2T	1.200	T (min)	1.35	1.49	1.58	1.68	1.75	1.81	1.86	1.96
			P (kN)	15.96	16.00	15.60	14.99	14.27	13.37	12.30	8.86
PG64-22 AR 10°C	WR10M	0.600	T (min)	4.09	4.74	5.09	5.39	5.67	6.83	7.63	8.27
			P (kN)	5.76	5.66	5.43	5.29	4.97	3.61	2.38	1.68
	WR9T	0.750	T (min)	1.76	2.39	2.80	3.05	3.19	3.47	3.60	3.78
			P (kN)	6.32	6.50	6.04	5.60	5.09	3.83	3.34	2.75
	WR3B	0.900	T (min)	1.86	2.15	2.28	2.61	3.01	3.18	3.36	3.53
			P (kN)	6.65	6.73	6.68	6.71	6.58	6.45	6.17	5.87
	WR9B	1.050	T (min)	2.14	2.35	2.54	2.74	2.86	3.00	3.12	3.34
			P (kN)	7.99	7.82	7.56	7.04	6.56	5.53	4.70	3.43
	WR1T	1.200	T (min)	1.60	1.97	2.13	2.30	2.50	2.50	2.68	3.03
			P (kN)	7.35	7.04	6.59	5.78	4.32	4.32	3.34	2.02

Table A.36 PennDOT I-78 specimen properties.

Specimen	Temp °C	Air Voids (%)	Thickness Summary				
			T_1 (mm)	T_2 (mm)	T_3 (mm)	Average (mm)	Stdev
WC9T	4.4	6.45	50.92	51.5	51.5	51.31	0.3349
WC7T		6.17	51.06	49.69	50.39	50.38	0.6851
WC12B		6.07	53.06	51.77	52.44	52.42	0.6452
WC12T		6.53	51.93	50.84	51.63	51.47	0.5631
WC9B		6.44	52.58	51.76	51.84	52.06	0.4521
WR8T		6.86	49.89	50.52	50.97	50.46	0.5425
WR9M		6.27	50.10	49.75	49.76	49.87	0.1992
WR10T		5.99	52.08	51.94	52.73	52.25	0.4215
WR8M		6.95	49.25	49.75	50.18	49.73	0.4654
WR8B		5.85	51.73	52.92	52.43	52.36	0.5981
WC2B	10	5.89	51.77	51.52	51.50	51.60	0.1504
WC1T		6.14	50.69	51.45	51.82	51.32	0.5761
WC1B		5.72	51.80	51.86	51.43	51.70	0.2329
WC2T		6.09	50.72	50.68	50.89	50.76	0.1115
WR10M		6.88	51.01	49.96	50.80	50.59	0.5556
WR9T		6.29	50.01	49.51	50.99	50.17	0.7529
WR3B		6.44	51.56	51.05	51.40	51.34	0.2608
WR9B		6.14	52.52	53.61	52.70	52.94	0.5843
WR1T		5.82	49.67	49.10	49.24	49.34	0.2970

APPENDIX B

B. MINITAB OUTPUT

Table B.1 Minitab Output – 150 x 50 mm versus 150 x 25 mm specimens

Test for Equal Variances: log a versus Size

95% Bonferroni confidence intervals for standard deviations

Size	N	Lower	StDev	Upper
0	5	0.168755	0.301429	1.04281
1	5	0.130232	0.232619	0.80476

F-Test (Normal Distribution)
Test statistic = 1.68, p-value = 0.628

Levene's Test (Any Continuous Distribution)
Test statistic = 0.45, p-value = 0.520

General Regression Analysis: log a versus log C, Size, log C * Size

Regression Equation

log a = 2.65747 + 1.33664 log C - 0.730779 Size - 0.3748 log C * Size

Coefficients

Term	Coef	SE Coef	T	P
Constant	2.65747	0.325301	8.16927	0.000
log C	1.33664	0.194403	6.87561	0.000
Size	-0.73078	0.434187	-1.68310	0.143
log C * Size	-0.37480	0.260852	-1.43683	0.201

Summary of Model

S = 0.0831583 R-Sq = 93.06% R-Sq(adj) = 89.60%
PRESS = 0.142008 R-Sq(pred) = 76.26%

Analysis of Variance

Source	DF	Seq SS	Adj SS	Seq MS	F	P
Regression	3	0.556765	0.556765	0.185588	26.8373	0.000710
log C	1	0.511487	0.326914	0.511487	73.9646	0.000136
Size	1	0.031001	0.019590	0.031001	4.4830	0.078576
log C * Size	1	0.014277	0.014277	0.014277	2.0645	0.200794
Error	6	0.041492	0.041492	0.006915		
Total	9	0.598257				

Fits and Diagnostics for Unusual Observations

Obs	log a	Fit	SE Fit	Residual	St Resid	
7	0.157906	0.302594	0.0419128	-0.144688	-2.01449	R

R denotes an observation with a large standardized residual.

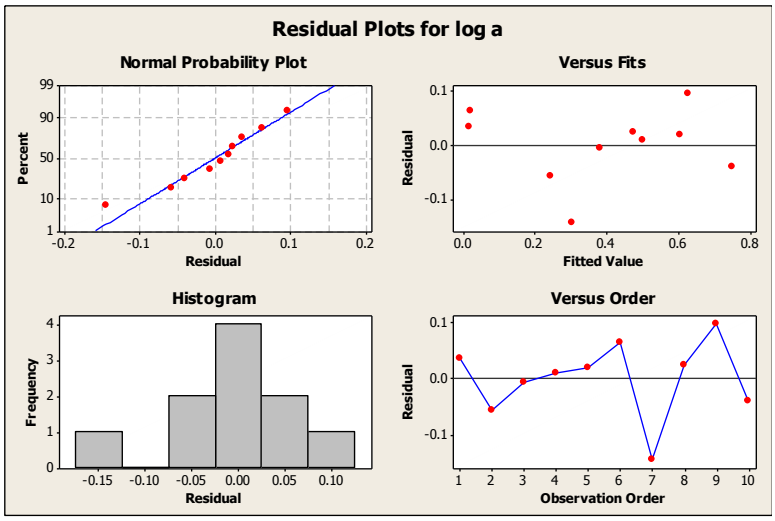

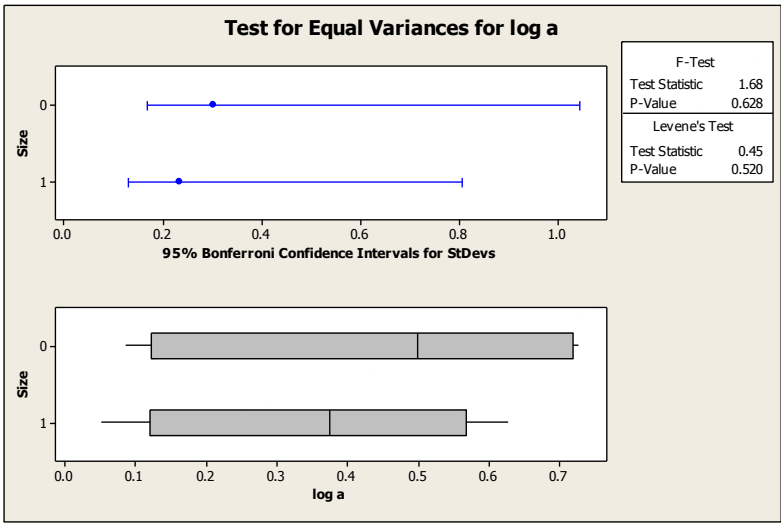

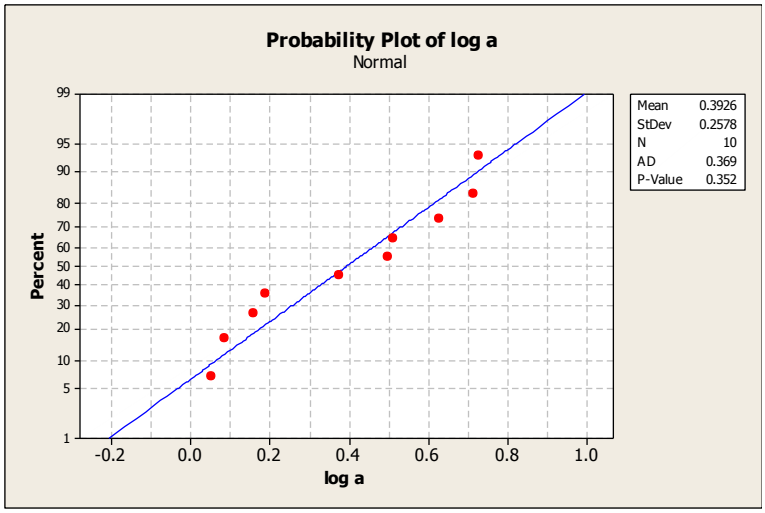

Figure B.1 Minitab output plots 150 x 50 mm versus 150 x 25 mm specimens

Table B.2 Minitab Output – 150 x 50 mm versus 100 x 50 mm specimens

Test for Equal Variances: log a versus Size

95% Bonferroni confidence intervals for standard deviations

Size	N	Lower	StDev	Upper
0	5	0.131425	0.234750	0.812128
1	5	0.130232	0.232619	0.804756

F-Test (Normal Distribution)
Test statistic = 1.02, p-value = 0.986

Levene's Test (Any Continuous Distribution)
Test statistic = 0.06, p-value = 0.816

General Regression Analysis: log a versus log C, Size, log C * Size

Regression Equation

log a = 1.96581 + 1.0158 log C - 0.0391156 Size - 0.0539663 log C * Size

Coefficients

Term	Coef	SE Coef	T	P
Constant	1.96581	0.273945	7.17594	0.000
log C	1.01580	0.169852	5.98050	0.001
Size	-0.03912	0.373607	-0.10470	0.920
log C * Size	-0.05397	0.229037	-0.23562	0.822

Summary of Model

S = 0.0734618 R-Sq = 92.59% R-Sq(adj) = 88.89%
PRESS = 0.147171 R-Sq(pred) = 66.33%

Analysis of Variance

Source	DF	Seq SS	Adj SS	Seq MS	F	P
Regression	3	0.404769	0.404769	0.134923	25.0014	0.000864
log C	1	0.398706	0.193018	0.398706	73.8806	0.000136
Size	1	0.005763	0.000059	0.005763	1.0680	0.341252
log C * Size	1	0.000300	0.000300	0.000300	0.0555	0.821562
Error	6	0.032380	0.032380	0.005397		
Total	9	0.437149				

Fits and Diagnostics for Unusual Observations

No unusual observations

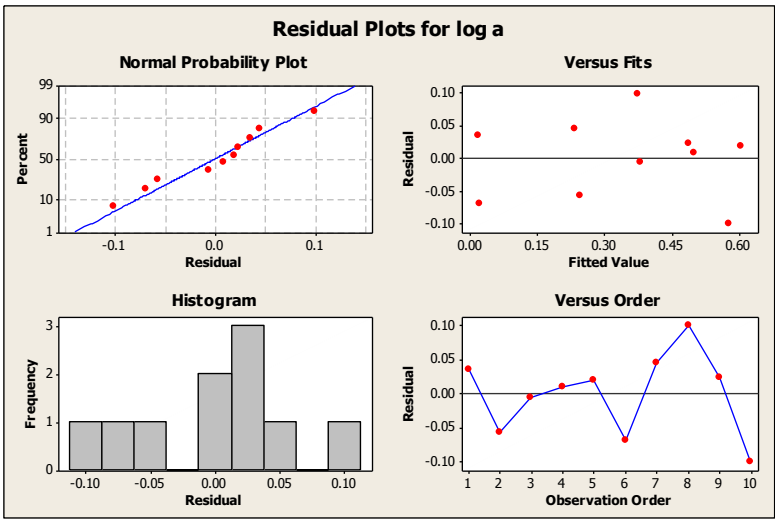

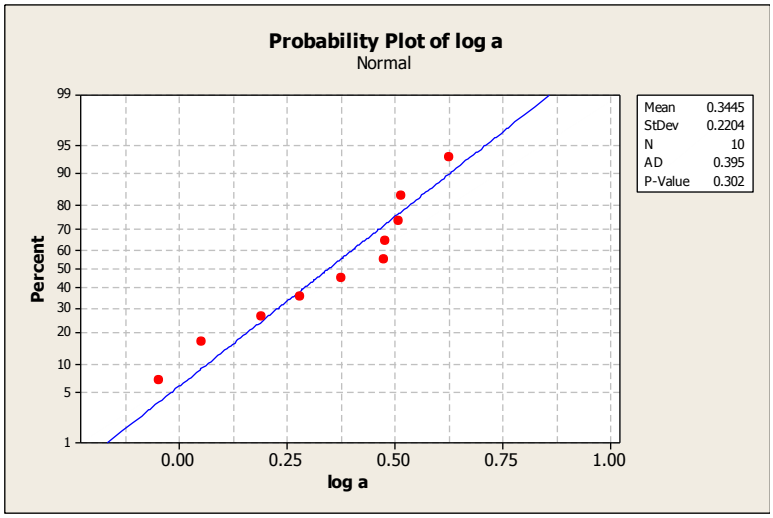

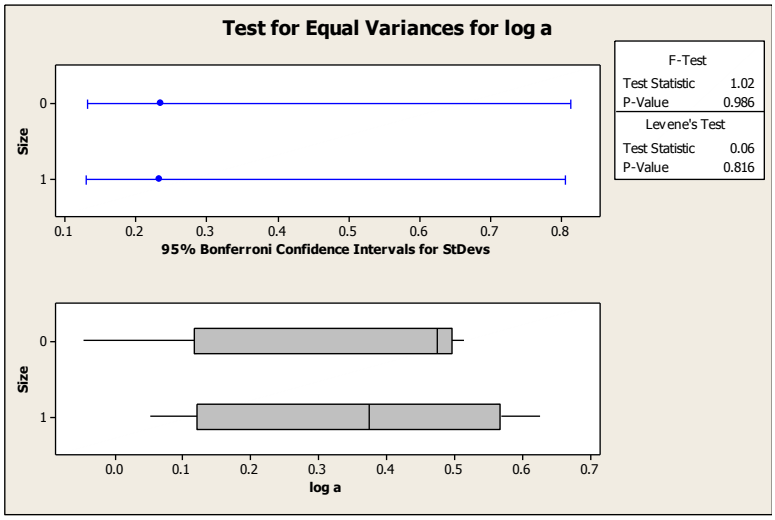

Figure B.2 Minitab output plots 150 x 50 mm versus 100 x 50 mm specimens

Table B.3 Minitab Output – 150 x 25 mm versus 100 x 50 mm specimens

Test for Equal Variances: log a versus Size

95% Bonferroni confidence intervals for standard deviations

Size	N	Lower	StDev	Upper
0	5	0.131425	0.234750	0.81213
1	5	0.168755	0.301429	1.04281

F-Test (Normal Distribution)
Test statistic = 0.61, p-value = 0.640

Levene's Test (Any Continuous Distribution)
Test statistic = 0.51, p-value = 0.494

General Regression Analysis: log a versus log C, Size, log C * Size

Regression Equation

log a = 1.96581 + 1.0158 log C + 0.691663 Size + 0.320834 log C * Size

Coefficients

Term	Coef	SE Coef	T	P
Constant	1.96581	0.384942	5.10676	0.002
log C	1.01580	0.238674	4.25603	0.005
Size	0.69166	0.557890	1.23978	0.261
log C * Size	0.32083	0.339411	0.94527	0.381

Summary of Model

S = 0.103227 R-Sq = 89.47% R-Sq(adj) = 84.20%
PRESS = 0.240426 R-Sq(pred) = 60.39%

Analysis of Variance

Source	DF	Seq SS	Adj SS	Seq MS	F	P
Regression	3	0.543062	0.543062	0.181021	16.9879	0.002453
log C	1	0.464701	0.193018	0.464701	43.6098	0.000580
Size	1	0.068840	0.016379	0.068840	6.4603	0.043980
log C * Size	1	0.009521	0.009521	0.009521	0.8935	0.381016
Error	6	0.063935	0.063935	0.010656		
Total	9	0.606997				

Fits and Diagnostics for Unusual Observations

No unusual observations

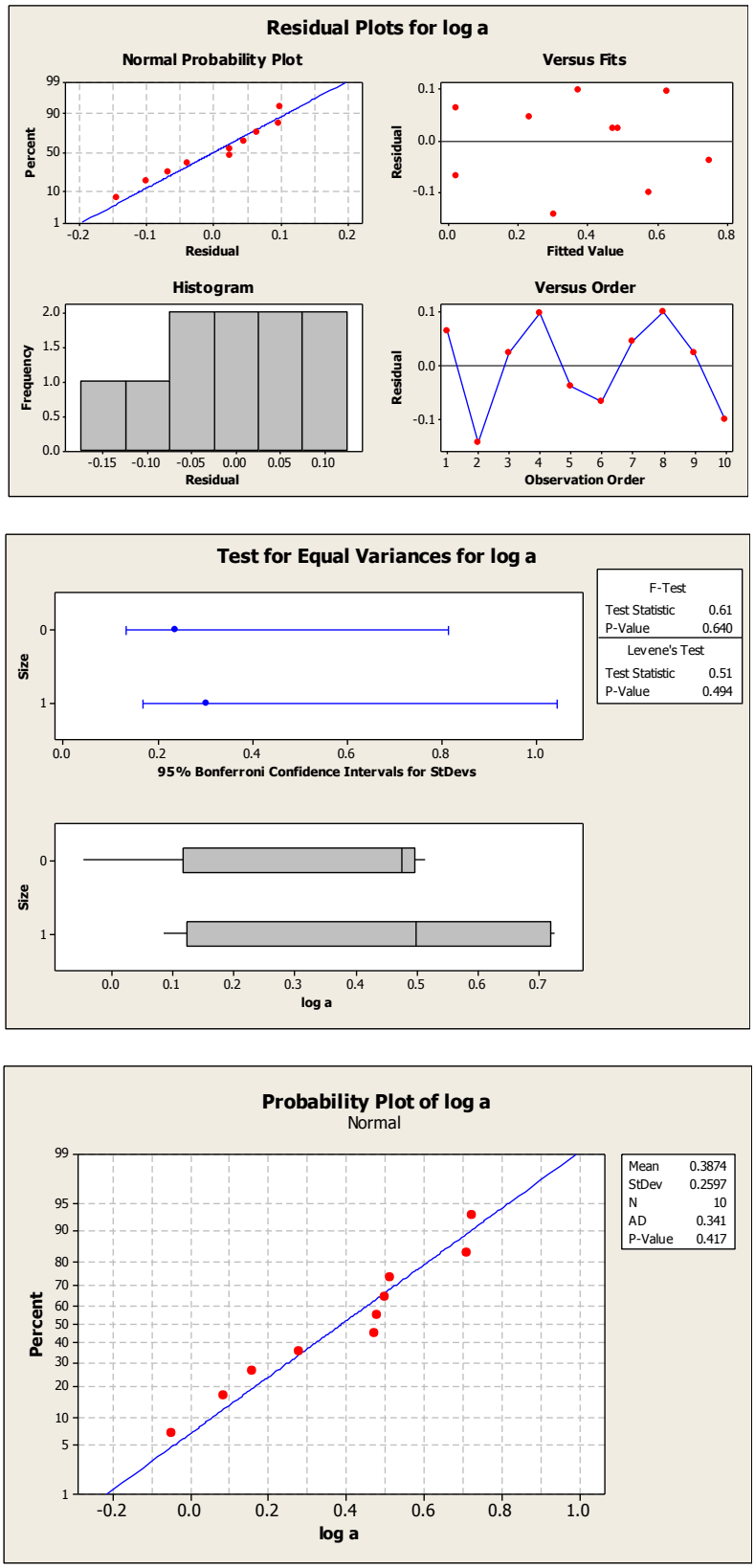

Figure B.3 Minitab output plots 150 x 50 mm versus 100 x 50 mm specimens

Table B.4 Minitab Output – 1 replicate versus 2 replicate series (ADOT Mixture, 150 x 50 mm, 21°C)

Regression Equation

log a = 1.74708 + 0.868933 log C + 0.179612 Rep-Series + 0.0929022 log C*Rep-Series

Coefficients

Term	Coef	SE Coef	T	P
Constant	1.74708	0.292517	5.97258	0.001
log C	0.86893	0.174517	4.97906	0.003
Rep-Series	0.17961	0.412398	0.43553	0.678
log C*Rep-Series	0.09290	0.247728	0.37502	0.721

Summary of Model

S = 0.0840626 R-Sq = 90.24% R-Sq(adj) = 85.37%
PRESS = 0.135619 R-Sq(pred) = 68.79%

Analysis of Variance

Source	DF	Seq SS	Adj SS	Seq MS	F	P
Regression	3	0.392203	0.392203	0.130734	18.5005	0.001955
log C	1	0.389491	0.175187	0.389491	55.1178	0.000307
Rep-Series	1	0.001718	0.001340	0.001718	0.2431	0.639501
log C*Rep-Series	1	0.000994	0.000994	0.000994	0.1406	0.720547
Error	6	0.042399	0.042399	0.007067		
Total	9	0.434602				

Fits and Diagnostics for Unusual Observations, No unusual observations

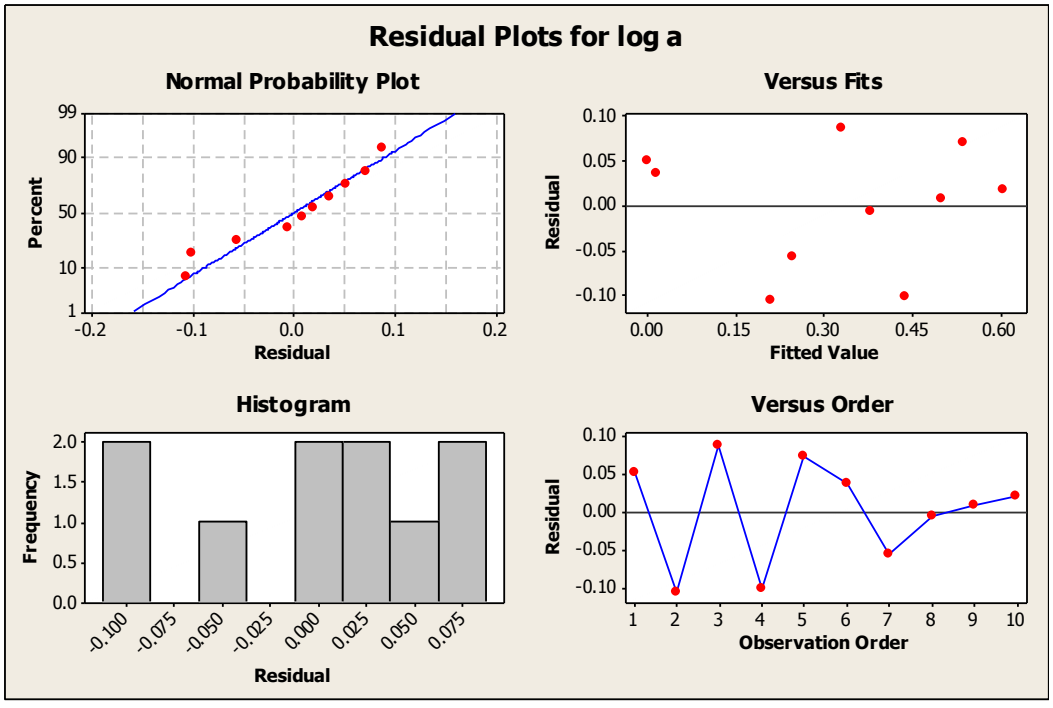

Figure B.4 Minitab output- Residual plot for 1 replicate versus 2 replicate series.

Table B.5 Minitab Output – 1 replicate versus 3 replicate series (ADOT Mixture, 150 x 50 mm, 21°C)

Regression Equation

log a = 1.74708 + 0.868933 log C + 0.292342 Rep-Series + 0.168613 log C*Rep-Series

Coefficients

Term	Coef	SE Coef	T	P
Constant	1.74708	0.291104	6.00156	0.001
log C	0.86893	0.173675	5.00322	0.002
Rep-Series	0.29234	0.415759	0.70315	0.508
log C*Rep-Series	0.16861	0.251196	0.67124	0.527

Summary of Model

S = 0.0836567 R-Sq = 90.73% R-Sq(adj) = 86.10%
PRESS = 0.126776 R-Sq(pred) = 72.01%

Analysis of Variance

Source	DF	Seq SS	Adj SS	Seq MS	F	P
Regression	3	0.411006	0.411006	0.137002	19.5761	0.001681
log C	1	0.407253	0.175187	0.407253	58.1920	0.000265
Rep-Series	1	0.000600	0.003460	0.000600	0.0857	0.779596
log C*Rep-Series	1	0.003153	0.003153	0.003153	0.4506	0.527048
Error	6	0.041991	0.041991	0.006998		
Total	9	0.452997				

Fits and Diagnostics for Unusual Observations, No unusual observations

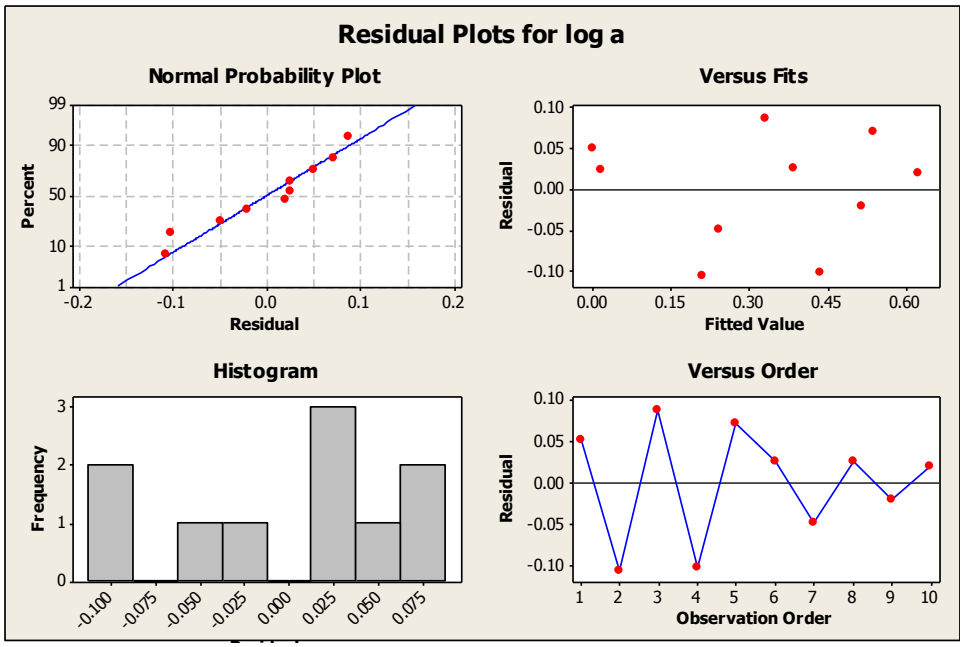

Figure B.5 Minitab output- Residual plot for 1 replicate versus 3 replicate series.

Table B.6 Minitab Output – 2 replicate versus 3 replicate series (ADOT Mixture, 150 x 50 mm, 21°C)

Regression Equation

log a = 1.92669 + 0.961835 log C + 0.11273 Rep-Series + 0.0757111 log C*Rep-Series

Coefficients

Term	Coef	SE Coef	T	P
Constant	1.92669	0.137805	13.9813	0.000
log C	0.96184	0.083347	11.5401	0.000
Rep-Series	0.11273	0.197443	0.5709	0.589
log C*Rep-Series	0.07571	0.120084	0.6305	0.552

Summary of Model

S = 0.0398495 R-Sq = 97.88% R-Sq(adj) = 96.82%
PRESS = 0.0399106 R-Sq(pred) = 91.13%

Analysis of Variance

Source	DF	Seq SS	Adj SS	Seq MS	F	P
Regression	3	0.440312	0.440312	0.146771	92.426	0.000021
log C	1	0.439393	0.211478	0.439393	276.699	0.000003
Rep-Series	1	0.000288	0.000518	0.000288	0.181	0.685260
log C*Rep-Series	1	0.000631	0.000631	0.000631	0.398	0.551620
Error	6	0.009528	0.009528	0.001588		
Total	9	0.449840				

Fits and Diagnostics for Unusual Observations, No unusual observations

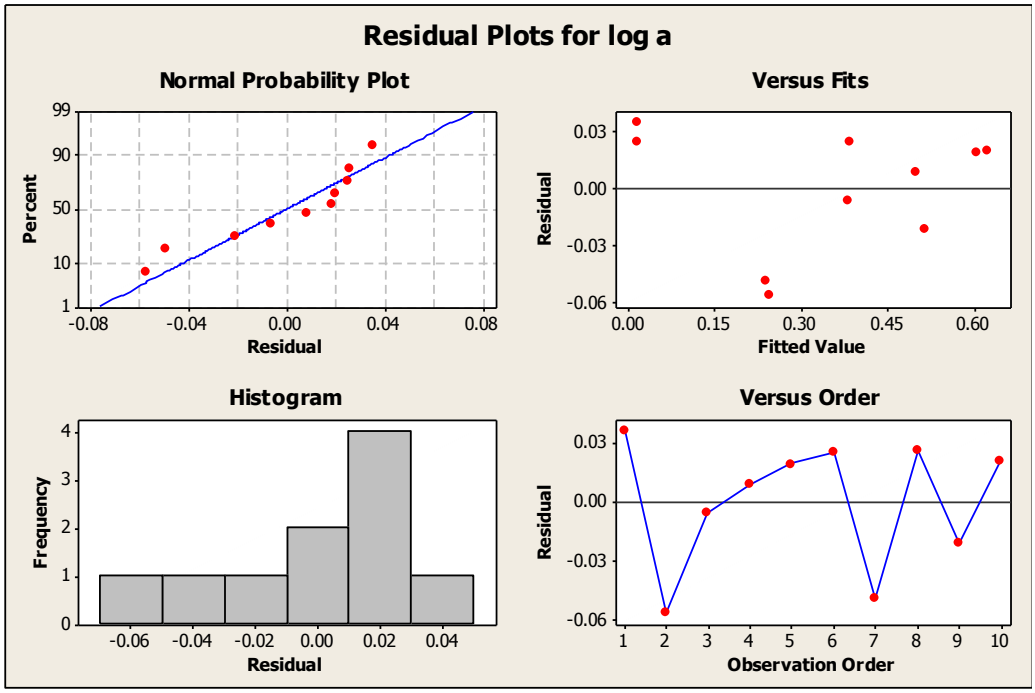

Figure B.6 Minitab output- Residual plot for 2 replicate versus 3 replicate series.

Table B.7 Minitab Output – Final Crack Growth Rate Prediction Model

Regression Equation

log a = 26.5848 + 0.977639 log C + 2.53324e-005 η + 0.343349 %B^2 + 0.00366102(η x C) + 2.45468e-009 E^2 - 11.6053 log (m) - 56.0271 log %B

Coefficients

Term	Coef	SE Coef	T	P
Constant	26.5848	9.8944	2.6869	0.009
log C	0.9776	0.0693	14.1086	0.000
η	0.0000	0.0000	1.9234	0.059
%B^2	0.3433	0.1562	2.1985	0.032
η x C	0.0037	0.0008	4.4534	0.000
E^2	0.0000	0.0000	7.3351	0.000
log m	-11.6053	0.8837	-13.1333	0.000
log %B	-56.0271	20.1871	-2.7754	0.007

Summary of Model

S = 0.129493 R-Sq = 91.68% R-Sq(adj) = 90.72%
PRESS = 1.38085 R-Sq(pred) = 88.77%

Analysis of Variance

Source	DF	Seq SS	Adj SS	Seq MS	F	P
Regression	7	11.2708	11.2708	1.61011	96.020	0.000000
log C	1	0.5466	3.3378	0.54659	32.596	0.000000
η	1	3.5768	0.0620	3.57680	213.304	0.000000
%B^2	1	2.5195	0.0811	2.51947	150.250	0.000000
η x C	1	1.4055	0.3326	1.40553	83.819	0.000000
E^2	1	0.0001	0.9022	0.00005	0.003	0.956533
log m	1	3.0932	2.8923	3.09317	184.463	0.000000
log %B	1	0.1292	0.1292	0.12916	7.703	0.007310
Error	61	1.0229	1.0229	0.01677		
Total	68	12.2937				

Fits and Diagnostics for Unusual Observations

Obs	log a	Fit	SE Fit	Residual	St Resid	
2	0.127105	0.369147	0.0609509	-0.242042	-2.11849	R
52	0.149858	0.438549	0.0440557	-0.288691	-2.37081	R
68	0.020526	0.264166	0.0531642	-0.243640	-2.06340	R

R denotes an observation with a large standardized residual.

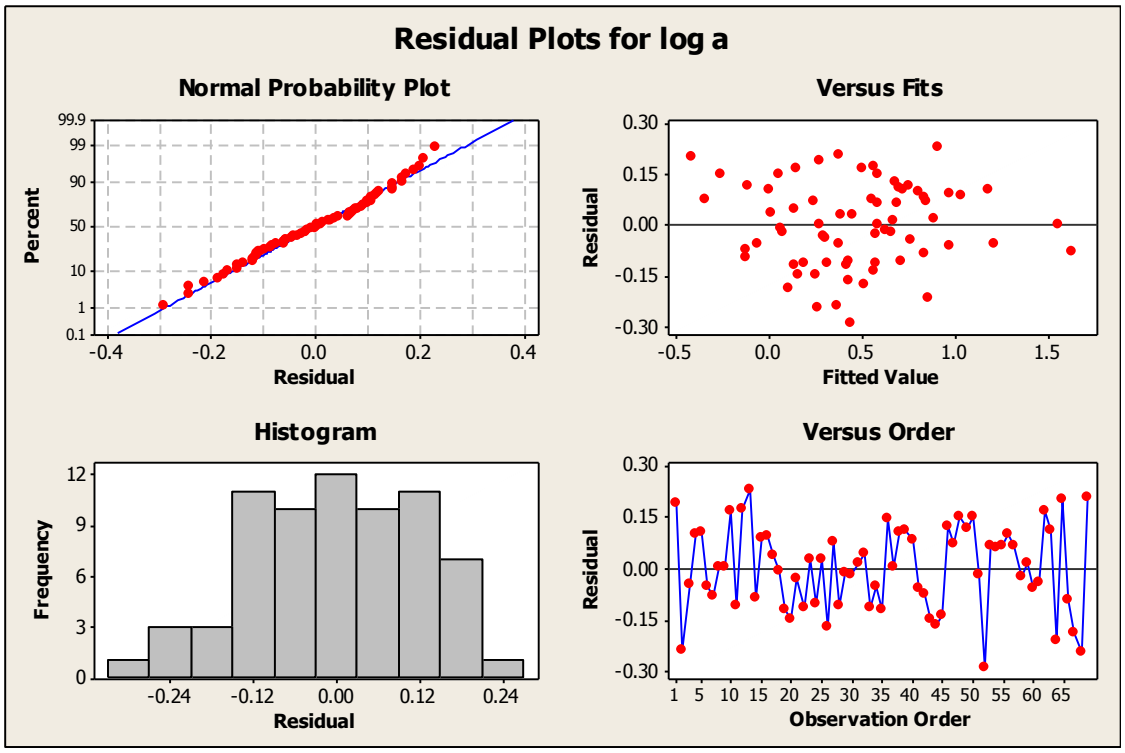

Figure B.7 Minitab residual plot for log a*.

Table B.8 Minitab Output – Final C* Prediction Model

Regression Equation

Log C = -0.339753 + 1.15875 log Δ + 0.610692 log E01 + 0.00491984 (ρ9.5 x log Δ)+ 5.26501 log m - 0.324008 log ρ9.5

Coefficients

Term	Coef	SE Coef	T	P
Constant	-0.33975	0.171015	-1.9867	0.051
log Δ	1.15875	0.047068	24.6188	0.000
log E01	0.61069	0.027681	22.0618	0.000
ρ9.5xlogΔ	0.00492	0.002273	2.1640	0.034
log m	5.26501	0.173285	30.3835	0.000
log ρ9.5	-0.32401	0.037110	-8.7310	0.000

Summary of Model

S = 0.0510224 R-Sq = 98.92% R-Sq(adj) = 98.84%
PRESS = 0.194155 R-Sq(pred) = 98.70%

Analysis of Variance

Source	DF	Seq SS	Adj SS	Seq MS	F	P
Regression	5	14.8117	14.8117	2.96233	1137.92	0.0000000
log Δ	1	9.4470	1.5778	9.44697	3628.87	0.0000000
log E01	1	2.4764	1.2671	2.47635	951.24	0.0000000
ρ9.5xlogΔ	1	0.4299	0.0122	0.42993	165.15	0.0000000
log m	1	2.2600	2.4032	2.25997	868.12	0.0000000
log ρ9.5	1	0.1984	0.1984	0.19845	76.23	0.0000000
Error	62	0.1614	0.1614	0.00260		
Lack-of-Fit	39	0.1201	0.1201	0.00308	1.71	0.0859805
Pure Error	23	0.0413	0.0413	0.00180		
Total	67	14.9731				

Fits and Diagnostics for Unusual Observations

Obs	Log C	Fit	SE Fit	Residual	St Resid	
9	-2.08034	-2.18371	0.0129767	0.103373	2.09492	R
47	-1.82938	-1.72718	0.0162088	-0.102204	-2.11255	R
48	-1.74733	-1.63794	0.0161950	-0.109388	-2.26084	R
49	-1.60241	-1.49071	0.0173363	-0.111696	-2.32764	R
50	-1.42510	-1.32588	0.0200258	-0.099220	-2.11431	R

R denotes an observation with a large standardized residual.

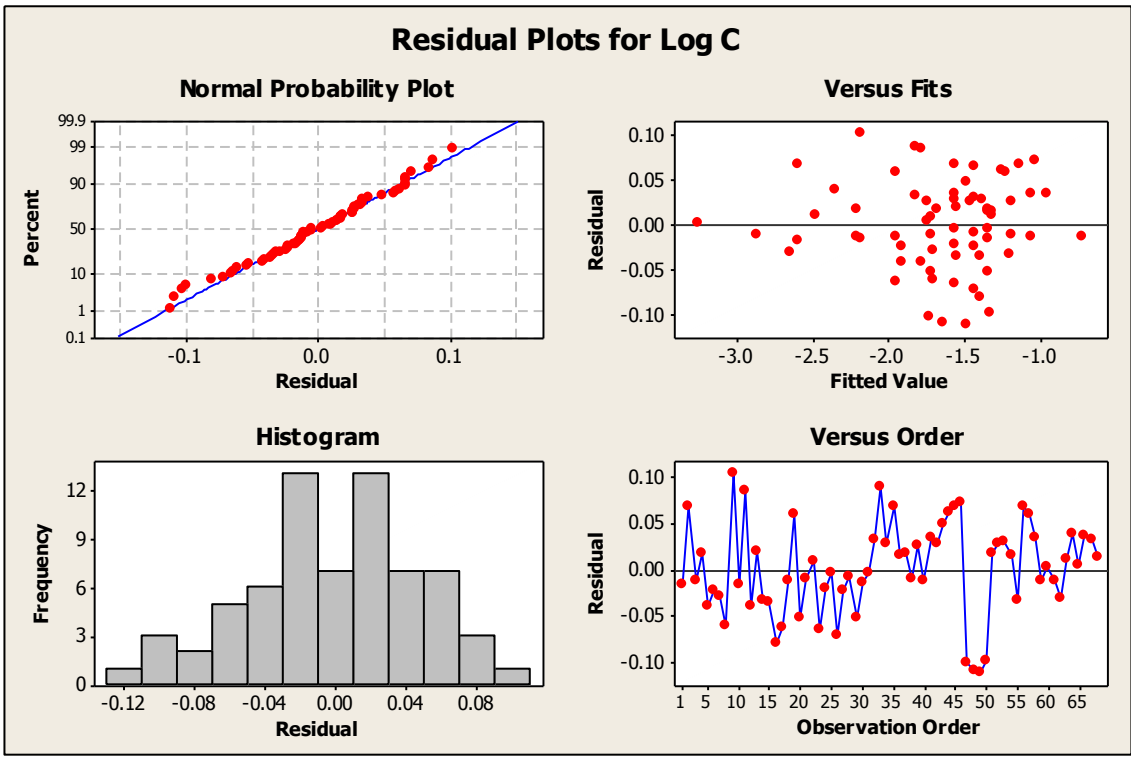

Figure B.8 Minitab residual plot for log C*.

APPENDIX C

C. MIXTURE CHARACTERIZATION DATA

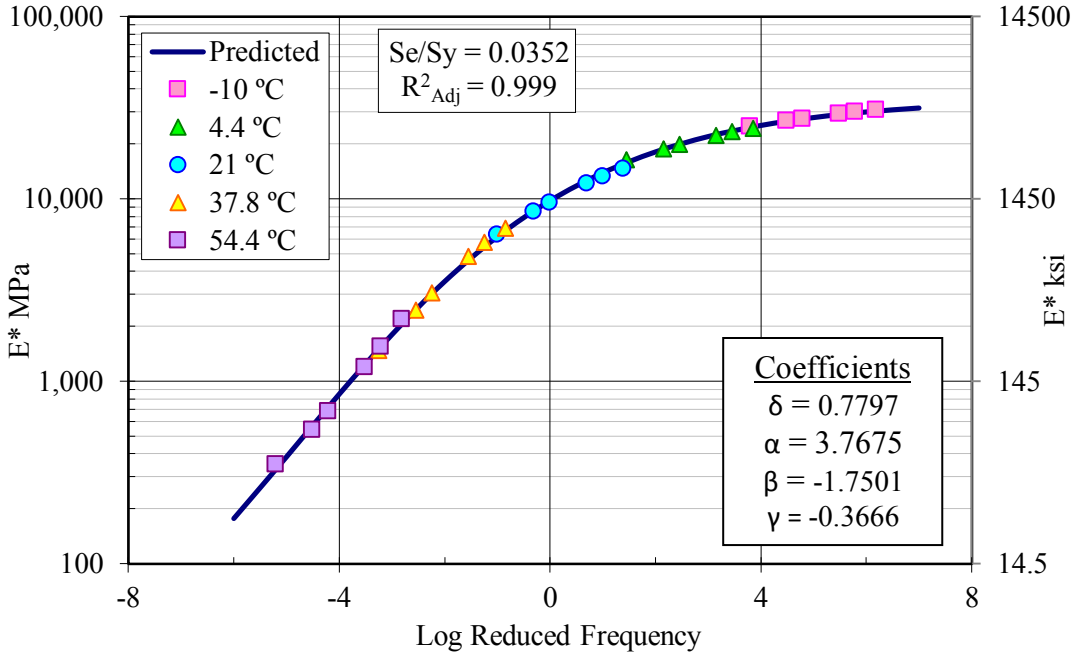

Figure C.1 Dynamic modulus master curve (ADOT mixture)

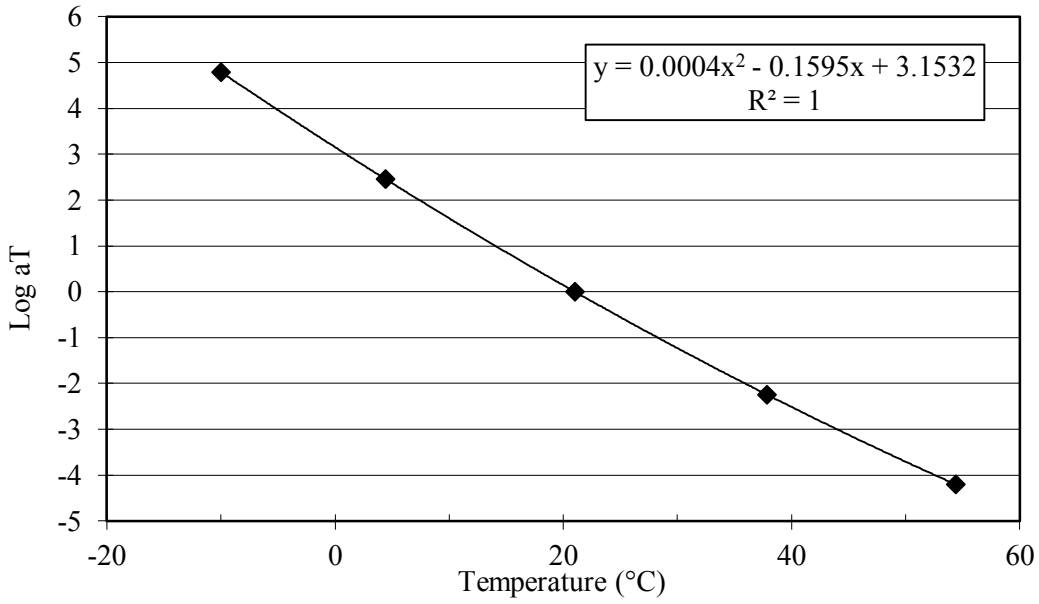

Figure C.2 MC shift factors versus temperature (ADOT mixture)

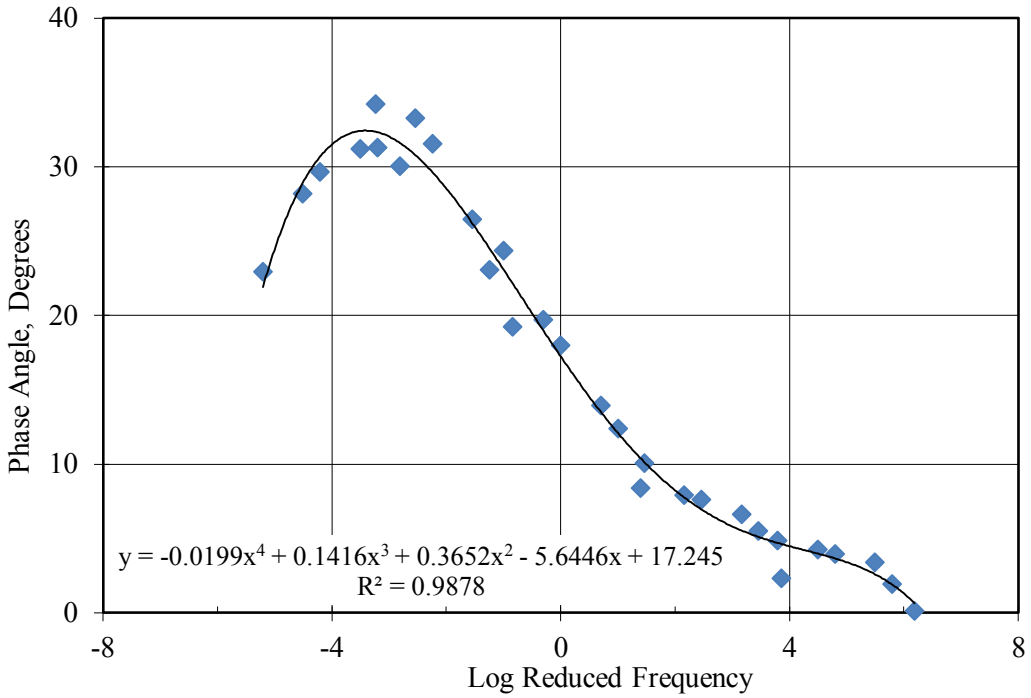

Figure C.3 Phase angle versus log reduced frequency (ADOT mixture)

Table C.1 Dynamic modulus summary data (ADOT mixture)

Temp.	Freq.	Dynamic Modulus, |E*| (MPa)						Phase Angle, ϕ (degree)					
°C	Hz	Rep1	Rep2	Rep3	Avg. |E*|	St. Dev.	%CV	Rep1	Rep2	Rep3	Avg. ϕ	St. Dev.	%CV
-10	25	24725	28899	38446	30690	7033	23	-1	0	0	-0.3	0.3	-114
	10	24477	28419	36952	29949	6377	21	2	2	2	1.9	0.2	11
	5	23821	28011	36059	29297	6219	21	3	3	4	3.4	0.5	14
	1	22490	26524	33677	27564	5665	21	4	4	4	3.9	0.1	3
	0.5	21999	25847	32645	26831	5391	20	4	4	4	4.2	0.2	6
	0.1	20632	24406	29989	25009	4707	19	5	5	5	4.8	0.4	9
4.4	25	19368	23851	29990	24403	5332	22	2	2	3	2.3	0.4	18
	10	18570	22969	28440	23327	4945	21	6	5	6	5.5	0.4	7
	5	17794	21947	26914	22219	4566	21	7	6	7	6.6	0.8	11
	1	15854	19729	23853	19812	4001	20	8	6	9	7.6	1.3	17
	0.5	15161	18758	22631	18850	3736	20	8	7	8	7.9	0.6	7
	0.1	13213	16341	19456	16337	3122	19	11	9	11	10.1	0.9	9
21	25	12701	14197	17048	14648	2208	15	8	8	9	8.4	0.6	7
	10	11944	12743	15035	13240	1604	12	13	12	12	12.4	0.6	5
	5	11087	11621	13608	12105	1328	11	14	13	14	13.9	0.7	5
	1	8746	9073	10724	9514	1060	11	19	17	18	18.0	0.7	4
	0.5	7907	8068	9609	8528	940	11	21	19	20	19.7	0.8	4
	0.1	5922	5959	7267	6382	766	12	25	23	25	24.3	1.1	5
37.8	25	6671	6321	7675	6889	703	10	20	19	19	19.3	1.0	5
	10	5563	5249	6455	5755	626	11	24	22	23	23.1	1.1	5
	5	4699	4375	5477	4850	566	12	27	25	27	26.5	1.3	5
	1	2922	2755	3507	3061	395	13	33	30	32	31.6	1.5	5
	0.5	2326	2199	2853	2459	347	14	34	32	34	33.3	1.3	4
	0.1	1384	1309	1738	1477	229	16	35	33	34	34.2	1.0	3
54.4	25	2249	1917	2391	2186	243	11	30	31	29	30.0	1.1	4
	10	1597	1343	1698	1546	183	12	32	31	31	31.3	0.6	2
	5	1229	1022	1325	1192	155	13	31	32	31	31.2	0.3	1
	1	703	570	779	684	106	15	30	30	29	29.6	0.5	2
	0.5	564	443	617	541	89	16	29	27	28	28.2	1.0	3
	0.1	365	292	394	350	53	15	24	21	24	22.9	1.9	8

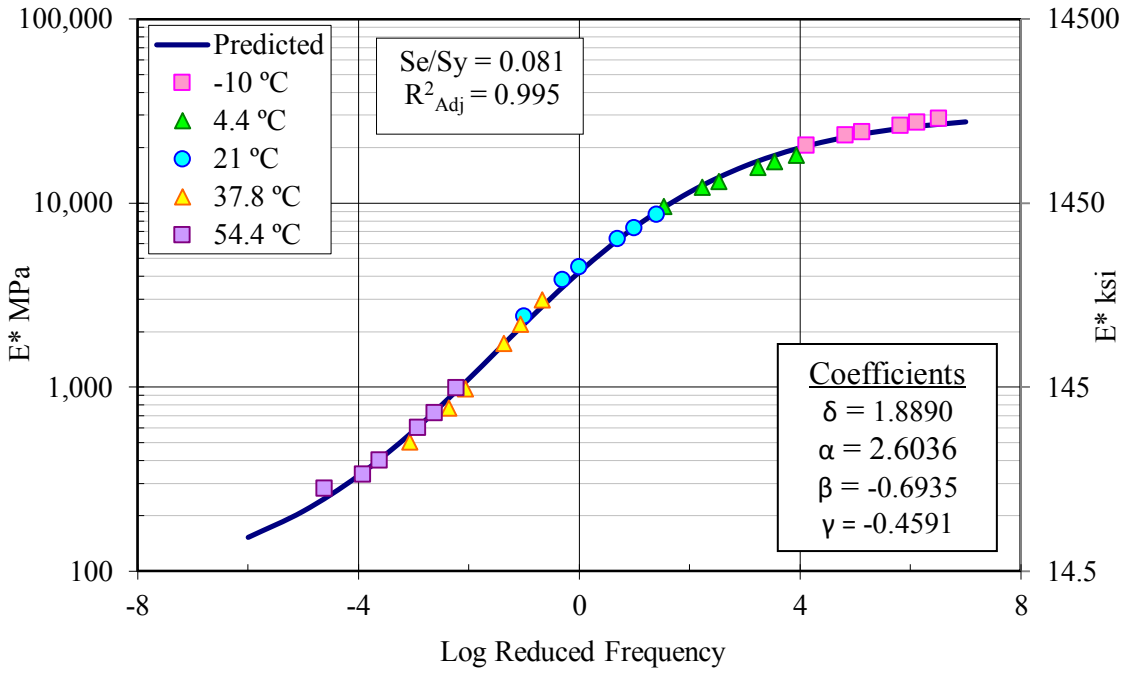

Figure C.4 Dynamic modulus master curve (PA Cranberry Twp Control).

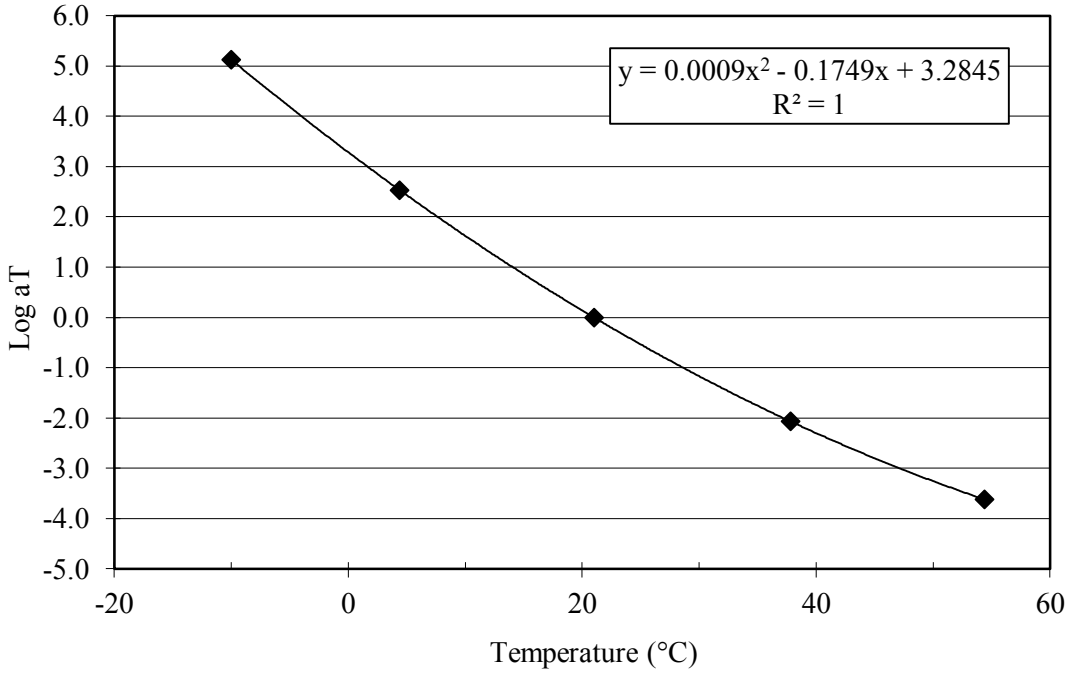

Figure C.5 MC shift factors versus temperature (PA Cranberry Twp Control)

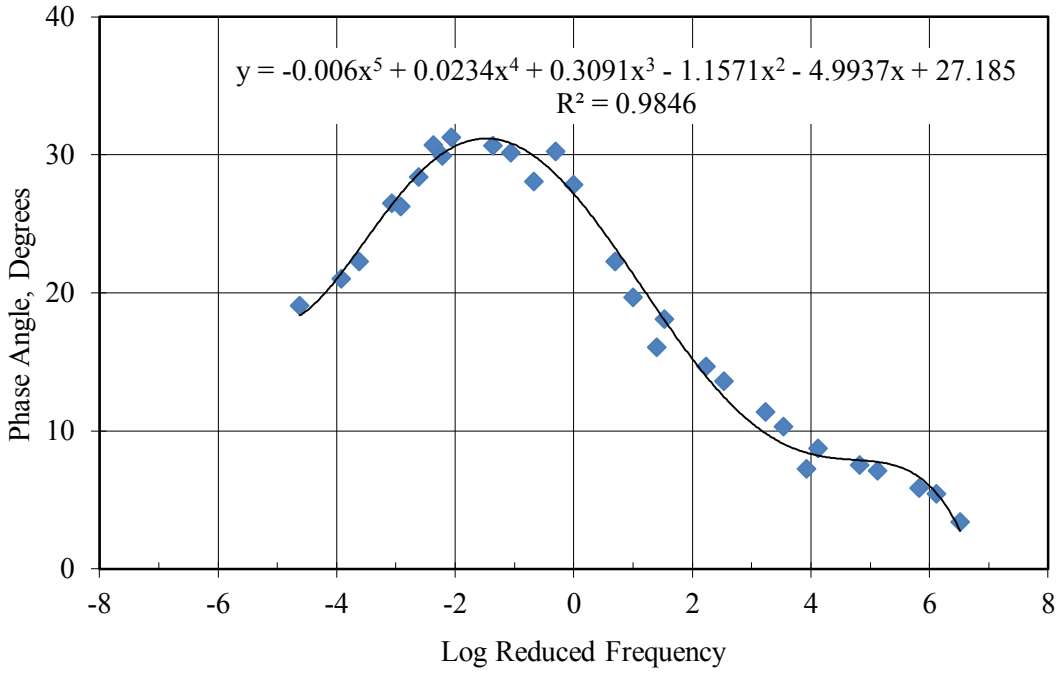

Figure C.6 Phase angle versus log reduced frequency (PA Cranberry Twp Control)

Table C.2 Dynamic Modulus Data (PA Cranberry Twp Control)

Temp.	Freq.	Dynamic Modulus, |E*| (MPa)						Phase Angle, ϕ (degree)					
°C	Hz	Rep1	Rep2	Rep3	Avg. |E*|	St. Dev.	%CV	Rep1	Rep2	Rep3	Avg. ϕ	St. Dev.	%CV
-10	25	25857	30523	29827	28736	2517	9	3.8	1.9	4.6	3.4	1.4	41
	10	24922	28960	28094	27325	2126	8	6.3	3.7	6.5	5.5	1.5	28
	5	24079	28104	26968	26384	2075	8	6.8	4.6	6.2	5.9	1.2	20
	1	21894	25878	24808	24193	2062	9	8.1	6.2	7.2	7.1	0.9	13
	0.5	20972	24940	23767	23226	2039	9	8.4	6.2	7.9	7.5	1.2	15
	0.1	18769	22042	20922	20578	1663	8	9.3	7.9	8.9	8.7	0.7	9
4.4	25	19912	19518	15136	18189	2651	15	7.6	6.5	7.7	7.3	0.7	10
	10	18731	17274	14246	16750	2288	14	9.1	10.1	11.7	10.3	1.3	13
	5	17638	15749	13343	15577	2153	14	10.7	11.3	12.2	11.4	0.8	7
	1	14783	13144	11281	13069	1752	13	13.3	13.1	14.5	13.6	0.7	5
	0.5	13970	12012	10466	12149	1756	14	14.5	14.2	15.3	14.7	0.6	4
	0.1	11004	9337	8404	9582	1317	14	18.2	17.6	18.5	18.1	0.5	3
21	25	10286	8076	7448	8603	1491	17	16.8	15.1	16.2	16.0	0.9	5
	10	8778	6772	6392	7314	1282	18	20.5	18.9	19.7	19.7	0.8	4
	5	7583	5927	5617	6376	1057	17	22.5	22.4	22.0	22.3	0.3	1
	1	5365	4128	3909	4467	785	18	28.4	27.2	28.0	27.9	0.6	2
	0.5	4588	3505	3306	3800	690	18	30.8	29.8	30.1	30.2	0.5	2
	0.1	2930	2286	2035	2417	462	19	35.0	32.4	34.1	33.8	1.3	4
37.8	25	3477	2868	2570	2972	462	16	28.5	26.0	29.8	28.1	1.9	7
	10	2568	2126	1884	2193	347	16	29.4	28.6	32.5	30.2	2.1	7
	5	2016	1679	1480	1725	271	16	30.0	29.4	32.7	30.7	1.7	6
	1	1161	970	809	980	176	18	31.6	29.5	32.7	31.3	1.6	5
	0.5	923	753	639	772	143	19	31.0	28.5	32.7	30.7	2.1	7
	0.1	612	491	405	503	104	21	26.5	25.5	27.6	26.5	1.1	4
54.4	25	1092	974	885	984	104	11	29.6	30.6	29.5	29.9	0.6	2
	10	791	747	626	721	85	12	27.6	26.1	31.4	28.4	2.8	10
	5	670	600	524	598	73	12	23.9	26.5	28.3	26.3	2.2	8
	1	470	393	337	400	67	17	19.2	21.8	25.8	22.3	3.4	15
	0.5	387	338	280	335	54	16	17.4	20.2	25.5	21.0	4.1	20
	0.1	311	284	246	280	33	12	15.9	18.2	23.1	19.1	3.7	19

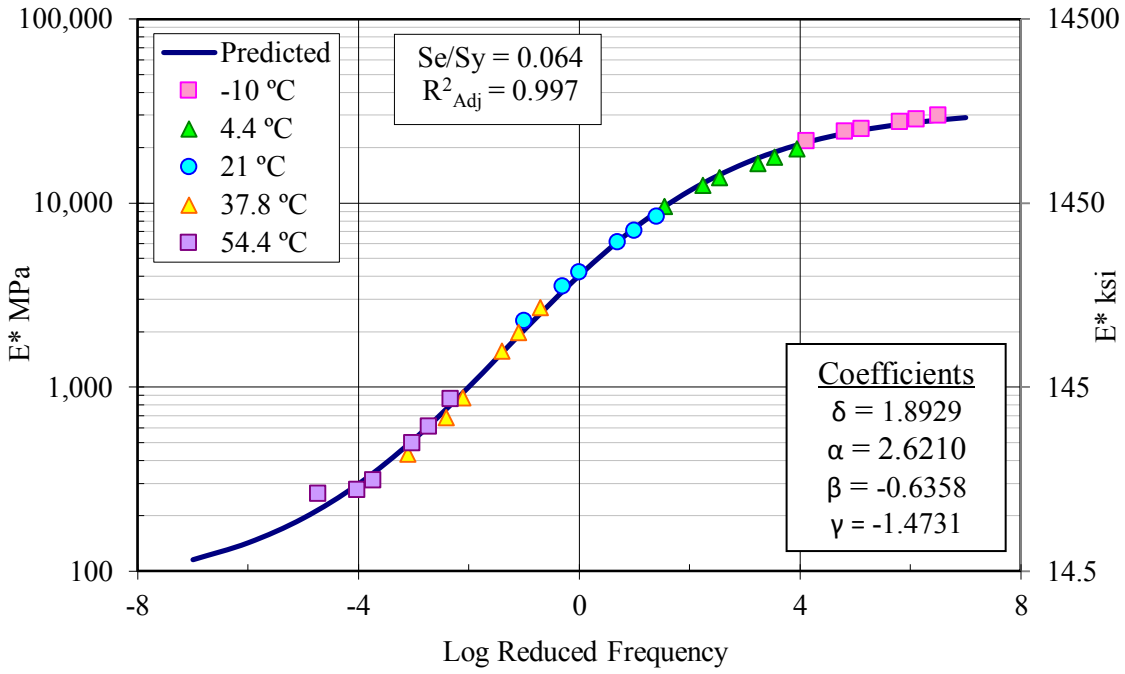

Figure C.7 Dynamic modulus master curve (PA Cranberry Twp Fiber Modified)

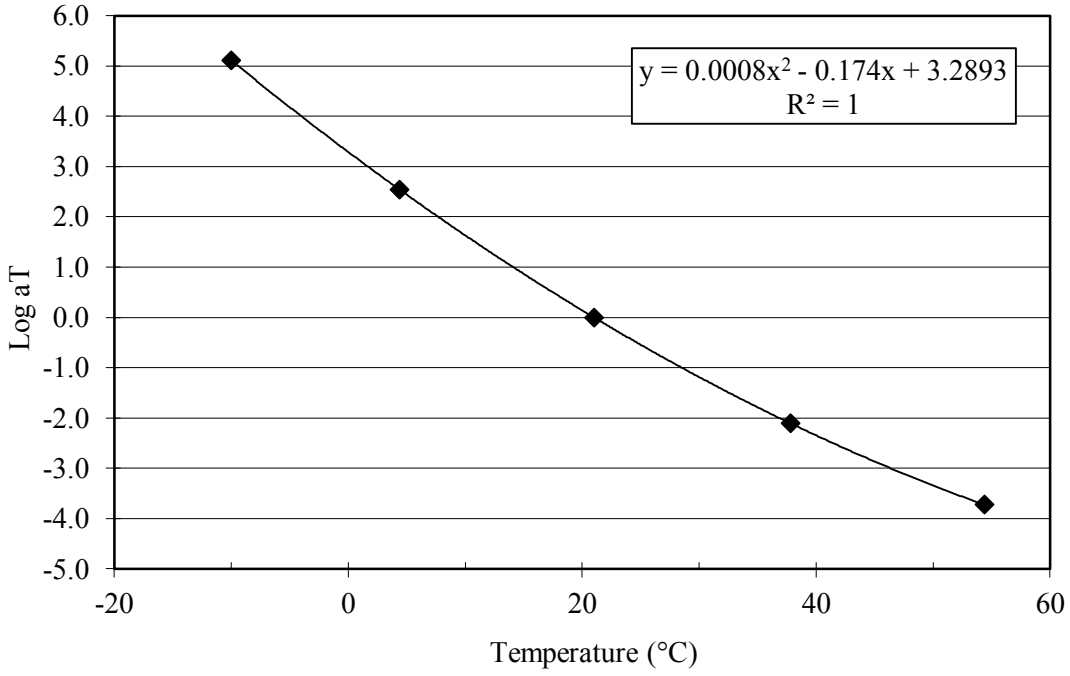

Figure C.8 MC shift factors versus temperature (PA Cranberry Twp Control)

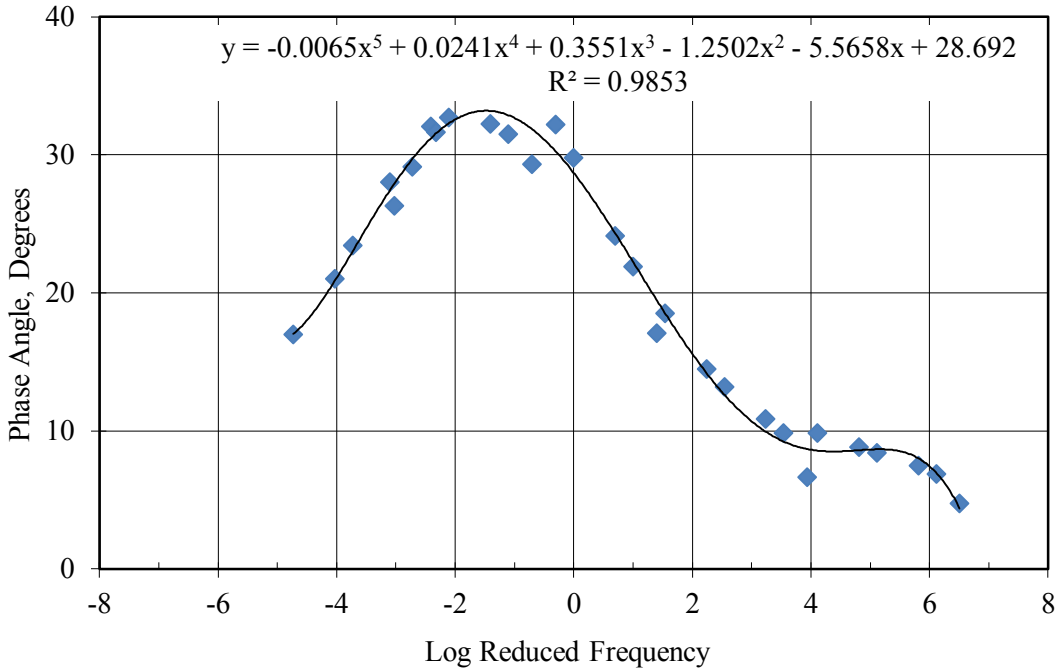

Figure C.9 Phase angle versus log reduced frequency (PA Cranberry Twp Control)

Table C.3 Dynamic Modulus Data (PA Cranberry Twp Control)

Temp.	Freq.	Dynamic Modulus, |E*| (MPa)						Phase Angle, ϕ (degree)					
°C	Hz	Rep1	Rep2	Rep3	Avg. |E*|	St. Dev.	%CV	Rep1	Rep2	Rep3	Avg. ϕ	St. Dev.	%CV
-10	25	22158	41618	25872	29883	10331	35	3.1	5.6	5.6	4.8	1.4	30
	10	21128	39948	24681	28586	9999	35	5.7	8.2	6.6	6.9	1.3	18
	5	20422	38570	23824	27605	9647	35	6.0	9.0	7.5	7.5	1.5	20
	1	18837	35217	21889	25314	8711	34	7.5	9.6	8.1	8.4	1.1	13
	0.5	18174	33956	20952	24361	8425	35	7.2	10.5	8.9	8.9	1.6	18
	0.1	16313	30229	18535	21692	7476	34	9.2	11.4	9.0	9.9	1.3	14
4.4	25	12852	26342	19761	19652	6746	34	6.9	6.3	6.8	6.7	0.3	4
	10	12263	23680	17467	17803	5716	32	10.0	9.9	9.7	9.8	0.2	2
	5	11613	21708	16006	16442	5062	31	11.1	11.2	10.4	10.9	0.4	4
	1	9836	17858	13373	13689	4020	29	13.2	14.3	12.1	13.2	1.1	8
	0.5	9156	16152	12086	12465	3513	28	14.3	15.6	13.6	14.5	1.0	7
	0.1	7515	12075	9263	9618	2301	24	18.4	19.6	17.6	18.5	1.0	5
21	25	8088	9257	7932	8426	724	9	17.0	18.0	16.3	17.1	0.9	5
	10	6944	7600	6704	7083	464	7	22.7	22.2	20.8	21.9	1.0	4
	5	6037	6485	5859	6127	323	5	25.1	24.2	23.1	24.1	1.0	4
	1	4158	4416	4066	4213	181	4	31.1	29.4	28.8	29.8	1.2	4
	0.5	3501	3691	3412	3535	143	4	33.6	31.7	31.2	32.2	1.3	4
	0.1	2243	2364	2228	2278	75	3	37.3	35.5	34.8	35.9	1.3	4
37.8	25	2652	2718	2726	2699	41	2	30.4	28.6	29.1	29.3	0.9	3
	10	1924	1947	2083	1985	86	4	32.2	31.1	31.2	31.5	0.6	2
	5	1522	1495	1682	1566	101	6	32.6	32.0	32.2	32.2	0.3	1
	1	853	821	953	876	69	8	33.3	32.3	32.5	32.7	0.5	2
	0.5	671	620	758	683	70	10	32.0	32.8	31.3	32.1	0.8	2
	0.1	428	368	498	431	65	15	28.6	28.5	27.0	28.0	0.9	3
54.4	25	790	767	1018	858	139	16	30.6	31.6	32.7	31.6	1.1	3
	10	545	524	766	612	134	22	28.2	29.8	29.4	29.1	0.8	3
	5	447	406	629	494	119	24	23.2	28.7	27.1	26.3	2.8	11
	1	287	242	402	310	83	27	19.9	24.7	25.7	23.4	3.1	13
	0.5	238	217	374	276	85	31	14.7	22.6	25.8	21.0	5.7	27
	0.1	203	184	402	263	121	46	15.1	19.5	16.4	17.0	2.3	13

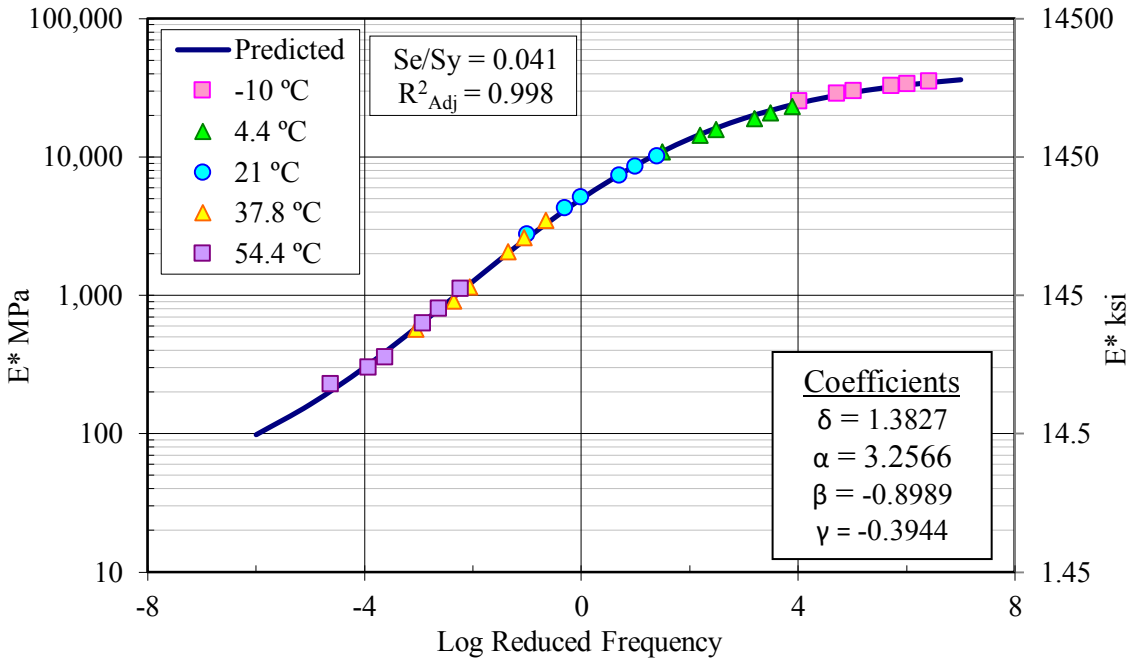

Figure C.10 Dynamic modulus master curve (PennDot I-78 PG76-22)

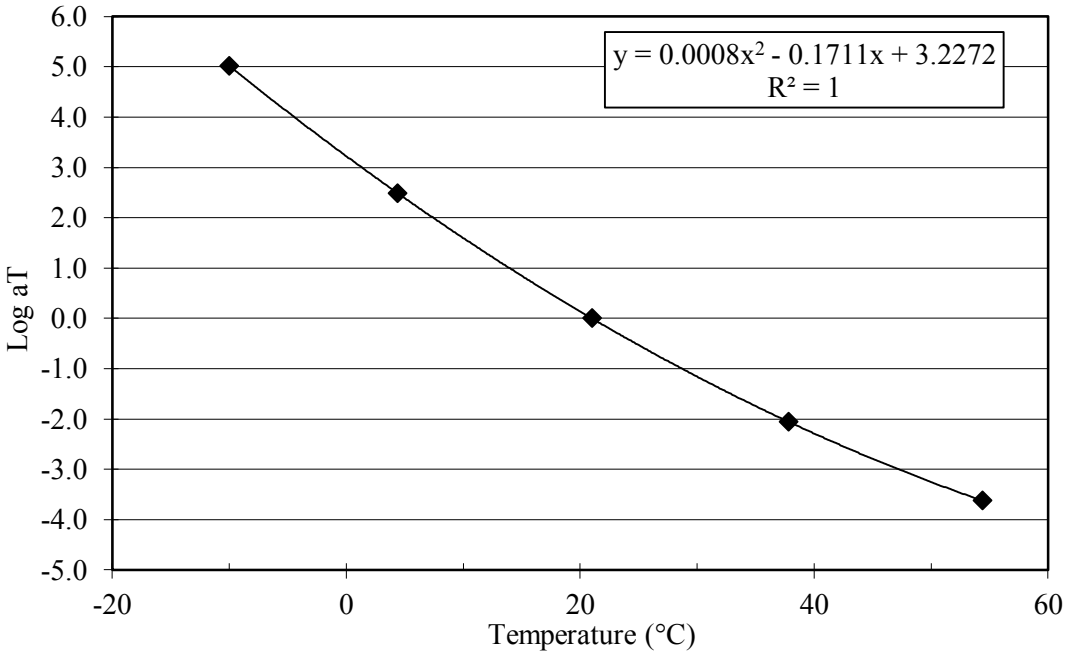

Figure C.11 MC shift factors versus temperature (PennDot I-78 PG76-22)

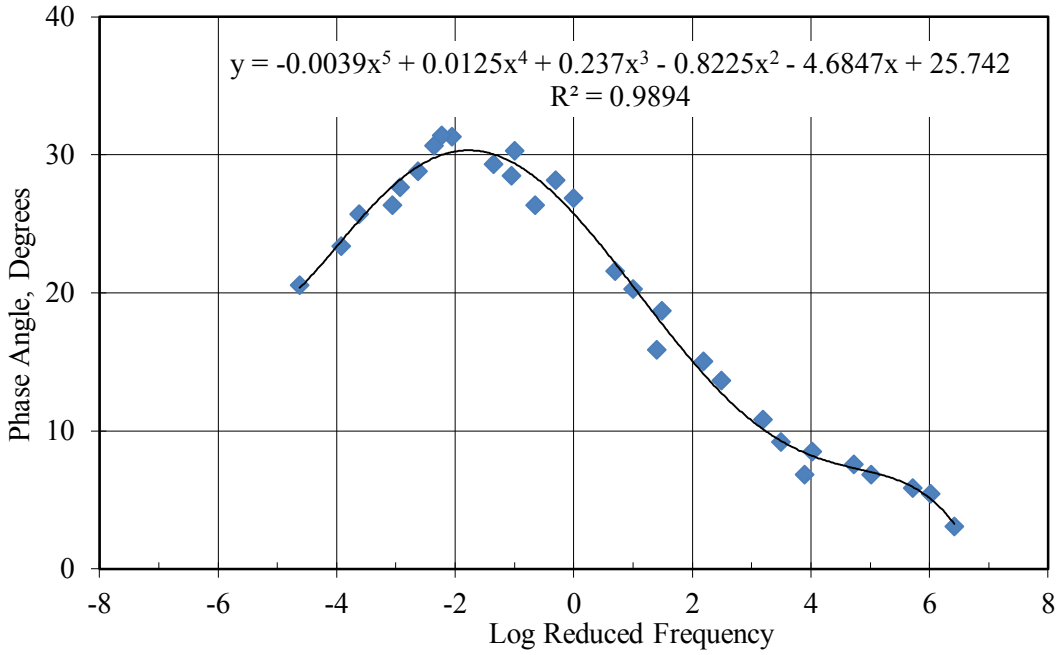

Figure C.12 Phase angle versus reduced frequency (PennDot I-78 PG76-22)

Table C.4 Dynamic Modulus Data (PennDOT I-78 PG76-22)

Temp.	Freq.	Dynamic Modulus, |E*| (MPa)						Phase Angle, ϕ (degree)					
°C	Hz	Rep1	Rep2	Rep3	Avg. |E*|	St. Dev.	%CV	Rep1	Rep2	Rep3	Avg. ϕ	St. Dev.	%CV
-10	25	36174	36632	32456	35087	2290	7	3.7	2.2	3.4	3.1	0.8	25
	10	34875	34899	31232	33669	2110	6	5.4	4.7	6.3	5.5	0.8	15
	5	33361	33799	30112	32424	2014	6	6.5	4.7	6.5	5.9	1.0	18
	1	30846	31041	27758	29882	1842	6	7.3	6.0	7.3	6.8	0.8	11
	0.5	29530	29848	26558	28645	1815	6	7.5	7.0	8.3	7.6	0.7	9
	0.1	26036	26117	23587	25247	1438	6	8.9	7.2	9.5	8.5	1.2	14
4.4	25	22755	24065	22442	23087	861	4	6.9	6.9	6.6	6.8	0.2	2
	10	20662	21715	20279	20885	744	4	9.4	9.8	8.4	9.2	0.7	8
	5	18981	19278	18667	18975	306	2	11.1	10.6	10.8	10.8	0.3	2
	1	15822	16138	15332	15764	406	3	13.2	13.7	14.0	13.6	0.4	3
	0.5	14442	14666	13845	14318	424	3	15.7	14.6	14.9	15.0	0.6	4
	0.1	11152	11049	10504	10902	348	3	18.2	18.5	19.4	18.7	0.6	3
21	25	10203	10246	9694	10048	307	3	16.1	16.1	15.5	15.9	0.3	2
	10	8497	8571	8427	8498	72	1	19.3	20.4	21.2	20.3	1.0	5
	5	7332	7435	7305	7357	69	1	21.3	21.8	21.7	21.6	0.2	1
	1	5073	5116	5043	5077	37	1	26.4	26.4	27.8	26.9	0.8	3
	0.5	4290	4275	4241	4269	25	1	27.7	27.6	29.1	28.2	0.8	3
	0.1	2765	2755	2732	2751	17	1	29.5	30.4	31.1	30.3	0.8	3
37.8	25	3812	3182	3485	3493	315	9	24.2	27.7	27.2	26.4	1.9	7
	10	2860	2348	2598	2602	256	10	27.1	30.0	28.4	28.5	1.4	5
	5	2260	1855	2076	2064	203	10	28.8	30.1	29.0	29.3	0.7	2
	1	1267	1016	1153	1145	126	11	31.7	32.4	29.8	31.3	1.3	4
	0.5	998	799	931	909	101	11	31.1	31.9	29.1	30.7	1.5	5
	0.1	625	485	604	571	76	13	28.1	26.5	24.5	26.3	1.8	7
54.4	25	1194	980	1183	1119	121	11	33.0	30.5	30.8	31.4	1.4	4
	10	865	692	833	797	92	12	32.3	26.9	27.4	28.8	3.0	10
	5	696	551	638	628	73	12	30.5	25.7	26.7	27.6	2.6	9
	1	404	331	335	357	41	12	28.9	23.2	25.0	25.7	2.9	11
	0.5	340	283	277	300	35	12	26.7	21.2	22.4	23.4	2.9	12
	0.1	263	216	202	227	32	14	26.5	18.4	16.9	20.6	5.2	25

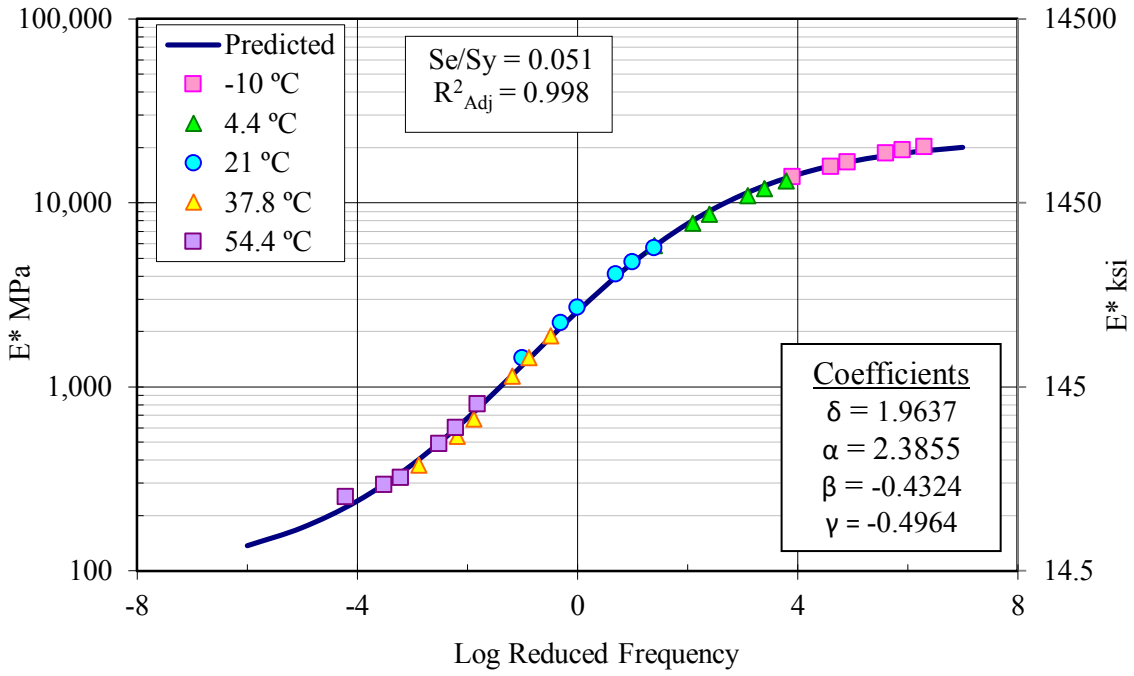

Figure C.13 Dynamic modulus master curve (PennDot I-78 PG64-22 AR)

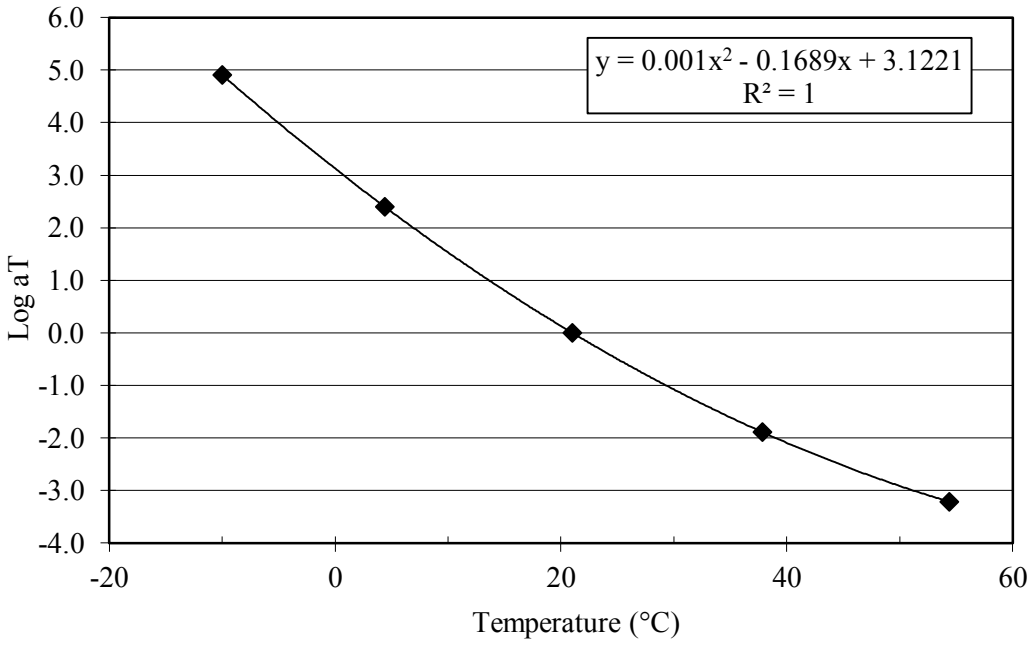

Figure C.14 MC shift factors versus temperature (PennDot I-78 PG64-22 AR)

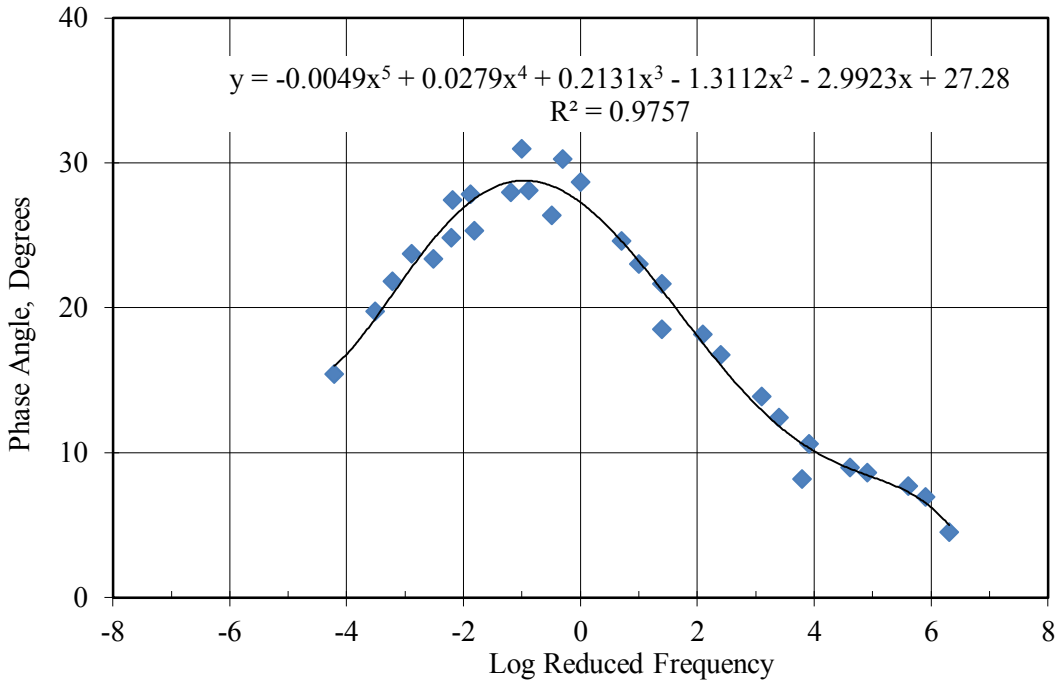

Figure C.15 Phase angle versus reduced frequency (PennDot I-78 PG76-22)

Table C.5 Dynamic Modulus Data (PennDOT I-78 PG76-22 Asphalt Rubber)

Temp.	Freq.	Dynamic Modulus, |E*| (MPa)						Phase Angle, ϕ (degree)					
°C	Hz	Rep1	Rep2	Rep3	Avg. |E*|	St. Dev.	%CV	Rep1	Rep2	Rep3	Avg. ϕ	St. Dev.	%CV
-10	25	24681	19240	16650	20190	4099	20	4.3	3.8	5.3	4.5	0.8	17
	10	23312	18623	16025	19320	3693	19	6.3	7.1	7.4	6.9	0.6	8
	5	22228	17953	15357	18513	3470	19	7.4	7.2	8.5	7.7	0.7	9
	1	19949	15959	13731	16546	3150	19	8.0	8.5	9.4	8.6	0.7	8
	0.5	18905	15243	13111	15753	2930	19	8.8	8.7	9.4	9.0	0.4	4
	0.1	16490	13459	11547	13832	2493	18	10.5	10.5	10.9	10.6	0.3	2
4.4	25	14961	13446	11087	13165	1952	15	8.6	7.5	8.4	8.2	0.6	8
	10	13347	12358	10313	12006	1547	13	12.7	12.2	12.4	12.4	0.3	2
	5	12022	11312	9587	10974	1252	11	15.7	13.3	12.6	13.9	1.6	12
	1	9326	9041	7695	8687	871	10	18.8	15.6	16.0	16.8	1.8	10
	0.5	8272	8131	6975	7793	712	9	20.8	16.2	17.4	18.1	2.4	13
	0.1	6007	6225	5351	5861	455	8	24.3	19.9	20.8	21.7	2.3	11
21	25	5913	5867	5215	5665	390	7	21.0	17.1	17.4	18.5	2.2	12
	10	4985	4878	4382	4748	322	7	25.1	22.1	21.9	23.0	1.8	8
	5	4263	4176	3822	4087	234	6	26.7	23.5	23.7	24.6	1.8	7
	1	2761	2804	2530	2698	147	5	31.2	26.2	28.6	28.7	2.5	9
	0.5	2297	2302	2099	2233	116	5	32.1	28.5	30.3	30.3	1.8	6
	0.1	1479	1480	1352	1437	74	5	32.7	28.9	31.4	31.0	1.9	6
37.8	25	2021	1833	1844	1899	106	6	28.3	24.6	26.3	26.4	1.8	7
	10	1551	1387	1390	1443	94	7	29.9	26.8	27.7	28.1	1.6	6
	5	1212	1105	1104	1140	62	5	29.1	27.2	27.6	28.0	1.0	4
	1	713	657	642	671	37	6	28.5	27.6	27.5	27.8	0.5	2
	0.5	572	529	516	539	29	5	27.2	27.3	27.9	27.5	0.3	1
	0.1	409	368	353	377	29	8	23.7	24.0	23.5	23.7	0.3	1
54.4	25	816	814	775	802	23	3	27.3	24.9	23.6	25.3	1.9	7
	10	602	603	587	597	9	2	23.7	26.6	24.1	24.8	1.6	6
	5	508	491	476	492	16	3	21.9	26.0	22.2	23.4	2.3	10
	1	332	326	302	320	16	5	20.6	23.4	21.5	21.8	1.4	6
	0.5	300	317	266	294	26	9	18.5	21.1	19.7	19.8	1.3	7
	0.1	254	286	216	252	35	14	13.9	15.4	17.0	15.4	1.5	10

Table C.6 Asphalt binder test data for PG70-10 (ADOT mixture)

Test	Temp (°C)	Temp (R)	Log Temp (R)	Pen (.1mm)	Viscosity (Poise)	Viscosity (cP)	Log Log Visc (cP)
Penetration	13.0	515.1	2.712	*6.20*	5.16E+08	5.16E+10	1.030
Penetration	25.0	536.7	2.730	*23.20*	2.64E+07	2.64E+09	0.974
Penetration	32.0	549.3	2.740	*47.40*	5.31E+06	5.31E+08	0.941
Softening Point, F	52.0	585.3	2.767	---	13,000	1.30E+06	0.786
Viscosity, cP	93.3	659.7	2.819	---	106	*1.06E+04*	0.605
Viscosity, cP	121.1	709.7	2.851	---	13.3	*1.33E+03*	0.495
Viscosity, cP	148.9	759.7	2.881	---	3.12	*3.12E+02*	0.397
Viscosity, cP	176.7	809.7	2.908	---	1.07	*1.07E+02*	0.307

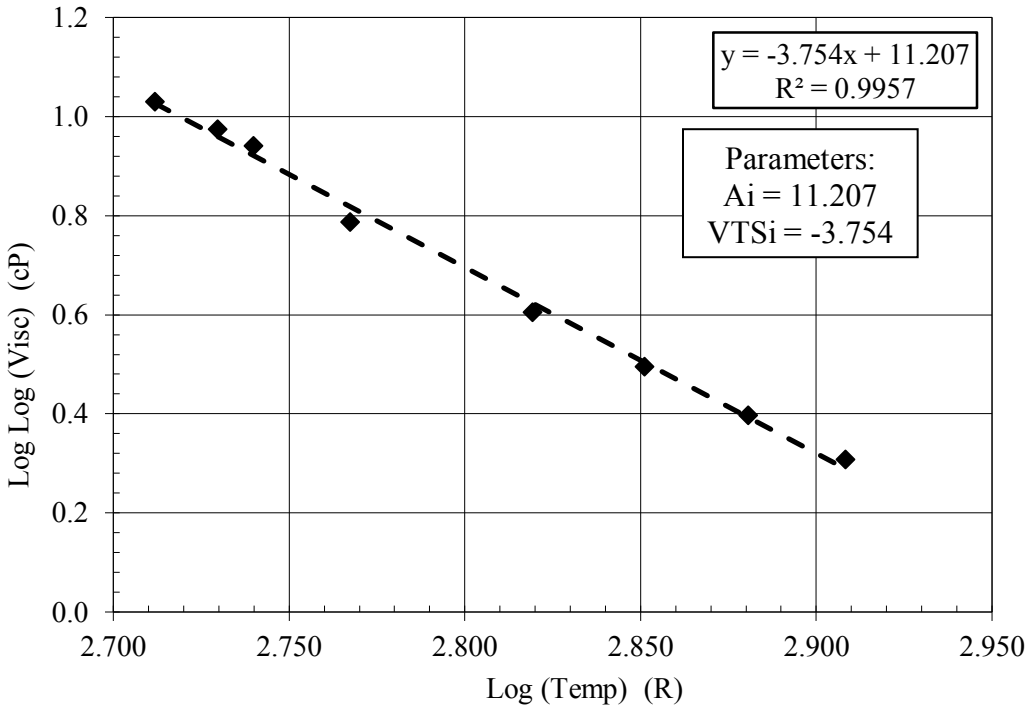

Figure C.16 Temperature-viscosity relationship for PG70-10 binder (ADOT mixture)

Table C.7 Indirect Tensile Test Results (ADOT mixture)

Specimen	Temp °C	Air Voids %	Tensile Strength			Total Fracture Energy		
			S_t kPa	Ave.	C.V.	G_f kJ/m^2	Ave.	C.V.
CS25B	21	5.8	2753	2700	2.8%	6.313	6.756	9.3%
CS29T	21	5.4	2647			7.198		
CS25T	4.4	5.8	4175	3708	17.8%	4.781	4.245	17.9%
CS29B	4.4	6.1	3241			3.709		

Table C.8 Indirect Tensile Test Results (PA Cranberry Township mixture)

Mixture	Specimen	Ave. t (mm)	Air Voids %	Tensile Strength			Total Fracture Energy		
				S_t kPa	Ave.	C.V.	G_f kJ/m^2	Ave.	C.V.
Control	PAC09T	50.1	5.96	2780	2725	3.4%	5.861	5.964	17.2%
	PAC09M	51.0	6.22	2619			7.038		
	PAC09B	51.6	6.30	2777			4.993		
Fiber	PAF10T	52.4	5.68	2641	2582	2.0%	6.612	6.742	2.4%
	PAF10M	51.2	6.17	2556			6.923		
	PAF10B	53.2	6.87	2548			6.692		

Table C.9 Indirect Tensile Test Results (PennDOT I-78 mixture)

Mixture	Specimen	Ave. t (mm)	Air Voids %	Tensile Strength			Total Fracture Energy		
				S_t kPa	Ave.	C.V.	G_f kJ/m^2	Ave.	C.V.
9.5 mm PG 76-22	PWC6B	52.4	6.23	2992	3267	7.4%	8.222	8.617	6.6%
	PWC6M	51.0	5.86	3362			8.362		
	PWC6T	52.8	5.82	3448			9.268		
12.5 mm PG 64-22 AR	PWR4B	52.3	5.88	2219	2107	6.6%	15.253	15.281	5.9%
	PWR4M	50.2	6.21	2149			16.199		
	PWR4T	49.4	6.22	1952			14.392		

APPENDIX D

D. PROPOSED C* FRACTURE TEST PROTOCOL

Proposed standard practice for

C* FRACTURE TEST TO ASSESS CRACK PROPAGATION IN ASPHALT CONCRETE

AASHTO Designation: TP XX-XX

1. SCOPE

1.1. This test method covers procedures for preparing and testing hot mix asphalt (HMA) to determine crack propagation using the C* Fracture Test.

1.2. This applies to mixtures with nominal maximum size aggregate less than or equal to 19 mm (0.75 in). Specimens shall be 50 ± 3 mm (1.97 ± 0.12 in) high and 150 ± 1 mm (5.91± 0.4 in) in diameter.

1.3. *This standard may involve hazardous materials, operations and equipment. This standard does not address all of the safety problems associated with its use. It is the responsibility of the user of this procedure to establish appropriate safety and health practices and to determine the applicability of regulatory limitations prior to its use.*

2. REFERENCED DOCUMENTS

2.1. *AASHTO Standards:*

- T 166, Bulk Specific Gravity of Compacted Hot Mix Asphalt (HMA) Using Saturated Surface-Dry Specimens.
- T 312, Preparing and Determining the Density of Hot Mix Asphalt (HMA) Specimens by Means of the Superpave Gyratory Compactor
- T 322-07, Determining the Creep Compliance and Strength of Hot Mix Asphalt (HMA) Using the Indirect Tensile Test Device.

3. DEFINITIONS

3.1. *CFT* – C* fracture test.

3.2. *C* Parameter* –energy rate line integral used to describe the stress and strain rate field surrounding the crack tip in a viscous material.

3.3. *U** – power or energy release rate for a given load, P and displacement rate.

3.4. *a** - crack growth rate measured as a function of time.

3.5. *Gyratory specimen* – Nominal 150 mm diameter by 180 mm high cylindrical specimen prepared using a Gyratory compactor in accordance with AASTHO T 312.

3.6. *Notched-disk specimen* – disk shaped test specimen with right angle notch cut diametrically to accommodate CFT loading apparatus.

3.7. *Kerf* – width of cut produced by a saw blade.

4. SUMMARY OF TEST METHOD

4.1. The C* Fracture Test is a crack propagation test in which a notched disk specimen is loaded diametrically under a constant displacement rate. Crack length and associated load are measured as a function of time during the duration of the test. Recorded values are used to obtain the fracture mechanics based C* parameter and crack growth rate. Figure 1 exhibits the schematic of the C* fracture test.

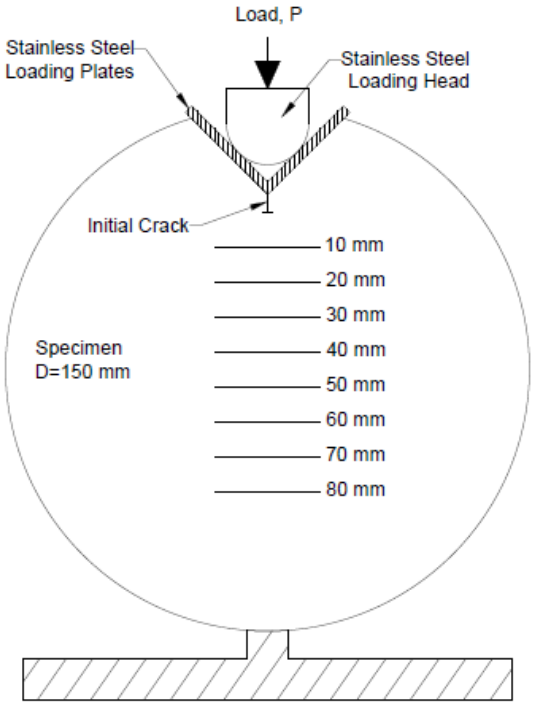

Figure 1 – Schematic of the C* Fracture Test

5. SIGNIFICANCE AND USE

5.1. This practice describes the procedure to perform the C* fracture test under constant actuator displacement rate loading to determine the C* parameter and crack growth rate.

5.2. The relationship between crack growth rate and C* can be used to rank asphalt concrete mixtures resistance to crack propagation.

6. APPARATUS

6.1. *C* fracture test system* – consists of a servo-hydraulic testing machine, environmental chamber, and video recording system.

6.2. *Test machine* – A servo hydraulic test machine should be capable of producing controlled actuator displacement rates between 0.05 to 2.0 mm/min (0.002 to 0.079 in/min) and loads up to 20 kN (4,500 lbf).

6.3. *Environmental chamber* – Chamber shall be capable of controlling test specimen temperature to desired test temperature from 0°C to 32°C (32°F to 90°F), within

±0.5°C (±1°F). Chamber must be able to accommodate five test specimens plus a temperature sensor specimen.

6.4. *Control and data acquisition system* – System shall be computer controlled and capable of measuring and recording the time history of the applied load and actuator displacement. Test system shall meet the minimum requirements detailed in Table 1.

Table 1 – Test System Minimum Requirements

Measurement	Range	Accuracy
Load	±0.12 to ±25 kN	Error ≤ 1.0 %
Deformation	At least 12 mm	Error ≤ 0.03 mm
Temperature	0°C to 32°C (32°F to 90°F)	±0.5°C (1°F)

6.5. *Video recording equipment* – a high definition video camera shall be used to record crack length as a function of elapsed time during the test.

6.6. *Load measurement* – a load cell shall be used to measure the applied load during the duration of the test and data and recoded using a computer system. The load cell shall have a minimum range of ±25 kN (± 5,600 lbs).

6.7. *Loading fixture and plates*– the load apparatus shall utilize a 150 mm (6 in) Lottman Breaking Head assembly or IPC AMPT Indirect Tensile Jig with modifications described herein. The curved top platen shall be removed from the load plate and a new loading platen shall be manufactured of stainless steel according to Figure 2 and fastened to the top load plate using existing bolts and holes. Loading plates (Figure 2) shall be manufactured of stainless steel and shall be 3 mm (0.12 in) thick by 54 mm (2.13 in) long. One long edge on each plate shall have a machined, 45 degree angle in order to form a 90 degree loading wedge. Final loading assembly for the C* fracture test shall be similar to Figure 3.

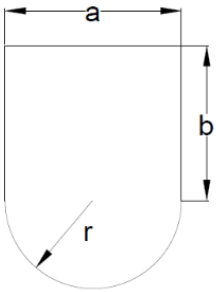

Specimen Diameter (mm)	Loading Head Dimension (mm)		
	a	b	r
150	25.3	19.8	12.65

Load Platen Side View

Load Plate Side View

Figure 2 – Modified load platen and plates for the C* fracture test.

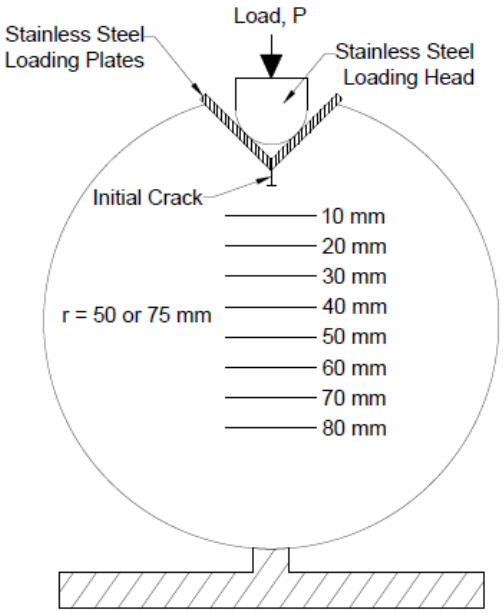

Figure 3 – Final load setup for C* fracture test.

6.8. *Compaction equipment* – Gyratory compaction equipment shall be used to compact all laboratory specimens. Equipment shall be capable of producing specimens 150 mm (5.9 in) in diameter by 180 mm (7.1 in) high.

6.9. *Sawing equipment* – a water cool saw with diamond blade shall be used to cut the notched disk specimens from gyratory specimens and to cut the right-angle notch. The saw blade diameter shall be 408 mm (16 in).

Note 1 – A 358 mm (14 in) diameter blade can be used when equipment limitations exist, however, this size blade is not ideal it cannot fully cut a 150 mm (6 in) diameter specimen.

---

7. HAZARDS

7.1. Ensure compliance with all laboratory safety procedures associated with specimen preparation and performing the C* fracture test.

---

8. EQUIPMENT CALIBRATION

8.1. Test system components shall be calibrated prior to initial use and in accordance with manufacturer recommendations.

8.2. Capability of the environmental chamber to maintain required temperature and accuracy shall be verified periodically.

8.3. Calibration the load cell and actuator LVDT of the test system shall be verified.

8.4. If equipment calibration yields data outside accuracy requirements, correct problems prior to further testing.

---

9. TEST SPECIMEN PREPARTION

9.1. *Aging* – Laboratory prepared mixtures shall be temperature-conditioned in accordance with AASHTO R-30. Field mixtures do not require short-term aging prior to compaction and testing.

9.2. *Size* – Laboratory test specimens subjected to C* fracture testing shall be cut from gyratory compacted specimens compacted to 150 mm (6 in) in diameter and 170 mm (6.7 in) in height. Average specimen height shall be 50 ± 3 mm (1.97 ± 0.12 in) and average diameter shall be 150 ± 1 mm (5.91± 0.04 in). Standard deviation of thickness shall not exceed 0.75 mm (0.3 in). End perpendicularity shall not exceed 1 mm (0.04 in) and end flatness shall not exceed 1 mm (0.04 in).

Note 2 – It is recommended to cut two notched disk specimens from the center of a single 170 mm (6.7 in) high gyratory specimen. This produces specimens with uniform air void distribution and also provides sufficient surface area to secure the specimen to cut uniform disks. In the case where field mixture is limited; three specimens can be cut from a 180 mm (7.1 in) high gyratory specimen. However, extreme care must be taken to meet required specimen tolerances.

Note 3 – A gyratory specimen should be securely fastened prior to cutting notched disk specimens using a core clamp manufactured by HMA Lab Supply, Inc. (or similar) as shown in Figure 4. It is important to note that a 358 mm (14 in) diameter saw blade will not fully cut through a gyratory specimen. If equipment limitations do not allow a larger diameter saw blade, use extreme care when rotating the specimen to finish the cut. Ensure that recommended specimen tolerances are met.

Figure 4 – Core clamp assembly.

9.3. *Notch* – a right angle notch shall be introduced vertically into the specimen to facilitate the loading plates and head. The notch shall be introduced using a water-cooled, diamond blade saw. The vertical, right angle notch shall be 25 ± 2 mm (1.0 ± 0.08 in) deep and the sides shall be 45 ± 2 degrees from the centerline as presented in Figure 5.

Note 4 –A transparent template is recommended for marking the vertical notch and specimen centerline. Secure disk specimen vertically using appropriate fixture prior to sawing. The notch is best cut by aligning one face of the notch vertically with the saw blade then rotating 90 degrees and vertically cutting the second face.

9.4. *Initial crack* – an initial crack shall be introduced at the bottom of the right angle notch using a diamond coated scroll saw blade. The blade shall be approximately 100 mm (4 in) in length and shall have a 1.6 mm (0.063 in) final cut thickness (kerf). The notch shall be introduced vertically to a depth of 3 ± 1 mm (0.12 ± 0.04 in)

Note 5 – Scroll saw blades manufactured by Kent Blades were found to be sufficient to introduce the initial crack to the specimen.

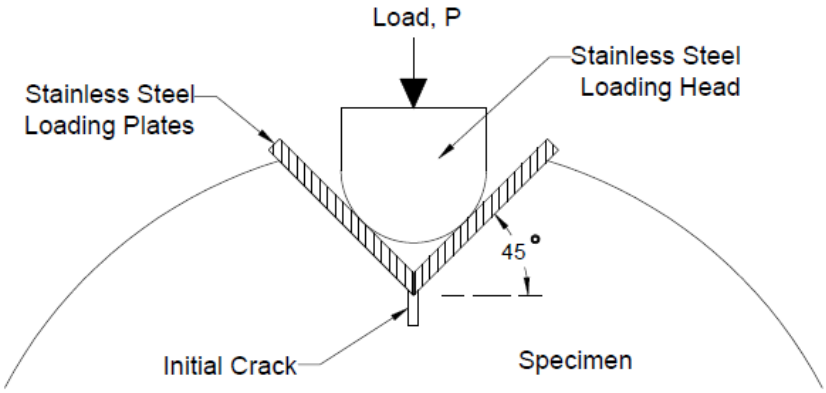

Figure 5 – Schematic of vertical notch and initial crack.

9.5. *Surface painting* – the surface of the specimen shall be painted white to facilitate crack length measurements. Acrylic paint shall be applied in two coats following dry time recommendations provided by the manufacturer. Cover approximately 40 mm (1.6 in) on each side of the specimen centerline for entire specimen height.

Note 6 – Acrylic paint from JoAnn Fabric Products was sufficient to view and record crack length. It is important to note that latex paint or other

paints with crack resistance properties should not be used as it can mask crack growth on the specimen surface.

9.6. *Crack length reference system*– using the transparent template, mark crack length reference lines at 10 mm (0.4 in) increments vertically from the tip of the initial crack to the bottom of the specimen. Mark lines according to length (e.g. 10 mm, 20 mm, etc.). Lines shall be dark and visible from approximately 310 mm (12 in).

9.7. *Replicates* – Two replicates are recommended at each loading rate in a C* fracture test sequence.

Note 7 – If five or more loading rates are used in a C* fracture test sequence, one replicate at each loading rate is sufficient. However, two replicates will produce a more reliable crack growth rate data.

9.8. *Sample storage* – If test specimens are not tested within three days, place specimens in sealed storage bags out of direct sunlight and store for up to one month.

9.9. *Final test specimen* – the final test specimen prepared for the C* fracture test shall be similar to schematic presented in Figure 6.

Figure 6 – Final C* fracture test specimen.

10. TEST PRODEDURE

10.1. Condition specimens in environmental chamber and allow sufficient time to reach to desired test temperature ±0.5°C (±1°F).

> **Note 8** – A temperature of 10°C (50°F) is recommended for general comparison between mixtures. However, it is recommended that the CFT test should be conducted at several temperatures in order to establish a crack growth rate master curve. Temperature range selection shall be such that the dynamic modulus value at 0.1 Hz test frequency is in the range of 5,000 to 17,000 MPa (725 to 2,466 ksi).

10.1. Place test specimen in loading apparatus such that it is aligned vertically and horizontally under the loading head.

10.2. Apply frictionless grease to upward faces of loading plates and place them into specimen notch such that the plates form a 90° angle at the tip.

10.3. Manually seat loading head into plates and ensure contact. Re-align loading plates to ensure contact between plates, specimen and loading head.

10.4. Zero the load cell prior to applying any load or aligning load apparatus under actuator.

10.5. Align specimen and loading apparatus under actuator center.

10.6. Place video recording equipment such that the specimen face is clearly visible and adjust zoom to capture notch tip and crack length markings.

> **Note 9** – It is recommended that a stand or fixture be used for the camera to ensure similar alignment during each test and to reduce temperature loss while preparing a specimen. Also, a light should be used to illuminate the specimen face to provide better visualization of crack lengths. Use of

LED light is not recommended as the reflection on the white paint hinders observation of crack length.

10.7. Allow 15 to 30 minutes for re-conditioning of specimen to desired temperature.

10.8. Select initial actuator displacement rates based on the following equation:

$$\dot{\Delta}_t = 3.3945 * e^{-0.0003*(E^*_{01})} \qquad R^2 = 0.97$$

For: 5,000 MPa < E^*_{01} < 17,000 MPa **Eq. 1**

For: $\dot{\Delta}_t$ between 0.06 - 1.2 mm/min

(Target a* = 2.0 m/hr @ Δ^*_i)

Where:

Δ^*_i = initial displacement rate of test sequence (mm/min), and

E^*_{01} = dynamic modulus value at test temperature (0.1 Hz).

Note 10 – It is recommended to select a range of displacement rates for the C* fracture to target crack growth rates between 1 and 15 m/hr (3.3 to 49.2 ft/hr). The aforementioned equation was developed based on a target initial crack growth rate of 2.0 m/hr. If dynamic modulus data are not available from laboratory tests or predictive equations, initial loading rates of 0.15 and 0.30 mm/min can be used at 4.4°C and 10°C, respectively.

10.9. Apply a 0.2 kN (45 lbf) or less seating load to ensure contact with specimen. Ensure that actuator displacement control is selected and begin test at selected constant displacement rate along with video recording.

10.10 Visually monitor crack growth during the test and terminate test and video recording when crack exceeds the 80 mm (3.15 in) and the applied load is less than 0.5 kN (112.4 lbf).

Note 11 – Crack should begin at or beyond peak load and will grow as load is decreased. If the crack deviates from centerline and does not return to within 12.5 mm (1 in) of either side of the centerline by the 80 mm (3.15 in) mark, discard test results.

10.11 Repeat test procedure on additional samples using different loading rates.

11. CALCULATIONS

11.1. Adjust video quality to gain a clear visualization of crack and marking lines on a computer monitor using video editing software. From the video, record average time at which the crack passes each mark on the specimen face using two separate views of the video.

Note 12 – If slight crack branching occurs, use the length of the main crack observed in the specimen. If more than two cracks appear, discard the specimen results.

11.2. Calculate the crack growth rate (a*) as the slope of the crack length versus time data in the average 20 to 80 mm (0.8 to 3.2 in) interval.

11.2. From the load-time test data collected, extract the load at times corresponding to each crack length interval and normalize by average specimen thickness.

11.3. Sort normalized load by crack length and applied displacement rate data similar to Table 2.

Table 2 – Example of sorted data.

P, (N/mm)					
Crack Length (mm)	Displacement Rate, (mm/min)				
	0.150	0.228	0.300	0.378	0.450
20	$P_{20, 0.15}$	$P_{20, 0.228}$	$P_{20, 0.30}$	$P_{20, 0.378}$	$P_{20, 0.45}$
30	$P_{30, 0.15}$	$P_{30, 0.228}$	$P_{30, 0.30}$	$P_{30, 0.378}$	$P_{30, 0.45}$
40	.	.	.	.	.
50	.	.	.	.	.
60	.	.	.	.	.
70	.	.	.	.	.
80	$P_{80, 0.15}$	$P_{80, 0.228}$	$P_{80, 0.30}$	$P_{80, 0.378}$	$P_{80, 0.45}$

11.5. Calculate the energy release rate (U*) according to the following equation for each crack length (a):

$$U_i^* = 0.8 * P_i * \dot{\Delta}_i \quad \text{For i = 1}$$

$$U_{i+1}^* = U_i^* + \frac{(P_{i+1}+P_i)}{2} * (\Delta_{i+1}^* - \Delta_i^*) \quad \text{For i = 2 to n} \qquad \textbf{Eq. 2}$$

Where:

U* = energy release rate for each crack length (N-mm/mm-min),

P = normalized load at each crack length and displacement rate (N/mm),

Δ^*_i = initial displacement rate of test sequence (mm/min), and

Δ^*_{i+1} = subsequent displacement rate of test sequence (mm/min).

11.5. Plot the U* values versus crack lengths (a) for each displacement rate as shown in Figure 7.

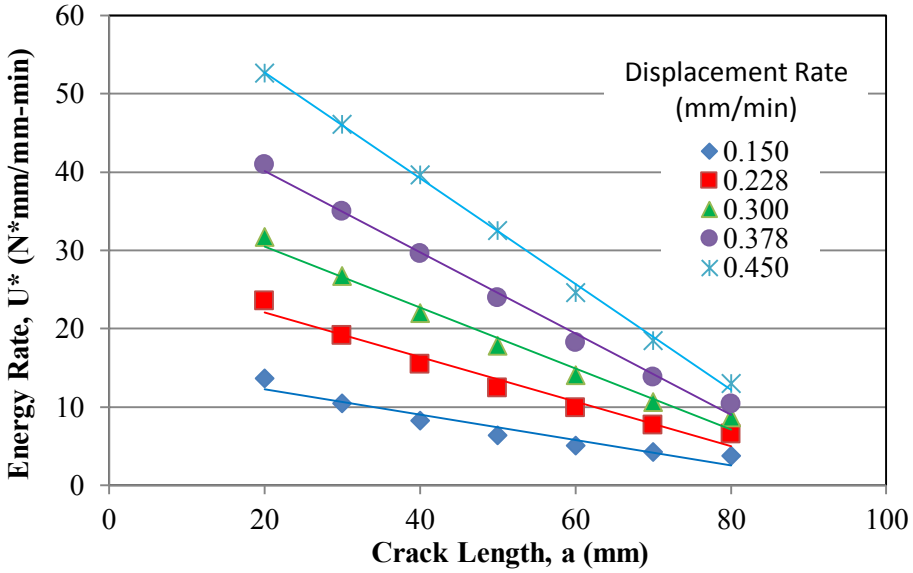

Figure 7 – Example plot of U* versus crack length.

11.6. The C* parameter (MJ/m^2-hr) for each displacement rate is determined by calculating the slope of a linear fit of the U* and crack length data between 20 and 80 mm (0.8 to 3.2 in) crack lengths.

11.7. Plot the relationship between crack growth rate, a* (y-axis) and the C*-parameter (x-axis) on a log-log scaled chart and fit data using a power function as shown in Figure 8. If R^2 falls below 0.80 consider testing replicate specimens at each displacement rate and recalculate the a*-C* relationship.

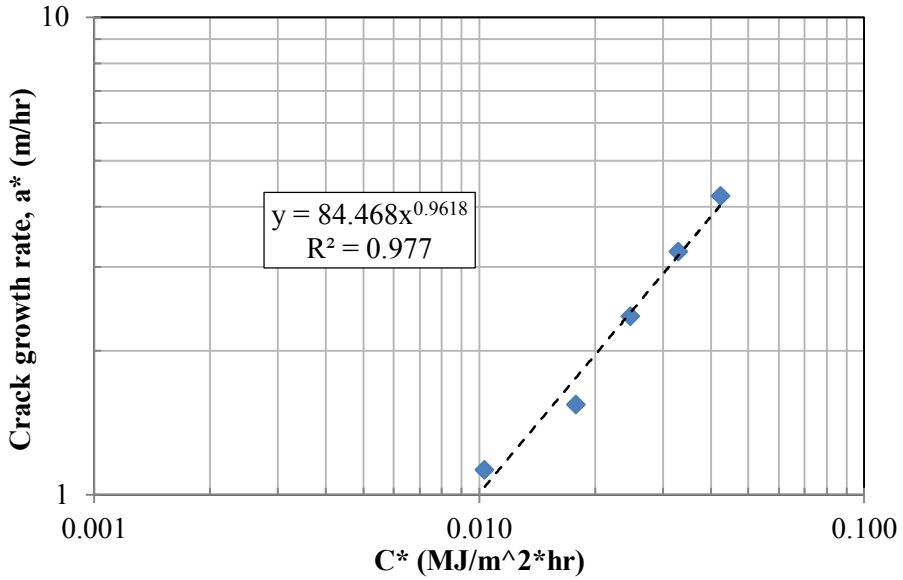

Figure 8 – Example plot crack growth rate relationship to the C*.

---

12. REPORT

12.1. HMA mixture properties.

12.2. Specimen dimensions.

12.3. C* Fracture Test: displacement rates, C*-parameters, crack growth rates. (Report average, standard deviation and coefficient of variation values if multiple replicates are tested at each displacement rate)

12.4. Plot of relationship between crack growth rates and C* parameter showing power model fit of data and coefficients.